รายงานวิจัยฉบับสมบูรณ์

โครงการเครื่องปฏิกรณ์แบบหลายหน้าที่สำหรับอุตสาหกรรมเคมีและปิโตรเคมี

โดย ศาสตราจารย์ ดร. สุทธิชัย อัสสะบำรุงรัตน์

พฤษภาคม 2551

สัญญาเลขที่ RMU4880017

รายงานวิจัยฉบับสมบูรณ์

โครงการเครื่องปฏิกรณ์แบบหลายหน้าที่สำหรับอุตสาหกรรมเคมีและปิโตรเคมี

ผู้วิจัย

ศาสตราจารย์ ดร. สุทธิชัย อัสสะบำรุงรัตน์

สังกัด

ภาควิชาวิศวกรรมเคมี

คณะวิศวกรรมศาสตร์

จุฬาลงกรณ์มหาวิทยาลัย

สนับสนุนโดยสำนักงานกองทุนสนับสนุนการวิจัย

(ความเห็นในรายงานนี้เป็นของผู้วิจัย สกว.ไม่จำเป็นต้องเห็นด้วยเสมอไป)

Abstract

Project Code: RMU4880017

Project Title: Multifunctional Reactors for Chemical and Petrochemical Industries

Investigator: Professor Suttichai Assabumrungrat,
Department of Chemical Engineering, Faculty of Engineering,
Chulalongkorn University

Email: Suttichai.A@chula.ac.th

Project Period: 1 August 2005 – 31 July 2008

This project was aimed to develop new basic knowledge related to multifunctional reactors for chemical and petrochemical industries. The works were focused on 3 sub-research topics including 1) Study on fuel cells, 2) Study on reaction and extraction system and 3) Study on periodic operation. From the works, 15 international papers have been accepted for publication and 3 international papers are under consideration. In addition, 5 papers were presented in international conferences. The followings summarize the lists of all outputs.

International Papers

1) W. Jamsak, S. Assabumrungrat, P.L. Douglas, N. Laosiripojana and S. Charojrochkul, "Theoretical Performance Analysis of Ethanol-Fueled Solid Oxide Fuel Cells with Different Electrolytes", Chemical Engineering Journal 119 (2006) 11–18. (IF-2006 = 1.594).
2) S. Assabumrungrat, N. Laosiripojana and P. Philunrekekun, "Determination of Boundary of Carbon Formation for Dry Reforming of Methane in Solid Oxide Fuel Cell", Journal of Power Sources, vol. 159 (2006) 1274-1282 (IF-2006 = 3.521).
3) Eakkapon Promaros, Suttichai Assabumrungrat, Navadol Laosiripojana, Piyasan Praserthdam, Tomohiko Tagawa and Shigeo Goto, "Carbon dioxide reforming of methane under periodic operation", Korean Journal of Chemical Engineering 24 (2007) 44-50 (IF-2006 = 0.808).
4) Garun tanarungsun, Worapon Kiatkittipong, Suttichai Assabumrungrat, Hiroshi Yamada, Tomohiko Tagawa and Piyasan Prasertdam, "Fe (III), Cu (II), V (V)/TiO2 for hydroxylation

of benzene to phenol with hydrogen peroxide at room temperature", Journal of Chemical Engineering of Japan, vol. 40 (2007) 415-421 (IF-2006 = 0.594).

5) Garun Tanarungsun, Worapon Kiatkittipong, Suttichai Assabumrungrat, Hiroshi Yamada, Tomohiko Tagawa and Piyasan Prasertdam, "Liquid phase hydroxylation of benzene to phenol with hydrogen peroxide catalyzed by Fe (III)/TiO_2 catalysts at room temperature", Journal of Industrial & Engineering Chemistry, vol. 13 (2007) 444-451 (IF-2006 = 0.957).
6) S. Vivanpatarakij, S. Assabumrungrat and N. Laosiripojana, "Improvement of SOFC performance by using non-uniform cell potential operation", Journal of Power Sources, vol. 167 (2007) 139-144 (IF-2006 = 3.521).
7) W. Jamsak, S. Assabumrungrat, P.L. Douglas, N. Laosiripojana, R. Suwanwarangkul, S. Charojrochkul and E. Croiset "Performance Assessment of Bioethanol-Fed Solid Oxide Fuel Cell System Integrated with a Distillation Column", ECS Transactions - Solid Oxide Fuel Cells vol. 7 (2007) 1475-1482 (IF-2006 = -).
8) W. Jamsak, S. Assabumrungrat, P.L. Douglas, N. Laosiripojana, R. Suwanwarangkul, S. Charojrochkul and E. Croiset "Performance of Ethanol-Fueled Solid Oxide Fuel Cells: Proton and Oxygen Ion Conductors", Chemical Engineering Journal, vol. 133/1-3 (2007) 187-194 (IF-2006 = 1.594).
9) Garun Tanarungsun, Worapon Kiatkittipong, Suttichai Assabumrungrat, Hiroshi Yamada, Tomohiko Tagawa and Piyasan Prasertdam, "Multi transition metal catalysts supported on TiO_2 for hydroxylation of benzene to phenol with hydrogen peroxide", Journal of Industrial & Engineering Chemistry, vol. 13 (2007) 870-877 (IF-2006 = 0.957).
10) W. Jamsak, S. Assabumrungrat, P.L. Douglas, E. Croiset, N. Laosiripojana, R. Suwanwarangkul and S. Charojrochkul, "Thermodynamic Assessment of Solid Oxide Fuel Cell System Integrated with Bioethanol Purification Unit", Journal of Power Sources, vol. 174 (2007) 191-198 (IF-2006 = 3.521).
11) W. Sangtongkitcharoen, S.Vivanpatarakij, N. Laosiripojana, A. Arpornwichanop and S. Assabumrungrat, "Performance analysis of methanol-fueled solid oxide fuel cell system incoporated with palladium membrane reactor", Chemical Engineering Journal, vol. 138 (2008) 436-441 (IF-2006 = 1.594).
12) Garun tanarungsun, Worapon Kiatkittipong, Suttichai Assabumrungrat, Hiroshi Yamada, Tomohiko Tagawa and Piyasan Prasertdam, "Hydroxylation of benzene to phenol on Fe/TiO_2

catalysts loaded with different types of second metal", Catalysis Communications, Vol. 9 (2008) 1886-1890 (IF-2006 = 1.878).

13) Hiroshi YAMADA, Tomoaki MIZUNO, Tomohiko TAGAWA, Garun TANARUNGSUN, Piyasan PRASERTHDAM and Suttichai ASSABUMRUNGRAT "Catalyst Regenerator for Partial Oxidation of Benzene in Reaction-Extraction System" Journal of the Japan Petroleum Institute, vol. 51 (2008), 114-117. (IF-2006 = 0.633)

14) P. Philunrekekun, S. Assabumrungrat, N. Laosiripojana and A.A. Adesina, "Selection of appropriate fuel processor for biogas-fuelled SOFC system", Chemical Engineering Journal, in press (IF-2006 = 1.594).

15) Garun Tanarungsun, Worapon Kiatkittipong, Suttichai Assabumrungrat, Hiroshi Yamada, Tomohiko Tagawa and Piyasan Prasertdam, "Ternary metal oxide catalysts for selective oxidation of benzene to phenol", accepted by Journal of Industrial & Engineering Chemistry, April 9, 2008 (IF-2005 = 0.957).

Submitted International Papers (under consideration)

1) S. Vivanpatarakij, S. Assabumrungrat, and N. Laosiripojana, "Performance improvement of solid oxide fuel cell system using palladium membrane reactor with different operation modes", submitted to Chemical Engineering Journal, December 2007 (IF-2006 = 1.594).

2) Boonrat Pholjaroen, Navadol Laosiripojana, Piyasan Praserthdam and Suttichai Assabumrungrat, "Reactivity of Ni/SiO_2.MgO toward carbon dioxide reforming of methane under steady state and periodic operations" submitted to Fuel Processing Technology, April 11, 2008 (IF-2006 = 1.323).

3) P. Philunrekekun, S. Assabumrungrat, N. Laosiripojana and A.A. Adesina, "Performance of biogas-fed solid oxide fuel cell systems integrated with membrane module for CO_2 removal", submitted to Chemical Engineering and Processing: Process Intensification, April 2, 2008 (IF-2006 = 1.129).

International Conferences

1) Eakkapon Promaros, Suttichai Assabumrungrat, Navadol Laosiripojana, Piyasan Praserthdam, Tomohiko Tagawa and Shigeo Goto, "Carbon dioxide reforming of methane under periodic operation", Fifth international conference on unsteady-state processes in catalysis, Suita City, Japan Nov. 22-25, 2006 (poster presentation).

2) Boonrat Pholjaroen, Eakkapon Promaros, Navadol Laosiripojana, Suttichai Assabumrungrat, Piyasan Praserthdam, Tomohiko Tagawa and Shigeo Goto "Characterization of deposited coke on Ni/SiO2.MgO catalyst from carbon dioxide reforming of methane under periodic operation", Singapore, December 3-5, 2006 (oral presentation).

3) W. Sangtongkitcharoen, S. Assabumrungrat, N. Laosiripojana, A. Arpornwichanop, S.Vivanpatarakij and P. Praserthdam "Performance analysis of methanol-fueled solid oxide fuel cell system Incorporated with palladium membrane reactor", The sixth International Symposium on Catalysis in Multiphase Reactors (CAMURE-6) and the fifth International Symposium on Multifunctional Reactors (ISMR-5), January 14-16, 2007 (poster presentation).

4) S. Vivanpatarakij, S. Assabumrungrat, N. Laosiripojana and P. Praserthdam, "Improvement of SOFC performance by using non-uniform cell potential operation", The sixth International Symposium on Catalysis in Multiphase Reactors (CAMURE-6) and the fifth International Symposium on Multifunctional Reactors (ISMR-5), January 14-16, 2007 (oral presentation).

5) W. Jamsak, S. Assabumrungrat, P.L. Douglas, N. Laosiripojana, R. Suwanwarangkul, S. Charojrochkul and E. Croiset "Performance Assessment of Bioethanol-Fed Solid Oxide Fuel Cell System Integrated with a Distillation Column", 10th International Symposium on Solid Oxide Fuel Cells (SOFC-X), Nara, Japan, June 3-8, 2007 (oral presentation).

บทคัดย่อ

รหัสโครงการ: RMU4880017

ชื่อโครงการ: เครื่องปฏิกรณ์แบบหลายหน้าที่สำหรับอุตสาหกรรมเคมีและปิโตรเคมี

ชื่อนักวิจัย: ศาสตราจารย์ ดร.สุทธิชัย อัสสะบำรุงรัตน์

Email: Suttichai.A@chula.ac.th

ระยะเวลาโครงการ: 1 สิงหาคม 2548 – 31 กรกฎาคม 2551

โครงการวิจัยนี้มีวัตถุประสงค์เพื่อสร้างองค์ความรู้พื้นฐานที่เกี่ยวข้องกับเครื่องปฏิกรณ์แบบหลายหน้าที่สำหรับอุตสาหกรรมเคมีและปิโตรเคมี งานที่ศึกษาสามารถแบ่งออกเป็น 3 หัวข้อย่อย คือ 1) การศึกษาทางด้านเซลล์เชื้อเพลิง 2) การศึกษาระบบการเกิดปฏิกิริยาที่มีการสกัด และ 3) การศึกษาการดำเนินงานแบบสลับ ผลงานที่ได้จากการศึกษานี้คือ บทความที่นำเสนอในวารสารระดับนานาชาติที่ได้รับการยอมรับให้ตีพิมพ์แล้ว 15 บทความ และบทความที่นำเสนอในวารสารระดับนานาชาติที่อยู่ระหว่างการพิจารณา 3 บทความ นอกจากนี้ยังมีการนำเสนอผลงานในที่ประชุมระดับนานาชาติอีก 5 บทความ โดยรายละเอียดสรุปได้ดังต่อไปนี้

บทความวิจัยระดับนานาชาติที่ได้รับการยอมรับให้ตีพิมพ์แล้ว

1) W. Jamsak, S. Assabumrungrat, P.L. Douglas, N. Laosiripojana and S. Charojrochkul, “Theoretical Performance Analysis of Ethanol-Fueled Solid Oxide Fuel Cells with Different Electrolytes”, Chemical Engineering Journal 119 (2006) 11–18. (IF-2006 = 1.594).
2) S. Assabumrungrat, N. Laosiripojana and P. Philunrekekun, “Determination of Boundary of Carbon Formation for Dry Reforming of Methane in Solid Oxide Fuel Cell”, Journal of Power Sources, vol. 159 (2006) 1274-1282 (IF-2006 = 3.521).
3) Eakkapon Promaros, Suttichai Assabumrungrat, Navadol Laosiripojana, Piyasan Praserthdam, Tomohiko Tagawa and Shigeo Goto, “Carbon dioxide reforming of methane under periodic operation”, Korean Journal of Chemical Engineering 24 (2007) 44-50 (IF-2006 = 0.808).
4) Garun Tanarungsun, Worapon Kiatkittipong, Suttichai Assabumrungrat, Hiroshi Yamada, Tomohiko Tagawa and Piyasan Prasertdam, “Fe (III), Cu (II), V (V)/TiO2 for hydroxylation of benzene to phenol with hydrogen peroxide at room temperature”, Journal of Chemical Engineering of Japan, vol. 40 (2007) 415-421 (IF-2006 = 0.594).
5) Garun Tanarungsun, Worapon Kiatkittipong, Suttichai Assabumrungrat, Hiroshi Yamada, Tomohiko Tagawa and Piyasan Prasertdam, “Liquid phase hydroxylation of benzene to

phenol with hydrogen peroxide catalyzed by Fe (III)/TiO_2 catalysts at room temperature", Journal of Industrial & Engineering Chemistry, vol. 13 (2007) 444-451 (IF-2006 = 0.957).

6) S. Vivanpatarakij, S. Assabumrungrat and N. Laosiripojana, "Improvement of SOFC performance by using non-uniform cell potential operation", Journal of Power Sources, vol. 167 (2007) 139-144 (IF-2006 = 3.521).
7) W. Jamsak, S. Assabumrungrat, P.L. Douglas, N. Laosiripojana, R. Suwanwarangkul, S. Charojrochkul and E. Croiset "Performance Assessment of Bioethanol-Fed Solid Oxide Fuel Cell System Integrated with a Distillation Column", ECS Transactions – Solid Oxide Fuel Cells vol. 7 (2007) 1475-1482 (IF-2006 = -).
8) W. Jamsak, S. Assabumrungrat, P.L. Douglas, N. Laosiripojana, R. Suwanwarangkul, S. Charojrochkul and E. Croiset "Performance of Ethanol-Fueled Solid Oxide Fuel Cells: Proton and Oxygen Ion Conductors", Chemical Engineering Journal, vol. 133/1-3 (2007) 187-194 (IF-2006 = 1.594).
9) Garun tanarungsun, Worapon Kiatkittipong, Suttichai Assabumrungrat, Hiroshi Yamada, Tomohiko Tagawa and Piyasan Prasertdam, "Multi transition metal catalysts supported on TiO_2 for hydroxylation of benzene to phenol with hydrogen peroxide", Journal of Industrial & Engineering Chemistry, vol. 13 (2007) 870-877 (IF-2006 = 0.957).
10) W. Jamsak, S. Assabumrungrat, P.L. Douglas, E. Croiset, N. Laosiripojana, R. Suwanwarangkul and S. Charojrochkul, "Thermodynamic Assessment of Solid Oxide Fuel Cell System Integrated with Bioethanol Purification Unit", Journal of Power Sources, vol. 174 (2007) 191-198 (IF-2006 = 3.521).
11) W. Sangtongkitcharoen, S.Vivanpatarakij, N. Laosiripojana, A. Arpornwichanop and S. Assabumrungrat, "Performance analysis of methanol-fueled solid oxide fuel cell system Incorporated with palladium membrane reactor", Chemical Engineering Journal, vol. 138 (2008) 436-441 (IF-2006 = 1.594).
12) Garun Tanarungsun, Worapon Kiatkittipong, Suttichai Assabumrungrat, Hiroshi Yamada, Tomohiko Tagawa and Piyasan Prasertdam, "Hydroxylation of benzene to phenol on Fe/TiO_2 catalysts loaded with different types of second metal", Catalysis Communications, Vol. 9 (2008) 1886-1890 (IF-2006 = 1.878).
13) Hiroshi YAMADA, Tomoaki MIZUNO, Tomohiko TAGAWA, Garun TANARUNGSUN, Piyasan PRASERTHDAM and Suttichai ASSABUMRUNGRAT "Catalyst Regenerator for

Partial Oxidation of Benzene in Reaction-Extraction System" Journal of the Japan Petroleum Institute, vol. 51 (2008), 114-117. (IF-2006 = 0.633)

14) P. Philunrekekun, S. Assabumrungrat, N. Laosiripojana and A.A. Adesina, "Selection of appropriate fuel processor for biogas-fuelled SOFC system", Chemical Engineering Journal, in press (IF-2006 = 1.594).

15) Garun Tanarungsun, Worapon Kiatkittipong, Suttichai Assabumrungrat, Hiroshi Yamada, Tomohiko Tagawa and Piyasan Prasertdam, "Ternary metal oxide catalysts for selective oxidation of benzene to phenol", accepted by Journal of Industrial & Engineering Chemistry, April 9, 2008 (IF-2005 = 0.957).

บทความวิจัยระดับนานาชาติที่อยู่ระหว่างการพิจารณา

1) S. Vivanpatarakij, S. Assabumrungrat, and N. Laosiripojana, "Performance improvement of solid oxide fuel cell system using palladium membrane reactor with different operation modes", submitted to Chemical Engineering Journal, December 2007 (IF-2006 = 1.594).

2) Boonrat Pholjaroen, Navadol Laosiripojana, Piyasan Praserthdam and Suttichai Assabumrungrat, "Reactivity of Ni/SiO_2.MgO toward carbon dioxide reforming of methane under steady state and periodic operations" submitted to Fuel Process Technol, April 11, 2008 (IF-2006 = 1.323).

3) P. Philunrekekun, S. Assabumrungrat, N. Laosiripojana and A.A. Adesina, "Performance of biogas-fed solid oxide fuel cell systems integrated with membrane module for CO_2 removal", submitted to Chemical Engineering and Processing: Process Intensification, April 2, 2008 (IF-2006 = 1.129).

การนำเสนอผลงานในที่ประชุมระดับนานาชาติ

1) Eakkapon Promaros, Suttichai Assabumrungrat, Navadol Laosiripojana, Piyasan Praserthdam, Tomohiko Tagawa and Shigeo Goto, "Carbon dioxide reforming of methane under periodic operation", Fifth international conference on unsteady-state processes in catalysis, Suita City, Japan Nov. 22-25, 2006 (poster presentation).

2) Boonrat Pholjaroen, Eakkapon Promaros, Navadol Laosiripojana, Suttichai Assabumrungrat, Piyasan Praserthdam, Tomohiko Tagawa and Shigeo Goto "Characterization of deposited coke on Ni/SiO2.MgO catalyst from carbon dioxide reforming of methane under periodic operation", Singapore, December 3-5, 2006 (oral presentation).

3) W. Sangtongkitcharoen, S. Assabumrungrat, N. Laosiripojana, A. Arpornwichanop, S.Vivanpatarakij and P. Praserthdam, "Performance analysis of methanol-fueled solid oxide fuel cell system Incorporated with palladium membrane reactor", The sixth International Symposium on Catalysis in Multiphase Reactors (CAMURE-6) and the fifth International Symposium on Multifunctional Reactors (ISMR-5), January 14-16, 2007 (poster presentation).
4) S. Vivanpatarakij, S. Assabumrungrat, N. Laosiripojana and P. Praserthdam, "Improvement of SOFC performance by using non-uniform cell potential operation", The sixth International Symposium on Catalysis in Multiphase Reactors (CAMURE-6) and the fifth International Symposium on Multifunctional Reactors (ISMR-5), January 14-16, 2007 (oral presentation).
5) W. Jamsak, S. Assabumrungrat, P.L. Douglas, N. Laosiripojana, R. Suwanwarangkul, S. Charojrochkul and E. Croiset "Performance Assessment of Bioethanol-Fed Solid Oxide Fuel Cell System Integrated with a Distillation Column", 10th International Symposium on Solid Oxide Fuel Cells (SOFC-X), Nara, Japan, June 3-8, 2007 (oral presentation).

Acknowledgement

This research project is financially supported by The Thailand Research Fund (TRF) and Commission of Higher Education. The project is completed successfully by the supports of my hard working students (Dr. Wasana Jamsak, Dr. Supawat Vivanpatarakij, Dr. Garun Tanarungsan, Mr. Wiboon Sangtongkitcharoen, Mr. Eakkapon Promaros, Mr. Boonrat Pholjaroen, Mr. Pakorn Philunrekekun and others), my good colleagues (Dr. Navadol Laosiripojana, Dr. Amornchai Arpornwichanop, Dr. Sumittra Charojrochkul, Dr. Rapeepong Suwanwarangkul) and my good collaborators (Professor Tomohiko Tagawa, Assistant Professor Hiroshi Yamada, Professor Peter Douglas, Associate Professor Eric Croiset and Professor Adesoji Adesina).

Table of Content

Research Outputs from the Study

The works on multifunctional reactors for chemical and petrochemical industries in this study were divided into 3 main parts as summarized below.

1) Study on fuel cell systems

The numbers of international papers that are published and being under consideration under this topic are 8 and 2, respectively (total = 10 papers).

Preliminary analysis of solid oxide fuel cell (SOFC) system fuelled by bioethanol was investigated. The performance of the SOFCs with an oxygen-conducting electrolyte (SOFC-O^{2-}) and a proton-conducting electrolyte (SOFC-H^{+}) was compared. It was found that although the theoretical performance of the SOFC-H^{+} is superior to that of the SOFC-O^{2-}, the presently available poor proton conductor makes the use of the proton-conducting electrolyte impractical. The development of novel proton conductor for SOFC is necessary. The possibility of the system integration between an SOFC and a distillation column for bioethanol purification was examined. Excessive heat from the SOFC system was utilized as a heat source for the reboiler of the distillation column. The study also focused on the performance of the integrated system under the energy-self sufficiency condition of the system.

Another SOFC system was focused on using biogas as a fuel. A suitable feed composition which was safe from anode deactivation by carbon formation was determined for different types of fuel processor (steam reforming, partial oxidation and dry reforming). Then the performance of the biogas-fuelled SOFC with different types of fuel processor was compared, considering the obtained electrical efficiency and power density of the SOFC stack.

The other project was focused on performance improvement of SOFC by using different approaches such as application of non-uniform potential operation and replacing a conventional reformer with a membrane reactor to increase hydrogen concentration in the product stream.

Publications

W. Jamsak, S. Assabumrungrat, P.L. Douglas, N. Laosiripojana and S. Charojrochkul, "Theoretical Performance Analysis of Ethanol-Fueled Solid Oxide Fuel Cells with Different

Electrolytes", Chemical Engineering Journal 119 (2006) 11–18. (IF-2006 = 1.594). **(Appendix 1)**

W. Jamsak, S. Assabumrungrat, P.L. Douglas, N. Laosiripojana, R. Suwanwarangkul, S. Charojrochkul and E. Croiset "Performance Assessment of Bioethanol-Fed Solid Oxide Fuel Cell System Integrated with a Distillation Column", ECS Transactions - Solid Oxide Fuel Cells vol. 7 (2007) 1475-1482 (IF-2006 = -). **(Appendix 2)**

W. Jamsak, S. Assabumrungrat, P.L. Douglas, N. Laosiripojana, R. Suwanwarangkul, S. Charojrochkul and E. Croiset "Performance of Ethanol-Fueled Solid Oxide Fuel Cells: Proton and Oxygen Ion Conductors", Chemical Engineering Journal, vol. 133/1-3 (2007) 187-194 (IF-2006 = 1.594). **(Appendix 3)**

W. Jamsak, S. Assabumrungrat, P.L. Douglas, E. Croiset, N. Laosiripojana, R. Suwanwarangkul and S. Charojrochkul, "Thermodynamic Assessment of Solid Oxide Fuel Cell System Integrated with Bioethanol Purification Unit", Journal of Power Sources, vol. 174 (2007) 191-198 (IF-2006 = 3.521). **(Appendix 4)**

S. Assabumrungrat, N. Laosiripojana and P. Philunrekekun, "Determination of Boundary of Carbon Formation for Dry Reforming of Methane in Solid Oxide Fuel Cell", Journal of Power Sources, vol. 159 (2006) 1274-1282 (IF-2006 = 3.521). **(Appendix 5)**

S. Vivanpatarakij, S. Assabumrungrat and N. Laosiripojana, "Improvement of SOFC performance by using non-uniform cell potential operation", Journal of Power Sources, vol. 167 (2007) 139-144 (IF-2006 = 3.521). **(Appendix 6)**

W. Sangtongkitcharoen, S.Vivanpatarakij, N. Laosiripojana, A. Arpornwichanop and S. Assabumrungrat, "Performance analysis of methanol-fueled solid oxide fuel cell system incoporated with palladium membrane reactor", Chemical Engineering Journal, vol. 138 (2008) 436-441 (IF-2006 = 1.594). **(Appendix 7)**

P. Philunrekekun, S. Assabumrungrat, N. Laosiripojana and A.A. Adesina, "Selection of appropriate fuel processor for biogas-fuelled SOFC system", Chem. Eng. J., accepted October 5, 2007 (IF-2006 = 1.594). **(Appendix 8)**

S. Vivanpatarakij, S. Assabumrungrat, and N. Laosiripojana, "Performance improvement of solid oxide fuel cell system using palladium membrane reactor with different operation modes", submitted to Chemical Engineering Journal, December 2007 (IF-2006 = 1.594). **(Appendix 9)**

P. Philunrekekun, S. Assabumrungrat, N. Laosiripojana and A.A. Adesina, "Performance of biogas-fed solid oxide fuel cell systems integrated with membrane module for CO_2 removal",

submitted to Chemical Engineering and Processing: Process Intensification, April 2, 2008 (IF-2006 = 1.129). **(Appendix 10)**

2) Study on reaction with separation

The number of international papers that are published under this topic is 6.

This work is aimed to study the reaction and extraction system by focusing on production of phenol from the liquid phase hydroxylation of benzene by hydrogen peroxide. The preliminary works were mainly focused on catalyst screening. Firstly a suitable TiO_2 support was selected and then various metal oxides (V, Cu and Fe) were tested. The Fe/TiO_2 was selected for further studies. Various second or third metals were added in the catalyst for the catalytic performance improvement. Some work was carried out to investigate the reaction system that combines both reaction and extraction functions.

Publications

Garun tanarungsun, Worapon Kiatkittipong, Suttichai Assabumrungrat, Hiroshi Yamada, Tomohiko Tagawa and Piyasan Prasertdam, "Fe (III), Cu (II), V (V)/TiO2 for hydroxylation of benzene to phenol with hydrogen peroxide at room temperature", Journal of Chemical Engineering of Japan, vol. 40 (2007) 415-421 (IF-2005 = 0.594). **(Appendix 11)**

Garun tanarungsun, Worapon Kiatkittipong, Suttichai Assabumrungrat, Hiroshi Yamada, Tomohiko Tagawa and Piyasan Prasertdam, "Liquid phase hydroxylation of benzene to phenol with hydrogen peroxide catalyzed by Fe (III)/TiO_2 catalysts at room temperature", Journal of Industrial & Engineering Chemistry, vol. 13 (2007) 444-451 (IF-2006 = 0.957). **(Appendix 12)**

Garun tanarungsun, Worapon Kiatkittipong, Suttichai Assabumrungrat, Hiroshi Yamada, Tomohiko Tagawa and Piyasan Prasertdam, "Multi transition metal catalysts supported on TiO_2 for hydroxylation of benzene to phenol with hydrogen peroxide", Journal of Industrial & Engineering Chemistry, vol. 13 (2007) 870-877 (IF-2006 = 0.957). **(Appendix 13)**

Garun tanarungsun, Worapon Kiatkittipong, Hiroshi Yamada, Tomohiko Tagawa, Piyasan Prasertdam and Suttichai Assabumrungrat, "Hydroxylation of benzene to phenol on Fe/TiO_2 catalysts loaded with different types of second metal", Catalysis Communications, vol. 9 (2008) 1886-1890 (IF-2006 = 1.878). **(Appendix 14)**

Hiroshi Yamada, Tomoaki Mizuno, Tomohiko Tagawa, Garun Tanarungsun, Piyasan Praserthdam and Suttichai Assabumrungrat "Catalyst Regenerator for Partial Oxidation of Benzene in Reaction-Extraction System" Journal of the Japan Petroleum Institute, vol. 51 (2008), 114-117. (IF-2006 = 0.633) **(Appendix 15)**

Garun tanarungsun, Worapon Kiatkittipong, Hiroshi Yamada, Tomohiko Tagawa, Piyasan Prasertdam and Suttichai Assabumrungrat, "Ternary metal oxide catalysts for selective oxidation of benzene to phenol", accepted by Journal of Industrial & Engineering Chemistry, April 9, 2008 (IF-2005 = 0.957). **(Appendix 16)**

3) Study on periodic operation

The numbers of international paper that are published and being under consideration under this topic are 1 and 1, respectively (total = 2 papers).

This work focuses on the use of periodic operation for hydrogen production from methane and carbon dioxide. The reactants were alternately fed to the catalyst bed. During the methane feed period, pure hydrogen was the product. Carbon dioxide was fed in the other period for catalyst regeneration, yielding carbon monoxide as the product. It was reported that only under some operating conditions, the periodic operation offered a comparable or superior performance over the conventional continuous operation. The operation was retarded by the incomplete regeneration of the catalyst covered by carbon from the methane cracking. Different types of carbon were observed from the operations at T = 650 and 750^{o}C.

Publication

Eakkapon Promaros, Suttichai Assabumrungrat, Navadol Laosiripojana, Piyasan Praserthdam, Tomohiko Tagawa and Shigeo Goto, "Carbon dioxide reforming of methane under periodic operation", Korean Journal of Chemical Engineering 24 (2007) 44-50 (IF-2006 = 0.808) **(Appendix 17)**

Boonrat Pholjaroen, Navadol Laosiripojana, Piyasan Praserthdam and Suttichai Assabumrungrat, "Reactivity of Ni/SiO_2.MgO toward carbon dioxide reforming of methane under steady state and periodic operations" submitted to Fuel Processing Technology, April 11, 2008 (IF-2006 = 1.323). **(Appendix 18)**

Appendix

Appendix 1

ELSEVIER

Chemical Engineering Journal 119 (2006) 11–18

Chemical Engineering Journal

www.elsevier.com/locate/cej

Theoretical performance analysis of ethanol-fuelled solid oxide fuel cells with different electrolytes

W. Jamsak [a], S. Assabumrungrat [a,*], P.L. Douglas [b], N. Laosiripojana [c], S. Charojrochkul [d]

[a] *Center of Excellence in Catalysis and Catalytic Reaction Engineering, Department of Chemical Engineering, Faculty of Engineering, Chulalongkorn University, Bangkok 10330, Thailand*

[b] *Department of Chemical Engineering, University of Waterloo, Ontario, Canada*

[c] *The Joint Graduate School of Energy and Environment, King Mongkut's University of Technology Thonburi, Bangkok 10140, Thailand*

[d] *National Metal and Materials Technology Center (MTEC), Thailand*

Received 31 July 2005; received in revised form 21 February 2006; accepted 4 March 2006

Abstract

The theoretical performance of ethanol-fuelled solid oxide fuel cells (SOFCs) with oxygen ion conducting and proton conducting electrolytes are presented in this paper. It was reported in a previous work that an SOFC with a proton conducting electrolyte (SOFC-H^+) offers higher efficiency than an SOFC with an oxygen ion conducting electrolyte (SOFC-O^{2-}). However, the study was based on the same steam-to-hydrocarbon feed ratio. Our previous work demonstrated the potential benefit of the SOFC-O^{2-} over the SOFC-H^+ in terms of a lower requirement for steam in the feed. Therefore, in this article, this benefit is taken into account in the performance comparison. Influences of mode of operation (i.e. plug flow (PF) and well-mixed (WM)) on the performance of SOFCs were also investigated. In the PF mode, two feeding patterns (i.e. co-current (Co) and counter-current (CC)) were considered.

The results show that theoretical SOFC efficiencies depend on the type of electrolyte, mode of operation, inlet H_2O:EtOH ratio and fuel utilization. Although it was found that the feeding pattern has an influence on EMF distribution along the cell, the average EMF is not affected. At the best conditions for each type of SOFC, it was observed that SOFC-O^{2-} yields a maximum efficiency at the minimum inlet H_2O:EtOH ratio which is the limit for carbon formation for each value of fuel utilization. On the other hand, in SOFC-H^+, optimum inlet H_2O:EtOH ratios are higher than the limit of carbon formation. At the optimum conditions, the rank of the various SOFCs is as follows: SOFC-H^+(PF) > SOFC-O^{2-}(PF) > SOFC-H^+(WM) > SOFC-O^{2-}(WM) over the temperature range (1000–1200 K). No difference in SOFC efficiency between both feeding patterns was observed. It is clear from our theoretical studies that the SOFC-H^+(PF) is the most promising SOFC system.

Keywords: Solid oxide fuel cells; Direct internal reforming; Oxygen ion conductor; Proton conductor; Efficiency

1. Introduction

Fuel cells are currently regarded as the most promising technology for conversion of chemical to electrical energy. Solid oxide fuel cells (SOFC) have attracted considerable interest as they offer the widest range of potential applications, possibility in operation with an internal reformer, and possessing a high system efficiency. Many fuels have been suggested for use in SOFCs; however, among these, ethanol is considered to be an attractive green fuel because of its renewability from various biomass sources including energy plants, waste materials from agro-industries, forestry residue materials, and even organic fractions from municipal solid wastes. They also offer advantages related to natural availability and safety in storage and handling.

There are a number of studies published dealing with the use of ethanol for fuel cells. Ethanol was found to provide higher electrical and overall efficiency than methane in a direct internal reforming molten carbonate fuel cell (DIR-MCFC) [1]. Thermodynamic analysis of an indirect internal reforming molten carbonate fuel cell (IIR-MCFC) revealed that among different fuels (i.e. methane, methanol, and ethanol), ethanol presented the highest power density and the highest cell voltage. At a constant power density, ethanol allows the system to operate close to its thermal equilibrium better than does methanol but not as well as methane [2]. Tsiakaras and Demin [3] investigated performances

* Corresponding author. Tel.: +662 218 6868; fax: +662 218 6877.
E-mail address: Suttichai.A@chula.ac.th (S. Assabumrungrat).

1385-8947/$ – see front matter © 2006 Elsevier B.V. All rights reserved.
doi:10.1016/j.cej.2006.03.001

Nomenclature

a	inlet moles of ethanol (mol)
b	inlet moles of steam (mol)
c	extent of the electrochemical reaction of hydrogen (mol)
E	electromotive force of a cell (V)
F	Faraday constant (C mol^{-1})
ΔH^0	lower heating value of ethanol (J mol^{-1})
K	equilibrium constant of the hydrogen oxidation reaction (kPa$^{-0.5}$)
n_i	number of moles of component i (mol)
p_i	partial pressure of component i (kPa)
$p_{r,i}$	relative partial pressure of component i
q	electrical charge (A)
R	gas constant (J mol^{-1} K^{-1})
T	temperature (K)
U_f	operating fuel utilization (%)
$U_{f,i,}$	partial fuel utilization (%)
W	electrical work (W)
x	converted moles associated with reaction (1) (mol)
y	converted moles associated with reaction (2) (mol)
z	converted moles associated with reaction (3) (mol)

Greek letters

η	electrical efficiency (%)
φ	potential (V)

Subscripts

a	anode
c	cathode

of SOFCs *fuelled* by products from different ethanol processing; i.e. steam reforming, dry reforming, and partial oxidation with air. The product from ethanol steam reforming showed the highest maximum efficiency. Performances of external reforming SOFCs (ER-SOFC) fed by different fuels, e.g. methane, methanol, ethanol, and gasoline, were compared within a temperature range of 800–1200 K [4]. It was observed that at low temperatures, methane required a lower inlet steam:fuel ratio to prevent unfavorable coke formation than did methanol and ethanol. Nevertheless, at high temperatures the steam:fuel ratio at the limit of coke formation for ethanol was the same as for methane.

Although two types of electrolytes are possible for the SOFC operation, an oxygen ion conducting electrolyte is more commonly used than a proton conducting electrolyte. Until now, there are very few studies related to the use of the proton conducting electrolytes in SOFCs in the open literature [5–8]. In addition, all the studies of the ethanol-fed SOFCs employed only the oxygen ion conducting electrolyte. Demin et al. [7] reported an interesting result that an SOFC with a proton conducting electrolyte (SOFC-H^+) provides higher efficiency than an SOFC with an oxygen ion conducting electrolyte (SOFC-O^{2-}) for the system fed with methane. The comparison study was based on the same steam:methane feed ratio for both SOFC-O^{2-} and SOFC-H^+. It was demonstrated in our previous work that the steam requirement of SOFC-O^{2-} *is* lower than that of the SOFC-H^+ because water produced from the electrochemical reaction of hydrogen appears in the anode chamber [9]. Therefore, when the benefit from the lower steam requirement in SOFC-O^{2-} is taken into account, it is unclear whether the SOFC-H^+ still shows better performance than the SOFC-O^{2-}.

In this study, the theoretical performance of ethanol-fuelled SOFCs with two electrolytes in different modes of operation (i.e. plug flow (PF) and well-mixed (WM)) were investigated. Two feeding patterns of the PF mode (i.e. co-current (Co) and counter-current (CC)) were also considered. The efficiencies of SOFC-O^{2-} and SOFC-H^+ were compared, taking into account the benefit from the lower steam requirement for SOFC-O^{2-}. This is important in determining whether future SOFCs should be based on the use of the proton conducting electrolyte.

2. Theory

The reaction system involving the production of hydrogen via ethanol steam reforming can be represented by the following reactions [1]:

$$C_2H_5OH + H_2O = 4H_2 + 2CO \quad (1)$$

$$CO + H_2O = H_2 + CO_2 \quad (2)$$

$$CO + 3H_2 = CH_4 + H_2O \quad (3)$$

Previous results confirmed that a gas mixture at thermodynamic equilibrium contains only five components with noticeable concentration, e.g. carbon monoxide, carbon dioxide, hydrogen, steam, and methane [10,11].

Two types of solid electrolytes can be employed in the SOFC, i.e. oxygen ion and proton conducting electrolytes. The reactions taking place in the anode and the cathode can be summarized as follows.

Oxygen ion conducting electrolyte:

$$\text{anode}: H_2 + O^{2-} = H_2O + 2e^- \quad (4)$$

$$\text{cathode}: \tfrac{1}{2}O_2 + 2e^- = O^{2-} \quad (5)$$

Proton conducting electrolyte:

$$\text{anode}: H_2 = 2H^+ + 2e^- \quad (6)$$

$$\text{cathode}: 2H^+ + \tfrac{1}{2}O_2 + 2e^- = H_2O \quad (7)$$

The difference between both electrolyte types is the location of the water produced. With the oxygen ion conducting electrolyte, water is produced in the reaction mixture in the anode chamber. In the case of the proton conducting electrolyte, water appears on the cathode side. The theoretical number of moles of each component at equilibrium is given by the following expressions:

$$n_{EtOH} = a - x \quad (8)$$

$$n_{CH_4} = z \tag{9}$$

$$n_{CO} = 2x - y - z \tag{10}$$

$$n_{CO_2} = y \tag{11}$$

$$n_{H_2} = 4x + y - 3z - c \tag{12}$$

$$\begin{aligned} n_{H_2O} &= b + c - y + z \text{ (for oxygen ion conducting electrolyte)} \\ n_{H_2O} &= b - y + z \text{ (for proton conducting electrolyte)} \end{aligned} \tag{13}$$

$$n_{tot} = \sum_{i=1}^{6} n_i \tag{14}$$

The following three reactions are the most probable reactions which lead to carbon formation in the reaction system.

$$2CO = CO_2 + C \tag{15}$$

$$CH_4 = 2H_2 + C \tag{16}$$

$$CO + H_2 = H_2O + C \tag{17}$$

The reactions take place under a carbon-free condition when the carbon activities are less than one [10].

2.1. Electromotive force (EMF) calculations

The EMF of a cell is the maximum possible voltage, which drives charges around an electrical circuit in an SOFC. In practice, the actual voltage is less than this theoretical value due to activation, ohmic, and concentration losses. In this article, only the maximum possible voltage or EMF of the cell was considered, neglecting all losses. The EMF can be calculated from a difference in potentials between both electrodes in the cell as shown in Eq. (18).

$$E = |\varphi_c - \varphi_a| \tag{18}$$

where φ_c and φ_a are the potentials at the cathode and the anode, respectively. The electrode potential can be calculated using the Nernst equation. Since the electrochemical reactions at the electrodes are different, depending on the type of electrolyte, the potential can be expressed as:

$$\begin{aligned} \text{SOFC} - O^{2-} : E &= \frac{RT}{4F} \ln p_{r,O_2} \\ &= -\frac{\Delta G}{2F} - \frac{RT}{2F} \ln \frac{P_{H_2O,a}}{P_{H_2,a} P_{O_2,c}^{0.5}} \end{aligned} \tag{19}$$

$$\begin{aligned} \text{SOFC} - H^{+} : E &= \frac{RT}{2F} \ln p_{r,H_2} \\ &= -\frac{\Delta G}{2F} - \frac{RT}{2F} \ln \frac{P_{H_2O,c}}{P_{H_2,a} P_{O_2,c}^{0.5}} \end{aligned} \tag{20}$$

where p_{r,O_2} and p_{r,H_2} are relative oxygen partial pressure and relative hydrogen partial pressure, respectively, R the universal gas constant, T the absolute temperature, F the Faraday's constant, ΔG the Gibb's free energy and P_i the partial pressure of component i. The second terms of the right-hand side expression of Eqs. (19) and (20) are the Nerstian term comprising the partial pressure of hydrogen, oxygen, and steam. It should be noted that the partial pressures of steam for the SOFC-H^+ and the SOFC-O^{2-} represent the values at the anode and the cathode, respectively.

Typically, conventional SOFC operations are close to plug flow mode in which the gas compositions vary along the length of the cell. However, SOFCs can be operated under a well-mixed mode by using a high recycle rate. In the PF mode, the feeding pattern of fuel and air to the SOFC stack affects the composition distribution and, consequently the, EMF distribution along the SOFC cell. Two feeding patterns (i.e. co-current and counter-current) were considered in this study. An average EMF ($\overline{E}$) in the PF mode can be determined by the numerical integration of EMF along the stack. It should be noted that the EMF also depends significantly on the inlet H_2O:EtOH ratio, operating temperature, and the fuel and air utilizations. To simplify the calculations, it was assumed that the gas compositions in the anode are at their equilibrium compositions along the stack. Deviation from this equilibrium condition would result in lower SOFC EMF values as less hydrogen was generated in the anode chamber to compensate for the hydrogen consumed by the electrochemical reaction. Therefore, the results shown in this work represent the best performances for all SOFC cases. Details of the calculations of the equilibrium composition were presented in our previous work [9]. It should be noted that our calculations were compared with the results of Hernandez-Pacheco et al. [12] and found to be in good agreement. Using the same operating conditions ($U_f = 80\%$, $T = 1200$ K and 100% hydrogen feed) our calculations gave an EMF of approximately 0.92 V whereas Hernandez obtained 0.9 V.

2.2. SOFC efficiency

When a current is drawn from the SOFC, the maximum work produced by the SOFC can be calculated using the following equation:

$$W = q\overline{E} \tag{21}$$

where W is the electrical work from the SOFC and q is an electrical charge passing through the electrolyte. The electrical efficiency is defined as the ratio of electrical work produced by the SOFC to the chemical energy of fuel fed to the SOFC. Therefore, the maximum SOFC efficiency is obtained from in the following equation:

$$\eta = \frac{q\overline{E}}{-\Delta H^0} \times 100\% \tag{22}$$

where $-\Delta H^0$ is lower heating value of ethanol at standard conditions.

3. Results and discussion

The influences of the mode of operation (plug flow and well-mixed), feeding pattern (co-current and counter-current) and

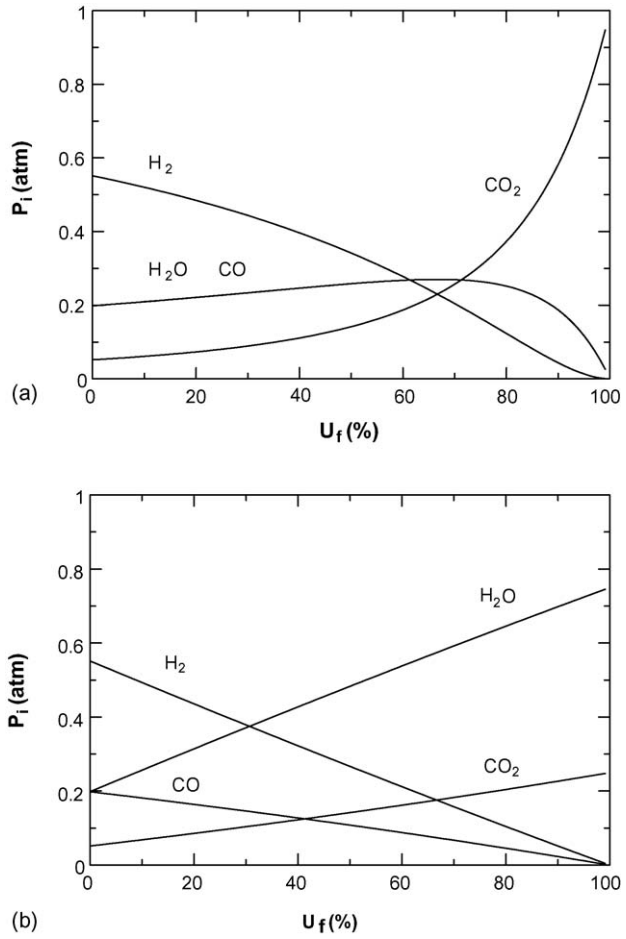

Fig. 1. Anode components' partial pressure at different fuel utilization for SOFCs with different types of electrolytes: (a) H^+ electrolyte and (b) O^{2-} electrolyte (inlet H_2O:EtOH = 3, T = 1200 K, P = 101.3 kPa, 400% excess air).

type of electrolyte on the partial pressure of each component along the cell are studied. Fig. 1 shows the anode components' partial pressure at different fuel utilizations (U_f) defined as the moles of hydrogen consumed by the electrochemical reaction divided by the maximum number of moles of hydrogen produced from ethanol (6 mol of hydrogen:1 mol of ethanol). The inlet H_2O:EtOH ratio is at the stoichiometic value of 3 and the temperature is 1200 K. For the WM mode, the partial pressure along the cell is equal to the value at the exit U_f due to the well-mixed condition. In contrast, in the PF mode, the composition change along the cell is represented by the partial pressure profiles from U_f of 0 to the exit U_f. The type of electrolyte has a significant effect on the anode partial pressure as shown in Fig. 1(a) and (b). The partial pressure of steam for the SOFC-H^+ and SOFC-O^{2-} are considerably different due to the different location of steam generation. In the SOFC-H^+ case, the partial pressure of steam increases slightly with increasing U_f because the total moles in the anode chamber decreases as hydrogen is consumed. However, at high fuel utilizations, the partial pressure of steam drops significantly because the hydrogen consumption shifts the water–gas shift reaction and results in higher carbon dioxide production as shown in Fig. 1(a). In contrast, for the SOFC-O^{2-} case, the partial pressure of steam increases dramatically over the entire anode chamber due to the major effect of electrochemical steam production at the anode side. The partial pressure of hydrogen in the SOFC-H^+ case is higher than that in the SOFC-O^{2-} case because there is no dilution effect of the electrochemical steam at the anode side in the SOFC-H^+ case. It should be noted that there is a negligible amount of ethanol and methane observed from the calculations due to the complete reforming reaction and insignificant methanation at this operating temperature.

As mentioned in the previous section, two feeding patterns (i.e. SOFC-(PF-Co) and SOFC-(PF-CC)) were considered for the PF mode. No difference in the profile of anode components' partial pressure for different feeding patterns was observed because it was assumed in our calculations that all anode components are in equilibrium which relates to the fuel utilization (U_f) along the anode chamber. Therefore, at the same operating fuel utilization the profiles of anode components in both feeding patterns are similar. In other words, the feeding patterns have no effect on the profile of anode components' partial pressure for both electrolytes.

The influence of mode of operation, feeding pattern, and type of electrolyte on the cathode components' partial pressure at various fuel utilizations are shown in Fig. 2. The partial pressure of oxygen in the SOFC-H^+ case is always lower than that in the SOFC-O^{2-} case due to the presence of the electrochemical steam at the cathode for the SOFC-H^+. However, the differences are not significant due to high value of excess air (400%) used in the calculations. It should be noted that 300–600% excess air is commonly used in SOFC operations for good heat management in SOFC cell stacks [13]. The mode of operation and feeding pattern show a slight impact on the partial pressure of oxygen in the cathode. For the SOFC (PF-Co) cases, air is fed cocurrently with the fuel. The partial pressure of oxygen decreases whereas the partial pressure of steam increases (for the SOFC-H^+ case) with increasing fuel utilization. The partial pressure profiles within the cell of the SOFC (PF-Co) cases are represented by the partial pressures between the fuel utilization at 0 and the exit U_f; however, those of the SOFC (WM) correspond to the value at the exit fuel utilization. In contrast, for the SOFC (PF-CC), air is introduced to the cathode entrance located at the exit of the anode stream and, therefore, the partial pressure profile is different among different fuel utilizations. The partial pressure of oxygen in the cathode is 0.21 atm at the entrance to the cathode side and decreases along the cathode chamber until the cathode exit located at the entrance of the anode feed.

From the obtained partial pressure profiles, the EMF at different fuel utilization for all SOFCs can be calculated using Eqs. (18) and (19). From Fig. 3, it is shown that the EMF distributions in all SOFC-H^+ cases are higher than those in all SOFC-O^{2-} cases. This can be explained by considering the partial pressure of components involved in the Nerstian term of Eqs. (19) and (20). Because the partial pressure of hydrogen in the anode for the SOFC-H^+ case is higher than that for the SOFC-O^{2-} case due to no dilution effect of the electrochemical steam at the anode side in the SOFC-H^+ case and the partial pressure of steam in the cathode side for the SOFC-H^+ case is much lower than that in the anode side for the SOFC-O^{2-} case

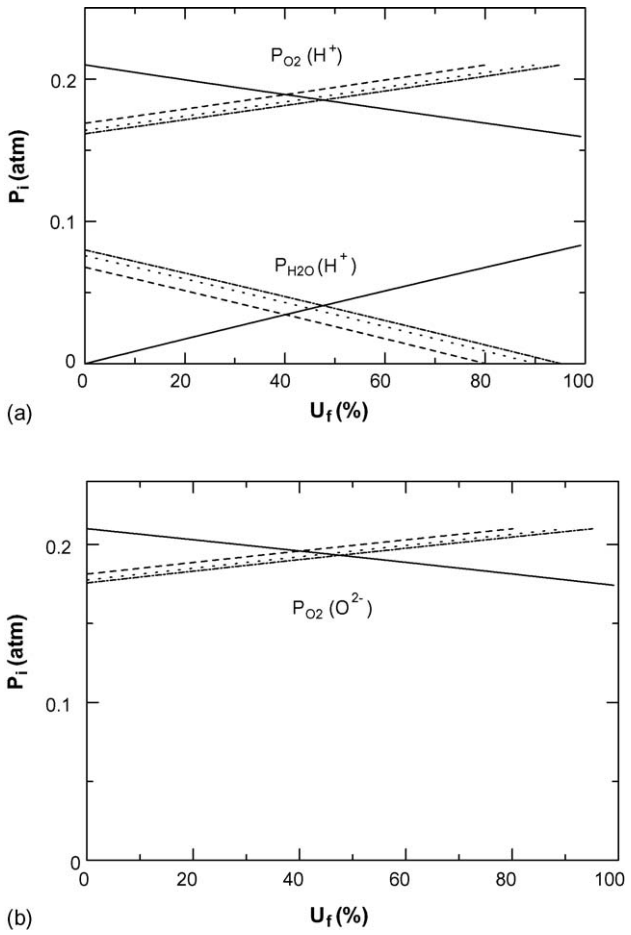

Fig. 2. Cathode components' partial pressure at different fuel utilization for SOFCs with different types of electrolytes for co-current (solid line) and counter-current at 80% U_f (dashed line), 90% U_f (dotted line), 95% U_f (dashed dotted line): (a) H^+ electrolyte and (b) O^{2-} electrolyte (inlet H_2O:EtOH = 3, T = 1200 K, P = 101.3 kPa, 400% excess air).

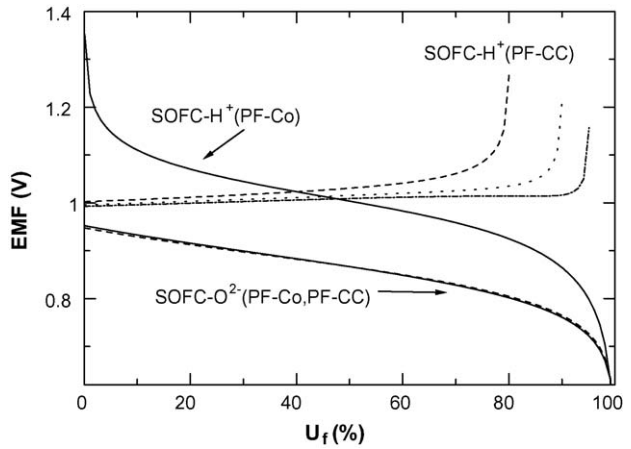

Fig. 3. EMF distribution along the SOFC-O^{2-} and SOFC-H^+ operated under PF and WM modes for co-current (solid line) and counter-current at 80% U_f (dashed line), 90% U_f (dotted line), 95% U_f (dashed dotted line): (a) H^+ electrolyte and (b) O^{2-} electrolyte (inlet H_2O:EtOH = 3, T = 1200 K, P = 101.3 kPa, 400% excess air).

(see Figs. 1 and 2), the Nerstian term of the SOFC-O^{2-} case shows a more negative value than that in the SOFC-H^+ case, and consequently, the SOFC-H^+ cell gives a higher EMF than does the SOFC-O^{2-} cell. It should be noted that the partial pressures of oxygen in the cathode for both SOFCs are not taken into account in the Nerstian term comparison due to the use of excess air in the operation. The result confirms that the SOFC-H^+ cell has a higher performance than the SOFC-O^{2-} cell when the steam:fuel feed ratio is the same as reported earlier in other system [7]. From Fig. 3, it is noticed that the feeding pattern has a significant impact on the EMF distribution in the SOFC-H^+ cell whereas only a slight effect is observed in the SOFC-O^{2-} cell. For the SOFC-H^+ case, the value of EMF is strongly dependent on both the partial pressures of oxygen and steam in the cathode. The components' partial pressures in the anode are not considered as they are similar for both feeding patterns as mentioned earlier. The feeding pattern significantly impacts the partial pressure profile of steam in the cathode as shown in Fig. 2(a) and, therefore, the EMF distribution is different with different feeding patterns. For the SOFC-O^{2-} case, the value of the EMF depends on the partial pressure of oxygen in the cathode, but it is not significantly dependent on the feeding pattern due to the high excess air. Consequently, with the same partial pressure profile in the anode, partial pressure profile of oxygen in the cathode for both feeding patterns and nearly identical, the observed values of the EMF are almost the same. The average value of the EMF for the SOFC (PF) can be obtained by the numerical calculation of the EMF distribution, while the EMF of SOFC (WM) can be achieved directly from the value at the corresponding fuel utilization. At 80% operating fuel utilization, the SOFC-H^+(WM) and the SOFC-O^{2-}(WM) yield EMF of 0.92 and 0.80 V, respectively, whereas the average values of the EMF are 1.03 and 0.89 V for the SOFC-H^+(PF) and the SOFC-O^{2-}(PF), respectively. It was found that the feeding pattern has no significant effect on the average EMF for both electrolytes although the EMF distributions are different. The average EMF of SOFCs at a inlet H_2O:EtOH ratio of 3 and 80% fuel utilization can be ordered as follows SOFC-H^+(PF-Co) ≈ SOFC-H^+(PF-CC) > SOFC-H^+(WM) > SOFC-O^{2-}(PF-Co) ≈ SOFC-O^{2-}(PF-Co) > SOFC-O^{2-}(WM).

Fig. 4(a) and (b) show the comparative results of average EMF and efficiency of SOFCs for various fuel utilizations, respectively. From Fig. 4(a), it is clear that the SOFC-H^+ provides greater EMF than the SOFC-O^{2-} for both PF and WM modes. Furthermore, it can be noticed that the WM mode results in a lower EMF than the PF mode for both electrolytes because the partial pressure of hydrogen in the WM mode is kept at its lowest value along the cell. In addition, there is no effect of feeding patterns on the average EMF in SOFCs although EMF distribution in both feeding patterns is different.

The electrochemical efficiency, η, is one indicator to identify the performance of fuel cells. The efficiency calculated from Eq. (22) is shown in Fig. 4(b). The efficiency increases in sequence SOFC-H^+(PF) > SOFC-H^+(WM) > SOFC-O^{2-}(PF) > SOFC-O^{2-}(WM); however, at high fuel utilization, the SOFC-O^{2-}(PF) case shows a higher efficiency than the SOFC-H^+(WM) case. It is obvious that under

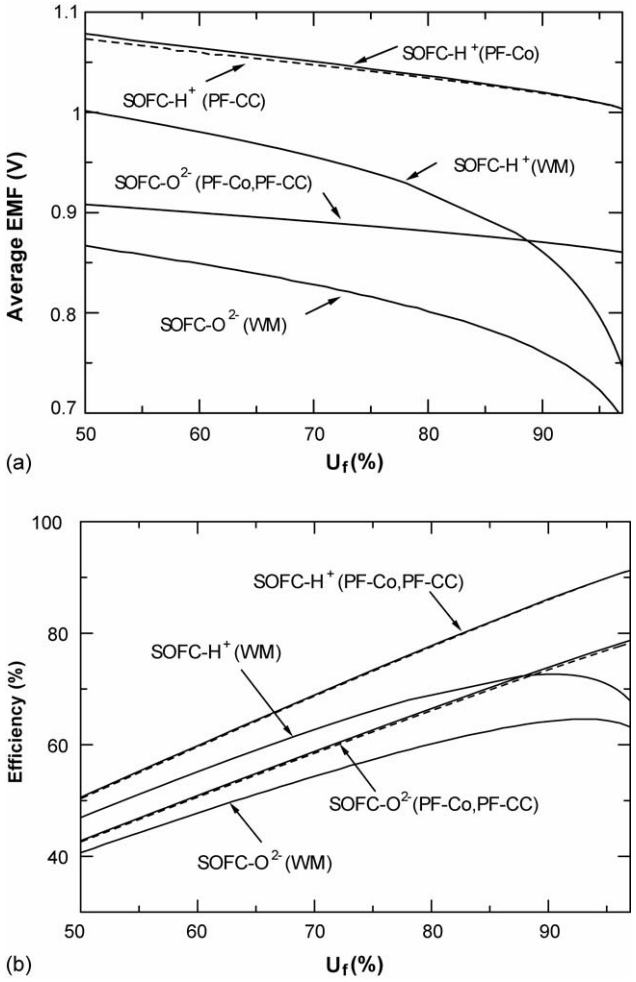

Fig. 4. Performances of SOFC-O^{2-} and SOFC-H^+ operated under PF and WM modes: (a) average EMF and (b) efficiency (inlet H_2O:EtOH = 3, T = 1200 K, P = 101.3 kPa, 400% excess air).

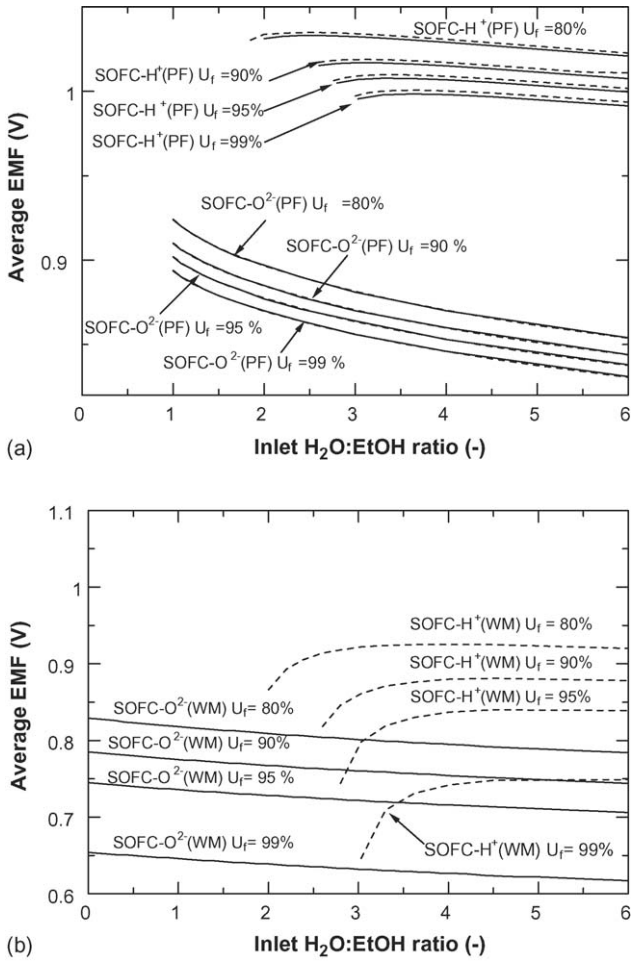

Fig. 5. Influence of inlet H_2O:EtOH ratio on SOFCs average EMF at different values of fuel utilization: (a) PF mode and (b) WM mode (T = 1200 K, P = 101.3 kPa, 400% excess air).

the same operation mode, the SOFC-H^+ cell is superior to the SOFC-O^{2-} cell. This is in good agreement with the previous work [7] which reported that the SOFC-H^+ case gives a maximum efficiency 15% higher than that of the SOFC-O^{2-} case in the range of inlet H_2O:CH_4 ratio of 2.0–3.0. Furthermore, it can be noticed that the feeding pattern has no influence on the calculated efficiency of SOFCs for both types of electrolyte.

It was reported in our previous study [9] that the SOFC-O^{2-} cell can be operated at much lower inlet H_2O:EtOH ratios than the SOFC-H^+ cell due to the difference in location of water production. Therefore, in order to compare the performance of SOFCs with different electrolyte types, it is necessary to take this SOFC-O^{2-} benefit into account in the calculations. The influence of the inlet H_2O:EtOH ratio on EMF and efficiency of SOFCs is investigated.

Figs. 5 and 6 show the influence of the inlet H_2O:EtOH ratio on the EMF and efficiency of SOFCs at different fuel utilizations. The inlet H_2O:EtOH ratio is considered only in the range where carbon formation is thermodynamically infeasible. The minimum ratio for the SOFC-O^{2-}(WM) and SOFC-O^{2-}(PF) cells is almost 0 and 1, respectively. However, the minimum ratio is higher for the SOFC-H^+ cell particularly at high fuel utilization for both modes of operation. The SOFC-O^{2-}(WM) cell can be operated without steam input because steam is produced from the electrochemical reaction of hydrogen. It should be noted that some steam is still needed in the feed during the start-up period before the cell can be self-sustaining. For both SOFC-O^{2-}(PF) and SOFC-O^{2-}(WM) cases, the EMF and efficiency decrease with increasing inlet H_2O:EtOH ratio. Therefore, their highest values are at the limit of carbon formation for each value of the fuel utilization. This indicates that the introduction of steam into the cell decreases the EMF and efficiency due to hydrogen dilution. In the SOFC-H^+(WM) and SOFC-H^+(PF) cases, the minimum inlet H_2O:EtOH ratios are 1.9 and 3.2 at 80 and 90% fuel utilization, respectively. The greater fuel utilization requires greater steam input. This is consistent with our previous work [9]. From Figs. 5 and 6, it is found that there is an optimum steam input in the SOFC-H^+ for both modes of operation at each fuel utilization. The introduction of steam initially increases the EMF and efficiency but has the negative effect at higher values. An appropriate inlet H_2O:EtOH ratio should be selected because steam is essential for the hydrogen production from the ethanol steam reforming but, on the other hand, it also acts as a diluent in the system. All optimum points found for

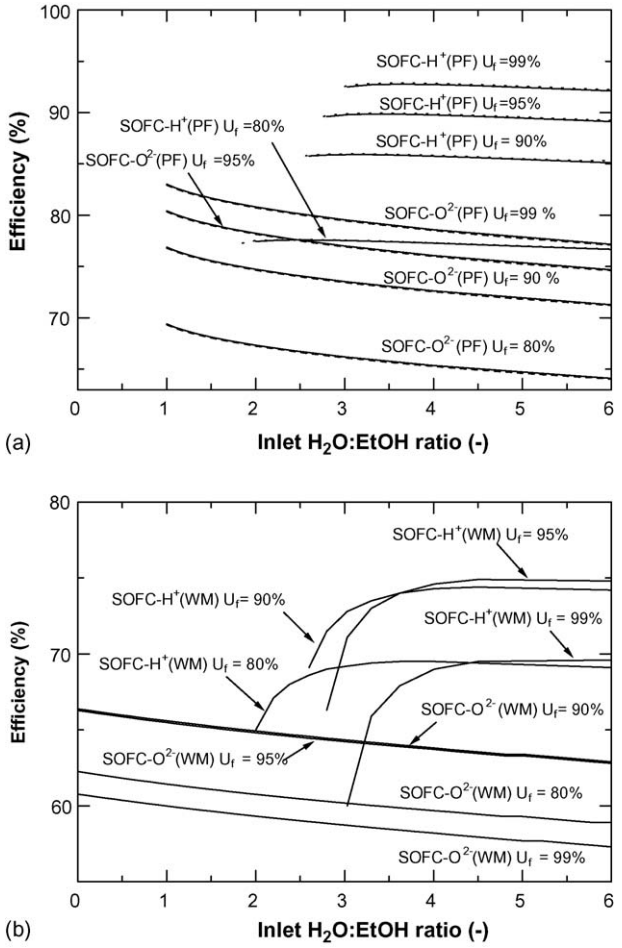

Fig. 6. Influence of inlet H_2O:EtOH ratios on SOFCs efficiency at different values of fuel utilization: (a) PF mode and (b) WM mode ($T = 1200$ K, $P = 101.3$ kPa).

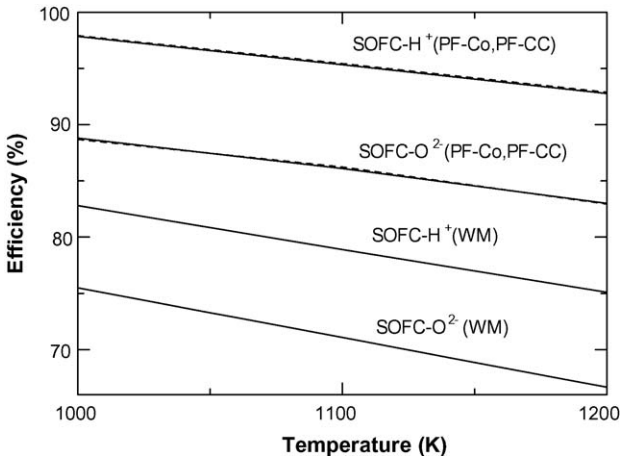

Fig. 7. Maximum efficiency of SOFC-O^{2-} and SOFC-H^+ at different operating temperatures ($P = 101.3$ kPa, 400% excess air).

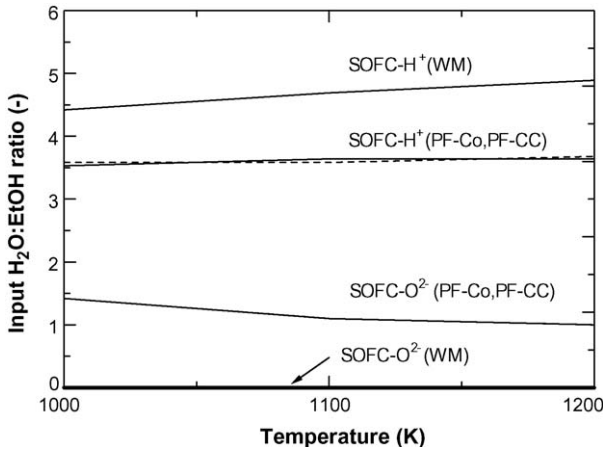

Fig. 8. Inlet H_2O:EtOH ratio at maximum efficiency ($P = 101.3$ kPa, 400% excess air).

each value of fuel utilization are beyond the limit of carbon formation. Furthermore, it is confirmed that there is no influence of feeding patterns on the EMF and efficiency for all ranges of the inlet H_2O:EtOH ratio.

By performing the calculations at various values of inlet H_2O:EtOH ratio and fuel utilization, it is possible to determine the maximum efficiency and the corresponding conditions for both SOFC-O^{2-} and SOFC-H^+ cells at each temperature level as shown in Figs. 7–9. It is obvious that the maximum SOFC efficiency follows the sequence of SOFC-H^+(PF) > SOFC-O^{2-}(PF) > SOFC-H^+(WM) > SOFC-O^{2-}(WM) for all temperatures (1000–1200 K). The maximum efficiency for all cases decreases with increasing temperature. This is consistent with the decrease in the EMF due to Gibb's free energy. The corresponding inlet H_2O:EtOH ratio is always approximately 0 for the SOFC-O^{2-}(WM). For the SOFC-O^{2-}(PF), the corresponding ratio is about 1.4 and 1 at 1000 and 1200 K, respectively. In the case of the proton conducting electrolyte, the SOFC-H^+(PF) requires a lower inlet H_2O:EtOH ratio than the SOFC-H^+(WM). For the SOFC-H^+(PF), the corresponding inlet H_2O:EtOH ratio is about 3.5 at 1000 K and increases with increasing temperature. While that for the SOFC-H^+(WM), is about 4.4 at 1000 K and also increases when operating temperature increases. This is probably because the water–gas shift reaction is exothermic and therefore more steam is required to move the reaction to the right to produce hydrogen. The corresponding fuel utilization at the maximum efficiency of the SOFC (PF) for both electrolytes is almost constant at approximately 99% but it slightly decreases

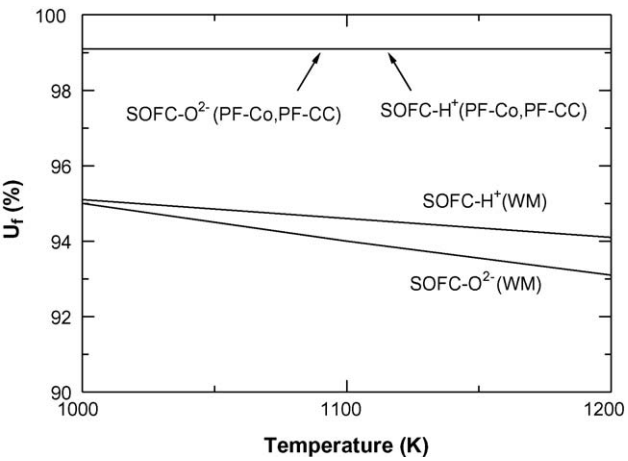

Fig. 9. Fuel utilization at maximum efficiency ($P = 101.3$ kPa, 400% excess air).

for the SOFC (WM) in both electrolytes when the temperature increases from 1000 to 1200 K.

From the above studies, it was found that although the benefit of lower steam requirement in the SOFC-O^2 is taken into account in the calculations, the SOFC-H^+ cell still shows higher efficiency than the SOFC-O^{2-} cell. This implies that the development of SOFCs should be directed to the use of a proton conducting electrolyte.

4. Conclusions

Thermodynamic analysis of ethanol-fuelled SOFCs using proton and oxygen ion conducting electrolytes in different modes of operation (plug flow and well-mixed) and feeding patterns (co-current and counter-current) has been presented in this article. At stoichiometric inlet H_2O:EtOH ratios, the SOFC-H^+(PF) provides the highest EMF and efficiency among various electrolytes and modes of operation. In order to compare the theoretical performances of SOFCs with different electrolytes, the benefit of reduced inlet steam requirement for the oxygen ion conducting electrolyte is taken into account.

It was demonstrated from the theoretical calculations assuming no polarization losses that the use of proton conducting electrolytes is more attractive than the use of oxygen ion conducting electrolytes. The SOFC-H^+(PF) gives the highest efficiency. Moreover, it was found that there is no influence of the feeding patterns on the average EMF and efficiency even though the EMF distribution along the cell is different.

Although the proton conducting electrolyte seems to be the most appropriate one for use in a solid oxide fuel cell from the theoretical calculations, it has a higher resistance than that of oxygen ion conducting electrolyte. If the ohmic loss of the electrolyte and other losses are considered, proton conducting electrolyte might perform worse than oxygen ion conducting electrolyte. If the overall resistance of proton conducting electrolyte could be reduced to be comparable with the oxygen ion conducting electrolyte, the proton conducting electrolyte is recommended as the most interesting electrolyte in the future. More details of the electrolyte selection including all resistances (i.e. ohmic loss and activation loss) must be calculated and justified.

Acknowledgements

The support from the Thailand Research Fund, Commission on Higher Education, and National Metal and Materials Technology Center are gratefully acknowledged.

References

[1] S. Freni, G. Maggio, S. Cavallaro, Ethanol steam reforming in a molten carbonate fuel cell: a thermodynamic approach, J. Power Sources 62 (1996) 67–73.
[2] G. Maggio, S. Freni, S. Cavallaro, Light alcohols/methane fuelled molten carbonate fuel cells: a comparative study, J. Power Sources 74 (1998) 17–23.
[3] T. Tsiakaras, A. Demin, Thermodynamic analysis of solid oxide fuel cell system fueled by ethanol, Chem. Eng. Sci. 102 (2001) 210–217.
[4] S.L. Douvartzides, F.A. Coutelieris, A.K. Demin, P.E. Tsiakaras, Fuel options for solid oxide fuel cell: a thermodynamic analysis, AIChE J. 49 (2003) 248–257.
[5] A. Demin, P. Tsiakaras, Thermodynamic analysis of a hydrogen fed solid oxide fuel cell based on a proton conductor, Int. J. Hydrogen Energy 26 (2001) 1103–1108.
[6] R. Salar, H. Taherparvar, I.S. Metcalfe, M. Sahibzada, SOFCs Based on $SrCe_{0.95}Yb_{0.05}O_3$ Proton Conductor, in 2001 Joint International Meeting—the 200th Meeting of The Electrochemical Society Inc. and the 52nd Annual Meeting of the International Society of Electrochemistry, San Francisco, California, 2001.
[7] A.K. Demin, P.E. Tsiakaras, V.A. Sobyanin, S.Yu. Hramova, Thermodynamic analysis of a methane fed SOFC system based on a protonic conductor, Solid State Ionics 152–153 (2002) 555–560.
[8] T. Shimada, C. Wen, N. Taniguchi, J. Otomo, H. Takahashi, The high temperature proton conductor $BaZr_{0.4}Ce_{0.4}In_{0.2}O_{3-\alpha}$, J. Power Sources 131 (2004) 289–292.
[9] S. Assabumrungrat, V. Pavarajarn, S. Charojrochkul, N. Laosiripojana, Thermodynamic analysis for solid oxide fuel cell with direct internal reforming fueled by ethanol, Chem. Eng. Sci. 59 (2004) 6015–6020.
[10] E.Y. Garcia, M.A. Laborde, Hydrogen production by the steam reforming of ethanol: thermodynamic analysis, Int. J. Hydrogen Energy 16 (1991) 307–312.
[11] K. Vasudeva, N. Mitra, P. Umasankar, S.C. Dhinggra, Steam reforming of ethanol for hydrogen production: thermodynamic analysis, Int. J. Hydrogen Energy 21 (1996) 13–18.
[12] E. Hernandez-Pacheco, D. Singh, P.N. Hutton, N. Patel, M.D. Mann, J. Power Sources 138 (2004) 174.
[13] K.W. Bedringas, I.S. Ertesvag, S. Byggstoyle, B.F. Magnussen, Energy analysis of solid-oxide fuel cell (SOFC) systems, Energy 22 (1997) 403–412.

Appendix 2

Performance Assessment of Bioethanol-Fed Solid Oxide Fuel Cell System Integrated with a Distillation Column

W. Jamsak[a], S. Assabumrungrat[a,†], P.L. Douglas[b,†], E. Croiset[b], N. Laosiripojana[c], R. Suwanwarangkul[d] and S. Charojrochkul[e]

[a] Center of Excellence in Catalysis and Catalytic Reaction Engineering, Department of Chemical Engineering, Faculty of Engineering, Chulalongkorn University, Thailand
[b] Department of Chemical Engineering, University of Waterloo, Canada
[c] The Joint Graduate School of Energy and Environment, King Mongkut's University of Technology Thonburi, Thailand
[d] Sirindhorn International Institute of Technology, Thammasat University, Thailand
[e] National Metal and Materials Technology Center (MTEC), Thailand
([†] Corresponding authors: suttichai.a@chula.ac.th or pdouglas@cape.uwaterloo.ca)

This paper investigated the performance of a bioethanol-fed Solid Oxide Fuel Cell (SOFC) system integrated with a distillation column (SOFC-D). Excess heat from the SOFC system was directly utilized in the distillation column where bioethanol (5 mol%) was purified to a desired concentration before feeding to the SOFC system consisting of an air heater, an ethanol/water heater, a reformer, an SOFC preheater, an SOFC stack and an afterburner. The SOFC-D system was simulated using Aspen Plus^{TM} for the distillation portion and Matlab^{TM} for the SOFC portion. The effects of operating parameters; i.e., ethanol concentration, ethanol recovery, fuel utilization and operating voltage on the performance and energy involved in the SOFC-D system (e.g. distillation energy: Q_D and the net exothermic heat of the SOFC system: $Q_{SOFC,Net}$) were examined. In addition, the performance of the SOFC-D system at the energy sufficient point where $Q_D = Q_{SOFC,Net}$ was considered. The integration of the distillation column with the SOFC system was found to offer superior SOFC performance. The ethanol recovery and fuel utilization significantly influenced the overall electrical efficiency and power density. Quite low performances are obtained when one operated the SOFC-D without an external heat source. The maximum overall efficiency and power density (~35% and 0.22 W cm^{-2}) occured at an ethanol recovery of 80% and U_f of 90%.

Introduction

A Solid Oxide Fuel Cell (SOFC) is considered to be an attractive power generation system nowadays. With high operating temperatures, it offers a wide range of applications, potential operation with an internal reformer and high system efficiency. Usually, an SOFC system consists of preheaters, a reformer, an SOFC stack and an afterburner. It has been known that there is always excess heat available when operating the SOFC system due to the presence of cell irreversibility and unreacted fuels. Therefore, most of SOFC systems are usually combined with other units to enhance the overall

efficiency. Two major integrated SOFC systems under current attention are SOFC-GT (gas turbine) and SOFC-CHP (combined heat and power). From an environmental point of view, bioethanol is an attractive green fuel which can be derived from renewable resources. It is also safe and easy to store and handle (1). Most studies on ethanol-fed SOFC systems are based on a feed containing a mixture of pure ethanol and water (2, 3). This operation is not efficient for an energy point of view because energy is consumed to purify bioethanol to pure ethanol which is subsequently mixed with water before feeding to the SOFC systems.

Therefore, in this study, the new ethanol-fed SOFC system is purposed. A distillation column is integrated with the SOFC system (SOFC-D) to purify bioethanol, which is typically available at about 5 mol%, to a desired concentration before feeding to the SOFC system. With this operation, the additional energy for producing pure ethanol is avoided and the excess heat from the SOFC system can be directly utilized in the distillation column. The paper is aimed at investigating the effects of distillation operating parameters (i.e. ethanol recovery and ethanol concentration) and SOFC operating parameters (i.e. fuel utilization and voltage) on the performance of the SOFC-D system.

SOFC system modelling

In this study, the SOFC system consisted of three heaters (an EtOH/H_2O vaporizer (Heater-1), an air heater (Heater-2) and an anode preheater (Heater-3)), a fuel cell stack, an external reformer and an afterburner. A distillation column was integrated with the SOFC system as presented in Figure 1. Bioethanol (5 mol%) was fed to the distillation column and the distillate with desired ethanol concentration and recovery was then fed to the SOFC system. A distillation column with equilibrium stages, a total condenser and a kettle reboiler was chosen. The feed stream was introduced at the stage above the reboiler. The *Radfrac* rigorous equilibrium stage module in *Aspen Plus*^{TM} was used for simulating the column and determining the heat duties in the condenser and reboiler, Q_C and Q_D respectively.

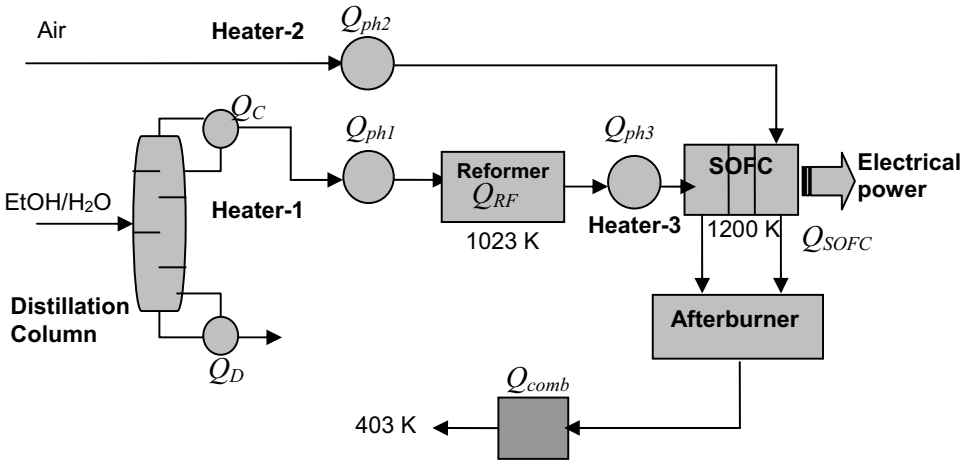

Figure 1. Schematic diagram of SOFC-D.

The minimum heat duty in the reboiler (Q_D) was obtained by varying number of stages and the reflux ratio. The distillate with a desired ethanol concentration was then heated to the reforming temperature (T_{RF}), in this case 1023 K, and reformed to generate a hydrogen-rich product, assuming that the reactions take place in an external reformer at equilibrium. The product was then heated to the SOFC temperature (T_{SOFC}) of 1200 K and introduced to the anode of the SOFC stack. In the SOFC stack, only the water gas shift reaction and electrochemical reactions were considered due to the complete ethanol reforming reaction in the reformer at high temperature. The reformer and the SOFC stack were assumed to operate under isothermal conditions and, therefore, Q_{RF} and Q_{SOFC} were involved in the reformer and the stack, respectively. Air (380% excess) was fed to the cathode chamber. In this study, the SOFC cell configuration was based on the tubular design (4). For activation losses, Achenbach's semi empirical correlation (9) was used to predict activation overpotentials for the anode and cathode. It should be noted that the chosen T_{SOFC} of 1200 K was within the accurate temperature range for Achenbach's correlation (5). The equations used in calculations are presented as follows.

$$V = E - i(r_{ohm} + r_{act}) \quad [1]$$

$$E = \frac{RT}{4F} \ln \frac{p_{O_2,c}}{p_{O_2,a}} \quad [2]$$

$$r_{act,c} = \left[\frac{4F}{RT} k (x_{O_2,c})^m \exp\left(-\frac{E_{a,c}}{RT} \right) \right]^{-1} \quad [3]$$

$$r_{act,a} = \left[\frac{2F}{RT} k (x_{H_2,a})^m \exp\left(-\frac{E_{a,a}}{RT} \right) \right]^{-1} \quad [4]$$

$$r_{ohm,i} = \rho_i \delta_i \quad [5]$$

$$P = iV \quad [6]$$

$$\eta_{elec,ov} = \frac{P}{n_{EtOH} * LHV_{EtOH}} \quad [7]$$

where E is the electromotive force of the cell, V the operating voltage, i the current density, R the gas constant, T the temperature, F the Faraday's constant, r_{act} the activation resistance, E_a the activation energy at the electrodes, $x_{O_2,c}$ and $x_{H_2,a}$ the mole fractions of oxygen in the cathode chamber and hydrogen in the anode chamber, respectively, r_{ohm} the ohmic resistance, ρ the resistivity of material, subscript i represents cell component, P the power density of the cell, n_{EtOH} the total ethanol flow rate fed to the distillation column, LHV_{EtOH} the low heating value of ethanol and $\eta_{elec,ov}$ the overall electrical efficiency. For calculating the SOFC performance, it was assumed that fuel and oxidant were well-diffused through the surface of the electrodes. Therefore, concentration loss could be omitted. Procedures for calculating composition and average EMF within SOFC stack were given in our previous works (6, 7). The values of parameters for the ohmic loss and activation polarization were adopted from the literature (4) and (5), respectively.

The effluent from the anode and the cathode were burnt in the afterburner in order to provide heat to the reformer (Q_{RF}), the EtOH/H_2O heater (Q_{ph1}), the air heater (Q_{ph2}) and

the anode preheater (Q_{ph3}). It should be noted that the heat of combustion (Q_{comb}) in the afterburner was calculated based on the exhaust gas temperature of 403 K. The values of energy involved in each unit can be determined from conventional energy balance calculations. The net exothermic heat from the SOFC part after transferring heat to the three heaters and the reformer ($Q_{SOFC,Net}$) can be calculated from Equation (8).

$$Q_{SOFC,Net} = Q_{SOFC} + Q_{Comb} - Q_{ph1} - Q_{ph2} - Q_{ph3} - Q_{RF} \quad [8]$$

Results and Discussion

Effects of ethanol concentration and recovery on SOFC performance

The effect of ethanol concentration (C_{EtOH}) on SOFC performance is shown in Figure 2. The cell is operated at T_{SOFC} = 1200 K, U_f = 80% and EtOH recovery = 90%. The range of ethanol concentration is between 5 and 41 mol%. The former value represents the concentration of bioethanol while the latter represents the boundary of carbon formation (7). Operation at higher concentrations is not recommended as deactivation of the reforming and anode catalysts by carbon formation are possible. The results indicate that the SOFC performance can be improved when the SOFC system is operated with a feed of high ethanol concentration since the presence of excessive amount of water in the feed lowers the hydrogen concentration, resulting in lower cell potential, power density and electrical efficiency.

When the distillation column is operated at different ethanol recoveries, different amounts of ethanol are introduced to the SOFC system. It is therefore not surprising, as shown in Figure 3, that the overall electrical efficiency decreases with the decreasing ethanol recovery. From the results, it is obvious that the operation of the SOFC system with a direct feed of bioethanol is not practical due to the low SOFC performance. The bioethanol should be purified to a higher concentration at high ethanol recovery prior to feeding to the SOFC system.

(a)

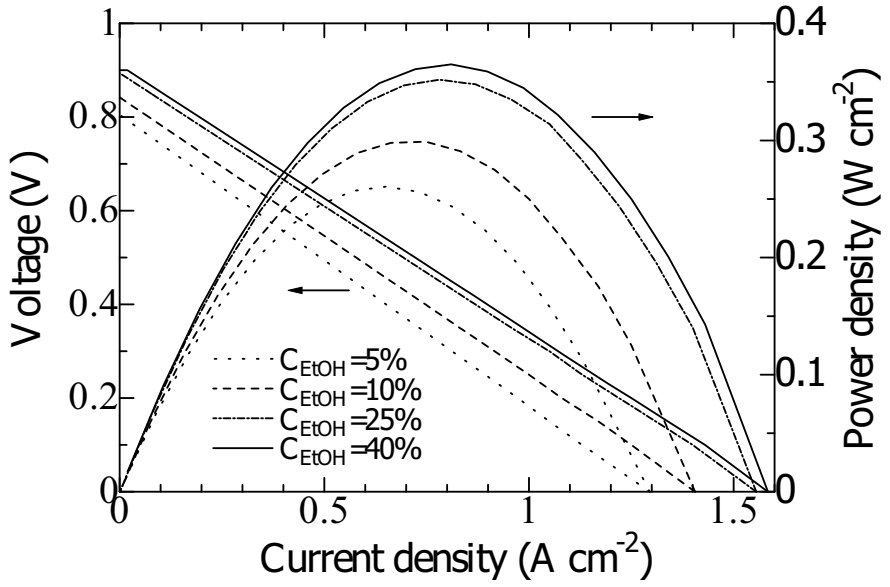

(b)

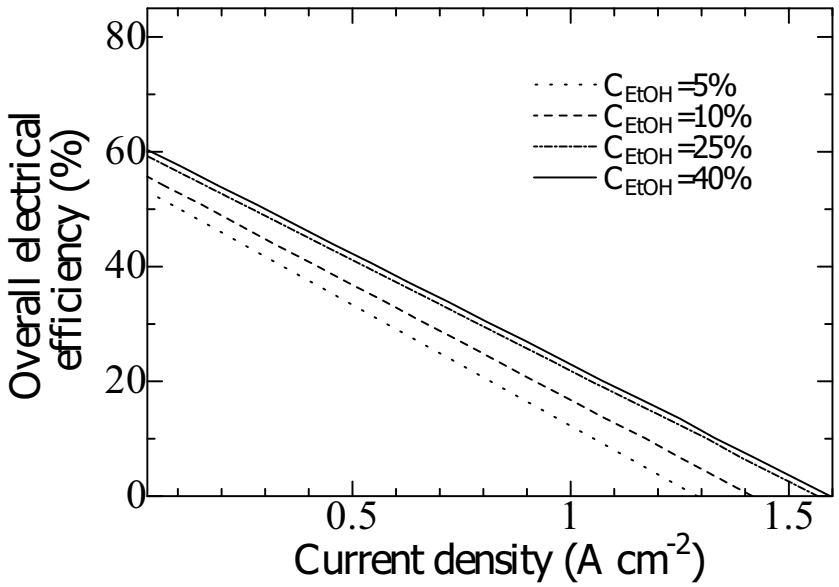

Figure 2. Effect of ethanol concentration on electrical performance: a) voltage and power density and b) overall electrical efficiency (EtOH recovery = 90%, U_f = 80%, P = 101.3 kPa).

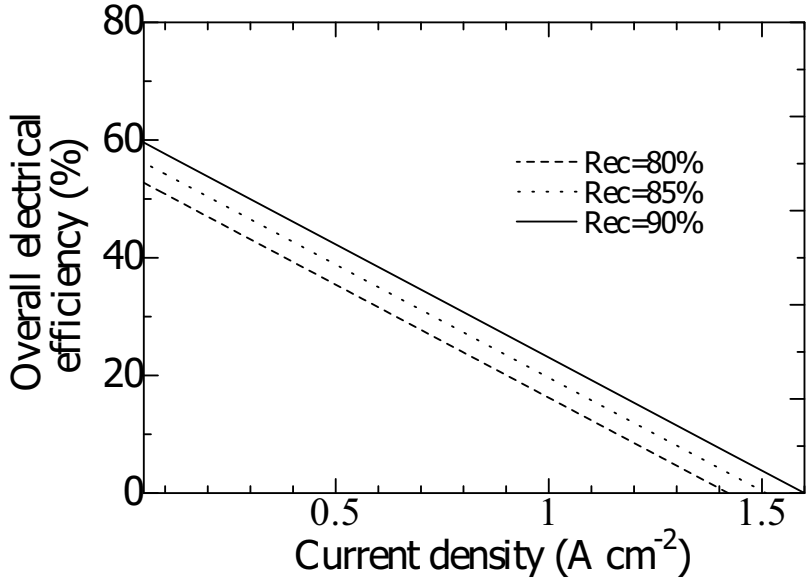

Figure 3. Effect of ethanol recovery on overall electrical efficiency (C_{EtOH} = 25% mol, U_f = 80%, P = 101.3 kPa).

Effects of ethanol concentration and recovery on energy involved in the SOFC-D system

Although the integration of the distillation column with the SOFC system is proven to offer superior SOFC performance, the energy involved in the overall SOFC-D system is another important issue of consideration for determining the potential use of the SOFC-D system. Figure 4 shows the effects of ethanol concentration and recovery on the distillation energy required for a reboiler (Q_D) and the net exothermic heat of the SOFC system ($Q_{SOFC,Net}$) operated at V = 0.7 V, U_f = 80%, T_{SOFC} =1200 K. From the results, it can be seen that both Q_D and $Q_{SOFC,Net}$ increase with increasing C_{EtOH} and EtOH recovery. For the reboiler heat duty, Q_D, it is obvious that more energy is required by the reboiler of the distillation column to produce a higher concentration product at a higher recovery. Considering the effect of ethanol concentration on $Q_{SOFC,Net}$, the increase of $Q_{SOFC,Net}$ with the increasing C_{EtOH} is mainly due to the decrease in the energy demand for heating the ethanol/water mixture (Q_{ph1}). When the system is operated at higher ethanol recoveries while keeping the fuel utilization (U_f) constant, more ethanol is present in the anode effluent stream, resulting in a higher combustion energy (Q_{comb}) and therefore $Q_{SOFC,Net}$. From the results, it should be noted that when the SOFC-D is operated at 80-90% recovery, $Q_{SOFC,Net}$ is lower than Q_D, indicating that the exothermic heat from the SOFC system is not sufficient to supply the demand from the reboiler for all ethanol concentrations (17-41%) at the base condition (V = 0.7 V, U_f = 80%) and therefore an external heat source will be needed to supply heat to the reboiler.

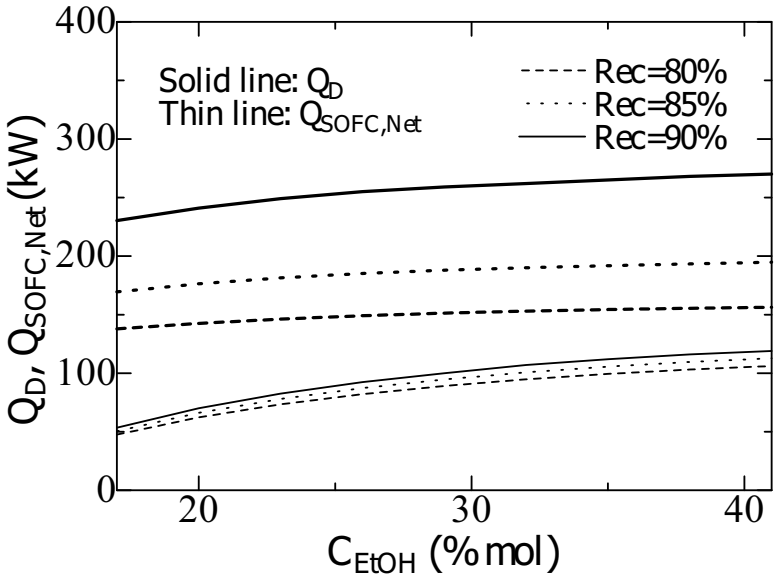

Figure 4. Effect of ethanol concentration and recovery on Q_D and $Q_{SOFC,Net}$ (V = 0.7 V, U_f = 80%, P = 101.3 kPa).

Effects of operating voltage and fuel utilization on energy involved in the SOFC-D system

When it is desired to operate the bioethanol-fed SOFC-D system without relying on other energy sources, $Q_{SOFC,Net}$ must be higher than Q_D. As mentioned earlier in Eq. (9), the exothermic heat in the SOFC system consists of two terms Q_{SOFC} and Q_{comb}. For

Q_{SOFC}, the energy arises from the irreversibility of the electrochemical reaction, in this case, entropy losses and losses due to the components of SOFC (e.g. activation losses and ohmic losses). The irreversibility due to the cell components can be observed through the difference between the maximum theoretical voltage (*EMF*) and the actual voltage. In practice, the operating voltage can be adjusted by changing an external load. For Q_{comb}, the energy is dependent on amount of unreacted fuel present in the anode effluent stream of the SOFC stack; therefore, fuel utilization (U_f) mainly influences Q_{comb}. Figure 5 shows the effects of operating voltage and fuel utilization on $Q_{SOFC,Net}$ at various values of ethanol recovery. C_{EtOH} is kept at 41 mol%. The values of Q_D are also provided in the figure. If one is to operate the bioethanol-fed SOFC-D system without relying on other energy sources, $Q_{SOFC,Net}$ must be greater than Q_D, in other words one must operate in the region above the Q_D curve. It can be seen that operating at lower fuel utilization or lower voltage can help keep $Q_{SOFC,Net}$ above Q_D. In particular, operating at low voltage (U_f = 80%, V = 0.5 V) or at low fuel utilization (U_f = 70%, V = 0.5 V), the SOFC-D can be operated at the ethanol recovery as high as 82% and 86%, respectively.

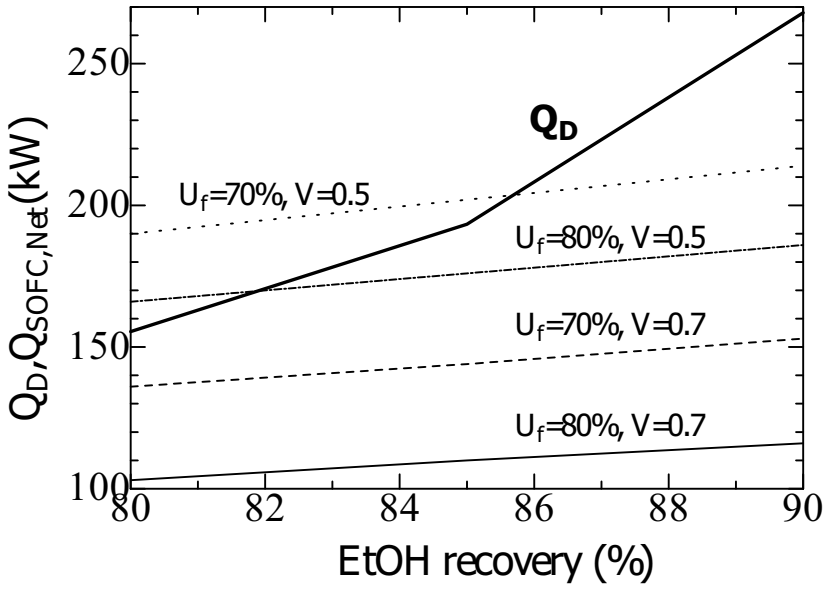

Figure 5. Effect of voltage and fuel utilization on Q_D and $Q_{SOFC,Net}$ for different values of EtOH recoveries (C_{EtOH} = 41%, P = 101.3 kPa).

Performance of the SOFC-D system at its maximum electrical power

In this section, the performance of the SOFC-D system at the energy sufficient point where $Q_D = Q_{SOFC,Net}$ is considered. The values of power density and overall electrical efficiency at different ethanol recoveries (60-90%) are shown in Figure 6. At this energy sufficient point, the maximum electrical power is obtained because no excess heat is left over from the SOFC-D system. When a value of U_f is specified, the corresponding value of the operating voltage and power density at each ethanol recovery can be determined. It is noticed that within this range of ethanol recovery, the overall electrical efficiency decreases with the increasing ethanol recovery particularly at high ethanol recovery. This is because the reboiler heat duty increases more rapidly than the energy gained from

having more ethanol in the feed to the SOFC system. The overall electrical efficiency is found to be independent on the value of fuel utilization. In contrast, the value of fuel utilization significantly influences the power density. As the fuel utilization increases, less amount of unreacted fuel is present in the anode effluent stream and therefore the value of Q_{comb} decreases. Consequently, the higher value of Q_{SOFC}, which is dependent on both the cell current and operating voltage, is required. From the results, it is obvious that the selection of the ethanol recovery and fuel utilization of the SOFC-D system is very important to achieve good SOFC-D performance. However, quite low performances are obtained when one operates the SOFC-D system without an external heat source. The maximum overall efficiency at the energy-sufficient point which does not require an external heat source as high as 35% can be obtained at an ethanol recovery of 60%. The power density of 0.22 W cm^{-2} occurs at U_f = 90%. It is likely that another ethanol purification process (such as pervaporation) which consumes less energy is essential to be integrated with the SOFC system to improve the overall electrical efficiency.

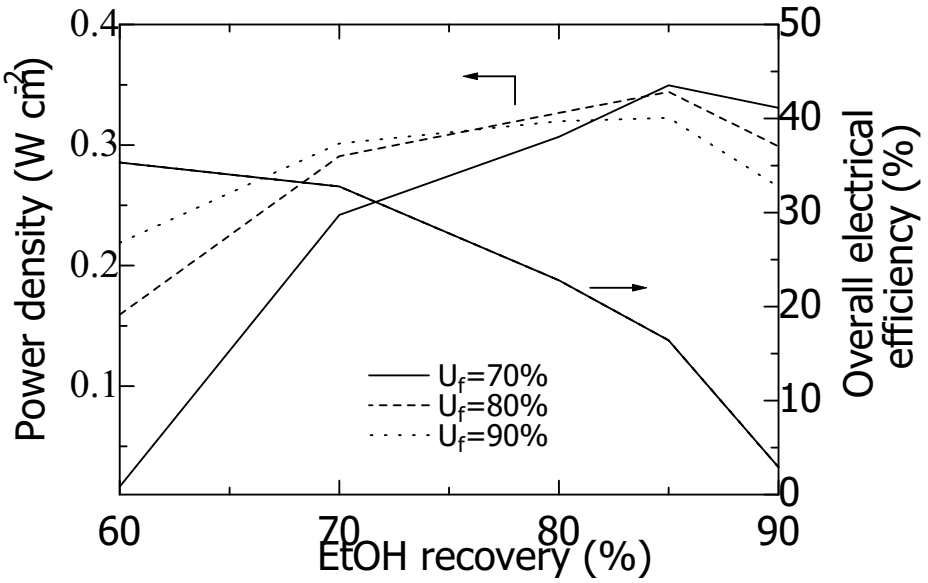

Figure 6. Performance of SOFC-D at the maximum electrical power for different values of EtOH recovery (C_{EtOH} = 41%, P = 101.3 kPa).

Conclusion

The SOFC system integrated with a distillation column (SOFC-D) has been proposed. Bioethanol with 5 mol% of EtOH in water was purified in a distillation column to a desired concentration and introduced to the SOFC system consisting of an ethanol/water vaporizer, an air heater, a reformer, an anode preheater, an SOFC stack and an afterburner. The effect of ethanol concentration and recovery on electrical performance and energy involving the SOFC system has been studied. Higher ethanol concentration and recovery yielded higher electrical performance and both increase the exothermic heat in the SOFC system; however, they require higher distillation energy. To operate the SOFC-D system without an external heat source, the effect of SOFC operating parameters (e.g. fuel

utilization and voltage) on the energy involving the SOFC-D system has been investigated. It was found that operating at lower fuel utilization or lower voltage can help in increasing the exothermic heat within the system. The conditions at the energy-sufficient point at various ethanol recoveries have been presented. The maximum overall efficiency and power density (~35% and 0.22 W cm^{-2}) occur at an ethanol recovery of 60% and U_f = 90%.

Acknowledgments

The supports from the Thailand Research Fund, Commission on High Education and National Metal and Materials Technology Center (MTEC) are gratefully acknowledged.

References

1. G. Maggio, S. Freni and S. Cavallar, *J. Power Sources*, **74**, 17 (1998).
2. S. Douvartzides, F.A. Coutelieris and P.E. Tsiakaras, *J. Power Sources*, **114**, 203 (2003).
3. S. Douvartzides, F. Coutelieris and P. Tsiakaras, *J. Power Source*, **131**, 224 (2004).
4. S.H. Chan and O.L. Ding, *Int. J. Hydrogen Energy*, **30**, 167 (2005).
5. E. Achenbach, J. Power Source, **49**, 333 (1994).
6. E. Hernandez-Pachenco, D. Singh, P. N. Hutton, N. Patel and M. D. Mann, *J. Power Source*, **138**, 174 (2004).
7. S. Assabumrungrat, V. Pavarajarn, S.Charojrochkul and N. Laosiripojana, *Chem. Eng. Sci*., **59**, 6015 (2004).
8. W. Jamsak, S. Assabumrungrat, P.L. Douglas, N. Laosiripojana and S. Charojrochkul *Chem. Eng. J.*, **119**, 11 (2006).

Appendix 3

ELSEVIER

Chemical Engineering Journal 133 (2007) 187–194

Chemical Engineering Journal

www.elsevier.com/locate/cej

Performance of ethanol-fuelled solid oxide fuel cells: Proton and oxygen ion conductors

W. Jamsak [a], S. Assabumrungrat [a,*], P.L. Douglas [b], N. Laosiripojana [c], R. Suwanwarangkul [d], S. Charojrochkul [e], E. Croiset [b]

[a] *Center of Excellence in Catalysis and Catalytic Reaction Engineering, Department of Chemical Engineering, Faculty of Engineering, Chulalongkorn University, Thailand*

[b] *Department of Chemical Engineering, University of Waterloo, Canada*

[c] *The Joint Graduate School of Energy and Environment, King Mongkut's University of Technology, Thonburi, Thailand*

[d] *Department of Chemical Engineering, Faculty of Engineering, King Mongkut's Institute of Technology, Ladkrabang, Thailand*

[e] *National Metal and Materials Technology Center (MTEC), Thailand*

Received 31 July 2006; received in revised form 8 February 2007; accepted 1 March 2007

Abstract

This paper investigates the performance of ethanol-fuelled solid oxide fuel cells (SOFCs) with two types of solid electrolytes, namely oxygen ion-conducting (SOFC-O^{2-}) and proton-conducting electrolytes (SOFC-H^+). Our previous work reported that the SOFC-H^+ shows superior theoretical performance over the SOFC-O^{2-} electrolyte. However, in this work when all resistances are taken into account, the actual performance of the SOFC-O^{2-} (Ni-YSZ|YSZ|YSZ-LSM) becomes significantly better than that of SOFC-H^+ (Pt|SCY|Pt). The maximum power density of the SOFC-O^{2-} is about 34 times higher than that of the SOFC-H^+ when operated at an inlet H_2O:EtOH ratio of 3, a fuel utilization factor of 80% and a temperature of 1200 K. Then the required values of the total resistance of the SOFC-H^+ to achieve the same power density as the SOFC-O^{2-} were determined. It was found that due to the superior theoretical performance of the SOFC-H^+, it is not necessary to reduce the SOFC-H^+ total resistance to the same values as the one for SOFC-O^{2-}. The study also indicates that reduction of only the electrolyte resistance is not sufficient to improve the SOFC-H^+ performance and, therefore, the other resistances including activation, electrodes and interconnect resistances need to be reduced simultaneously. Finally, the improvement of the electrolyte resistance by changing its resistivity and thickness is discussed.

Keywords: Solid oxide fuel cell; Oxygen conductor; Proton conductor; Performance; Losses

1. Introduction

Fuel cells are considered to be the most promising technology for chemical to electrical energy conversion. Solid oxide fuel cells (SOFC) have attracted considerable interest as they offer a wide range of potential applications, possibility for operation with an internal reformer and high system efficiency. Many fuels have been suggested for use in SOFCs; among these, ethanol is considered to be an attractive green fuel because it can be produced renewably from biomass, waste materials from agro-industries, forestry residue materials, or even organic fractions from municipal solid waste. Ethanol also offers other advantages related to natural availability and safety in storage and handling.

There are a number of published studies dealing with the use of ethanol for producing hydrogen for use in fuel cells [1–7]. However, only a few studies of ethanol utilization in SOFCs operation have been undertaken. The performance of SOFCs fuelled by products from different ethanol processes, such as ethanol steam reforming, ethanol dry reforming and ethanol partial oxidation with air were investigated. Ethanol steam reforming showed the highest maximum efficiency for high operating temperature [8]. The performance of external reforming SOFC (ER-SOFC) with different fuels, such as methane, methanol, ethanol and gasoline, were compared over a temperature range of 800–1200 K [9]. The maximum efficiency was obtained near the boundary of carbon formation for all fuels. The highest efficiency was obtained from methane (96%) followed by ethanol (94%) and then methanol (91%). By using an exergy-energy analysis, it was reported that the methane-fed SOFC provides higher efficiency than when ethanol is fed [10].

* Corresponding author. Tel.: +66 2 218 6868; fax: +66 2 218 6877.
E-mail address: Suttichai.A@chula.ac.th (S. Assabumrungrat).

1385-8947/$ – see front matter © 2007 Elsevier B.V. All rights reserved.
doi:10.1016/j.cej.2007.03.003

Nomenclature

E	electromotive force (V)
E_a	activation energy (kJ mol^{-1})
F	Faraday's constant (C mol^{-1})
i	current density (A cm^{-2})
I	current (A)
K	equilibrium constant of hydrogen oxidation reaction (kPa$^{-0.5}$)
n_i	number of moles of component i (mol)
p_i	partial pressure of component i (kPa)
P	power density (W cm^{-2})
r	resistance (Ω cm^2)
r_{act}	activation polarization area specific resistance (Ω cm^2)
r_e	electrolyte area specific resistance (Ω cm^2)
r_o	other area specific resistance (Ω cm^2)
r_{tot}	total area specific resistance (Ω cm^2)
R	gas constant (J mol^{-1} K^{-1})
T	temperature (K)
V	voltage (V)
x_i	mole fraction of component i

Greek letters

δ	thickness (cm)
ρ	resistivity (Ω cm)

Subscripts

a	anode
c	cathode

Noticeably, most SOFC studies have employed oxygen-ion conducting electrolytes although proton-conducting electrolytes are also possible for SOFC operation. There are several studies on the development of proton-conducting ceramic electrolytes for high temperature applications [11–14]; however, these studies mostly focus on the characterization of material properties, such as conductivities under various atmospheres. To date, there are very few studies using proton-conducting electrolyte in an SOFC operation [15,16]. The performance of SOFC with proton-conducting electrolytes (SOFC-H^+) in Yb-doped $SrCeO_3$ (SCY) electrolyte with platinum electrodes system (Pt|SCY|Pt) were investigated. The SOFC-H^+ was tested with various fuels (H_2 and CH_4) and atmospheres (dry and wet) at high temperatures (873–1273 K). It was shown that the SOFC-H^+ (dry-CH_4) system provided the highest performance [16].

Theoretical performance comparisons of SOFCs with different electrolytes revealed that the SOFC-H^+ provides higher efficiency than the SOFC with oxygen-ion conducting electrolytes (SOFC-O^{2-}) for a system fed with hydrogen and methane [17,18]. However, these studies were based on the same steam/methane feed ratio for the methane-fed case. It was demonstrated in our previous work [19–21] that the steam requirement for the SOFC-O^{2-} is lower than that for the SOFC-H^+ due to the presence of steam generated by the anodic electrochemical reaction. Therefore, the benefit from lower steam requirements in the SOFC-O^{2-} should be taken into account in the comparison between the two processes. When this benefit was considered, it was still observed that the SOFC-H^+ yielded higher EMF and efficiency than the SOFC-O^{2-} [22]. However, the calculations neglected the presence of actual losses encountered in a real SOFC operation. Therefore, this article aims at comparing the actual performance of SOFCs with different electrolytes. Although it is well known that current proton-conducting electrolytes have high resistivity and thus the performance of SOFC-H^+ should be inferior to SOFC-O^{2-}, it is still necessary to determine the status of the SOFC-H^+ technology compared to that of SOFC-O^{2-}. In our previous work, the theoretical performance of SOFC-H^+ and SOFC-O^{2-} was compared. Only the EMF and maximum theoretical efficiency were considered at that time and no losses were taken into consideration. In contrast, this study focuses on the actual performance of SOFC-H^+ and SOFC-O^{2-}. The losses in the SOFC cell (e.g. activation losses and ohmic losses) are now considered. The information from this theoretical study is also important in determining property targets (e.g. resistivity, electrolyte thickness and other resistance) for SOFC-H^+ in order to yield similar performance as the SOFC-O^{2-}.

2. Theory

The reaction system involving in the production of hydrogen via ethanol steam reforming reaction is represented by the following reactions [23]:

$$C_2H_5OH + H_2O \rightarrow 4H_2 + 2CO \quad (1)$$

$$CO + H_2O \rightarrow H_2 + CO_2 \quad (2)$$

$$CO + 3H_2 \rightarrow CH_4 + H_2O \quad (3)$$

Previous results [24,25] confirmed that a gas mixture in thermodynamic equilibrium contains only five components of noticeable concentration: carbon monoxide, carbon dioxide, hydrogen, steam, and methane.

The following three reactions are the most likely reactions leading to carbon formation:

$$2CO \rightarrow CO_2 + C \quad (4)$$

$$CH_4 \rightarrow 2H_2 + C \quad (5)$$

$$CO + H_2 \rightarrow H_2O + C \quad (6)$$

The Boudard reaction (Eq. (4)) has the largest Gibb's free energy; therefore, it was used to determine the possibility of carbon formation. The carbon activity (α_c) can be calculated from the following equation:

$$\alpha_c = \frac{K_c p_{CO}}{p_{CO_2}} \quad (7)$$

where K_c represents the equilibrium constant in Eq. (4) and p_i is the partial pressure of component i. The carbon formation can take place when $\alpha_c \geq 1$ [9,26]. In this study, conditions for SOFC operation under carbon formation were avoided.

Two types of solid electrolytes can be employed; namely, oxygen-conducting and proton-conducting electrolytes, which differ in the location were water is produced. For the oxygen-conducting electrolyte, water is produced in the anode chamber whereas it appears in the cathode side for the proton-conducting electrolyte.

2.1. Voltage calculations

2.1.1. Electromotive force

The electromotive force (EMF) for different electrolytes can be calculated as follows:

$$\text{SOFC-O}^{2-}: \quad E = \frac{RT}{4F} \ln \frac{p_{O_2,c}}{p_{O_2,a}} \tag{8}$$

$$\text{SOFC-H}^{+}: \quad E = \frac{RT}{2F} \ln \frac{p_{H_2,a}}{p_{H_2,c}} \tag{9}$$

where p_{O_2} and p_{H_2} are oxygen and hydrogen partial pressures, respectively, while the subscripts 'a' and 'c' represent anode and cathode, respectively. R is the universal gas constant, T the absolute temperature and F is the Faraday's constant.

In SOFC-O^{2-}, the partial pressure of oxygen in the cathode chamber is calculated directly from its mole fraction whereas the value in the anode chamber is calculated by assuming that the oxygen content is in equilibrium with hydrogen and water. Accordingly, the oxygen pressure in the anode chamber is determined from the following equation:

$$p_{O_2,a} = \left(\frac{p_{H_2O,a}}{K p_{H_2,a}} \right)^2 \tag{10}$$

where K is the equilibrium constant of the hydrogen oxidation reaction.

In contrast, for the SOFC-H^+, the partial pressure of hydrogen in the anode chamber is determined directly from its mole fraction while that at the cathode side is determined by assuming that the hydrogen content is in equilibrium with oxygen and water. Accordingly, the hydrogen pressure in the cathode chamber is calculated from the following equation:

$$p_{H_2,c} = \frac{p_{H_2O,c}}{K p_{O_2,c}^{1/2}} \tag{11}$$

Since the gas composition typically varies along the chamber, so does the local EMF. Accordingly, the average EMF ($\bar{E}$) is determined by numerical integration of the local EMF per unit cell length. It should be noted that the EMF also depends significantly on the inlet H_2O:EtOH ratio, operating temperature and fuel utilization. To simplify the calculations, it is assumed that gas compositions at the anode are at their equilibrium compositions along the cell length. For the calculation of the equilibrium composition in the SOFCs the reader can refer to our previous work [19–22]. However, it should be noted that a deviation from this equilibrium condition would result in lower EMF values as less hydrogen was generated in the anode chamber to compensate for the hydrogen consumed by the electrochemical reaction. Therefore, the results shown in this work represent the best performances for all SOFC cases.

In this paper, the electrochemical cells composed of Ni-YSZ|YSZ|YSZ-LSM and Pt|SCY|Pt are considered for the SOFC-O^{2-} and the SOFC-H^+, respectively. In this study, the state-of-the-art Ni-YSZ|YSZ|YSZ-LSM was chosen to represent SOFC-O^{2-}. Pt|SCY|Pt was chosen for SOFC-H^+ because the SCY electrolyte is known as one of the classical proton conducting materials with a high proton transport number [13]. Indeed it has high chemical stability and high proton conductivity at high temperatures.

2.1.2. Actual voltage

In practice, there is a deviation between EMF and the actual cell voltage (V) due to several losses (e.g. ohmic loss, activation loss, etc.). The actual cell voltage (V) is determined as follows:

$$V = E - i r_{tot} \tag{12}$$

$$r_{tot} = r_e + r_o \tag{13}$$

$$r_o = r_{act} + r_{ohm,electrode} + r_{ohm,interconnect} \tag{14}$$

where i is the current density (A cm^{-2}), r_{tot} the total resistance (Ω cm^2), r_e the electrolyte resistance (Ω cm^2) and r_o is the other resistance (Ω cm^2) including activation, electrodes and interconnect resistances. In this article, it is assumed that fuels and oxidants are well-diffused in/out of the electrodes. Therefore, the concentration losses can be ignored. This assumption is valid when the SOFC does not operate at too high current density.

- Activation loss:

  Activation loss is the loss caused by electrochemical reactions at the electrodes. In this study, Achenbach's correlation [26] is used for calculations of the SOFC-O^{2-}:

$$\text{cathode}: \quad r_{act,c} = \left[\frac{4F}{RT} k (x_{O_2,c})^m \exp\left(-\frac{E_{a,c}}{RT} \right) \right]^{-1} \tag{15}$$

$$\text{anode}: \quad r_{act,a} = \left[\frac{2F}{RT} k (x_{H_2,a})^m \exp\left(-\frac{E_{a,a}}{RT} \right) \right]^{-1} \tag{16}$$

  where $x_{O_2,c}$ and $x_{H_2,a}$ are mole fractions of oxygen in the cathode chamber and hydrogen in the anode chamber, respectively. The parameters used in Eqs. (15) and (16) are summarized in Table 1. It should be noted that these parameters are valid in the temperature range of 1173–1273 K [27].

- Ohmic loss:

  Ohmic losses are caused by the resistance of materials (i.e., electrodes, interconnect and current collectors) from the flow of electrons and by the resistance of electrolyte from the flow of ions passing through it. Ohmic resistances can be calculated by using the following equations:

$$r_{ohm,i} = \rho_i \delta_i \tag{17}$$

Table 1
Parameters used in Eqs. (15) and (16)

r_{act} (Ω cm^2)	k ($\times 10^{-5}$ A cm^{-2})	E_a (kJ mol^{-1})	m
$r_{act,c}$	14.9	160	0.25
$r_{act,a}$	0.213	110	0.25

Table 2
Parameters of SOFC cell components in Eqs. (17) and (18)

Materials	Parameters		Thickness (μm)
	α (Ω cm)	β (K)	
Anode (40% Ni/YSZ cermet)	2.98×10^{-5}	−1,392	150
Cathode (Sr-doped $LaMnO_3$:LSM)	8.11×10^{-5}	600	2000
Electrolyte (Y_2O_3 doped ZrO_2:YSZ)	2.94×10^{-5}	10,350	40
Interconnect (Mg doped $LaCrO_3$)	1.256×10^{-3}	4,690	100
Protonic electrolyte (Yb doped $SrCeO_3$:SCY)	7×10^{-5}	5.5×10^{-3}	1000

with

$$\rho_i = \alpha_i \, e^{(\beta_i/T)} \tag{18}$$

where subscript i represents the cell component (i.e., electrodes, electrolyte and interconnect), ρ the resistivity, δ_i the thickness of component i, and α and β are the constants specific to the materials. The parameters used in these calculations are adopted from Chan et al. [28] for the SOFC-O^{2-} and from Iwahara [13] and Salar et al. [16] for the SOFC-H^+ and are shown in Table 2.

As the SOFC-H^+ is not as developed as the SOFC-O^{2-}, the resistances of the components in the cell are not available in the open literature. Consequently, the other resistance is derived from the deviation of the total resistance and the electrolyte resistance. The values of the total resistance are obtained from the literature [13]. It should be noted that the SOFC-O^{2-} model was verified by comparing the calculated maximum power density and its corresponding current density with the results from Hernandez-Pacheco et al. [29]. Small deviations between those results were observed, i.e., the maximum power density from the calculation at the current density of 0.75 A cm^{-2} is 0.33 W cm^{-2} compared to 0.30 W cm^{-2} as reported in the literature [29].

2.2. SOFC electrical efficiency

When current is drawn from the SOFC, the power density, P, in W cm^{-2}, produced can be calculated by:

$$P = iV \tag{19}$$

The electrical efficiency is defined as the ratio of electrical work produced by SOFC to the chemical energy contained in the fuel fed to the SOFC system as shown in the following equation:

$$\eta = \frac{IV}{n_{\mathrm{EtOH}}(\mathrm{LHV}_{\mathrm{EtOH}})} \tag{20}$$

where I is the total current (A) determined by numerical integration of the local current density along the cell length, $\mathrm{LHV}_{\mathrm{EtOH}}$ the lower heating value of ethanol at the standard condition (1235 kJ/mol) and n_{EtOH} is the molar flow rate of ethanol fed to the system.

3. Results and discussion

Fig. 1 shows the main characteristics of SOFC performances at different fuel utilizations for both SOFC-O^{2-} and SOFC-H^+.

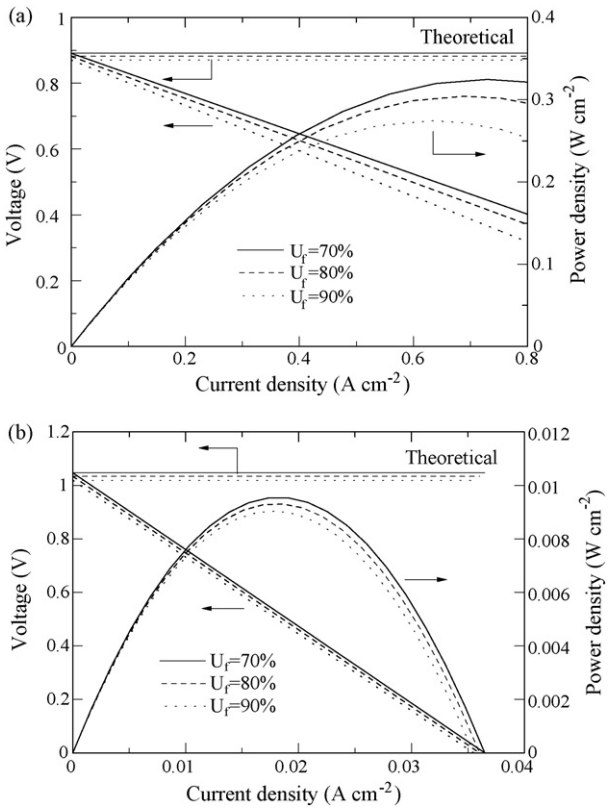

Fig. 1. Performance of SOFCs for various fuel utilizations: (a) SOFC-O^{2-} and (b) SOFC-H^+ (inlet H_2O:EtOH ratio = 3, T = 1200 K, P = 101.3 kPa, 400% excess air).

The calculations were based on a feed with an H_2O:EtOH ratio of 3 and temperature of 1200 K. The cell voltage decreases as the current density increases due to increasing losses. The power density initially increases with increasing the current density and drops at the higher values. For each value of fuel utilization, there is an optimum current density that maximizes the power density. The maximum power density decreases with increasing fuel utilization due to the effect of fuel depletion downstream. The observed values of the maximum power density of the SOFC-O^{2-} are within the range of the best value of 0.4 W cm^{-2} reported in the literature with an ethanol-fed system [30]. Fig. 1 also shows that the value of the current density for which the power density is maximum is essentially insensitive to the fuel utilization factor (at least in the range 70–90%) in the case of SOFC-H^+. The insensitivity of power density to fuel utilization in the case of SOFC-H^+ is due to the very large ohmic resis-

tance. The ohmic loss in the SOFC-H^+ electrolyte overshadows all other losses and since it is independent of the fuel utilization there is almost no difference in cell voltage for the different fuel utilizations, as seen in Fig. 1(a). As a consequence, the obtained maximum power density is insensitive to fuel utilization. For the SOFC-O^{2-}, the current density for which the power density is maximum decreases as the fuel utilization factor increases.

Performance comparisons between the two ethanol-fed SOFCs show that the SOFC-H^+ results in an EMF of around 1.01 V whereas it is approximately 0.89 V for the SOFC-O^{2-}. It is clear that the performance of SOFC-H^+ is theoretically superior to that of SOFC-O^{2-}, which is in good agreement with previous reports on SOFCs fed with H_2 and CH_4 [17,18] and ethanol [22]. The difference in the EMF between the SOFCs with different types of electrolytes is mainly due to the location of the steam generated by the electrochemical reaction, whether it is at the anode side for the SOFC-O^{2-} or at the cathode side for the SOFC-H^+. However, for an actual operation, losses strongly affect the performances of the SOFCs. It is clearly seen from Fig. 1 that the SOFC-H^+ does not perform as well as the SOFC-O^{2-}. The voltage in the SOFC-H^+ decreases significantly faster than that of the SOFC-O^{2-} as the current density increases, and the resulting maximum power density for the SOFC-H^+ is approximately 34 times lower than that of the SOFC-O^{2-}.

Another important indicator representing SOFC performance is the electrical efficiency defined in Eq. (20). The values of the electrical efficiencies at various current densities and fuel utilizations are illustrated in Fig. 2. When operating at a constant fuel utilization, the efficiency decreases with the increasing current density. The SOFC-H^+ can be operated over a much smaller range of current density than the SOFC-O^{2-} due to its higher losses. The maximum or theoretical efficiency is obtained when the current density approaches zero. At this condition, the SOFC-H^+ yields a higher efficiency than the SOFC-O^{2-} although it is not a practical operating condition as the power density is very low and, therefore, a large cell area would be required. When the fuel utilization increases, the efficiency increases although the opposite trend may be observed at high current densities, which yield low efficiency. It should be noted that the selection of suitable operating fuel utilization and current density is important as they influence the electrical efficiency and the power density, which are among the key parameters to evaluate SOFC performance.

The feed composition is another important parameter to be considered. From our previous work [22], it was reported that the SOFCs with different electrolytes required different inlet H_2O:fuel ratios to obtain their maximum EMFs. The effect of inlet H_2O:EtOH ratio on the voltage and power density is shown in Figs. 3 and 4, respectively. In the calculations, the fuel utilization was kept at 80% which is a typical operating condition used in the literature [27,29]. The inlet H_2O:EtOH ratio starts from its boundary of carbon formation which can be determined by following the procedure illustrated in our previous work [19–21]. It was found that the SOFC-O^{2-} yields the maximum voltage and power density at the boundary of carbon formation whereas those of the SOFC-H^+ are found at a ratio beyond the boundary of carbon formation. In order to compare the performance of

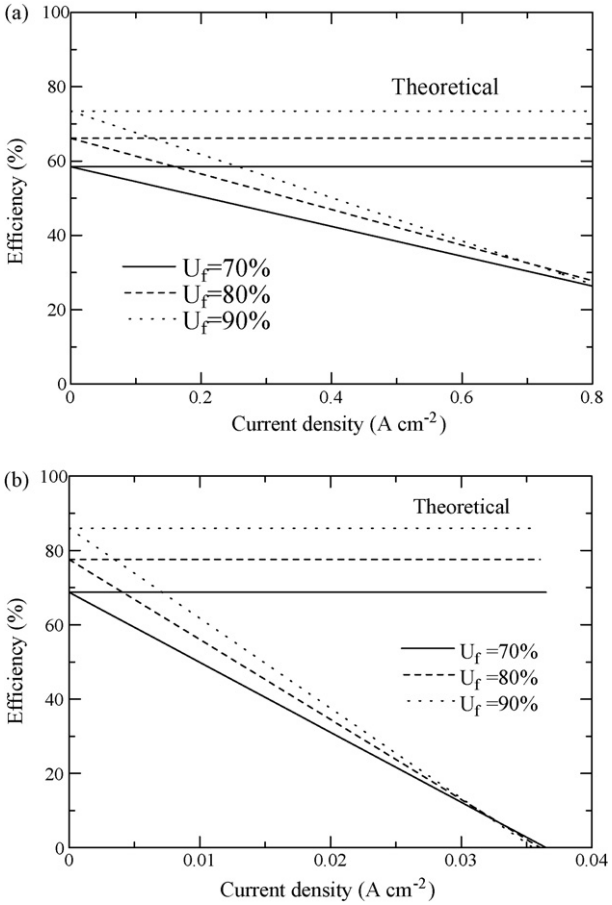

Fig. 2. Efficiency of SOFCs for various fuel utilizations: (a) SOFC-O^{2-} and (b) SOFC-H^+ (inlet H_2O:EtOH ratio = 3, T = 1200 K, P = 101.3 kPa, 400% excess air).

the SOFCs with different types of electrolytes, the best performance of each SOFC should be considered. The current density, H_2O:EtOH ratio and fuel utilization were varied to determine values which yield the highest power density for each type of SOFC.

Fig. 5 shows the maximum power density and the corresponding current density and inlet H_2O:EtOH ratio at different fuel utilizations. As expected, the maximum power density and the

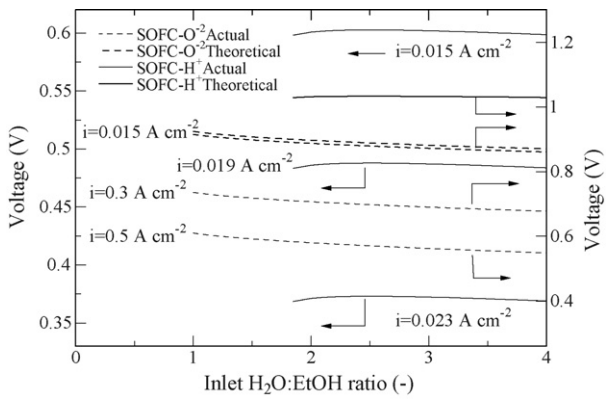

Fig. 3. Influence of inlet H_2O:EtOH ratio on voltage at various current densities (T = 1200 K, P = 101.3 kPa, U_f = 80%, 400% excess air).

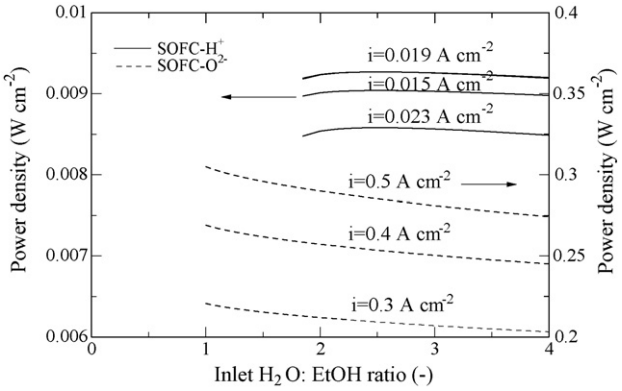

Fig. 4. Influence of inlet H_2O:EtOH ratio on power density at various current densities (T = 1200 K, P = 101.3 kPa, U_f = 80%, 400% excess air).

corresponding current density decrease with an increase in fuel utilization due to the effect of fuel depletion. Considering the corresponding values of the inlet H_2O:EtOH ratio, it can be noticed that for the SOFC-O^{2-} the values are independent of fuel utilization whereas it increases with increasing fuel utilization for the SOFC-H^+. The results can be explained by considering the influence of fuel utilization on the boundary of carbon formation. For the SOFC-O^{2-} case, the optimum H_2O:EtOH ratio is at the boundary of carbon formation. The fuel utilization does not affect the boundary of carbon formation because the critical condition for carbon formation occurs at the feed inlet in which the value of fuel utilization is zero. The possibility

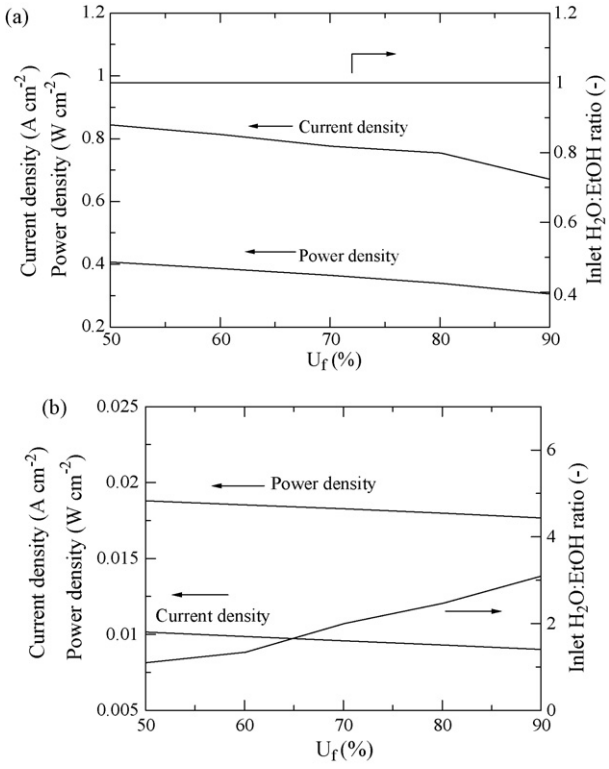

Fig. 5. Maximum power density of SOFC and their corresponding conditions (inlet H_2O:EtOH ratio and current density) at various fuel utilizations: (a) SOFC-O^{2-} and (b) SOFC-H^+ (T = 1200 K, P = 101.3 kPa, 400% excess air).

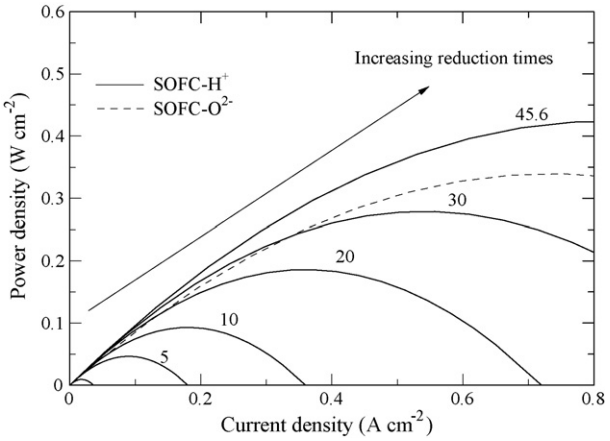

Fig. 6. Influences of total resistance on the performance of SOFC-H^+ compared with that of SOFC-O^{2-} (T = 1200 K, P = 101.3 kPa, 400% excess air).

for carbon formation becomes less severe when more hydrogen is consumed, i.e., higher fuel utilization, yielding water which helps suppress carbon formation. However, for the SOFC-H^+ case, at high fuel utilization, more hydrogen disappears without benefiting from the steam generated from the electrochemical reaction in the anode gas mixture, leading to higher possibility for carbon formation. Therefore, higher inlet H_2O:EtOH ratios are required to thermodynamically suppress carbon formation. From the results shown in Fig. 5, it is clear that the best performance of SOFC-H^+ is still lower than that of SOFC-O^{2-} for the entire range of fuel utilization, which confirms that the SOFC-H^+ does not show great promise, at least with the current extremely high resistance in SOFC-H^+.

To enhance the performance of SOFC-H^+, it is obvious that the resistance of the cell must be reduced due to the sudden drop in voltage. Fig. 6 depicts the influence of the total resistance of the SOFC-H^+ cell on the cell performances at 1200 K. It should be noted that the total resistance is termed as the summation of electrolyte resistance and the other resistances. In this section, the reduction time is defined as the ratio by which the total resistance is reduced compared to the current value. The dashed line represents the values of the SOFC-O^{2-}. Obviously, the total resistance is an important factor for improving the performance of SOFC-H^+. Higher power density can be obtained when decreasing the total resistance. It was found that when the total resistance of the SOFC-H^+ is reduced to 1/45.6 of the present value (28.7 $\Omega\,cm^2$), which would be equal to the total resistance of the current SOFC-O^{2-} (0.628 $\Omega\,cm^2$), the performance of the SOFC-H^+ is better than that of the SOFC-O^{2-}. It is clear that due to the superior theoretical performance of the SOFC-H^+, it is unnecessary to reduce the total resistance of the SOFC-H^+ to the level of that of the SOFC-O^{2-}. The total resistance in the SOFC-H^+, which yields an equivalent power density as the SOFC-O^{2-} is presented in Fig. 7 as function of temperature. It can be seen that a reduction by 1/30.7 (0.935 $\Omega\,cm^2$) is sufficient to offer the same power density as the SOFC-O^{2-} at 0.7 V and 1200 K. When increasing the operating temperature, the required resistance of SOFC-H^+ has to be further decreased due to a rapid decrease in the total resistance of SOFC-O^{2-}.

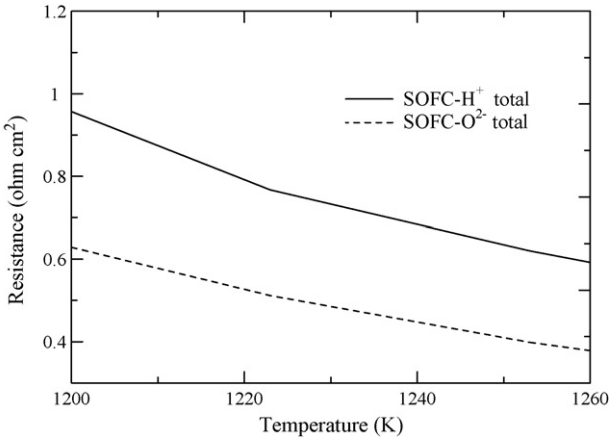

Fig. 7. Required total resistance of SOFC-H^+ with comparable SOFC-O^{2-} performance at various temperatures.

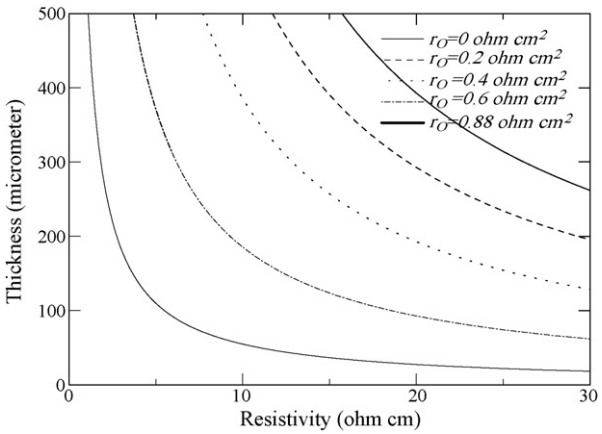

Fig. 8. Resistivity and thickness of proton-conducting electrolyte at various values of the other resistances, r_o (T = 1200 K, P = 101.3 kPa, 400% excess air).

Considering the Pt|SCY|Pt SOFC-H^+ cell in this study, the electrolyte, other and total resistances at 1200 K are 8.5, 20.2 and 28.7 $\Omega\,cm^2$, respectively. It is seen that the expected value of 0.935 $\Omega\,cm^2$ cannot be achieved by only reducing the electrolyte resistance. Both the electrolyte and the other resistances need to be improved simultaneously. At T = 1200 K, the electrolyte and the other resistances of the SOFC-H^+ are about 130 and 35 times, respectively, higher than those of the SOFC-O^{2-}. The high value of the other resistances of the SOFC-H^+ is possibly because platinum is not a good ionic conductor although it has high catalytic activity and high electronic conductivity [31]. In addition, since the cermet structure is not applied for the anode, the platinum is more likely to sinter rather than compacted to the electrolyte at high temperature [32]. These lead to low interfacial conductivity between the platinum electrodes and the electrolyte. From these comparisons, significant efforts are required to reduce both the electrolyte and the other resistances of the SOFC-H^+ cell.

Because the electrolyte resistance depends on its thickness and physical properties of material, it is possible to reduce the resistance by reducing the electrolyte thickness and/or using new materials with lower resistivity. Some materials with high proton conductivity have been reported, for example, $BaCe_{0.8}Y_{0.2}O_{3-\alpha}$ (BCY) and $BaCe_{0.9}Nd_{0.1}O_{3-\alpha}$ in which the resistivities at T = 1200 K are 12.5 and 28.6 Ω cm, respectively, compared to 85.0 Ω cm for the SCY used in this study [13]. Fig. 8 shows the required electrolyte thickness for different values of material resistivity of the electrolyte and the other resistance. It is clear that for a given value of the other resistance, the higher the material resistivity, the thinner the electrolyte is required. For the currently available high proton conducting material of SCY, when the electrolyte is reduced to a thickness as small as 150 μm which is in the range of an electrode-supported cell for 8YSZ [31], the other resistance should be reduced to 0.6 $\Omega\,cm^2$ which is approximately 1/33.7 that of the present value. To achieve the expected value of the other resistance, the electrical conductivities and activity of the cathode and anode must be significantly improved to replace the use of Pt. In addition, the interfacial resistivity between electrolyte/anode and electrolyte/cathode must be suppressed by a careful selection of material and suitable microstructure to enhance the triple-phase boundary. In addition, some other considerations such as mechanical strength, chemical compatibilities and thermal expansion compatibilities among the cell components need to be taken into account in the cell development. However, it is unfortunate that most of these data are currently not available. Therefore, considerable effort in the development of an SOFC-H^+ cell is necessary to eventually commercialize this type of fuel cell.

4. Conclusions

Although the theoretical EMF and electrical efficiency of the SOFC-H^+ are superior to those of the SOFC-O^{2-}, its actual voltage and power density are much lower than those of the SOFC-O^{2-} due to large resistance of the cell. It was calculated that in order to achieve an equivalent power density to the SOFC-O^{2-}, the total resistance of the SOFC-H^+ should be reduced to 0.935 $\Omega\,cm^2$, which is equal to 1/30.7 of the present value (28.7 $\Omega\,cm^2$), compared to the value of 0.628 $\Omega\,cm^2$ of the SOFC-O^{2-} at 1200 K. Due to the superior theoretical performance of the SOFC-H^+, it is unnecessary to reduce the total resistance of the SOFC-H^+ to the same value of the SOFC-O^{2-}. It was found that the reduction of the electrolyte resistance alone is not sufficient to reach the expected value of the total resistance. Both the electrolyte and the other resistances need to be improved simultaneously. The electrolyte resistance could be improved by reducing the electrolyte thickness and/or finding new materials with lower resistivity. When the electrolyte thickness of SCY, the currently available high proton conducting material, is reduced to 150 μm, in the range of an electrode supported cell for 8YSZ, the other resistance should be reduced to 0.6 $\Omega\,cm^2$ (1/33.7 of the present value). It is clear that the success of the SOFC-H^+ technology depends on the development of improved cell components.

Acknowledgements

The support from the Thailand Research Fund, Commission on High Education and National Metal and Materials Technology Center (MTEC) are gratefully acknowledged.

References

[1] S. Cavallaro, S. Freni, Ethanol steam reforming in a molten carbonate fuel cell. A preliminary kinetic investigation, Int. J. Hydrogen Energy 21 (1996) 465–469.

[2] G. Maggio, S. Freni, S. Cavallaro, Light alcohols/methane fuelled molten carbonate fuel cells: a comparative study, J. Power Sources 74 (1998) 17–23.

[3] T. Ioannides, S. Neophytides, Efficiency of a solid polymer fuel cell operating on ethanol, J. Power Sources 91 (2000) 150–156.

[4] T. Ioannides, Thermodynamic analysis of ethanol processors for fuel cell applications, J. Power Sources 92 (2001) 17–25.

[5] S. Cavallaro, N. Mondello, S. Freni, Hydrogen produced from ethanol for internal reforming molten carbonate fuel cell, J. Power Sources 102 (2001) 198–204.

[6] V. Klouz, V. Fierro, P. Denton, H. Katz, J.P. Lisse, S. Bouvot-Mauduit, C. Mirodatos, Ethanol reforming for hydrogen production in a hybrid electric vehicle: process optimisation, J. Power Sources 105 (2002) 26–34.

[7] N.A. Fatsikostas, D.I. Kondarides, X.E. Verykios, Production of hydrogen for fuel cells by reformation of biomass-derived ethanol, Catal. Today 75 (2002) 145–155.

[8] T. Tsiakaras, A. Demin, Thermodynamic analysis of a solid oxide fuel cell system fuelled by ethanol, J. Power Sources 102 (2001) 210–217.

[9] S.L. Douvartzides, F.A. Coutelieris, A.K. Demin, P.E. Tsiakaras, Fuel options for solid oxide fuel cell: a thermodynamic analysis, AIChE J. 49 (2003) 248–257.

[10] S. Douvartzides, F.A. Coutelieris, P.E. Tsiakaras, Exergy analysis of solid oxide fuel cell power plant fed by either ethanol or methane, J. Power Sources 131 (2004) 224–230.

[11] T. Shimada, C. Wen, N. Taniguchi, J. Otomo, H. Takahashi, The high temperature proton conductor $BaZr_{0.4}Ce_{0.4}In_{0.2}O_{3-\alpha}$, J. Power Sources 131 (2004) 289–292.

[12] T. Schober, F. Krug, W. Schilling, Criteria for the application of high temperature proton conductor in SOFCs, Solid State Ionics 97 (1997) 369–373.

[13] H. Iwahara, Proton conducting ceramics and their application, Solid State Ionics 86–88 (1996) 9–15.

[14] T. Schneller, T. Schober, Chemical solution deposition prepared dense proton conducting Y-doped $BaZrO_3$ thin films for SOFC and sensor devices, Solid State Ionics 164 (2003) 131–136.

[15] D. Browning, M. Weston, J.B. Lakeman, P. Jones, M. Cherry, J.T.S. Irvine, D.J.D. Corcoran, Proton conducting ceramics for use in intermediate temperature proton conducting fuel cells, J. New Mater. Electrochem. Syst. 5 (2002) 25–30.

[16] R. Salar, H. Taherparvar, I.S. Metcalfe, M. Sahibzada, Proceedings of the 2001 Joint International Meeting—The 200th Meeting of The Electrochemical Society Inc. and the 52nd Annual Meeting of the International Society of Electrochemistry, San Francisco, California, 2001.

[17] A. Demin, P. Tsiakaras, Thermodynamic analysis of a hydrogen fed solid oxide fuel cell based on a proton conductor, Int. J. Hydrogen Energy 26 (2001) 1103–1108.

[18] A.K. Demin, P.E. Tsiakaras, V.A. Sobyanin, S.Yu. Hramova, Thermodynamic analysis of a methane fed SOFC system based on a protonic conductor, Solid State Ionics 152–153 (2002) 555–560.

[19] S. Assabumrungrat, V. Pavarajarn, S. Charojrochkul, N. Laosiripojana, Thermodynamic analysis for solid oxide fuel cell with direct internal reforming fueled by ethanol, Chem. Eng. Sci. 59 (2004) 6015–6020.

[20] S. Assabumrungrat, N. Laosiripojana, V. Pavarajarn, W. Sangtongkitcharoen, A. Tangjitmatee, P. Praserthdam, Thermodynamic analysis of carbon formation in a solid oxide fuel cell with direct internal reformer fuelled by methanol, J. Power Sources 139 (2005) 55–60.

[21] W. Sangtongkitcharoen, S. Assabumrungrat, V. Pavarajarn, N. Laosiripojana, P. Praserthdam, Comparison of carbon formation boundary in different modes of solid oxide fuel cells fueled by methane, J. Power Sources 142 (2005) 75–80.

[22] W. Jamsak, S. Assabumrungrat, P.L. Douglas, N. Laosiripojana, S. Charojrochkul, Theoretical performance analysis of ethanol-fuelled solid oxide fuel cells with different electrolytes, Chem. Eng. J. 119 (2006) 11–18.

[23] S. Freni, G. Maggio, S. Cavallaro, Ethanol steam reforming in a molten carbonate fuel cell: a thermodynamic approach, J. Power Sources 62 (1996) 67–73.

[24] E.Y. Garcia, M.A. Laborde, Hydrogen production by the steam reforming of ethanol: thermodynamic analysis, Int. J. Hydrogen Energy 16 (1991) 307–312.

[25] K. Vasudeva, N. Mitra, P. Umasankar, S.C. Dhinggra, Steam reforming of ethanol for hydrogen production: thermodynamic analysis, Int. J. Hydrogen Energy 21 (1996) 13–18.

[26] E. Achenbach, Three-dimensional and time-dependent simulation of a planar solid oxide fuel cell stack, J. Power Sources 49 (1994) 333–348.

[27] E. Hernandez-Pacheco, D. Singh, P.N. Hutton, N. Patel, M.D. Mann, A macro-level model for determining the performance characteristics of solid oxide fuel cells, J. Power Sources 138 (2004) 174–186.

[28] S.H. Chan, C.F. Low, O.L. Ding, Energy and exergy analysis of simple solid-oxide fuel-cell power systems, J. Power Sources 103 (2002) 188–200.

[29] E. Hernandez-Pacheco, M.D. Mann, P.N. Hutton, D. Singh, K.E. Martin, A cell-level model for a solid oxide fuel cell operated with syngas from a gasification process, Int. J. Hydrogen Energy 30 (2005) 1221–1233.

[30] Fuel Cells Bulletin 8 (2005) 8.

[31] Handbook of Fuel Cells—Fundamentals, Technology and Applications, vols. 1–2, John Wiley & Sons Ltd., 2003.

[32] F.H. Garzon, R. Mukundan, R. Lujan, E.L. Brosha, Solid state ionic devices for combustion gas sensing, Solid State Ionics 175 (2004) 487–490.

Appendix 4

Available online at www.sciencedirect.com
ScienceDirect
Journal of Power Sources 174 (2007) 191–198
JOURNAL OF POWER SOURCES
www.elsevier.com/locate/jpowsour

Thermodynamic assessment of solid oxide fuel cell system integrated with bioethanol purification unit

W. Jamsak [a], S. Assabumrungrat [a,*], P.L. Douglas [b,**], E. Croiset [b], N. Laosiripojana [c], R. Suwanwarangkul [d], S. Charojrochkul [e]

[a] *Center of Excellence in Catalysis and Catalytic Reaction Engineering, Department of Chemical Engineering, Faculty of Engineering, Chulalongkorn University, Thailand*
[b] *Department of Chemical Engineering, University of Waterloo, Canada*
[c] *The Joint Graduate School of Energy and Environment, King Mongkut's University of Technology, Thonburi, Thailand*
[d] *School of Bio-Chemical Engineering and Technology, Sirindhorn International Institute of Technology, Thammasart University, Rangsit Campus, Patum Thani 12121, Thailand*
[e] *National Metal and Materials Technology Center (MTEC), Thailand*

Received 8 May 2007; received in revised form 27 August 2007; accepted 28 August 2007
Available online 7 September 2007

Abstract

A solid oxide fuel cell system integrated with a distillation column (SOFC–DIS) has been proposed in this article. The integrated SOFC system consists of a distillation column, an EtOH/H_2O heater, an air heater, an anode preheater, a reformer, an SOFC stack and an afterburner. Bioethanol with 5 mol% ethanol was purified in a distillation column to obtain a desired concentration necessary for SOFC operation. The SOFC stack was operated under isothermal conditions. The heat generated from the stack and the afterburner was supplied to the reformer and three heaters. The net remaining heat from the SOFC system ($Q_{SOFC,Net}$) was then provided to the reboiler of the distillation column. The effects of fuel utilization and operating voltage on the net energy (Q_{Net}), which equals $Q_{SOFC,Net}$ minus the distillation energy (Q_D), were examined. It was found that the system could become more energy sufficient when operating at lower fuel utilization or lower voltage but at the expense of less electricity produced. Moreover, it was found that there were some operating conditions, which yielded Q_{Net} of zero. At this point, the integrated system provides the maximum electrical power without requiring an additional heat source. The effects of ethanol concentration and ethanol recovery on the electrical performance at zero Q_{Net} for different fuel utilizations were investigated. With the appropriate operating conditions (e.g. $C_{EtOH} = 41\%$, $U_f = 80\%$ and EtOH recovery = 80%), the overall electrical efficiency and power density are 33.3% (LHV) and 0.32 W cm^{-2}, respectively.

Keywords: Solid oxide fuel cell; Combined process; Bioethanol; Distillation unit

1. Introduction

A solid oxide fuel cell is an attractive power generation system as it offers a wide range of applications, low emissions, fuel flexibility and high system efficiency. Generally, the major components of an SOFC system are preheaters, a fuel processor, a fuel cell stack and an afterburner. It is known that useful heat is always available when operating the SOFC because of the presence of irreversibility and unreacted fuel [1]. To enhance the system efficiency, an SOFC is usually integrated with other energy devices for further utilization of excess heat to generate extra electrical power and/or hot water/steam. Nowadays, the two most promising systems are SOFC–Gas Turbine system (SOFC–GT) [2–4] and SOFC–Combined Heat and Power system (SOFC–CHP) [5–8].

For the SOFC–GT system, Palsson et al. [2] investigated a 500 kW methane-fuelled SOFC–GT system. The system consisted of preheaters, a pre-reformer, an SOFC stack, a combustor, an air compressor, a booster and an expander. Part of the anode effluent was recycled in order to supply heat and steam to the external reformer. The rest of the anode effluent was combined with the cathode effluent and burnt in the combustor. The out-

* Corresponding author. Tel.: +662 218 6868; fax: +662 218 6877.
** Corresponding author.
E-mail addresses: Suttichai.A@chula.ac.th (S. Assabumrungrat), pdouglas@cape.uwaterloo.ca (P.L. Douglas).

0378-7753/$ – see front matter © 2007 Elsevier B.V. All rights reserved.
doi:10.1016/j.jpowsour.2007.08.105

Nomenclature

C_{EtoH}	ethanol concentration (% mol)
E	electromotive force of a cell (V)
E_a	activation energy (J mol^{-1})
F	Faraday constant (C mol^{-1})
i	current density (A cm^{-2})
I	current (A)
LHV_{EtOH}	lower heating value of ethanol (J mol^{-1})
n_{EtOH}	total ethanol flow rate fed to the distillation column (mol s^{-1})
p_i	partial pressure of component i (kPa)
P	pressure (kPa)
P_{den}	power density (A cm^{-2})
Q_1	the energy required for Preheater 1 (kW)
Q_2	the energy required for Preheater 2 (kW)
Q_3	the energy required for Preheater 3 (kW)
Q_4	the energy required for a reformer (kW)
Q_5	the exothermic heat released from an SOFC stack (kW)
Q_6	the energy involved the combustion of exhausted gases and cooled to the exit temperature (kW)
Q_{Con}	condenser duty (kW)
Q_D	reboiler duty (kW)
Q_{Net}	net useful heat (kW)
$Q_{SOFC,Net}$	net exothermic from SOFC (kW)
r	area specific resistance (Ω cm^2)
r_{act}	activation polarization area specific resistance (Ω cm^2)
r_{ohm}	ohmic polarization area specific resistance (Ω cm^2)
$r_{H_2,cons}$	rate of hydrogen consumed by the electrochemical reaction (mol s^{-1})
R	gas constant (J mol^{-1} K^{-1})
T_{SOFC}	SOFC temperature (K)
T_{RF}	reforming temperature (K)
U_f	fuel utilization (%)
V	operating voltage (V)
W_e	electrical power (kW)

Greek letters

$\eta_{elec,ov}$	overall electrical efficiency (%)
ρ	resistivity (Ω cm)

Subscripts

a	anode
c	cathode

let stream from the combustor was then delivered to the gas turbine for generating additional electrical power whereas the exhaust gas from the gas turbine was used for preheating the feeds. The influences of operating parameters such as pressure, air flow rate, fuel flow rate and air inlet temperature on the system performance were analyzed. Fredriksson Möller et al. [3] studied a methane-fuelled SOFC–GT system integrated with a CO_2 capture plant. The desulfurizer unit was also implemented in the SOFC system. The CO_2 capture plant consisted of a condenser, an absorber and a regenerator. Two SOFC stacks were employed in this study. The reformed gas was split between the two stacks and fed to the anode sides in parallel. The obtained electrical efficiency of the SOFC–GT system integrated with the CO_2 capture plant reached above 60%. Inui et al. [4] investigated SOFC–GTs with CO_2 recovery systems. Two new CO_2 recovery systems were proposed as a bottoming cycle, i.e. (1) CO_2 recycle system and (2) water vapor injection system. The results showed that the former system achieved an overall efficiency of 70.88% (LHV) while the latter system yielded 72.13%.

For the SOFC–CHP system, Chan et al. [5] studied a methane-fuelled SOFC system and compared its efficiency with that of a hydrogen-fuelled system. The system consisted of a vaporizer, preheaters, a pre-reformer, an SOFC stack and an afterburner. The unreacted fuel was burnt in the afterburner and the heat from the afterburner was supplied to the reformer, vaporizer, steam boiler and preheaters. Some heat from the SOFC stack was used for the steam boiler. The results indicated that the efficiency of the methane-fuelled system was higher than that of the hydrogen-fuelled system. Fontell et al. [6] examined a methane-fuelled SOFC combined with a desulfurizer unit, a power conversion unit and system controllers. The system configuration was different from Chan's work [5] as the anode effluent was re-circulated for preheating the reformed gas before being split into two streams: one was mixed with the desulfurized stream and the other was fed to the combustor. The results revealed that the system efficiency achieved was around 85%. Zhang et al. [7] also examined an SOFC fuelled with methane. The equipment setting was almost similar to that in Fontell's work [6]; however, no desulfurizer, power conversion and controllers were included. In addition, the anode effluent was also split into two streams: one for combustion and the other for anode re-circulation. No anode effluent was used for preheating the anode inlet. An electrical efficiency of 52% was obtained for the desired power of 120 kW. Omosun et al. [8] studied an SOFC fuelled by product gas from gasified biomass. The system consisted of a gasifier, separation units (i.e. cyclone and filter), a fuel cell stack and a combustor. The study focused on a performance comparison between cold and hot processes. The major differences between those processes were the gasification and clean-up processes. The hot process used a fluidized bed gasifier and a ceramic filter whereas the cold process used a fixed-bed gasifier and a wet precipitator. For a heat recovery, both anode and cathode effluents were re-circulated and mixed with the incoming streams. The results showed that the hot process yielded higher electrical and system efficiencies than the cold process. However, the cost of the hot process was higher than that of the cold process.

Among the many possible fuels for SOFC, ethanol is an attractive green fuel as it can be derived from renewable resources and it is safe and easy for storage and handling [9]. The group of Tsiakaras has been particularly active in investigating the ethanol-fuelled SOFCs [10–12]. They compared the theoretical SOFC performances for different ethanol reforming reactions (steam reforming, CO_2 reforming and par-

tial oxidation) [10]. It was reported that the products from steam reforming yielded the highest maximum efficiency when $T < 950$ and >1100 K whereas those from the CO_2 reforming was more preferable at the intermediate temperatures. For the partial oxidation, its efficiency was 20% less than the other cases. An energy–exergy analysis was also employed to examine the system comprising an external steam reformer, an SOFC stack, an afterburner, two preheaters, a water vaporizer and a mixer [11,12]. No anode and cathode recycles were considered. The heat from the combustor was provided to the preheaters, the vaporizer and the reformer. An optimization of the combustor was performed by matching appropriate reforming temperature and fuel utilization. Moreover, the minimization of SOFC loss was examined by searching for suitable reforming and air preheating temperatures. It should be noted from all studies related to SOFCs fuelled by ethanol that pure ethanol was usually mixed with water in order to obtain a desired ethanol concentration before being fed into the reformer. From an energy point of view, this might not be an efficient strategy as unnecessary energy is consumed to purify bioethanol to a needless high concentration ethanol, which is subsequently mixed with water and fed to the reformer.

In this work, it was proposed to integrate the SOFC with an ethanol purification unit. The ethanol was purified to a desired concentration using a distillation column whose required energy can be directly supplied from the excessive heat from the SOFC system. It was expected that by carefully selecting suitable operating conditions, the integrated system could be operated without any requirement of additional energy sources apart from the bioethanol feed. The influences of operating parameters including ethanol concentration, ethanol recovery, fuel utilization and voltage on electrical performance and net energy of the integrated system (Q_{Net}) were investigated.

2. SOFC system modelling

Fig. 1 shows the proposed SOFC system integrated with a distillation column (SOFC–DIS). The SOFC system consisted of three heat exchangers (for preheating feeds), a reformer and an afterburner. The distillation column was integrated with the SOFC system to purify bioethanol to desired levels of ethanol concentration and recovery. Generally, the ethanol concentration from a fermentation process is in the range of 1–7 mol% [13–16]. In this work, the value of 5 mol% was selected as a representative of bioethanol. Aspen Plus™ and the Radfrac rigorous

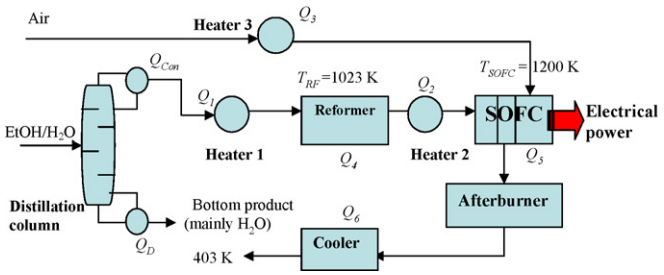

Fig. 1. Schematic diagram of SOFC system integrated with a distillation column (SOFC–DIS).

equilibrium stage distillation module were used for simulating the distillation column. A total condenser and a kettle boiler were employed. The bioethanol feed was introduced to the stage above the reboiler. The minimum reboiler heat duty, which could be obtained by adjusting the number of stages and reflux ratio, was used in the present study of the SOFC–DIS system.

The distillate leaving the distillation column was heated up to the reforming temperature (T_{RF}) by Heater 1 (here $T_{RF} = 1023$ K), and fed to the external reformer, which was assumed to operate isothermally. It should be noted that considering such high reforming temperature, negligible extent of ethanol was present in the reformed gas. The reformed gas was then heated up to the SOFC temperature (T_{SOFC}) by Heater 2 and introduced to the anode chamber of the SOFC stack. The SOFC stack was also assumed to operate isothermally ($T_{SOFC} = 1200$ K). Excess air (380%) preheated by Heater 3 was fed to the cathode chamber. The equations describing the electrochemical model are as follows:

$$V = E - i(r_{ohm} + r_{act}) \tag{1}$$

$$E = \frac{RT}{4F} \ln \frac{p_{O_2,c}}{p_{O_2,a}} \tag{2}$$

$$r_{act,c} = \left[\frac{4F}{RT} k (p_{O_2,c})^m \exp\left(-\frac{E_{a,c}}{RT}\right)\right]^{-1} \tag{3}$$

$$r_{act,a} = \left[\frac{2F}{RT} k (p_{H_2,a})^m \exp\left(-\frac{E_{a,a}}{RT}\right)\right]^{-1} \tag{4}$$

$$r_{ohm,j} = \rho_j \delta_j \tag{5}$$

$$\rho_j = \alpha_j exp\left(\frac{\beta_j}{T}\right) \tag{6}$$

$$P_{den} = iV \tag{7}$$

$$I = r_{H_2,cons} \times 2F \tag{8}$$

$$r_{H_2,cons} = r_{H_2 in,equiv.} \times U_f \tag{9}$$

$$r_{H_2 in,equivalent} = 6 \times r_{EtOH,d} \tag{10}$$

$$A = \frac{I}{i} \tag{11}$$

$$W_e = IV \tag{12}$$

where E is the electromotive force (EMF), V the operating voltage, i the current density, I the overall current, R the gas constant, T the SOFC temperature, F the Faraday's constant, r_{act} the activation resistance, $E_{a,a}$ and $E_{a,c}$ the activation energies at anode and cathode, respectively, $p_{O_2,c}$ and $p_{H_2,a}$ the mole fractions of oxygen in the cathode chamber and hydrogen in the anode chamber, respectively, r_{ohm} the ohmic resistance, ρ_j the resistivity of material j, α_j and β_j the constants specific to material j, $r_{H_2,cons}$ the molar flow rate of hydrogen consumed in the electrochemical reaction, $r_{H_2 in,equiv.}$ the maximum hydrogen molar flow rate coming into the anode chamber (6× that of ethanol flow rate), $r_{EtOH,d}$ the ethanol flow rate in the distillate fed into the SOFC system, A the total active area of SOFC stack, W_e the electrical power, P_{den} the power density, LHV_{EtOH} the low heating value

Table 1
Parameters for activation loss [17]

r_{act} (Ω cm^2)	k ($\times 10^{-13}$ A cm^2)	E_a (kJ mol^{-1} K^{-1})	m (−)
$r_{act,c}$	14.9	160	0.25
$r_{act,a}$	0.213	110	0.25

of ethanol. The parameters used for calculating the ohmic and activation overpotentials are listed in Tables 1 and 2.

It should be noted that the SOFC cell was based on the tubular configuration [5]. Concerning the activation losses, the Achenbach's semi-empirical correlation [17] was used to predict the activation overpotentials for the anode and cathode. Hernandez-Pacheco et al. [18] compared the values from the Achenbach's correlation and the Butler–Volmer equation and found that the Achenbach's correlation gave reliable results for temperatures between 1173 and 1273 K. The operating temperature of 1200 K in this study was within the reliable range of the Achenbach's correlations. For calculating SOFC performance, a concentration polarization loss could be omitted when an SOFC does not operate at high current density. The concentration losses can be estimated by using an equation given in Ref. [19]. A concentration loss of 0.03 V was thus estimated at the current densities around 0.6 A cm^{-2}. This is why the concentration polarization was neglected. Details on the calculations of composition and EMF distributions within the SOFC stack were given in our previous works [20,21]. Note that the flow rate of ethanol is kept constant for all conditions; therefore, the active area of the SOFC stack were changed when the voltage and fuel utilization changed. The appropriate size of SOFC stack was not investigated in this work.

The effluent from the anode and the cathode was burnt in the afterburner. Assuming that the combusted gas was discharged to the environment at 403 K, the useful heat remaining in the exhaust stream could be calculated. The useful heat is used to supply the energy to the energy-demanding units in the system (such as reboiler, heaters and reformer). It should be noted that the temperature of the exhaust gas to the environment should be higher than the dew point of water to avoid water condensation, which may cause corrosion due to acidic condensate in pipelines. For efficient heat utilization in the system, the exothermic heat from the SOFC stack (Q_5) and the afterburner (Q_6) were supplied to the energy-consuming units of the SOFC system (the heaters (Q_1, Q_2 and Q_3) and the reformer (Q_4)). The net useful heat from the SOFC system ($Q_{SOFC,Net}$) was defined as the difference between the exothermic heat (SOFC stack and afterburner) and the endothermic heat (preheaters and reformer) of the SOFC system. Generally, $Q_{SOFC,Net}$ was positive and could be further utilized for the distillation column. The net useful heat (Q_{Net}) of the SOFC–DIS system was calculated as the difference between the net useful heat of the SOFC system ($Q_{SOFC,Net}$) and the distillation energy (Q_D), in this case the reboiler heat duty. For energy calculation, the heat involved in each unit can be calculated using a conventional energy balance. The overall electrical efficiency was calculated as follows:

$$\eta_{elec,ov} = \frac{IV}{n_{EtOH} \times LHV_{EtOH}} \quad \text{when } Q_{Net} \geq 0 \tag{13}$$

$$\eta_{elec,ov} = \frac{IV}{(n_{EtOH} \times LHV_{EtOH}) - Q_{Net}} \quad \text{when } Q_{Net} \leq 0 \tag{14}$$

where n_{EtOH} represents the total ethanol flow rate fed to the distillation column. For $Q_{Net} \leq 0$, the SOFC–DIS system required more energy from an external heat source. To calculate the actual overall electrical efficiency, the energy required from the external heat source should be taken into account.

Table 2
Parameters of ohmic loss in SOFC cell components [5]

Materials	Parameters		Thickness (μm)
	α (Ω cm)	β (K)	
Anode (40% Ni/YSZ cermet)	2.98×10^{-5}	−1392	150
Cathode (Sr-doped $LaMnO_3$: LSM)	8.11×10^{-5}	600	2000
Electrolyte (Y_2O_3-doped ZrO_2: YSZ)	2.94×10^{-5}	10350	40
Interconnect (Mg-doped $LaCrO_3$)	1.256×10^{-3}	4690	100

3. Results and discussion

3.1. Effect of ethanol concentration on SOFC performance and energy requirement in the distillation column

It is impractical to directly reform bioethanol to generate a fuel gas for an SOFC stack due to the high water content [22]. Fig. 2 shows the performance curves of SOFCs fed by various reformed gases from the reforming of ethanol at different concentrations. The SOFC operated at a T_{SOFC} of 1200 K with a fuel utilization (U_f) of 80%. From Fig. 2 it is clear that the power density, cell voltage and electrical efficiency increase with increasing ethanol concentration. This implies that the SOFC stacks perform better when a distillation column is integrated with the SOFC system to purify the bioethanol. However, in practice, the maximum ethanol concentration should be kept below the range of carbon formation to avoid deactivation of the reforming catalyst and anode of the SOFC cell. For example, at T_{RF} = 1023 K, the boundary of carbon formation was at 41 mol% [20].

Although it is advantageous to use ethanol at high concentrations for the SOFC system, an additional energy is required to concentrate the bioethanol. Fig. 3 shows the minimum reboiler and condenser heat duties as a function of ethanol purity and recovery. It is clear that more energy is required when the distillation column is operated to achieve higher ethanol concentration and recovery. The reboiler and condenser heat duties increase dramatically at low ethanol purity and rises steadily at the higher ethanol purity. This is due to a narrow vapor–liquid equilibrium gap for ethanol–water mixture at low ethanol purity and a wider vapor–liquid gap at higher purity.

3.2. Performance of the SOFC system integrated with a distillation column (SOFC–DIS) at base case conditions

Fig. 4 indicates the temperature and energy requirement for all important units in the SOFC–DIS system operating at base

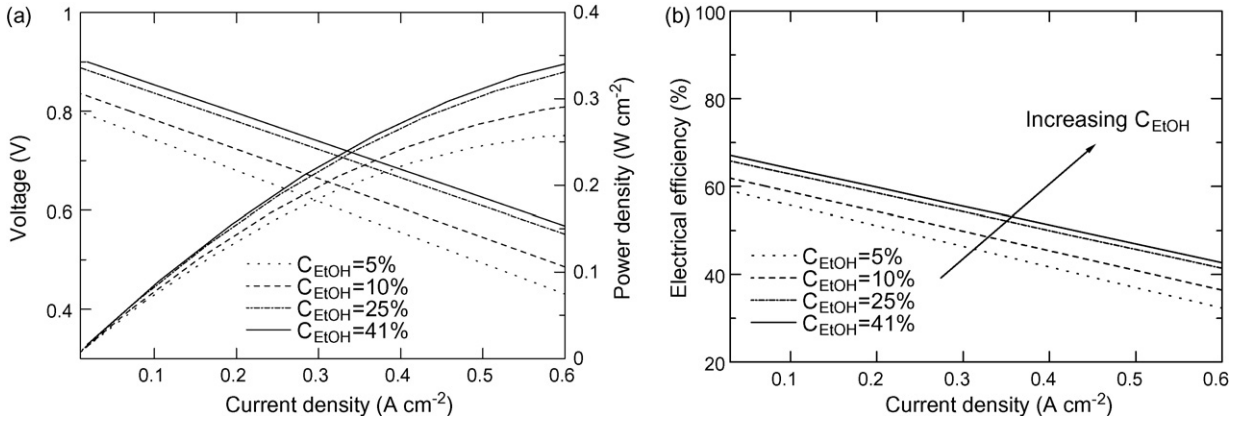

Fig. 2. Effect of ethanol concentration on SOFC performance: (a) voltage and power density and (b) electrical efficiency ($U_f = 80\%$ and $P = 101.3$ kPa).

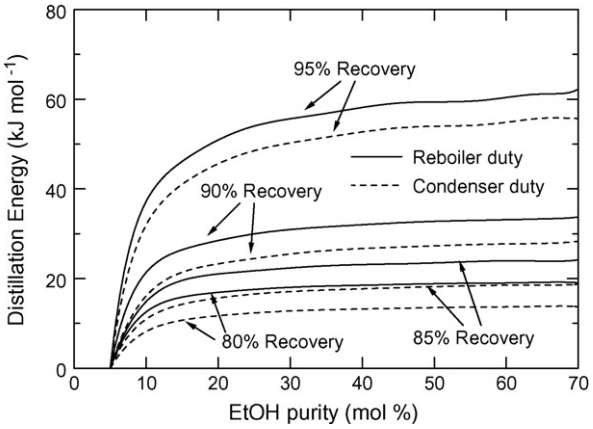

Fig. 3. Effect of ethanol concentration and ethanol recovery on distillation energy.

Table 3
Summary of operating conditions and the performance of SOFC for the base case

Parameter	Value/quality
Bioethanol flow rate (mol s^{-1})	8.42
Ethanol recovery (%)	80
Fuel option	Bioethanol with 5 mol% EtOH in water
Reforming temperature (K)	1023
SOFC temperature (K)	1200
Fuel utilization (%)	80
Voltage (V)	0.7
Power (kW)	218.77
Q_{Net} (kW)	−60.75
Overall electrical efficiency (%)	37.72

case conditions, i.e. $C_{EtOH} = 25$ mol%, EtOH recovery = 80%, cell operating voltage = 0.7 V and $U_f = 80\%$. An electrical power (W_e) of 218.77 kW with an overall electrical efficiency (based on LHV) of 37.72% was achieved. The net useful heat of the SOFC system ($Q_{SOFC,Net}$) and the heat required for the distillation column (Q_D) are 88.36 and 149.11 kW, respectively. In this case, although $Q_{SOFC,Net}$ can be used for supplying heat to the reboiler directly, it is obvious that the amount of $Q_{SOFC,Net}$ is not enough for the required Q_D under these base conditions. The conditions and the performance of SOFC–DIS system (power, power density, Q_{Net}) at the base case are presented in Table 3. However, by carefully adjusting the operating conditions such as operating voltage, fuel utilization, ethanol concentration and recovery, excess heat from the SOFC system can be increased to satisfy the energy requirements of the reboiler in the distillation column. A proper adjustment of these operating conditions for the system to be self-sufficient ($Q_{Net} = Q_{SOFC,Net} - Q_D = 0$) is the subject of the subsequent sections.

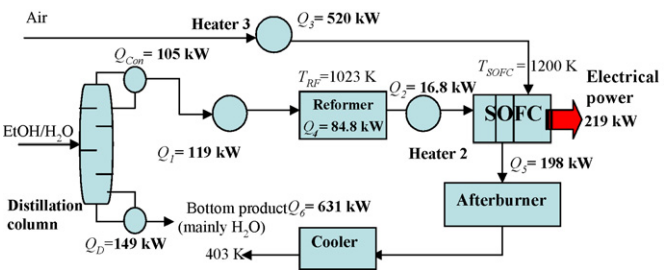

Fig. 4. Energy and temperature for various units in the SOFC–DIS system (EtOH recovery = 80%, $C_{EtOH} = 25$ mol%, $U_f = 80\%$, and $P = 101.3$ kPa).

3.3. Effects of operating parameters

3.3.1. Effects of SOFC operating voltage and fuel utilization

Fig. 5 represents the effect of operating voltage and fuel utilization on the overall efficiency and electrical power, W_e, (Fig. 5a), net useful heat, Q_{Net}, (Fig. 5b) and power density (Fig. 5c). As mentioned earlier, Q_{Net} is $Q_{SOFC,Net}$ subtracted by Q_D. Therefore, the value of Q_{Net} can be positive, zero or negative. A positive value of Q_{Net} indicates that some extra heat is left from the overall SOFC–DIS system. For the case where Q_{Net} is negative, $Q_{SOFC,Net}$ is not enough to supply all the required heat to the distillation column; therefore, an external heat source is required. At the point where Q_{Net} is equal to zero, $Q_{SOFC,Net}$ satisfies exactly the reboiler demand. Consequently, this condition offers the maximum electrical power for the SOFC–DIS system without requiring an external heat source. From Fig. 5b it can be seen that higher Q_{Net} (i.e. the system becomes more energy sufficient) can be obtained when the SOFC–DIS system operates

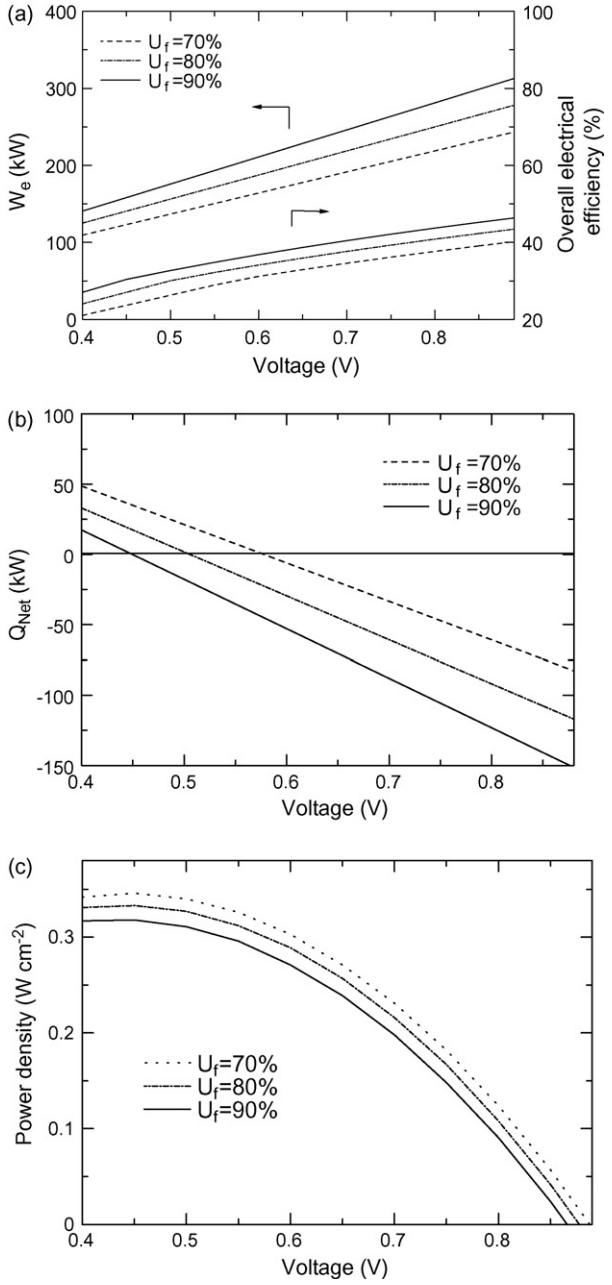

Fig. 5. Effect of operating voltage and U_f on SOFC–DIS performance: (a) W_e and overall efficiency, (b) Q_{Net} and (c) power density (EtOH recovery = 80%, C_{EtOH} = 25 mol%, and P = 101.3 kPa).

at lower voltage and/or lower fuel utilization. For lower voltage operation, the difference between the theoretical voltage and the actual one is large and results in higher heat losses emitted from the SOFC stack and therefore, Q_{Net} increases. For operation at a lower fuel utilization, more unreacted fuel exiting the SOFC stack is burnt in the afterburner. This leads to higher combustion energy and, as a result, higher Q_{Net}. However, lower electrical power and overall efficiency are obtained at higher Q_{Net}. There is an appropriate voltage for which $Q_{Net} = 0$ for U_f ranging from 70 to 90% (at C_{EtOH} = 25% and EtOH recovery = 80%). The corresponding voltages are 0.58, 0.51 and 0.45 V, for U_f = 70, 80 and 90%, respectively. Operation at higher fuel utilization requires lower operating voltage for generating more heat from the stack to compensate for the heat required in the overall system.

Another important SOFC performance indicator, which should be of concern, is the power density. The effects of voltage and fuel utilization on power density are shown in Fig. 5(c). An operation at low voltage is of no practical value (hence, not shown in Fig. 5). However, at high voltage Fig. 5c shows a rapid decrease in power density, resulting in larger (increased area) and more expensive SOFC stacks. Fig. 5b and c also indicate that for voltages corresponding to Q_{Net} equal to zero, the power densities are equal to 0.31, 0.33 and 0.32 W cm^{-2} for U_f = 70, 80 and 90%, respectively, which also corresponds to an overall electrical efficiency of 30.3% for all fuel utilizations. The fuel utilization factor (at least in the range of 70–90%) has thus no notable influence on the overall electrical efficiency and power density when Q_{Net} is kept at zero (at constant ethanol concentration).

In summary, the SOFC–DIS system can be made self-sufficient by adjusting the fuel utilization and operating voltage. However, it should be noted that a number of operating parameters must be carefully examined. An operation of SOFC at too low voltage may result in a significant reduction in power density. Moreover, the excessive heat generated in the stack will directly damage the thermophysical property of the SOFC cell components and raises the issue of how to remove this high amount of heat from the stack. It is recommended that adjusting fuel utilization is a better option to control $Q_{SOFC,Net}$. Also, for practical operation, the electrical power, overall efficiency and power density should be acceptably high.

3.3.2. *Effect of ethanol concentration*

From the previous section, it was found that an adjustment of voltage and fuel utilization can render the system self-sufficient. However, Q_{Net} also depends on the amount of required distillation energy (Q_D), which is strongly influenced by ethanol concentration (C_{EtOH}) and ethanol recovery (Fig. 3). In this section, the effect of ethanol concentration on electrical performance (W_e, overall efficiency, and corresponding voltage and power density) at conditions for which $Q_{Net} = 0$ is investigated. The ethanol recovery was kept at 80%. The results shown in Fig. 6(a) indicate that, for ethanol concentrations between 15 and 41%, W_e, and overall efficiency increase with increasing ethanol concentration, independent of the fuel utilization (U_f = 70–80%). We know that increasing ethanol concentration is beneficial in terms of power produced, but is detrimental in terms of energy demand in the column reboiler (see Fig. 3). Fig. 6a illustrates the fact that, for ethanol concentrations between 15 and 41%, the benefit of increasing ethanol concentration is more important than the negative effect of increased reboiler duty. This could be explained by the relatively gentle increase in reboiler duty for ethanol concentrations greater than 15%, as seen in Fig. 3. The effect of fuel utilization on SOFC performance when Q_{Net} equals zero is also presented in Fig. 6(b). It can be seen that the SOFC would run at lower voltage for an operation at higher fuel utilization. This result is in good agreement with the results described earlier. It can be seen that the operating voltage is around 0.6 and 0.5 V at U_f = 70 and 80%,

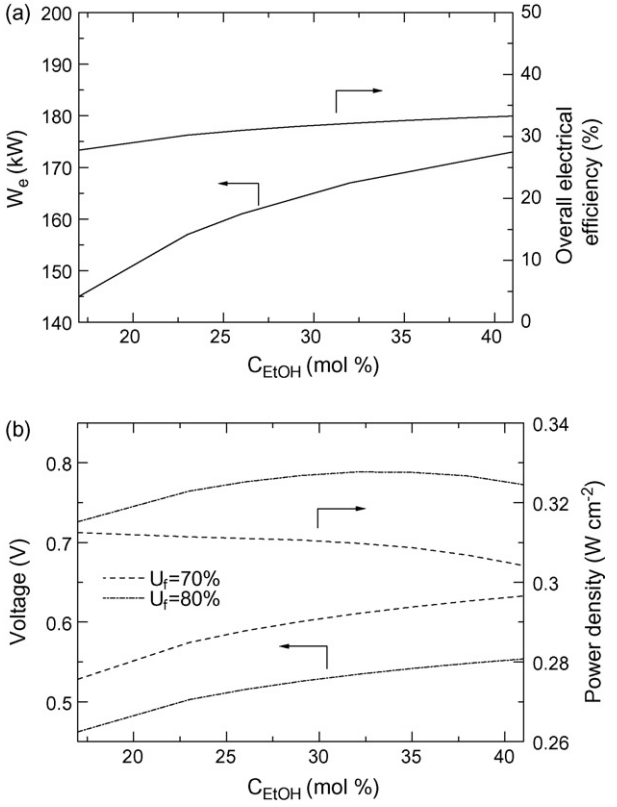

Fig. 6. Effect of ethanol concentration on SOFC–DIS performance for various U_f when $Q_{Net} = 0$: (a) W_e and overall efficiency and (b) corresponding voltage and power density (EtOH recovery = 80%, and $P = 101.3$ kPa).

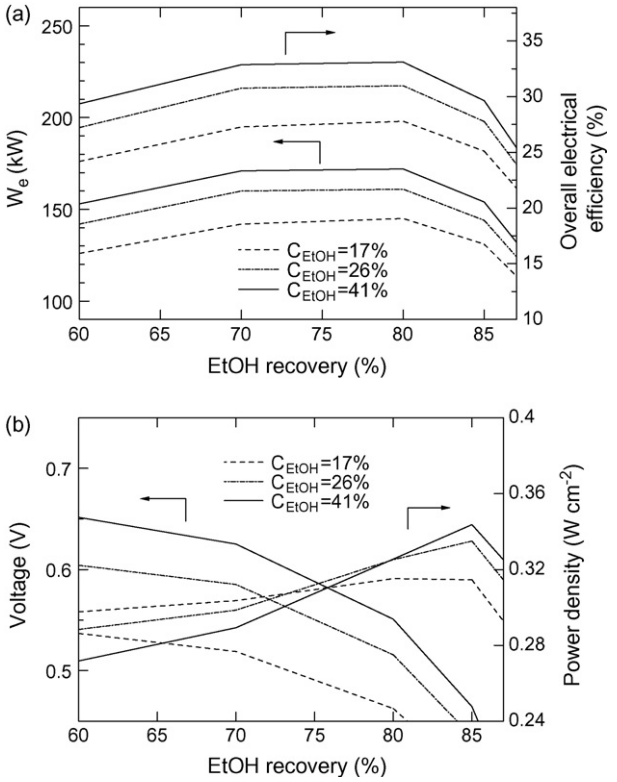

Fig. 7. Effect of ethanol recovery on SOFC–DIS performance when $Q_{Net} = 0$ at different C_{EtOH}: (a) W_e and overall efficiency, and (b) corresponding voltage and power density ($U_f = 80\%$ and $P = 101.3$ kPa).

respectively. Fig. 6(b) also presents the effect of ethanol concentration on power density. For $U_f = 80\%$, the power density slightly increases when operated at higher C_{EtOH} whereas the opposite is true for $U_f = 70\%$. As expected, the power density is consistently higher at $U_f = 80\%$ than at 70%.

In summary, Fig. 6 indicates that, when keeping Q_{Net} equals to zero, better overall performance (higher overall electrical efficiency, higher power density) is achieved when operating at higher fuel utilization factor (e.g. 80%) and at the highest possible ethanol concentration (i.e. 41%). At these conditions, the overall efficiency reaches 33.3% and the power density 0.32 W cm^{-2} (corresponding to a voltage of 0.55 V and current density of 0.58 A cm^{-2}). It should be noted that in this study the SOFC cell is based on the tubular configuration. In a practical operation, a planar SOFC with higher current densities may be an attractive choice.

3.3.3. *Effect of ethanol recovery*

As mentioned earlier, an ethanol recovery is an important parameter affecting Q_D and the overall energy within the system. Fig. 7(a) presents the effect of ethanol recovery on W_e and overall efficiency at different ethanol concentrations for $Q_{Net} = 0$. Higher W_e and overall efficiency are obtained when increasing the ethanol recovery up to 80%; however, the performance significantly decreases at ethanol recoveries greater than 80%. This is because of the competition between an increase of current and a decrease of operating voltage at that point. By increasing the ethanol recovery, this effect also increases the current at the same fuel utilization while the operating voltage is also dependent on the required Q_D. It can be seen that at lower ethanol recovery, the required operating voltage is slightly changed due to a small change in Q_D. Therefore, the electrical power becomes higher because of the increase in current. However, at high ethanol recovery, Q_D is dramatically increased and causes a sudden drop in voltage as shown in Fig. 7(b). This results in a decrease in electrical power. The corresponding voltage and power density at different EtOH recovery is also shown in Fig. 7(b). It can be seen that an increase of ethanol recovery still requires lower voltage. The SOFC–DIS system still needs some energy from the SOFC stack to compensate for the higher demand in Q_D. This is different from the results in Fig. 6(b), which shows that lower voltage is not required because the SOFC–DIS system gain some benefits from the less preheating energy for EtOH/H_2O mixture. For the effect of ethanol recovery, more ethanol and water are fed to the SOFC–DIS system when operated at higher ethanol recovery. More energy is therefore required for the reformer and EtOH/H_2O preheater. The SOFC stack has to be operated at lower voltages to compensate for the heat, which results in a decrease in voltage as shown in Fig. 7(b). Moreover, it was found that at higher EtOH recovery, a higher power density is obtained.

From the above studies, it is possible to operate the SOFC–DIS system in an energy sufficient mode. The obtained efficiency and power density of SOFC–DIS system are 33.3% and 0.32 W cm^{-2} at $C_{ETOH} = 41\%$, $U_f = 80\%$ and ethanol recov-

ery = 80%. The reboiler heat duty is the limit in achieving a higher performance because the SOFC–DIS has to be operated under inferior conditions in order to provide the required heat to the distillation column. Moreover, a large amount of heat (105 kW) was emitted from the SOFC–DIS at the condenser. The management of this condenser duty could be used to enhance the SOFC–DIS performance and allow the SOFC to operate at more optimal conditions. It is expected that the performance of SOFC–DIS could be further improved.

4. Conclusions

An SOFC system integrated with a distillation column (SOFC–DIS) was studied. Bioethanol was used as a feed stream for the SOFC–DIS system. The influence of operating parameters (EtOH concentration, EtOH recovery, cell operating voltage and fuel utilization) on electrical performance (e.g. electrical power, overall efficiency and power density) and thermal energy involved in the SOFC system (e.g. reboiler heat duty and the net useful heat) was presented. The study showed that it is possible to operate the SOFC–DIS system in an energy self-sufficient mode by adjusting the operating voltage and/or fuel utilization. The effect of ethanol concentration (17–41 mol%) and ethanol recovery at the energy-sufficient point ($Q_{Net} = 0$) was presented. It was found that higher ethanol concentration yielded higher electrical power (for C_{EtOH} in the range of 15–17%), higher overall electrical efficiency and acceptably high power density. For the effect of ethanol recovery, there is an optimum ethanol recovery at 80%, which yielded the optimum electrical power and overall electrical efficiency. Higher power densities can be obtained when operating at higher ethanol recoveries. In brief, this thermodynamic study of the SOFC–DIS system showed the potential of the system when operated without external heat sources. However, the obtained performance of the SOFC–DIS system was quite low (0.32 W cm^{-2}, 173.07 kW, 33.3% overall efficiency based on total ethanol flow rate fed to SOFC–DIS system at $U_f = 80\%$, EtOH recovery = 80% and $C_{EtOH} = 41\%$). It was found that the reboiler heat duty was the limit of the SOFC–DIS system. Moreover, a huge amount of heat was lost at the condenser. To improve the performance of the SOFC–DIS system, it is recommended that (1) the heat emitted at a condenser should be utilized for other purposes and (2) another purifying process (e.g. membranes) which consumes less energy should be investigated.

Acknowledgements

The support from the Thailand Research Fund, Commission of Higher Education and National Metal and Materials Technology Center (MTEC) are gratefully acknowledged.

References

[1] EG&G Service Parsons Inc., Fuel Cell Handbook, 5th ed., Science Applications International Corporation, Morgantown, WV, 2000, pp. 234.
[2] J. Palsson, A. Selimovic, L. Sjunnesson, J. Power Sources 86 (2000) 442–448.
[3] B. Fredriksson Möller, J. Arriagada, M. Assadi, I. Potts, J. Power Sources 131 (2004) 320–326.
[4] Y. Inui, T. Matsumae, H. Koga, K. Nishiura, Energy Convers. Manage. 46 (2005) 1837–1847.
[5] S.H. Chan, C.F. Low, O.L. Ding, J. Power Sources 103 (2002) 188–200.
[6] E. Fontell, T. Kivisaari, N. Christiansen, J.B. Hansen, J. Pålsson, J. Power Sources 131 (2004) 49–56.
[7] W. Zhang, E. Croiset, P.L. Douglas, M.W. Fowler, E. Entchev, Energy Convers. Manage. 46 (2005) 181–196.
[8] A.O. Omosun, A. Bauen, N.P. Brandon, C.S. Adjiman, D. Hart, J. Power Sources 131 (2004) 96–106.
[9] G. Maggio, S. Freni, S. Cavallar, J. Power Sources 74 (1998) 17–23.
[10] P. Tsiakaras, A. Demin, J. Power Sources 102 (2001) 210–217.
[11] S. Douvartzides, F.A. Coutelieris, P.E. Tsiakaras, J. Power Sources 114 (2003) 203–212.
[12] S. Douvartzides, F. Coutelieris, P. Tsiakaras, J. Power Sources 131 (2004) 224–230.
[13] D.J. Shell, C.J. Riley, N. Dowe, J. Farmer, K.N. Ibson, M.F. Ruth, S.T. Toon, R.E. Lumpkin, Bioresour. Technol. 91 (2004) 179–188.
[14] C.A. Cardona Alzate, O.J. Sanchez Toro, Energy 31 (2006) 2447–2459.
[15] P.L. Roger, K.J. Lee, D.E. Tribe, Process Biochem. (1980) 7–11.
[16] S.E. Buchholz, M.M. Dooley, D.E. Eveleigh, Trends Biotechnol. 5 (1987) 199–204.
[17] E. Achenbach, J. Power Sources 49 (1994) 333–348.
[18] E. Hernandez-Pachenco, D. Singh, P.N. Hutton, N. Patel, M.D. Mann, J. Power Sources 138 (2004) 174–186.
[19] M.C. Williams, J.P. Starkey, S.C. Singhal, J. Power Sources 131 (2004) 79–85.
[20] S. Assabumrungrat, V. Pavarajarn, S. Charojrochkul, N. Laosiripojana, Chem. Eng. Sci. 59 (2004) 6015–6020.
[21] W. Jamsak, S. Assabumrungrat, P.L. Douglas, N. Laosiripojana, S. Charojrochkul, Chem. Eng. J. 119 (2006) 11–18.
[22] S.L. Douvartzides, F.A. Coutelieris, A.K. Demin, P.E. Tsiakaras, AIChE J. 49 (2003) 248–257.

Appendix 5

Available online at www.sciencedirect.com
ScienceDirect
Journal of Power Sources 159 (2006) 1274–1282
JOURNAL OF POWER SOURCES
www.elsevier.com/locate/jpowsour

Determination of the boundary of carbon formation for dry reforming of methane in a solid oxide fuel cell

S. Assabumrungrat [a,*], N. Laosiripojana [b], P. Piroonlerkgul [a]

[a] *Center of Excellence in Catalysis and Catalytic Reaction Engineering, Department of Chemical Engineering, Faculty of Engineering, Chulalongkorn University, Bangkok 10330, Thailand*
[b] *The Joint Graduate School of Energy and Environment, King Mongkut's University of Technology Thonburi, Bangkok 10140, Thailand*

Received 8 November 2005; received in revised form 14 December 2005; accepted 15 December 2005
Available online 20 January 2006

Abstract

The boundary of carbon formation for the dry reforming of methane in direct internal reforming solid oxide fuel cells (DIR-SOFCs) with different types of electrolyte (i.e., an oxygen ion-conducting electrolyte (SOFC-O^{2-}) and a proton-conducting electrolyte (SOFC-H^+)) was determined by employing detailed thermodynamic analysis. It was found that the required CO_2/CH_4 ratio decreased with increasing temperature. The type of electrolyte influenced the boundary of carbon formation because it determined the location of water formed by the electrochemical reaction. The extent of the electrochemical reaction also played an important role in the boundary of carbon formation. For SOFC-O^{2-}, the required CO_2/CH_4 ratio decreased with the increasing extent of the electrochemical reaction due to the presence of electrochemical water in the anode chamber. Although for SOFC-H^+ the required CO_2/CH_4 ratio increased with the increasing extent of the electrochemical reaction at high operating temperature ($T > 1000$ K) following the trend previously reported for the case of steam reforming of methane with addition of water as a carbon suppresser, an unusual opposite trend was observed at lower operating temperature. The study also considered the use of water or air as an alternative carbon suppresser for the system. The required H_2O/CH_4 ratio and air/CH_4 ratio were determined for various inlet CO_2/CH_4 ratios. Even air is a less attractive choice compared to water due to the higher required air/CH_4 ratio than the H_2O/CH_4 ratio; however, the integration of exothermic oxidation and the endothermic reforming reactions may make the use of air attractive. Water was found to be more effective than carbon dioxide in suppressing the carbon formation at low temperatures but their effect was comparable at high temperatures. Although the results from the study were based on calculations of the SOFCs with different electrolytes, they are also useful for selecting suitable feed compositions for other reactors; including conventional reformers and membrane reactors with hydrogen removal.

Keywords: Solid oxide fuel cell; Carbon formation; Thermodynamic analysis; Dry reforming of methane

1. Introduction

A solid oxide fuel cell (SOFC) is a more efficient electrical power generator than many conventional processes. Due to its high operating temperature, it offers wide potential applications, flexibility of fuel choices, possibility for operation with an internal reformer and a high system efficiency. Recent developments on SOFCs seem to move towards to two main issues: intermediate temperature operation and the use of other fuels instead of hydrogen. The uses of various alternative fuels; e.g., natural gas, bio-ethanol, coal, biomass, biogas, methanol, gasoline and other oil derivatives, in SOFCs have been investigated [1–3]. As SOFCs are operated at high temperatures, these fuels can be internally reformed at the anode side of SOFCs producing a H_2-CO rich gas, which is eventually used to generate the electrical energy and heat. This operation is called a direct internal reforming (hence, DIR-SOFCs). Regarding the global environmental problems and current fossil fuel concerns, the development of SOFCs fed by renewable fuels attract more attention as an alternative method for power generation in the near future. Among renewable sources, biogas is a promising candidate, since it is produced readily from the fermentation of biomasses and agricultural wastes. Typically, biogas consists mainly of methane and carbon dioxide. Due to the rich CO_2 in biogas, carbon dioxide (or dry) reforming reaction would be one of the most suitable processes to convert biogas to hydrogen or

* Corresponding author. Tel.: +66 2 218 6868; fax: +66 2 218 6877.
E-mail address: Suttichai.A@chula.ac.th (S. Assabumrungrat).

0378-7753/$ – see front matter © 2006 Elsevier B.V. All rights reserved.
doi:10.1016/j.jpowsour.2005.12.010

Nomenclature

a	inlet moles of methane (mol)
b	inlet moles of carbon dioxide (mol)
c	inlet moles of steam (mol)
d	inlet moles of inert (mol)
e	extent of the electrochemical reaction of hydrogen (mol)
K_1	equilibrium constant of reaction (16) (kPa)
K_2	equilibrium constant of reaction (17) (kPa)
K_3	equilibrium constant of reaction (18) (kPa)
n_i	number of moles of component i (mol)
p_i	partial pressure of component i (kPa)
x	converted moles associated with reaction (1) (mol)
y	converted moles associated with reaction (2) (mol)
z	converted moles associated with reaction (3) (mol)

Greek letter

α_c	carbon activity

synthesis gas (CO and H_2) for later utilization in SOFCs or other processes.

However, in order to operate SOFCs on the direct feed of alternative fuels (i.e., biogas) rather than hydrogen, several major problems remain to be solved. One of them is the problem of carbon deposition on the anode, causing loss of active sites and cell performance as well as poor durability. The growth of carbon filaments attached to the anode crystallites can generate massive forces within the electrode structure leading to rapid breakdown [4]. A number of efforts have been carried out to alleviate this problem. One approach is to search for appropriate anode formulations and operating conditions. A number of additives were added to the anode to lower the rate of carbon formation. For example, the addition of molybdenum and cerium metal oxides to the Ni-based anode was reported to reduce carbon deposition, and in some cases, to increase fuel conversion [5,6]. The addition of alkalis such as potassium can accelerate the reaction of carbon with steam and also neutralize the acidity of the catalyst support, hence reducing carbon deposition [7].

Another conventional approach to avoid carbon deposition is the addition of extra oxidant to the feed. According to the dry reforming of methane, it was suggested that the use of excess carbon dioxide in the dry reforming reaction could avoid carbon formation [8]. Experimental studies on dry reforming using an excess of carbon dioxide with carbon dioxide to methane (CO_2/CH_4) ratios of 3/1 and 5/1 over a nickel catalyst supported on alumina were carried out. It was reported that the rate of disintegration is smaller for the case with higher ratio. Selection of a suitable CO_2/CH_4 ratio is therefore an important issue [9,10]. Carbon formation can occur when the SOFCs are operated at low CO_2/CH_4 ratios. However, use of high CO_2/CH_4 ratios is unattractive as it lowers the electrical efficiency of the SOFCs by the dilution of fuel, the yield of hydrogen production and the system efficiency. Consequently, it is necessary to find the CO_2/CH_4 ratio at the boundary of carbon formation at which represents the minimum ratio required to operate the SOFCs in a carbon-free condition.

In this paper, a detailed thermodynamic analysis is carried out to predict the boundary of carbon formation for DIR-SOFCs fueled by mixtures of methane and carbon dioxide. The effects of electrolyte type (i.e., oxygen ion-conducting and proton-conducting electrolytes), operating temperature, and extent of electrochemical reaction on the required CO_2/CH_4 ratio have been investigated. Our previous work employed thermodynamic calculations to predict the required H_2O/fuel ratio for SOFCs fed by methane [11] and methanol [12]. It was found that the SOFCs with an oxygen-conducting electrolyte (SOFC-O^{2-}) require less H_2O/fuel ratio than those with a hydrogen-conducting electrolyte (SOFC-H^+) because extra water generated from the electrochemical reaction is available for use in the anode chamber. In this present work, alternative methods to alleviate the carbon formation by adding water or air to the system were considered as it is practical to add these components along with methane and carbon dioxide in the feed to reduce the degree of carbon deposition.

2. Theory

The main reaction involved in the production of hydrogen from methane and carbon dioxide is the dry reforming of methane (Eq. (1)). When the SOFC is operated using an oxygen ion-conducting electrolyte, water is also generated by the electrochemical reaction of hydrogen and oxygen ion, and therefore, the steam reforming of methane (Eq. (2)) and the water gas shift reaction (WGS) (Eq. (3)) also take place.

$$CH_4 + CO_2 = 2H_2 + 2CO \quad (1)$$

$$CH_4 + H_2O = 3H_2 + CO \quad (2)$$

$$CO + H_2O = H_2 + CO_2 \quad (3)$$

The dry and steam reforming reactions are strongly endothermic while the WGS is mildly exothermic. Both steam and dry reforming reactions have similar thermodynamic characteristics except that the carbon formation in the dry reforming is more severe than in the steam reforming due to the lower H/C ratio of this reaction [13]. The activities toward steam and dry reforming over several catalysts were investigated [14]. It was observed that replacing water with carbon dioxide gave similar activation energies, which indicated a similar rate-determining step in these two reactions. Nickel and cobalt are usually applied as the catalysts for this reaction. The dry reforming reaction with a stoichiometric feed ratio over several catalysts was studied [15]. It was found that Ni/SiO_2 exhibited this reaction near equilibrium and had high selectivity to carbon monoxide. The activity of the catalyst over other supports was found to be deactivated rapidly due to carbon deposition.

When a SOFC is operated with an internal reformer, hydrogen produced from the reforming process is consumed simultaneously by the electrochemical reaction generating electricity. Theoretically, two types of solid electrolytes can be employed in the SOFC: oxygen ion- and proton-conducting electrolytes. The reactions taking place in the anode and the cathode can be summarized as follows:

Oxygen ion-conducting electrolyte:

Anode:

$$H_2 + O^{2-} = H_2O + 2e^- \quad (4)$$

$$CO + O^{2-} = CO_2 + 2e^- \quad (5)$$

Cathode:

$$O_2 + 4e^- = 2O^{2-} \quad (6)$$

Proton-conducting electrolyte:

Anode:

$$H_2 = 2H^+ + 2e^- \quad (7)$$

Cathode:

$$2H^+ + \tfrac{1}{2}O_2 + 2e^- = H_2O \quad (8)$$

The difference between the SOFCs with the two electrolyte types is the location of the water produced. For the SOFC with the oxygen ion-conducting electrolyte (SOFC-O^{2-}), water is produced in the anode chamber whereas it appears in the cathode chamber for the SOFC with the proton-conducting electrolyte (SOFC-H^+). It should be noted that for the SOFC-H^+, carbon monoxide cannot be electrochemically consumed. It is, therefore, not so practical to use only the dry reforming of methane in the SOFC-H^+ unless water is included in the feed to enhance the hydrogen production by steam reforming (Eq. (2)) and WGS (Eq. (3)). For the SOFC-O^{2-}, both hydrogen and carbon monoxide can electrochemically react with oxygen. However, the electrochemical reaction of hydrogen is much faster than that of CO [16]. Therefore, in this study it was assumed that only hydrogen reacts electrochemically with oxygen supplied from the cathode side. For comparative purpose between the SOFCs with different electrolytes, only the range of possible electrochemical reaction from hydrogen in the SOFC-H^+ was considered in the study.

The number of moles of each component in the anode gas mixture is given by the following expressions:

$$n_{CH_4} = a - x - y \quad (9)$$

$$n_{CO_2} = b - x + z \quad (10)$$

$$n_{CO} = 2x + y - z \quad (11)$$

$$n_{H_2} = 2x + 3y + z - e \quad (12)$$

$$n_{H_2O} = c - y - z + e \text{ (for oxygen ion-conducting electrolyte)}$$
$$n_{H_2O} = c - y - z \text{ (for proton-conducting electrolyte)} \quad (13)$$

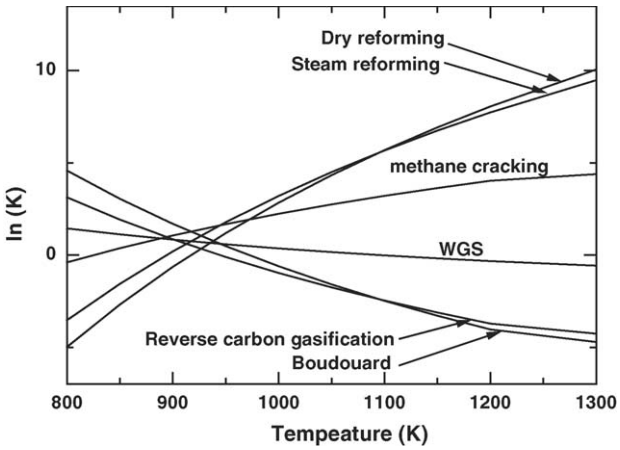

Fig. 1. Values of the equilibrium constants.

$$n_{inert} = d \quad (14)$$

$$n_{total} = \sum_{i-1}^{6} n_i \quad (15)$$

where a, b, c and d represent the inlet moles of methane, carbon dioxide, steam and inert respectively, e the extent of the electrochemical reaction of hydrogen, and x, y and z represent the converted moles associated to the reactions (1)–(3), respectively. The thermodynamic equilibrium composition can be determined by solving a system of nonlinear equations relating the moles of each component to the equilibrium constants of the reactions whose values are given in Fig. 1.

The following reactions are the most probable carbon formation reactions in the system [17]:

$$2CO = CO_2 + C \quad (16)$$

$$CH_4 = 2H_2 + C \quad (17)$$

$$CO + H_2 = H_2O + C \quad (18)$$

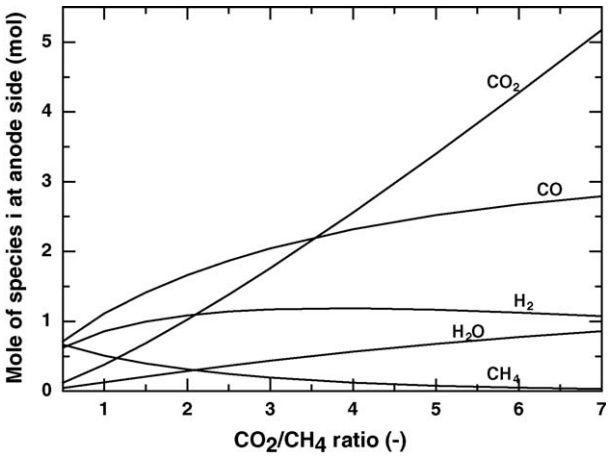

Fig. 2. Effect of inlet CO_2/CH_4 ratio on the moles of each component in a conventional reformer (a = 1 mol, P = 101.3 kPa and T = 900 K).

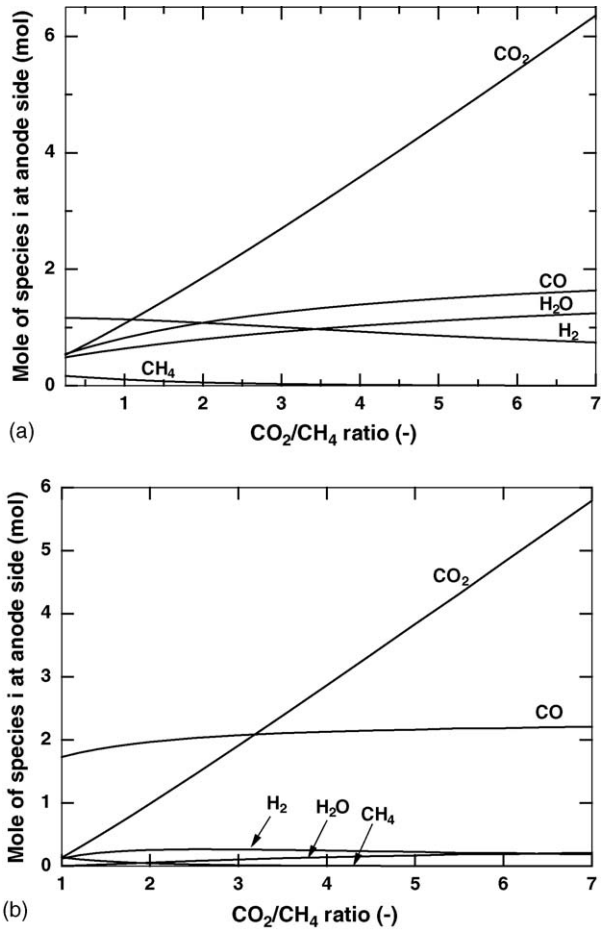

Fig. 3. Effect of inlet CO_2/CH_4 ratio on the moles of each component: (a) SOFC-O^{2-} and (b) SOFC-H^+ ($a = 1$ mol, $e = 1.6$ mol, $P = 101.3$ kPa and $T = 900$ K).

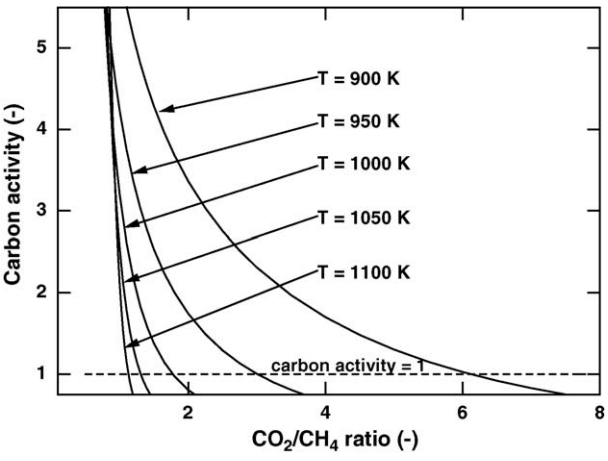

Fig. 4. Effect of inlet CO_2/CH_4 ratio on carbon activity ($a = 1$ mol, $e = 1.6$ mol, $P = 101.3$ kPa and $T = 900$ K).

It should be noted that due to the endothermic nature of the dry reforming of methane (Eq. (1)) and the mildly exothermic nature of the WGS reaction (Eq. (3)), the amount of CO becomes significant at high operating temperatures [18]. All reactions are employed to examine the thermodynamic possibility of carbon formation by calculating the values of their carbon activities (α_c)

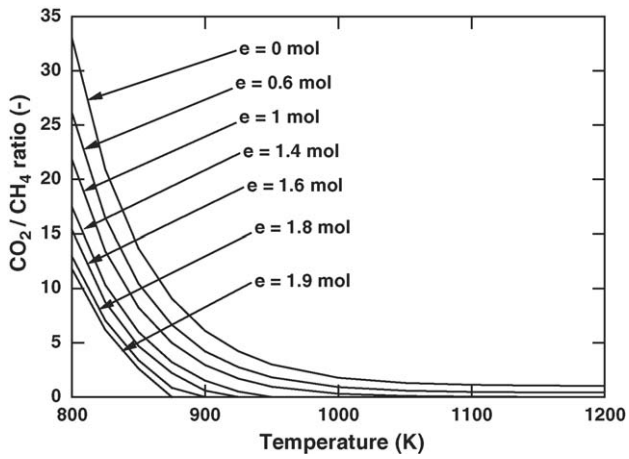

Fig. 5. Influence of the extent of the electrochemical reaction of H_2 on the requirement of the inlet CO_2/CH_4 ratio at different operating temperature (SOFC-O^{2-}, $a = 1$ mol and $P = 101.3$ kPa).

as defined in Eqs. (19)–(21).

$$\alpha_{c,\mathrm{CO}} = \frac{K_1 p_{\mathrm{CO}}^2}{p_{\mathrm{CO_2}}} \tag{19}$$

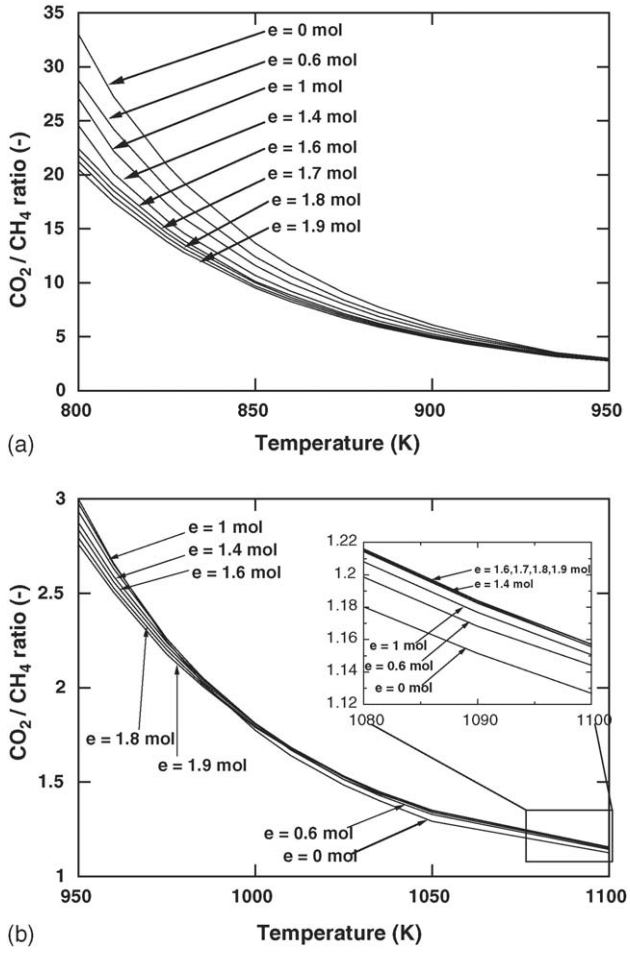

Fig. 6. Influence of the extent of electrochemical reaction of H_2 on the requirement of inlet CO_2/CH_4 ratio at different operating temperature: (a) $T = 800$–950 K and (b) 950–1100 K (SOFC-H^+, $a = 1$ mol and $P = 101.3$ kPa).

$$\alpha_{c,CH_4} = \frac{K_2 p_{CH_4}}{p_{H_2}^2} \quad (20)$$

$$\alpha_{c,CO\text{-}H_2} = \frac{K_3 p_{CO} p_{H_2}}{p_{H_2O}} \quad (21)$$

where K_1, K_2 and K_3 represent the equilibrium constants of the reactions (16)–(18), respectively, and p_i represents the partial pressure of component i. When $\alpha_c > 1$, the system is not in equilibrium and carbon formation is observed. The system is at equilibrium when $\alpha_c = 1$. It is noted that the carbon activity is only the indicator for the presence of carbon in the system. It does not give the information regarding the amount of carbon formed. Finally, when $\alpha_c < 1$, carbon formation is thermodynamically impossible.

To find the range of SOFC operation which does not suffer from the carbon formation, the operating temperature and the extent of the electrochemical reaction of hydrogen are specified. Then, the initial value of the CO_2/CH_4 ratio is varied and the corresponding values of α_c are calculated. The carbon formation boundary is defined as the value of CO_2/CH_4 ratio whose value of $(1 - \alpha_c)$ is approaching zero. This value represents the minimum inlet CO_2/CH_4 ratio at which carbon formation in the equilibrium mixture is thermodynamically impossible. When the inlet CO_2/CH_4 ratio is fixed at a certain value and water is added to the feed for the purpose of suppressing the carbon formation, the same calculation procedure can be applied to find the value of H_2O/CH_4 ratio whose value of $(1 - \alpha_c)$ is approaching zero. When air is employed instead of water, the calculation is carried out by assuming the complete combustion of oxygen in air with methane to yield water and carbon dioxide. Then the obtained feed composition is used to calculate the carbon activity. The value of air/CH_4 ratio is varied until the value of $(1 - \alpha_c)$ approaching zero is obtained.

It should be noted that although recent investigators have estimated the carbon concentration in the reforming reactions by the method of Gibbs energy minimization [19], the principle of equilibrated gas to predict the carbon formation in this study is still meaningful since the calculations are carried to find the carbon formation boundary where the carbon just begins to form. In addition, other factors such as mass and heat transfer or rate of reactions may also affect the prediction of the carbon formation boundary. Local compositions which allow the local carbon formation may exist, although the carbon formation is unfavorable according to the calculations based on equilibrium bulk compositions. Moreover, other forms of carbonaceous compounds such as C_nH_m may be formed and result in comparable damages.

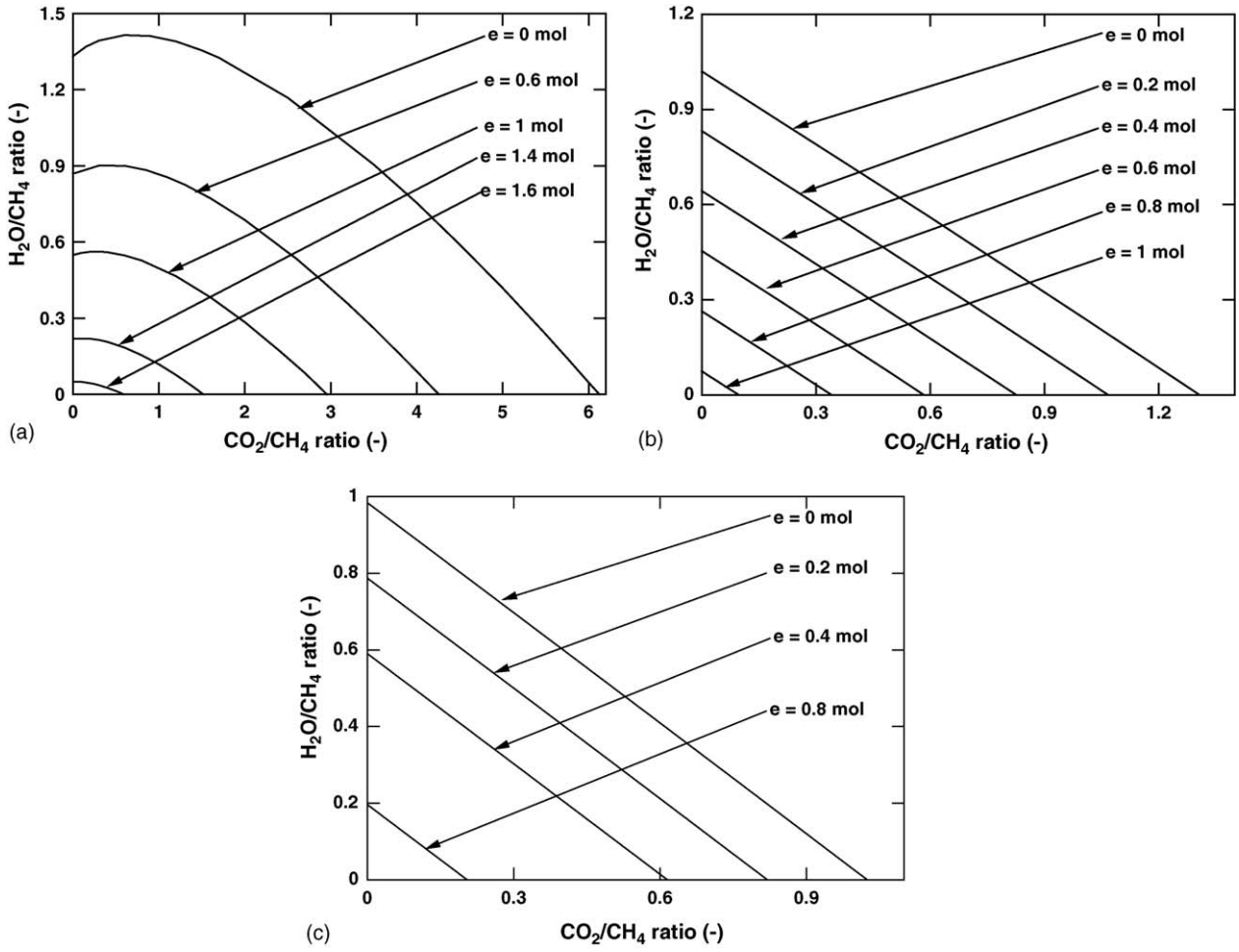

Fig. 7. Required inlet H_2O/CH_4 ratio at different inlet CO_2/CH_4 ratios: (a) $T = 900$ K, (b) $T = 1050$ K and (c) $T = 1200$ K (SOFC-O^{2-}, $a = 1$ mol and $P = 101.3$ kPa).

3. Results and discussion

The influences of the inlet CO_2/CH_4 ratio on equilibrium composition of the dry reforming reaction in a conventional reactor at the isothermal condition ($T = 900$ K) are shown in Fig. 2. It was found that the amounts of carbon monoxide and hydrogen increased with increasing moles of carbon dioxide in the feed, and that some hydrogen was converted to water particularly at high CO_2/CH_4 ratios due to the reverse water gas shift reaction (RWGS) and methanation reaction (reverse steam reforming of methane). However, at higher operating temperatures, the contribution of the methanation reaction was much less pronounced due to the high value of the equilibrium constant of the steam reforming of methane as shown in Fig. 1. It should be noted that some methane still existed even with high CO_2/CH_4 ratios at a moderate temperature of 900 K. For SOFC-O^{2-} operation, hydrogen was electrochemically consumed and water was generated in the anode chamber. It is shown in Fig. 3(a) that negligible amount of methane was observed because the consumption of hydrogen moved the dry reforming of methane forward and, in addition, the steam reforming of methane promoted the methane consumption. When the extent of carbon dioxide in the feed was increased, a lower amount of hydrogen and a higher amount of water were observed according to the RWGS reaction. For SOFC-H^+ operation, hydrogen was also electrochemically consumed; however, the electrochemical water appeared in the cathode chamber and played no role in the anode reactions unlike in the SOFC-O^{2-}. It should be noted that the SOFC-H^+ behaved quite similarly to a membrane reactor in which the forward reaction is enhanced by removing some products (e.g., hydrogen) from the reaction zone. From Fig. 3(b), it was observed that the amounts of hydrogen and water involved in the SOFC-H^+ were much less than those in the SOFC-O^{2-}. Moreover, when higher amount of carbon dioxide was added in the feed, more hydrogen was converted to water and a slight increase of carbon monoxide was observed.

The effect of the inlet CO_2/CH_4 ratio on the carbon activity for the conventional reformer is shown in Fig. 4. The carbon activity decreased dramatically with increasing CO_2/CH_4 ratio and operating temperature, implying that the chance of carbon formation can be rapidly decreased by adding CO_2 to the system or operating the system at a high temperature. Increasing the amount of CO_2 in the feed promoted the consumption of methane and generation of water, which reduced the possibility of carbon formation. Because the Boudard (Eq. (16)) and reverse carbon gasification (Eq. (18)) reactions are exothermic,

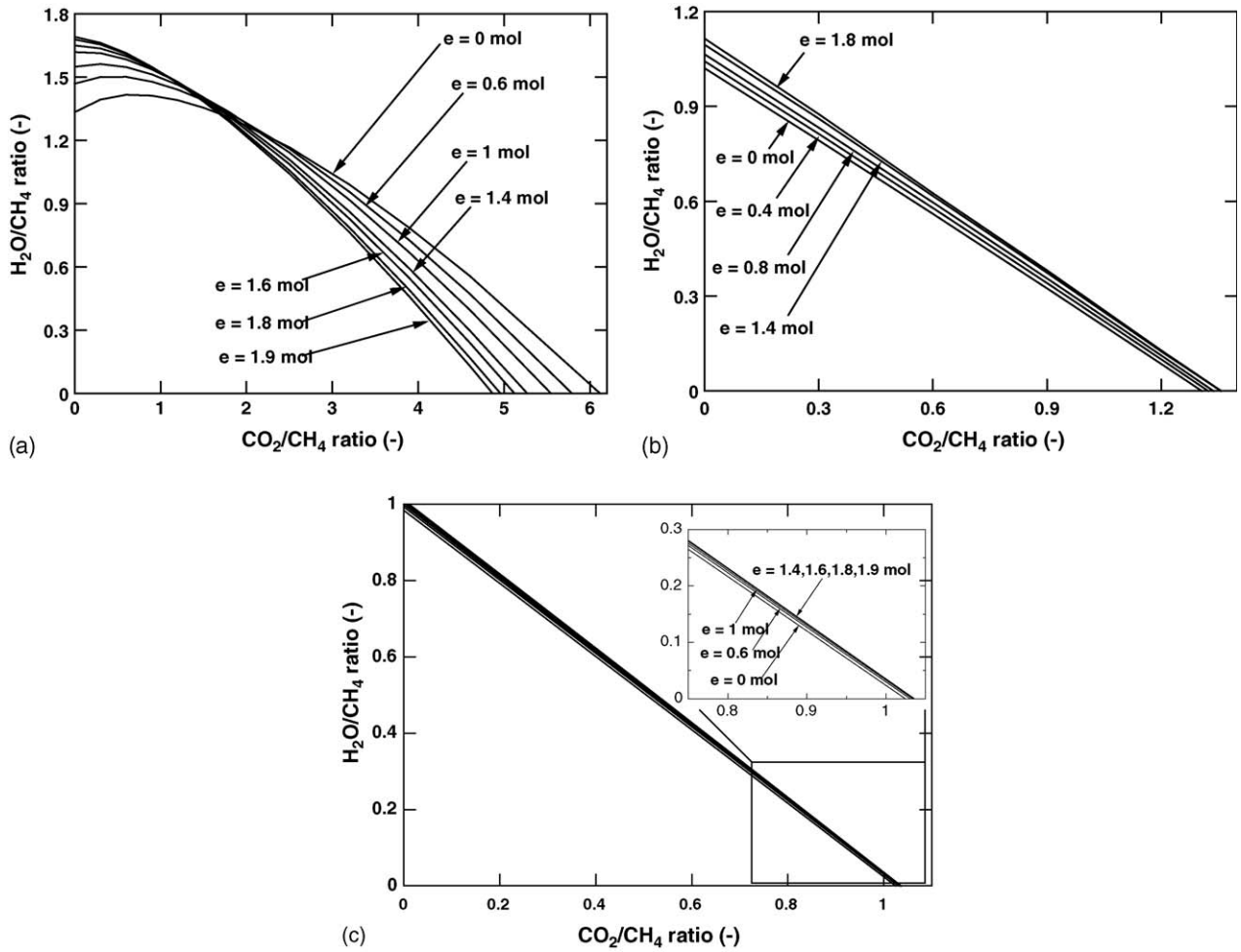

Fig. 8. Required inlet H_2O/CH_4 ratio at different inlet CO_2/CH_4 ratios: (a) $T = 900$ K, (b) $T = 1050$ K and (c) $T = 1200$ K (SOFC-H^+, $a = 1$ mol and $P = 101.3$ kPa).

the carbon activity was significantly reduced at high operating temperatures. Although the carbon formation from methane cracking (Eq. (17)) should be more significant at high temperature, the much higher values of the equilibrium constants of the dry and steam reforming reactions compared to that of the methane cracking make it become less likely at high operating temperatures (see Fig. 1). It should be noted that the carbon activity calculated from Eqs. (19)–(21) yield the same value, which is in good agreement with previous literature [11,20]. Fig. 5 shows the required CO_2/CH_4 ratio at the boundary of carbon formation for the SOFC-O^{2-} at different temperatures and extent of electrochemical reaction of hydrogen (e). Lower CO_2/CH_4 is required for the SOFC-O^{2-} compared to that of the conventional reformer due to the presence of electrochemical water in the anode chamber. The difference was particularly pronounced at for a higher extent of the electrochemical reaction. For the SOFC-H^+, at moderate operating temperatures (T = 800–1000 K) when the extent of the electrochemical reaction (e) was increased, the lower CO_2/CH_4 ratio was sufficient to alleviate carbon formation as shown in Fig. 6(a). However, the opposite trend was observed at higher operating temperatures (T > 1000 K) as shown in Fig. 6(b). The trend at lower operating temperatures was quite unusual as it has been reported earlier for the systems of the steam reforming of methane [11] and methanol [12] that a higher H_2O/fuel ratio was required at the higher extent of electrochemical reaction because hydrogen was consumed and no benefit of electrochemical water was realized in the anode gas mixture in the SOFC-H^+. In addition, there was a general concern in using a membrane reactor for dehydrogenation reactions where the carbon formation problem could be more severe due to the removal of hydrogen from the reaction system. Therefore, it is likely that for the SOFC-H^+, more carbon dioxide would be needed when the extent of the electrochemical reaction is higher in the dry reforming system.

To explain the reasons for the unusual behavior of the dry reforming of methane in the SOFC-H^+ at moderate temperatures (800–1000 K), the moles of each species at different CO_2/CH_4 ratios at T = 900 K for the conventional reactor (Fig. 2) and the SOFC-H^+ (Fig. 3(b)) were compared. Note that because the carbon activity of all the possible carbon formation reactions provided the same value when the gas mixtures are at their equilibrium conditions, for simplicity the carbon activity based on the Boudard reaction (Eq. (19)) is considered as an example for understanding the behavior of the system when carbon dioxide is added to the system. From the figures, when hydrogen was electrochemically removed from the anode gas mixture, the dry

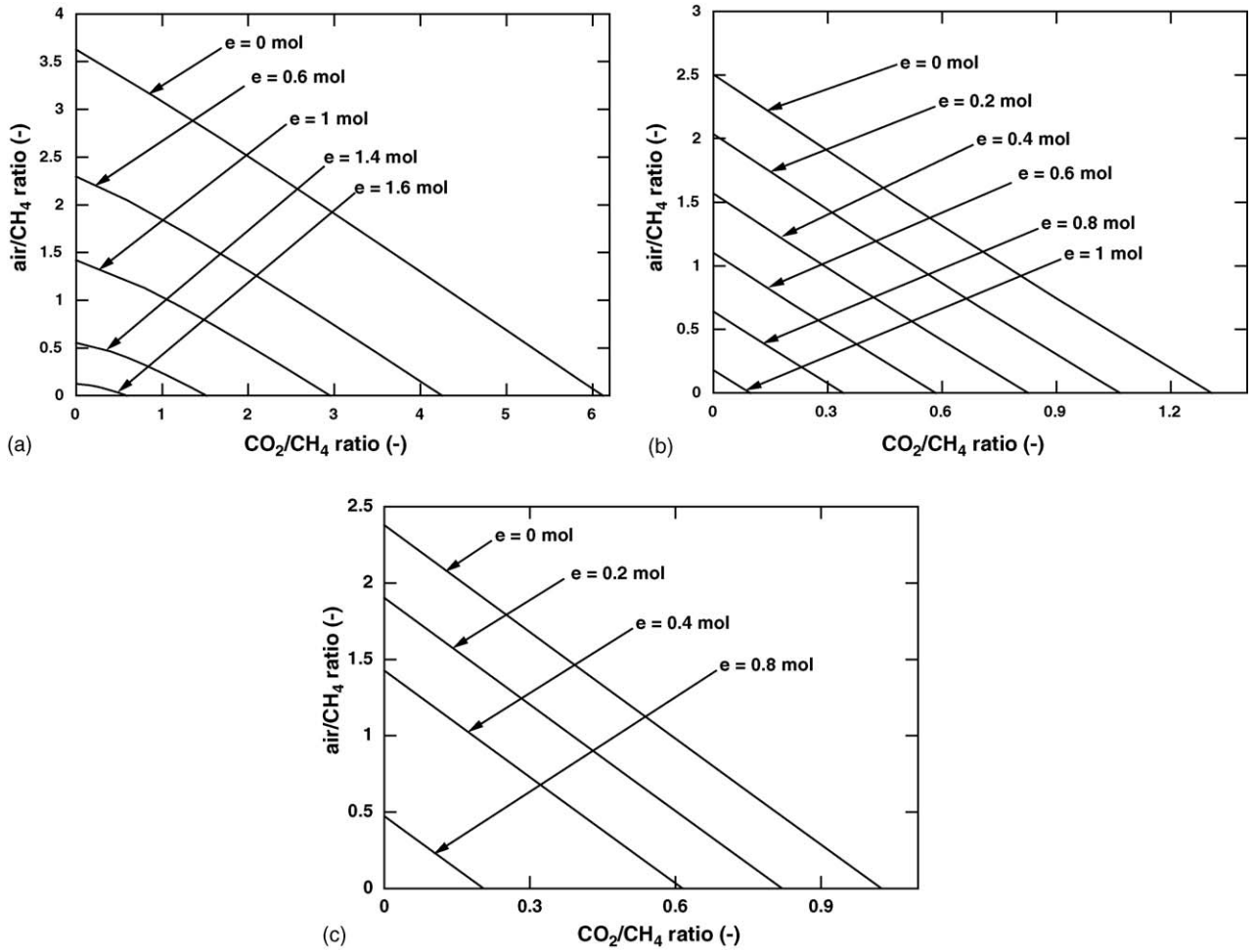

Fig. 9. Required inlet air/CH_4 ratio at different inlet CO_2/CH_4 ratios: (a) T = 900 K, (b) T = 1050 K and (c) T = 1200 K (SOFC-O^{2-}, a = 1 mol and P = 101.3 kPa).

reforming of methane moved forward, resulting in a low content of CH_4 in the gas mixture. It is observed that the moles of CO in the gas mixture for the SOFC-H^+ were less dependent on the CO_2/CH_4 ratio than for the conventional reactor because the RWGS played a less significant role when smaller amounts of hydrogen was present in the system. Consequently, the value of the carbon activity ($K_1 p_{CO}^2/p_{CO_2}$) for the SOFC-H^+ decreased with increase of the CO_2/CH_4 ratio more rapidly than that for the conventional reactor and, therefore, reached the boundary of carbon formation ($\alpha_c = 1$) at a lower value of CO_2/CH_4 ratios.

In practical operation, carbon dioxide is unlikely to be added to the system to suppress carbon formation. Other components such as water and air are more practical additive choices. The calculations were carried out to find the required H_2O/CH_4 or air/CH_4 ratio for different inlet CO_2/CH_4 ratios, the extent of the electrochemical reaction and the operating temperature. This information is important for selecting a suitable feed composition which avoids the carbon formation problem. Figs. 7 and 8 show the H_2O/CH_4 ratio at the boundary of carbon formation for different CO_2/CH_4 ratios in the feed for SOFC-O^{2-} and SOFC-H^+, respectively. It was found that for the SOFC-O^{2-}, the required H_2O/CH_4 ratio decreased with the increases of inlet CO_2/CH_4 ratio, extent of electrochemical reaction and operating temperature. The operation at a high extent of the electrochemical reaction and high temperature significantly reduced the risk of carbon formation. For the SOFC-H^+, the required H_2O/CH_4 ratio also decreased with increase of the inlet CO_2/CH_4 ratio and operating temperature. Higher H_2O/CH_4 ratios were required at higher extents of the electrochemical reaction. However, the reverse trend was observed when the system was operated at a moderate operating temperature ($T = 900$ K) with high inlet CO_2/CH_4 ratio (approximately higher than 1.5) which is in good agreement with the previous case in which only carbon dioxide was used as the carbon suppresser. When comparing between the required H_2O/CH_4 ratio for the case with no carbon dioxide present in the inlet feed (CO_2/CH_4 ratio = 0) and the required CO_2/CH_4 of the case without the addition of water for both SOFC-O^{2-} and SOFC-H^+, it is clear that water showed a more pronounced influence on inhibiting the carbon formation than carbon dioxide particularly at low operating temperatures. The results also revealed that for the SOFC-H^+ the extent of the electrochemical reaction had no significant effect on the required H_2O/CH_4 ratio at high temperatures. It should be noted that when comparing between the dry reforming and the steam reforming of methane with addition of carbon dioxide and water, respectively, as the components for inhibiting the carbon formation, the addition of water always provided a beneficial effect to the system as water reacted with methane to reduce the extent

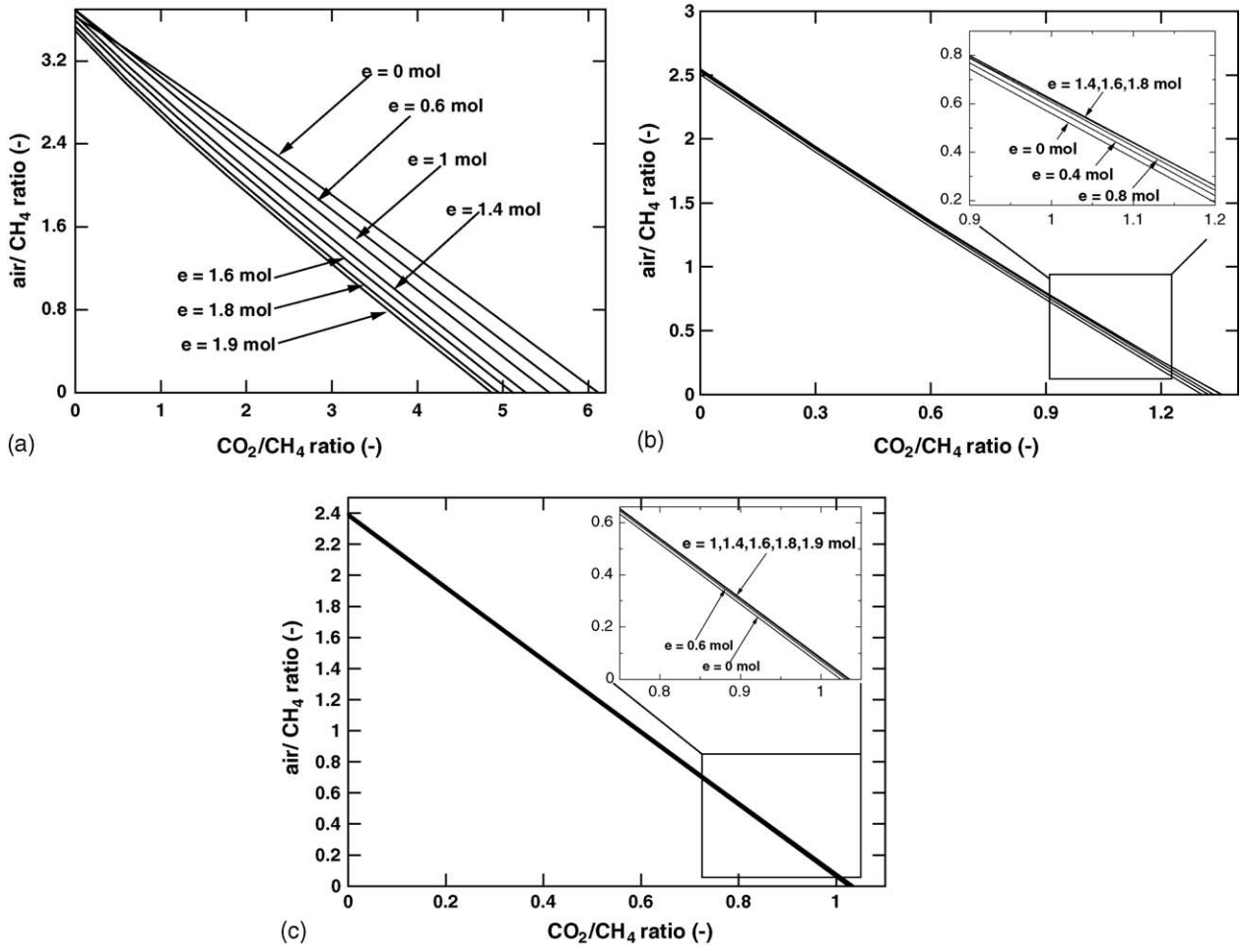

Fig. 10. Required inlet air/CH_4 ratio at different inlet CO_2/CH_4 ratios: (a) $T = 900$ K, (b) $T = 1050$ K and (c) $T = 1200$ K (SOFC-H^+, $a = 1$ mol and $P = 101.3$ kPa).

of methane and with carbon monoxide to reduce the extent of carbon monoxide, forming hydrogen and carbon dioxide. The presence of high amounts of carbon dioxide, hydrogen and water was important in preventing the carbon formation in the system. For the case of addition of carbon dioxide, although extra carbon dioxide promoted the consumption of methane from the dry reforming reaction, unlike water, carbon dioxide did not help reduce the extent of carbon monoxide in the system. In addition, more carbon monoxide could be generated by the RWGS reaction.

When air is used as an alternative oxidant for preventing carbon formation, oxygen in air can react with methane, carbon monoxide or hydrogen whose products are beneficial for preventing the carbon formation. Figs. 9 and 10 show the required air/CH_4 ratios for the SOFC-O^{2-} and SOFC-H^+, respectively. It was found that the similar trend as that of the addition of water was observed for both cases. It should be noted that, the advantage of air addition, that although the presence of nitrogen diluted the partial pressure of hydrogen in the anode gas mixture, which resulted in lower fuel cell performance, the exothermic heat from the oxidation reactions was useful for the endothermic dry reforming reaction in the system.

4. Conclusion

Thermodynamic analysis was employed to predict the boundary of carbon formation for DIR-SOFCs. The required CO_2/CH_4 ratio to prevent carbon formation has been determined by varying the operating temperature, electrolyte type and the extent of the electrochemical reaction. Operation at high temperatures dramatically reduced the required inlet CO_2/CH_4 ratio. The benefit of the presence of electrochemical H_2O in the anode chamber on suppression of carbon formation was realized in the SOFC-O^{2-} which resulted in a lower requirement for the CO_2/CH_4 ratio. For the SOFC-H^+, due to the disappearance of H_2 without gaining the benefit of the electrochemical H_2O in the anode chamber, a higher CO_2/CH_4 ratio was necessary. However, at moderate temperatures ($T = 800$–1000 K) an unexpected and opposite trend was observed. The additions of water and air to a feed with a certain inlet CO_2/CH_4 ratio were considered as alternative strategies for suppressing the carbon formation. Water was a more effective choice than CO_2 particularly at low temperatures. Although air is less attractive to water, the benefit of the exothermic heat from the reactions with oxygen may make the system more practical.

It should be noted that although the thermodynamic calculations can be used to predict the boundary of carbon formation, the deactivation of the anode is not solely the result of the deposition of carbon. Deposition of other forms of carbonaceous compounds such as polymeric coke (C_nH_m) may result in comparable damage. Therefore, the results obtained in this study should be considered only as a crude guideline for selecting suitable operating conditions for SOFCs and other related reactors.

Acknowledgements

This research is financially supported by the Thailand Research Fund and Ministry of University Affairs. The support from Professor Piyasan Praserthdam is also gratefully acknowledged.

References

[1] S.L. Douvartzides, F.A. Coutelieris, K. Demin, P.E. Tsiakaras, AIChE J. 49 (2003) 248–257.
[2] L.F. Brown, Int. J. Hydrogen Energy 26 (2001) 381–397.
[3] G. Maggio, S. Freni, S. Cavallaro, J. Power Sources 74 (1998) 17–23.
[4] S.H. Clarke, A.L. Dicks, K. Pointon, T.A. Smith, A. Swann, Catal. Today 38 (1997) 411–423.
[5] C.M. Finnerty, R.M. Ormerod, J. Power Sources 86 (2000) 390–394.
[6] S. Park, R.J. Gorte, J.M. Vohs, Appl. Catal. A 200 (2000) 55–61.
[7] C.M. Finnerty, N.J. Coe, R.H. Cunningham, R.M. Ormerod, Catal. Today 46 (1998) 137–145.
[8] L. Topor, L. Bejan, E. Ivana, N. Georgescu, Rev. Chim. Bucharest 30 (1979) 539.
[9] T.A. Chubb, Sol. Energy 24 (1980) 341.
[10] T.A. Chubb, J.H. McCrary, G.E. McCrary, J.J. Nemecek, D.E. Simmons, Proc. Meet. Am. Sect. Int. Sol. Eng. Soc. 4 (1981) 166.
[11] W. Sangtongkitcharoen, S. Assabumrungrat, V. Pavarajarn, N. Laosiripojana, P. Praserthdam, J. Power Sources 142 (2005) 75–80.
[12] S. Assabumrungrat, N. Laosiripojana, V. Pavarajarn, W. Sangtongkitcharoen, A. Tangjitmatee, P. Praserthdam, J. Power Sources 139 (2005) 55–60.
[13] J.H. Edwards, A.M. Maitra, Fuel Proc. Tech. 42 (1995) 269.
[14] J.R. Rostrup-Nielsen, J.H.B. Hansen, J. Catal. 144 (1993) 38.
[15] T. Sodesawa, A. Dobashi, F. Nozaki, React. Kinet. Catal. Lett. 12 (1979) 107.
[16] J.H. Hirschenhofer, D.B. Stauffer, R.R. Engleman, M.G. Klett, Fuel Cell Handbook, fourth ed., Parsons Corporation, Reading, 1998, p. 2.
[17] P. Pietrogrande, M. Bezzeccheri, in: L.J.M.J. Blomen, M.N. Mugerwa (Eds.), Fuel Cell Systems, Plenum Press, New York, 1993, p. 142.
[18] L.F. Brown, Int. J. Hydrogen Energy 26 (2001) 381–397.
[19] J.R. Grace, X. Li, C.J. Lim, Catal. Today 64 (2001) 141–149.
[20] S. Nagata, A. Momma, T. Kato, Y. Kasuga, J. Power Sources 101 (2001) 60–71.

Appendix 6

Available online at www.sciencedirect.com
ScienceDirect
Journal of Power Sources 167 (2007) 139–144
JOURNAL OF POWER SOURCES
www.elsevier.com/locate/jpowsour

Short communication

Improvement of solid oxide fuel cell performance by using non-uniform potential operation

S. Vivanpatarakij [a], S. Assabumrungrat [a,*], N. Laosiripojana [b]

[a] *Center of Excellence in Catalysis and Catalytic Reaction Engineering, Department of Chemical Engineering, Faculty of Engineering, Chulalongkorn University, Bangkok 10330, Thailand*

[b] *The Joint Graduate School of Energy and Environment, King Mongkut's University of Technology Thonburi, Bangkok 10140, Thailand*

Received 7 November 2006; received in revised form 6 February 2007; accepted 6 February 2007
Available online 21 February 2007

Abstract

Theoretical study was carried out to investigate the possible improvement of SOFC performance by using a non-uniform potential operation (SOFC-NUP) in which the operating voltage was allowed to vary along the cell length. Preliminary results of a simple SOFC-NUP with a cell divided into two sections of equal size in term of range of fuel utilization (U_f) indicated that the SOFC-NUP can offer higher power density than an SOFC with uniform potential operation (SOFC-UP) without a reduction of the electrical efficiency. In this work, voltages and section splits were optimized to obtain the maximum power density of the SOFC-NUP. At the optimum splits ($S_{p,1} = 0.55$ and $S_{p,2} = 0.45$), the power density improvement as high as 9.2% could be achieved depending on the level of electrical efficiency. It was further demonstrated that the increase in the number of separated section (n) of the cell could increase the achieved maximum power density but the improvement became less pronounced after $n > 3$.

Keywords: SOFC; Non-uniform potential; Power generation

1. Introduction

Fuel cells are promising electrochemical devices that convert the chemical energy of a fuel directly into electrical energy. Compared to conventional power generation processes, fuel cells are attractive due to their better environmental friendliness, practical noise-free operation, and higher efficiency. A number of researches have been carried out in many directions with a major aim to improve performances of the fuel cells and their systems. For instance, several gas turbine cycles such as steam injected gas turbine cycle, gas turbine/steam turbine combined cycle, and humid air turbine cycle have been combined with solid oxide fuel cell (SOFC) for efficiency improvement [1]. An operation with anodic offgas recirculation was proposed for a polymer electrolyte membrane fuel cell (PEMFC) system equipped with a fuel processor. Under this operation, a significant efficiency increase for the fuel processor and the gross efficiency of the combined system of 30% were reported [2]. A novel gas distributor with current-collecting elements distributed in gas-delivery fields for effective current collection and heat/mass transfer enhancement was designed to improve power density [3,4]. In addition, many researches have been devoted on development of cell components with superior characteristics [5–7]. The performance improvement of PEMFC from operation at a higher pressure was reported although the power loss due to air compression was taken into account in the comparisons [8].

Among several procedures for improving fuel cell performance, the use of non-uniform potential operation concept for fuel cells in which the cell voltage is allowed to vary along the cell length is another interesting approach. However, until now only some works have focused on the potential benefits of this approach. It was demonstrated that an improvement in electrical efficiency of about 1% could be achieved by splitting the cell of a molten carbonate fuel cell (MCFC) into two sections [9]. Selimovic and Plasson [10] examined performances of networked solid oxide fuel cell (SOFC) stacks combined with a gas turbine cycle. Two multistage configurations, i.e. (i) both anode and cathode flows were serially connected and (ii) only the anode

* Corresponding author. Tel.: +66 2 216 6868; fax: +66 2 218 6877.
E-mail address: Suttichai.A@chula.ac.th (S. Assabumrungrat).

0378-7753/$ – see front matter © 2007 Elsevier B.V. All rights reserved.
doi:10.1016/j.jpowsour.2007.02.026

Nomenclature

a	constant in Eq. (11) (Ω m)
A	area (m^2)
b	constant in Eq. (11) (K)
E	activation polarization energy in Eqs. (12) and (13) (kJ mol^{-1})
E_0	open circuit voltage (V)
F	Faraday constant (96485.34) (C mol^{-1})
i	current density (A m^{-2})
LHV	lower heating value of methane feed (W)
m	constant polarization parameters in Eqs. (12) and (13)
n	number of separated section
p	partial pressure (atm)
P	power density (W cm^{-2})
r	activation polarization parameters in Eqs. (12) and (13) (A m^{-2})
R	universal gas constant (8.31447×10^{-3}) (kJ mol^{-1} K^{-1})
S_p	section split
T	absolute temperature (K)
U_f	fuel utilization (%)
V	operating voltage (V)
W	electrical work (W)

Greeks letters

δ	thickness (m)
ε	electrical effiency (%)
η	overpotential (Ω m^2)
φ	potential (V)
ρ	specific ohmic resistance (Ω m)

Subscript

A	anode
Act	activation
C	cathode
Conc	concentration
k	section number
Ohm	ohmic

flow was serially connected while the cathode flow was parallel connected, were considered. An increase of system efficiency of about 5% was reported for the former configuration mainly due to an improved thermal management. The similar multi-stage configurations were also considered for a combined heat and power MCFC plant [11]. Detailed flowsheet calculations showed that the improvement in efficiency was about 0.6% for the former configuration, and 0.8% for the latter configuration. The concept was also extended to PEMFCs divided into many stages (or stacks) of equal size [12]. It was demonstrated that the non-uniform cell potential operation allowed for enhanced maximum power densities compared to the traditional concept involving a uniform cell potential distribution. The improvement within 6.5% was reported.

In this study, the concept of non-uniform potential operation implemented to SOFCs fed by methane was investigated in an effort to optimize cell operating voltages and sizes so that a maximum power density could be achieved without a reduction of electrical efficiency. Values of power density of a simple SOFC with a cell divided into two sections whose operating voltages and sizes were allowed to vary were compared to those of a typical SOFC with uniform cell potential at various electrical efficiencies. Additionally, the effect of number of cell section on the obtained performance was determined.

2. Theory

The schematic diagram of an SOFC with non-uniform potential operation (SOFC-NUP) is illustrated in Fig. 1. Compositions of fuel and air streams change along the cell channel according to changes in value of fuel utilization defined as the mole of hydrogen electrochemically consumed divided by the theoretical mole of hydrogen generated from complete reforming of the methane feed. In section k, the fuel utilization changes from $U_{f,k-1}$ to $U_{f,k}$, and the cell is operated at a constant potential of V_k within the section. In practice, the non-uniform cell potential can be realized by using segmented current collectors for a single-cell SOFC or it can be carried out in a series of SOFC stacks operated at different stack potentials. The section split of section k ($S_{p,k}$) is defined by

$$S_{p,k} = \frac{U_{f,k} - U_{f,k-1}}{U_{f,final}} \quad (1)$$

When the SOFC is fed by a non-hydrogen fuel (e.g. methane), a reformer is generally required to reform the fuel with an oxidant (e.g. steam) to a hydrogen-rich stream before feeding to the SOFC stack. The main reactions involved in the production of hydrogen from methane and steam are the methane steam reforming and water gas shift reactions as shown in Eqs. (2) and (3), respectively.

$$CH_4 + H_2O = 3H_2 + CO \quad (2)$$

$$CO + H_2O = H_2 + CO_2 \quad (3)$$

In the SOFC stack, both hydrogen and CO can react electrochemically with oxygen. However, it is assumed that the CO electro-oxidation is neglected. It was estimated earlier that about 98% of current is produced by H_2 oxidation in common situations [13]. This is due to the fast rate of water gas shift reaction at an SOFC operating temperature. The electrochemical reactions of hydrogen and oxygen take place according to Eqs. (4) and (5).

$$\text{Anode}: \quad H_2 + O^{2-} = H_2O + 2e^- \quad (4)$$

$$\text{Cathode}: \quad O_2 + 4e^- = 2O^{2-} \quad (5)$$

Electromotive force (E_0) of the cell is a difference of potentials between both electrodes of the cell. It can be represented as follows:

$$E_0 = |\varphi_C - \varphi_A| \quad (6)$$

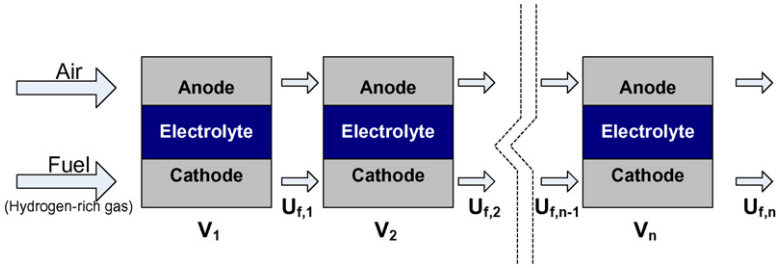

Fig. 1. Schematic diagrams of SOFC-NUP.

where φ_C and φ_A are the potentials of the cathode and the anode, respectively. The electrode potential can be calculated from Nernst equation which can be expressed as follows:

$$\varphi = \left(\frac{RT}{4F}\right) \ln p_{O_2} \tag{7}$$

where R is the universal gas constant, T the absolute temperature and F is the Faraday's constant. The partial pressure of oxygen in the cathode chamber is calculated from its mole fraction while the partial pressure of oxygen in the anode chamber is given by:

$$p_{O_2} = \left(\frac{p_{H_2O}}{K p_{H_2}}\right)^2 \tag{8}$$

where p_i is the partial pressure, and K is the equilibrium constant of the hydrogen oxidation reaction.

When the SOFC is operated at a potential of V_k, the local current density can be determined according to Eq. (9). It should be noted that as the value of E_0 changes along the cell length within the section due to the change in gas compositions, the current density varies within the cell section.

$$i = \frac{E_0 - V_k}{\eta_{Ohm} + \eta_{Act,A} + \eta_{Act,C} + \eta_{Conc,A} + \eta_{Conc,C}} \tag{9}$$

where

$$\eta_{Ohm} = \sum \rho_j \delta_j \tag{10}$$

$$\rho_j = a_j \exp(b_j T) \tag{11}$$

$$\eta_{Act,C} = \left(\frac{4F}{RT} r_C \left(\frac{p_{O_2}}{p}\right)^m \exp\left(\frac{-E_C}{RT}\right)\right)^{-1} \tag{12}$$

$$\eta_{Act,A} = \left(\frac{2F}{RT} r_A \left(\frac{p_{H_2}}{p}\right)^m \exp\left(\frac{-E_A}{RT}\right)\right)^{-1} \tag{13}$$

The parameters used in the calculations are provided in Table 1 [14] and Table 2 [15]. It was reported that the correlations of the activation polarization can predict the cell performance close to the Butler–Volmer equation within the temperature range of 1173–1273 K [16]. In this study, the operating temperature is kept at 1173 K which is in the reliable limit.

To simplify the calculations of the SOFC performance, it is assumed that both fuel and oxidant are well-diffused through the surface of the electrodes. Therefore, concentration polarization losses ($\eta_{Conc,A}$ and $\eta_{Conc,C}$) can be omitted. This assumption is valid when the cell is not operated at too high current density or too low concentration. In addition, it is further assumed that the cell is operated at isothermal condition and the fuel stream is always at its equilibrium composition along the length of the SOFC cell. It should be noted that an external reformer is usually connected to the SOFC system in order to generate hydrogen-rich feed for the stack and to suppress the cell deactivation due to the carbon formation. In addition, state-of-the-art SOFC nickel cermet anodes are usually active for the steam reforming and shift reactions particularly at high operating temperature of SOFC [16,17]. Calculations of the thermodynamic equilibrium composition are accomplished by following details given in our previous work [18].

Table 1
Resistivity and thickness of cell component [12]

Material used	Ni–YSZ/YSZ/LSM–YSZ
Anode thickness (μm)	150
Anode ohmic resistance constant	$a = 0.0000298$, $b = -1392$
Cathode thickness (μm)	2000
Cathode ohmic resistance constant	$a = 0.0000811$, $b = 600$
Electrolyte thickness (μm)	40
Electrolyte ohmic resistance constant	$a = 0.0000294$, $b = 10350$
Interconnect thickness (μm)	10
Interconnect ohmic resistance constant	$a = 0.001256$, $b = 4690$

When the current density is known, the cell area (A_k) and electrical power (W_k) involved in each cell section can be determined. The values of overall electrical efficiency (ε) and average power density (P) can be determined according to Eqs. (14) and (15), respectively.

$$\varepsilon = \sum_{k=1}^{n} \frac{W_k}{LHV} \times 100\% \tag{14}$$

$$P = \frac{\sum_{k=1}^{n} W_k}{\sum_{k=1}^{n} A_k} \tag{15}$$

where LHV is the lower heating value of methane feed.

Table 2
Summary of activation polarization parameters [13]

	r (A m^{-2})	$E_{A,pol}$ (kJ mol^{-1})	m
Cathode	1.489×10^{10}	160	0.25
Anode	2.128×10^{8}	110	0.25

3. Results and discussion

Fig. 2 shows the performances of a typical SOFC with uniform potential operation (SOFC-UP). Each line represents the results at a constant value of fuel utilization (U_f). It should be noted that because concentration polarization becomes an importance loss at high current densities and small fuel concentrations ($U_f \geq 80\%$) [15], the simulations were performed only in the ranges of high voltages (low current densities) and fuel utilizations (U_f) of lower than 80%. In order to validate the calculations, the simulation results from a previous literature [19] at a condition close to our work ($U_f = 85\%$) are included in Fig. 2. Our calculations show good agreement within a range of high operating voltages (0.65–0.75 V). However, at lower voltages, the data from the literature shows higher power density. This is probably due to the observed temperature increase (within 100 K) which is particularly pronounced at high current density (low voltage) whereas our calculations were based on the isothermal condition. From Fig. 2, regarding the electrical efficiency, it is favorable to operate the SOFC at high voltage in order to obtain high efficiency. However, when taking into account the power density, operation at a high value of voltage is not practical due to the achievement of low power density. Therefore, in practice suitable operating voltage and fuel utilization should be carefully selected. Some workers suggested to operate the cell at 70% of maximum power density [20] and fuel utilization of 80–95% [21–24]. In the present work, the fuel utilization (U_f) of 80% was considered and SOFC with non-uniform potential operation (SOFC-NUP) was investigated with the aim to improve the power density without lowering the electrical efficiency.

Fig. 3 shows the relationship between power density and electrical efficiency of a simple SOFC-NUP with a cell divided into two sections of equal range of fuel utilization ($S_{p,1} = S_{p,2} = 0.5$). V_1 and V_2 represent the operating voltages of sections 1 and 2, respectively. The thick solid line indicates the results of the SOFC-UP. It is indicated that there are some ranges of operation in which the SOFC-NUP offers higher power density than the SOFC-UP without lowering the electrical efficiency (area above of the thick solid line). The improvement becomes significant when the cell is operated at high electrical efficiency.

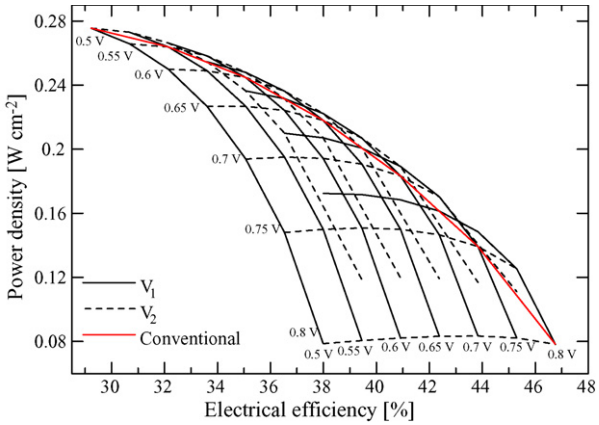

Fig. 3. Relationship between power density and electrical efficiency of SOFC-UP and SOFC-NUP ($U_f = 80\%$ and $T = 1173$ K; for SOFC-NUP: $n = 2$, $S_{p,1} = 0.5$).

In order to indicate suitable operating voltages which offer the highest average power density, the value of electrical efficiency was specified and the value of V_1 was varied. Then V_2, which gives the desired value of the electrical efficiency, and its corresponding power density can be calculated. For example, as shown in Fig. 4, for an electrical efficiency of 43%, the values of V_2 are 0.623, 0.673 and 0.723 V for $V_1 = 0.7$, 0.75 and 0.80 V, respectively, and the corresponding values of the power density are 0.178, 0.156 and 0.159 W cm^{-2}, respectively. By varying V_1, the maximum power density of 0.162 W cm^{-2} is obtained at $V_1 = 0.773$ V and $V_2 = 0.700$ V.

According to the above study, the section splits were maintained at $S_{p,1} = S_{p,2} = 0.5$. Those values were then adjusted in order to achieve better performance. Fig. 5 shows the effect of section split ($S_{p,1}$) on the power density improvement at different values of electrical efficiency. It should be noted that the reported values are based on the operation using optimum voltages for each value of the section split. It was found that the power density improvement as high as 9.2% can be achieved at the electrical efficiency of 45% but the improvement becomes less significant when the SOFC is operated at lower electrical efficiency. In addition, the optimum $S_{p,1}$ for all cases was found

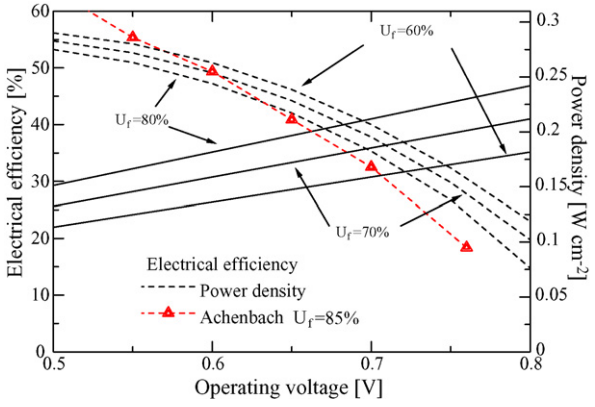

Fig. 2. Performance characteristic curves of typical SOFC-UP (H_2O/CH_4 ratio = 2.2 and $T = 1173$ K).

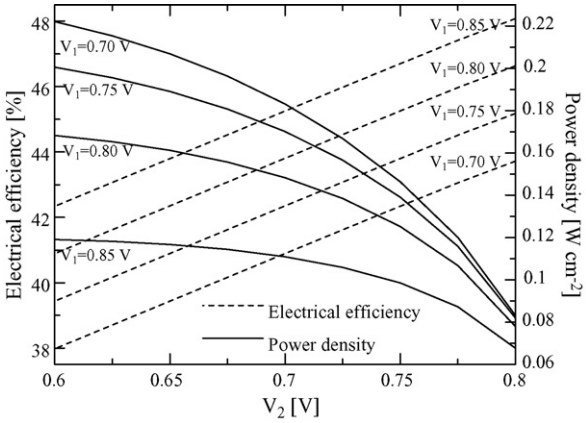

Fig. 4. Effect of operating voltages on performance of SOFC-NUP ($n = 2$, $U_f = 80\%$, $T = 1173$ K, $S_{p,1} = 0.5$ and $S_{p,2} = 0.5$).

Table 3
Comparison of power density between SOFCs with different number of section and section splits

Electrical efficiency (%)	Power density (W cm^{-2})			
	$n=1$	$n=2$ ($S_{p,1}=S_{p,2}=0.5$)	$n=2$ ($S_{p,1}=0.55$, $S_{p,2}=0.45$)	$n=3$ ($S_{p,1}=S_{p,2}=S_{p,3}=(1/3)$)
35	0.246 (0.598 V)	0.248 (0.619, 0.571 V)	0.249 (0.631, 0.560 V)	0.250 (0.644, 0.608, 0.544 V)
37	0.229 (0.632 V)	0.232 (0.669, 0.598 V)	0.232 (0.666, 0.594 V)	0.233 (0.682, 0.632, 0.583 V)
40	0.196 (0.683 V)	0.201 (0.721, 0.649 V)	0.201 (0.717, 0.645 V)	0.202 (0.740, 0.666, 0.647 V)
43	0.154 (0.734 V)	0.162 (0.7726, 0.7001 V)	0.162 (0.768, 0.697 V)	0.164 (0.782, 0.736, 0.688 V)
45	0.120 (0.768 V)	0.131 (0.8069, 0.7342 V)	0.131 (0.803, 0.731 V)	0.134 (0.817, 0.772, 0.720 V)

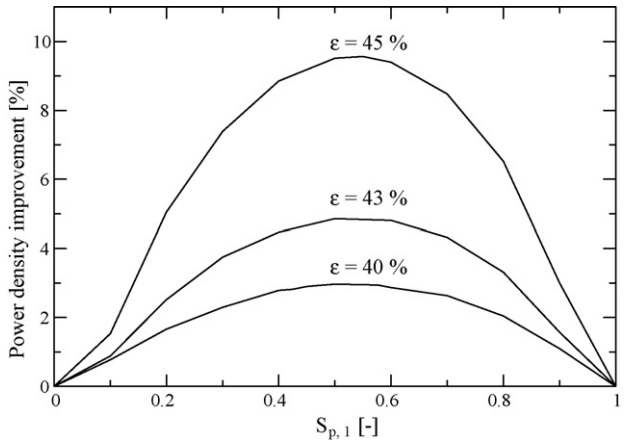

Fig. 5. Effect of section split on power density improvement of SOFC-NUP ($n=2$, $U_f=80\%$ and $T=1173$ K).

to be around 0.55. Table 3 summarizes the values of the power density and the corresponding optimum voltages at different electrical efficiency of the SOFC-UP and the SOFC-NUPs with $S_{p,1}=S_{p,2}$ and with the optimum $S_{p,1}$ and $S_{p,2}$. It was found that the results of the SOFC-NUP with the optimum $S_{p,1}$ and $S_{p,2}$ are not significantly different from those of the SOFC-NUP with $S_{p,1}=S_{p,2}$ although the voltages are different.

To further enhance the performance of the SOFC-NUP, the number of separated section (n) was increased. Fig. 6 shows the effect of the number of section on the power density improvement for three values of electrical efficiency. The section splits of all sections are specified to be at the same value of $S_{p,k}=1/n$ in order to simplify the calculations. The optimum voltages of the SOFC-NUPs which offer the highest power density for each case were determined by following the procedure described earlier for the case with $n=2$. It was assumed that the maximum power density achieved from the case with adjustable section splits does not significantly differ from that achieved from the case with equally divided sections. This assumption is valid at least for the case of the SOFC-NUP with $n=2$ as shown earlier. The calculated results indicate that the obtained maximum power density increases with increasing the number of sections (n). However, the improvement becomes less significant after $n>3$. The SOFC-NUP with $n=3$ is likely to be a suitable system for improving the power density without the reduction of electrical efficiency. Table 3 also shows the values of the maximum power density and the corresponding voltages at different values of electrical efficiency. At the electrical efficiency of 45%, the power density of the SOFC-NUP with $n=3$ is 11.7% higher than that of the typical SOFC-UP.

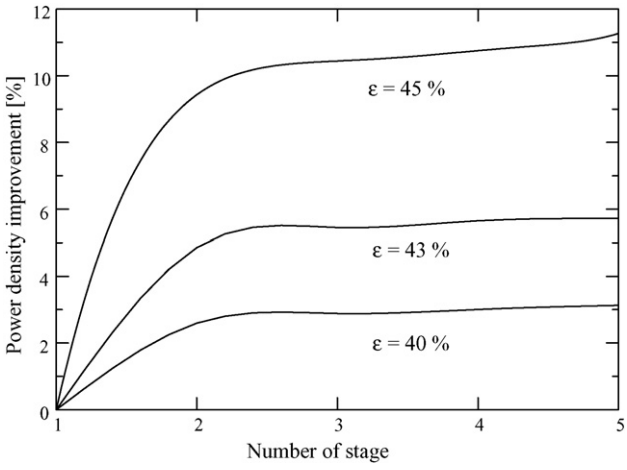

Fig. 6. Effect of number of stage on power density improvement of SOFC-NUP ($U_f=80\%$, $T=1173$ K and $S_{p,k}=1/n$).

From the above results, it has been demonstrated that the use of the non-uniform potential operation with SOFC is technically feasible. The cell area can be reduced without lowering the electrical efficiency. However, the SOFC-NUP would require more sophisticated cell arrangement, power conditioning system and so on. The system control would inevitably become more complicated. Further investigations are required before implementing this system for commercial use.

4. Conclusions

An SOFC-NUP can provide higher power density than a typical SOFC-UP without a reduction of electrical efficiency. The optimum SOFC-NUP was determined by allowing the operating voltage and section split of each section to be appropriately adjusted to achieve the highest power density for each level of electrical efficiency. The maximum power density can be further improved by increasing the number of separated section (n) of the cell; however, it became less pronounced after $n>3$. Although it is obvious that the non-uniform operation can allow the SOFC to be operated at higher performance, further investigation is necessary to determine whether the cost reduction by the reduced stack size would be sufficiently attractive compared to the increases of power conditioning cost and complication of the SOFC operation.

Acknowledgements

The supports from The Thailand Research Fund and Commission on Higher Education are gratefully acknowledged. The second author also would like to acknowledge kind supports from Professor Piyasan Praserthdam.

References

[1] P. Kuchonthara, S. Bhattacharya, A. Tsutsumi, J. Power Sources 124 (2003) 65–75.
[2] A. Heinzel, J. Roes, H. Brandt, J. Power Sources 145 (2005) 312–318.
[3] P.W. Li, S.P. Chen, M.K. Chyu, J. Power Sources 140 (2005) 311–318.
[4] Y.G. Yoon, W.Y. Lee, G.G. Park, T.H. Yang, C.S. Kim, Electrochim. Acta 50 (2004) 709–712.
[5] S.P. Yoon, J. Han, S.W. Nam, T.H. Lim, S.A. Hong, J. Power Sources 136 (2004) 30–36.
[6] S.D. Kim, S.H. Hyun, J. Moon, J.H. Kim, R.H. Song, J. Power Sources 139 (2005) 67–72.
[7] S.P. Simner, J.F. Bonnett, N.L. Canfield, K.D. Meinhardt, J.P. Shelton, V.L. Sprenkle, J.W. Stevenson, J. Power Sources 113 (2003) 1–10.
[8] A. Kazim, J. Power Sources 143 (2005) 9–16.
[9] F. Standeart, Analytical fuel cell modelling and exergy analysis of fuel cells, Ph.D. Thesis, Delft University of Technology, 1998.
[10] A. Selimovic, J. Palsson, J. Power Sources 106 (2002) 76–82.
[11] S.F. Au, N. Woudstra, K. Hemmes, J. Power Sources 122 (2003) 28–36.
[12] S.M. Senn, D. Poulikakos, Electrochem. Commun. 7 (2005) 773–780.
[13] M.A. Khaleel, Z. Lin, P. Singh, W. Surdoval, D. Collin, J. Power Sources 130 (2004) 136–148.
[14] S.H. Chan, C.F. Low, O.L. Ding, J. Power Source 103 (2002) 188–200.
[15] E. Hernandez-Pacheco, D. Singh, P.N. Hutton, N. Patel, M.D. Mann, J. Power Sources 138 (2004) 174–186.
[16] S.H. Clarke, A.L. Dicks, K. Pointon, T.A. Smith, A. Swann, Catal. Today 38 (1997) 411–423.
[17] A.L. Dicks, J. Power Sources 71 (1998) 111–122.
[18] W. Sangtongkitcharoen, S. Assabumrungrat, V. Pavarajarn, N. Laosiripojana, P. Praserthdam, J. Power Source 142 (2005) 75–80.
[19] E. Achenbach, J. Power Sources 49 (1994) 333–348.
[20] A.K. Demin, P. Tsiakaras, E. Gorbova, S. Hramova, J. Power Sources 131 (2004) 231–236.
[21] J.R. Rostrup-Nielsen, Phys. Chem. Chem. Phys. 3 (2001) 283–288.
[22] S. Campanari, J. Power Sources 92 (2001) 26–34.
[23] E. Riensche, U. Stimming, G. Unverzagt, J. Power Sources 73 (1998) 251–256.
[24] A. Criscuoli, A. Basile, E. Drioli, O. Loiacono, J. Membr. Sci. 181 (2001) 21–27.

Appendix 7

ELSEVIER

Chemical Engineering Journal 138 (2008) 436–441

Chemical Engineering Journal

www.elsevier.com/locate/cej

Performance analysis of methanol-fueled solid oxide fuel cell system incorporated with palladium membrane reactor

W. Sangtongkitcharoen [a], S.Vivanpatarakij [a], N. Laosiripojana [b], A. Arpornwichanop [c], S. Assabumrungrat [a,*]

[a] *Center of Excellence in Catalysis and Catalytic Reaction Engineering, Department of Chemical Engineering, Faculty of Engineering, Chulalongkorn University, Bangkok 10330, Thailand*

[b] *The Joint Graduate School of Energy and Environment, King Mongkut's University of Technology Thonburi, Bangkok 10140, Thailand*

[c] *Control and Systems Engineering, Department of Chemical Engineering, Faculty of Engineering, Chulalongkorn University, Bangkok 10330, Thailand*

Received 3 January 2007; received in revised form 8 June 2007; accepted 25 June 2007

Abstract

The paper presents preliminary results from the performance analysis of a methanol-fueled solid oxide fuel cell (SOFC) system incorporated with a palladium membrane reactor. A conventional SOFC system comprises major components of preheaters, a reformer, an SOFC unit and a burner. The performance of the SOFC unit was dependent on operating current density, fuel utilization and temperature. When the conventional reformer is replaced by a palladium membrane reactor, pure hydrogen is extracted from the reformed gas and fed to the anode of the SOFC unit. It was demonstrated that the incorporation of the palladium membrane reactor to the SOFC system could improve the performance of the SOFC unit. When the membrane reactor is operated at a hydrogen recovery of 90%, the maximum power density is about 12.6% higher than that from the system with the conventional reformer. The performance comparison between the two SOFC systems which provide the same net electrical efficiency indicates that the SOFC system with the membrane reactor requires a smaller SOFC stack than the conventional SOFC system; however, the former requires an extra cost on palladium membranes and extra electrical power for operating the compressor for the membrane reactor. The preliminary economic analysis reveals that the implementation of the membrane reactor to the SOFC system is not cost-effective due to high cost of palladium membranes. Finally it was indicated that the use of the palladium membrane reactor in the SOFC system is still technically attractive even when an SOFC cell with lower resistance can be further developed.

Keywords: Solid oxide fuel cell; Palladium membrane reactor; Performance analysis

1. Introduction

Fuel cell is considered as an efficient electrical power generator compared to conventional heat engines, steam and gas turbine, and combined cycles. Among the various types of fuel cell, solid oxide fuel cell (SOFC) has attracted considerable interest as it offers wide application ranges, flexibility in the choice of fuel, high system efficiency and possibility of operation with an internal reformer. Hydrogen is a main fuel for most type of fuel cells. Nevertheless, other fuels such as methane, methanol, ethanol, gasoline and oil derivatives can also be used when a reformer is included in a fuel cell system for converting the fuel to hydrogen. A thermodynamic analysis was carried out to evaluate the performances of SOFCs fuelled by different fuels; that is, methane, methanol, ethanol and gasoline. The results obtained in terms of electromotive force and efficiency indicate that ethanol and methanol are very promising alternatives to hydrogen [1]. However, methanol is a preferable choice with respect to its availability, high energy density and ready storage and distribution [2,3].

A number of research efforts have been carried out on advanced SOFC operations such as development of intermediate temperature-SOFCs [4] and integration of SOFCs with intercool gas turbine [5]. Some researchers attempted to improve the performance of SOFC systems by focusing on the different integration modes of a reformer and an SOFC unit (i.e., external reforming, indirect internal reforming and direct internal reforming) [4]. Because it has been demonstrated that hydrogen

* Corresponding author. Fax: +662 218 6877.
E-mail address: Suttichai.A@chula.ac.th (S. Assabumrungrat).

1385-8947/$ – see front matter © 2007 Elsevier B.V. All rights reserved.
doi:10.1016/j.cej.2007.06.021

Nomenclature

a	Constant in Eq. (8) (Ω m)
A	Area (m^2)
b	Constant in Eq. (8) (K)
$E_{A,pol}$	Activation energy involved in activation loss ($kJ\,mol^{-1}$)
E_D	Activation energy for diffusion through membrane ($kJ\,mol^{-1}$)
E_0	Open circuit voltage (V)
f	Volumetric flow rate of permeated hydrogen ($m^3\,s^{-1}$)
F	Faraday constant ($C\,mol^{-1}$)
i	Current density ($A\,cm^{-2}$)
n_i	Number of moles of component i (mol)
N_{H_2}	Permeation flux of hydrogen through membrane ($mol\,m^{-2}$)
P	Total pressure (kPa)
P_{com}	Power requirement of the compression unit (kW)
p_i	Partial pressure of component i (Pa)
Q_0	Pre-exponential constant for membrane permeability ($mol\,m^{-1}\,s^{-1}\,Pa^{-0.5}$)
Q_i	Heat involved in each unit (kW)
R	Universal gas constant (8.31447×10^{-3}) ($kJ\,mol^{-1}\,K^{-1}$)
T	Absolute temperature (K)
U_f	Fuel utilization (%)
V	Operating voltage (V)

Greeks letters

η	Overpotential (V)
δ	Thickness (m)
ϕ	Hydrogen recovery (%)
ψ_{com}	Efficiency of compressor (−)
ρ	Specific ohmic resistant (Ω m)
ξ	Level of SOFC cell resistance (%)

Subscripts

a	Anode
Act	Activation
c	Cathode
Conc	Concentration
Ohm	Ohmic
p	Permeate side
r	Reaction side

concentration in feed influences SOFC performance [6], the use of a palladium membrane reactor, which has been successfully implemented in a number of hydrogen-generating reactions [7], should provide potential advantages when it is incorporated with the SOFC system. It is expected that due to a high concentration of hydrogen obtained from the membrane reactor, the SOFC unit should be operated at a higher stack power density, and therefore a smaller SOFC stack as well as a cell area is required. However, the operation of the palladium membrane reactor requires additional costs on membrane and compressor. Unfortunately, there is still no effort in the literatures to analyze the potential benefits and economics of the incorporation of the palladium membrane reactor to the SOFC system.

In this study, the performances of the methanol-fuelled SOFC system incorporated with the palladium membrane reactor are compared with those of the conventional SOFC system. The benefits from the use of the membrane reactor and the preliminary economic analysis are investigated. The obtained information from this study is important for determining whether the research effort should be carried out further on this proposed system.

2. Theory

A conventional SOFC system normally consists of preheaters, a reformer, an SOFC unit, and a burner (Fig. 1(a)). As shown in the figure, a mixture of methanol and water is firstly preheated in Preheater I before being converted to hydrogen-rich gas in the reformer. Simultaneously, air is also preheated (in Preheater II) by the exhaust heat from Preheater I before feeding to the SOFC unit where electrical power is generated. Heat required in the system is obtained from the combustion of exhaust gases and the irreversible losses in the SOFC unit.

For the SOFC system with a palladium membrane reactor, the conventional reformer is replaced by the membrane reactor

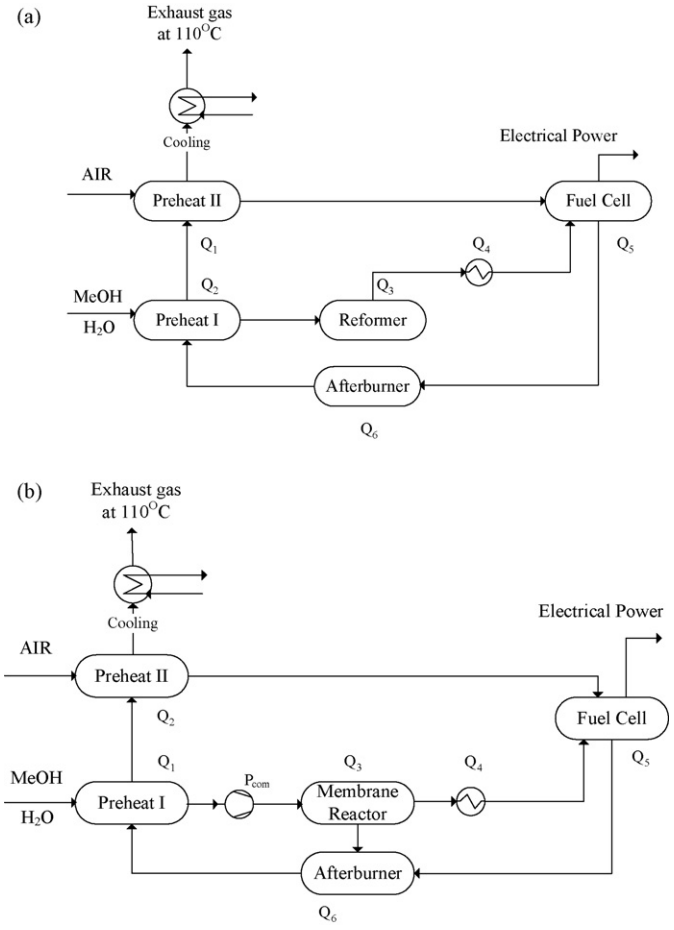

Fig. 1. Flow diagrams of SOFC systems; (a) a conventional SOFC system and (b) an SOFC system with a membrane reactor.

(Fig. 1(b)). In addition, a compressor is required for this system in order to increase the driving force for hydrogen separation. According to this operating system, pure hydrogen is extracted from the reformed gas and fed to the anode compartment of the SOFC unit, whereas the residual reformed gas is combined with the exhaust gases from the SOFC unit and combusted in the burner in order to supply heat to the system.

2.1.1. Reformer/membrane reactor

At the reformer/membrane reactor, the reactions involved in the production of hydrogen from the steam reforming of methanol can be represented by the following equations [8,9]

$$CH_3OH = 2H_2 + CO \quad (1)$$

$$CO + H_2O = H_2 + CO_2 \quad (2)$$

$$CO + 3H_2 = CH_4 + H_2O \quad (3)$$

In this work, the reactor is assumed to be operated at equilibrium condition. This assumption may be reasonable because the rates of methanol steam-reforming and the water gas shift reaction are fast, particularly at high temperature [10]. It was reported that the conversion of methanol from the methanol steam-reforming always close to 100% when the operating temperature above 623 K is performed [11]. According to the substantial works on developing selective hydrogen permeable membranes, a dense palladium-based membrane reactor has attracted many research interests. Recent research efforts have focused on the fabrication of thin membrane layers and determination of alloy compositions with better stability and resistance to poisonings. In the present work, the palladium membrane reactor with a membrane thickness of 10 μm was chosen due to its minimum in palladium material cost, defects and manufacturing difficulties of a thin membrane [12].

The hydrogen flux through a palladium membrane (N_{H_2}) is typically limited by the diffusion of hydrogen atoms through the membrane film, in which the flux can be represented by Eq. (4)

$$N_{H_2} = \frac{Q_0}{\delta} \exp\left(\frac{-E_D}{RT}\right)(p_{H_2,r}^{0.5} - p_{H_2p}^{0.5}) \quad (4)$$

The flux is inversely proportional to the membrane thickness (δ) and proportional to the difference in the square roots of the hydrogen partial pressure on the reaction side and the permeate side of the membrane. The resistance of the porous support is assumed negligible. The parameters of Eq. (4) are presented in Table 1. It should be noted that the required area of the palladium membrane can be calculated from the average hydrogen flux through the membrane as shown in the following equation:

$$\text{Area}_{Mem} = \frac{\text{molar flowrate of } H_2 \text{ recovered}}{\bar{N}_{H_2}} \quad (5)$$

As described earlier, the SOFC system with the palladium membrane reactor needs to install the compressor to operate in the palladium membrane reactor. The required power for the compressor (P_{com}) can be calculated from the following equation.

$$P_{com} = \frac{\Delta(Pf)}{\psi_{com}} \quad (6)$$

where f and P are volumetric flow rate and total pressure, respectively. It is assumed that the efficiency of compressor (ψ_{com}) is 80%.

Table 1
Parameters for hydrogen permeation through a palladium membrane [13]

Q_0 (mol m^{-1} s^{-1} Pa$^{-0.5}$)	4.40×10^{-7}
E_D (kJ mol^{-1})	15.7
Thickness (μm)	10

Table 2
Summary of parameters of ohmic resistance and thickness of each cell component [14]

Materials for anode/electrolyte/cathode	Ni–YSZ/YSZ/LSM–YSZ
Anode thickness (μm)	150
Constants for anode ohmic resistance	$a = 0.0000298$, $b = -1392$
Cathode thickness (μm)	200
Constants for cathode ohmic resistance	$a = 0.0000811$, $b = 600$
Electrolyte thickness (μm)	40
Constants for electrolyte ohmic resistance	$a = 0.0000294$, $b = 10350$
Interconnect thickness (μm)	100
Constants for interconnect ohmic resistance	$a = 0.001256$, $b = 4690$

2.2. SOFC unit

An SOFC unit consists of two porous ceramic electrodes (i.e. an anode and a cathode), a solid ceramic electrolyte, and an interconnector. The theoretical open-circuit voltage of the cell, which is the maximum voltage under specific operating conditions, can be calculated from the following equation:

$$V = E_0 - (\eta_{ohm} + \eta_{Act,a} + \eta_{Act,c} + \eta_{Conc,a} + \eta_{Conc,c}) \quad (7)$$

where E_0 is open circuit voltage determined by Nernst's equation and η_i is a polarization loss in the SOFC unit.

It is well established that several losses could occur during SOFC operation. The voltage drop is normally caused by three major irreversibilities; that is, ohmic polarization (Eq. (8)), activation polarization (Eq. (9)) and concentration polarization. The summaries of ohmic polarization and activation polarization parameters are given in Tables 2 and 3, respectively. In the present work, the concentration polarization is assumed to be negligible. This assumption is valid when the cell is not operated at too high current density or too low concentration [16].

$$\eta_{Ohm} = \frac{i\rho\delta}{A} \quad (8)$$

Table 3
Summary of activation polarization parameters [15]

	k (A m^{-2})	$E_{A,pol}$ (kJ mol^{-1})	m
Cathode	14.9×10^9	160	0.25
Anode	0.213×10^9	110	0.25

where $\rho = a\exp(b/T)$; a and b are the constant values dependent on a type of material.

$$\tilde{\eta}_{\mathrm{Act}} = i\left[\left[\frac{4F}{RT}k_{\mathrm{O_2}}(p_{\mathrm{O_2},c})^{m_{\mathrm{O_2}}}\exp\left(-\frac{E_{\mathrm{A,pol,O_2}}}{RT}\right)\right]^{-1} + \left[\frac{2F}{RT}k_{\mathrm{H_2}}(p_{\mathrm{H_2,a}})^{m_{\mathrm{H_2}}}\exp\left(-\frac{E_{\mathrm{A,pol,H_2}}}{RT}\right)\right]^{-1}\right] \quad (9)$$

The electrical power can be calculated by Eq. (10). Generally, the SOFC is suggested to operate at the relative power (ratio of power to the maximum achievable power at the specific condition) of 0.7 [17]. The fuel cell operation at lower power is attractive from the point of view that the higher efficiency is obtained. However, too low power is not practical due to high cost of SOFC cell.

$$\text{Electrical power} = \text{Current} \times \text{Operating Voltage} \quad (10)$$

The amount of heat involved in each unit (Q_i) shown in Fig. 1 can be calculated from the enthalpy change of each unit based on the assumption that no heat loss occurs in the unit.

3. Results and discussion

Various operating parameters influence the performance of SOFC stack. In operation, hydrogen in the fuel is consumed along the fuel channel by the electrochemical reaction. Fig. 2 shows the voltage (dashed lines) and average power density (solid lines) at different operating current density (i) and fuel utilization (U_f) for the conventional system fed by a feed with a H_2O:MeOH ratio of 1:1 at a temperature of 1173 K. The voltage decreases with the increase of operating current density due to the increased voltage loss from the irreversible SOFC cell resistances. Power density increases initially to a maximum value and then decreases. These characteristics are often observed in most SOFC systems. However, it should be noted that the values at high current density are likely to be overestimated because the concentration polarization is neglected. When the stack is operated at high fuel utilization, both the voltage and power density decrease. This is mainly due to the fuel depletion particularly near the exit of the anode chamber. Fig. 3 shows the

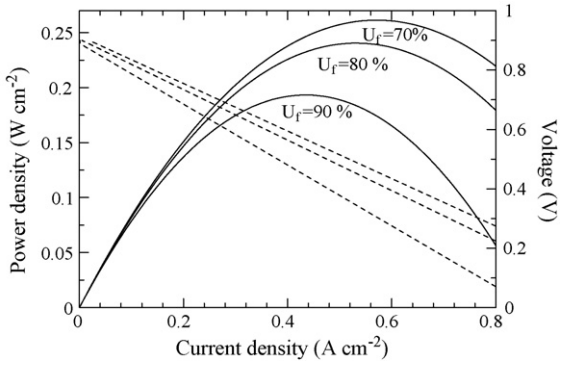

Fig. 2. Characteristic curves of SOFC stack at different fuel utilization (inlet H_2O:MeOH = 1:1 and T = 1173 K).

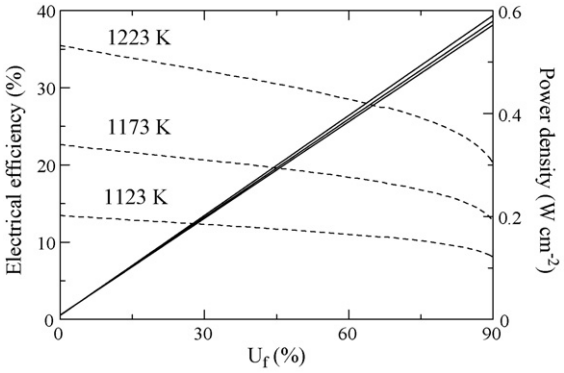

Fig. 3. Maximum power density and electrical efficiency at different operating fuel utilization and temperature (inlet H_2O:MeOH = 1:1).

effect of fuel utilization on the maximum power density (dashed lines) and its corresponding electrical efficiency (solid line) at three temperature levels. It is clearly shown that although the operation at high fuel utilization is desirable in term of achieving high electrical efficiency, the main drawback is its lower power density, implying that larger cell area is required to operate the system. Therefore, the fuel utilization should be carefully selected to achieve a high electrical efficiency at a reasonable stack power density. The fuel utilization of 80–95% has been reported in many studies [17–19]. It was also found that the temperature significantly influences the values of maximum power density. At high temperature the cell resistance becomes smaller and therefore the maximum power density increases. However, it does not affect the corresponding electrical efficiency at the maximum power density. It should be noted that high operating temperature is a favorable operating condition regarding the SOFC performance; however, it is limited by the presence of some technical constraint, such as availability of high temperature seal. The operating temperature of 1173 K is used in the further studies in this work.

When an SOFC system is incorporated with a palladium membrane reactor, pure hydrogen is extracted from the reformed gas and fed to the SOFC stack. The operating temperature of the palladium membrane was reported in a range of 673–873 K [20,21]. In this study, the operating temperature of 873 K was considered as it provided the highest hydrogen flux. Fig. 4 shows the characteristic curves of the SOFC unit fed by pure hydrogen at different hydrogen recovery (ϕ). The SOFC unit is operated at T = 1173 K and a fuel utilization of 80%. The dashed line and solid lines show the power density for the case of the conventional SOFC system and the case of the SOFC system with the membrane reactor, respectively. It is obvious that hydrogen recovery significantly influences the performance of the SOFC unit. The value must be sufficiently high to offer superior performance to the case with the conventional reformer. The maximum power density increases from 0.238 W cm^{-2} for the conventional SOFC system to 0.247 W cm^{-2} (3.8%) and 0.268 W cm^{-2} (12.6%), for the SOFC system with the palladium membrane operated at hydrogen recovery of 85% and 90%, respectively. When the SOFC unit is operated at constant fuel utilization, the hydrogen concentration along the fuel channel is governed by

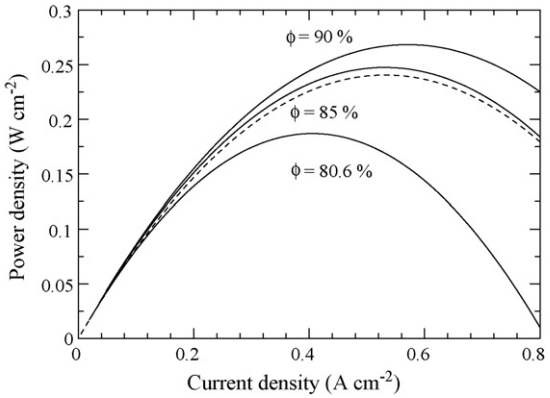

Fig. 4. Comparison of characteristic curves between the conventional SOFC system and the SOFC system with palladium membrane reactor operated at different values of percentage hydrogen recovery (ϕ; inlet H_2O:MeOH = 1:1, U_f = 80%, T = 1173 K).

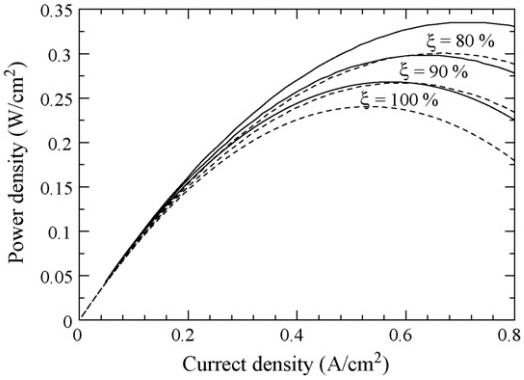

Fig. 5. Comparison of characteristic curves between the conventional SOFC system and the SOFC system with palladium membrane reactor at different cell resistance (inlet H_2O:MeOH = 1:1, U_f = 80%, ϕ = 90%, T = 1173 K).

the value of hydrogen recovery. At low hydrogen recovery, the fuel depletion near the exit of the SOFC unit is pronounced, which deteriorates the SOFC performance as observed by the reduction of power density. From this study, it is obvious that the percentage hydrogen recovery is an important factor which determines whether the inclusion of the membrane reactor in the SOFC system is beneficial to the SOFC system.

Although it was clearly demonstrated that the use of the membrane reactor shows a potential technical benefit for the SOFC system, it requires additional cost on expensive palladium membranes and a compressor to operate the membrane reactor. A preliminary analysis is necessary to determine whether the SOFC system with the membrane reactor is economically feasible. Table 4 shows the calculation results of two cases; i.e., case I the conventional SOFC system and case II the SOFC system with a palladium membrane reactor. For both cases the SOFC is operated at 1173 K and a fuel utilization of 80%. Details of the other operating conditions are also provided in the table. The net electrical efficiency for both cases is 287.2 kW which is equivalent to an electrical efficiency of 45%. For the case II, the extra electrical power (21.6 kW) is generated in the SOFC stack to provide the electrical power for operating the compressor. It was found that the SOFC cell area for case II (131.7 m^2) is lower than that of case I (143.6 m^2), resulting in the reduction of SOFC cell area of 11.9 m^2 when using the membrane reactor in the system. However, the operation in case II requires a palladium membrane area of 120.1 m^2 at 873 K. From the literatures, the prices of SOFC cell and palladium membrane are 1,500 US$/$m^2$ [22] and 746 US$/$m^2$ [23], respectively. Assuming the equivalent life time for both the SOFC cell and the palladium membrane and neglecting the cost of the compressor, it is obvious that the saving of 62.2 US$/kW from the reduction of the SOFC cell area is still much lower than the extra palladium membrane cost of 312.0 US$/kW, indicating that the incorporation of the palladium membrane reactor in the SOFC system is not economical at the present state of art. To make it economical, significant effort is required to reduce the price of the membrane. However, it should be noted that nowadays an SOFC cell is also progressively developed to improve the cell performance as well as to reduce its price. The calculations of heat requirement in the system indicate that both systems can be operated without additional requirement of an external heat source.

Table 4
Performance comparison between the conventional SOFC system and the SOFC system with the palladium membrane reactor

Items	Unit	Case I	Case II
Inlet H_2O:MeOH ratio	–	1	1
Reformer/palladium membrane reactor			
Pressure	kPa	101.3	2026
Temperature	K	973	873
Afterburner stack data	K	1173	1173
Pressure	kPa	101.3	101.3
Temperature	K	1173	1173
Fuel utilization (U_f)	%	80	80
Cell voltage	V	0.62	0.67
Current density	A cm^{-2}	0.323	0.35
Power density	W cm^{-2}	0.203	0.234
Cell area	m^2	143.6	131.7
Palladium membrane reactor			
% recovery	%	–	90.0
Membrane area	m^2	–	120.1
Power production			
Electrical power	kW	287.2	308.8
Power consumption			
Compressor	kW	–	21.6
Net electrical efficiency	%	45	45

In order to determine whether the use of palladium membrane reactor is technically advantageous for the SOFC system when a better cell is developed, the characteristic curves of the SOFC at different levels of cell resistance (ξ = 80%, 90% and 100%) are calculated (see Fig. 5). The dashed lines indicate the results for the conventional SOFC system while the solid lines represent those for the SOFC system with the palladium membrane reactor. The fuel utilization is kept at 80% for both cases and the hydrogen recovery is fixed at 90% for the case with the palladium membrane reactor. From the results, it is clear that when the cell is further developed to have lower resistance, the use of a palladium membrane reactor still shows a potential technical benefit to the SOFC system. It should be noted that the

use of other membranes (such as zeolite membrane) which offer similar or slightly lower separation efficiency may be another attractive option to be considered.

4. Conclusions

Performance of the SOFC system fuelled by methanol was analyzed to investigate the potential benefit from incorporating a palladium membrane reactor to the system. The electrical efficiency and power density of the SOFC unit were governed by the operating current density, fuel utilization and temperature. It was demonstrated that the SOFC unit can be operated at higher power density when the system is equipped with the membrane reactor. Compared with the conventional SOFC system, the system with the membrane reactor requires lower SOFC cell area, resulting in lower cost of the stack. However, the cost of the required palladium membrane was found to be much more expensive than the saving cost. Therefore the SOFC system incorporated with the palladium membrane is not economically attractive unless the membrane can be made at much lower cost. Finally it was revealed that the improvement of the stack power density by the use of the palladium membrane reactor is still technically significant even when an advanced cell with lower cell resistance can be developed.

Acknowledgements

The supports from The Thailand Research Fund, Commission on Higher Education, and the Chulalongkorn University Graduate Scholarship commemorating the 72nd Anniversary of H.M. King RAMA IX are gratefully acknowledged. The authors also would like to acknowledge the support from Professor Piyasan Praserthdam.

References

[1] S.L. Douvartzides, F.A. Coutelieris, K. Demin, P.E. Tsiakaras, AIChE 49 (2003) 248–257.
[2] B. Emonts, J.B. Hansen, S.L. Jorgensen, B. Hohlein, R. Peters, J. Power Sources 71 (1998) 288.
[3] K. Ledjeff-Hey, V. Formanski, T. Kalk, J. Roes, J. Power Sources 71 (1998) 199–207.
[4] P. Aguiar, C.S. Adjiman, N.P. Brandon, J. Power Sources 138 (2004) 120–136.
[5] Y. Yi, A.D. Rao, J. Brouwer, G.S. Samuelsen, J. Power Sources 132 (2004) 77–85.
[6] S.H. Chan, O.L. Ding, Int. J. Hydrogen Energy 30 (2005) 167–179.
[7] E. Kikuchi, Catal. Today 56 (2000) 97–101.
[8] J.C. Amphlett, M.J. Evans, R.A. Jones, R.F. Mann, R.D. Weir, Can. J. Chem. Eng. 59 (1981) 720–727.
[9] J.C. Amphlett, R.F. Mann, R.D. Weir, Can. J. Chem. Eng. 66 (1988) 950–956.
[10] C. Pakornphant, C. Sumaeth, S. Johannes, Chem. Eng. J. 97 (2004) 161–171.
[11] H. Amanduson, L.G. Ekedahl, H. Dannetun, Surf. Sci. 442 (1999) 199–205.
[12] R. Dittmeyer, V. Hollein, K. Daub, J. Mol. Catal. A: Chem. 173 (2001) 135–184.
[13] G.L. Hollock, J. Phys. Chem. 74 (1970) 503–511.
[14] S.H. Chan, C.F. Low, O.L. Ding, J. Power Sources 103 (2002) 188–200.
[15] E. Achenbach, J. Power Sources 49 (1994) 333–348.
[16] M. Pfafferodt, P. Heidebrecht, M. Stelter, K. Sundmacher, J. Power Sources 140 (2005) 53–62.
[17] A.K. Demin, P. Tsiakaras, E. Gorbova, S. Hramova, J. Power Sources 131 (2004) 231–236.
[18] J.R. Rostrup-Nielsen, Phys. Chem. Chem. Phys. 3 (2001) 283–288.
[19] S. Campanari, J. Power Sources 92 (2001) 26–34.
[20] G. Marigliano, G. Barbieri, E. Drioli, Chem. Eng. Process. 42 (2003) 231–236.
[21] F.A.N. Fernandes, A.B. Soares Jr., Fuel 85 (2006) 569–573.
[22] E. Riensche, U. Stimming, G. Unverzagt, J. Power Sources 73 (1998) 251–256.
[23] A. Criscuoli, A. Basile, E. Drioli, O. Loiacono, J. Membr. Sci. 181 (2001) 21–27.

Appendix 8

ELSEVIER

Chemical Engineering Journal xxx (2007) xxx–xxx

Chemical Engineering Journal

www.elsevier.com/locate/cej

Selection of appropriate fuel processor for biogas-fuelled SOFC system

P. Piroonlerkgul [a], S. Assabumrungrat [a,*], N. Laosiripojana [b], A.A. Adesina [c]

[a] *Center of Excellence in Catalysis and Catalytic Reaction Engineering, Department of Chemical Engineering, Faculty of Engineering, Chulalongkorn University, Bangkok 10330, Thailand*

[b] *The Joint Graduate School of Energy and Environment, King Mongkut's University of Technology Thonburi, Bangkok 10140, Thailand*

[c] *Reactor Engineering & Technology Group, School of Chemical Sciences & Engineering, University of New South Wales, Sydney, NSW 2052, Australia*

Received 9 August 2007; received in revised form 4 October 2007; accepted 5 October 2007

Abstract

The performance of biogas-fed solid oxide fuel cell (SOFC) systems utilizing different reforming agents (steam, air and combined air/steam) has been investigated via thermodynamic analysis to determine the most suitable feed. The boundary of carbon formation was first calculated to specify the minimum amount of each reforming agent necessary to avoid carbon formation. The SOFC performance (electrical efficiency and power density) was determined at different biogas compositions and reforming agent:biogas ratios. The SOFC performance is better when the methane content in the biogas is higher. Steam is considered to be the most suitable reforming agent in this study as the steam-fed SOFC offers much higher power density than the air-fed SOFC although its electrical efficiency is slightly lower. When steam is added in the air-fed SOFC as in the case of the co-fed SOFC, the power density can be improved but the electrical efficiency becomes lower compared with the case of the air-fed SOFC. Finally, in order to improve the electrical efficiency of the steam-fed SOFC, the biogas split option was proposed. It was found that a higher electrical efficiency can be achieved. In addition, although the power density is lowered by this operation, the value is still higher than the case of the air-fed SOFC.

Keywords: Biogas; Dry reforming; Partial oxidation; Solid oxide fuel cell; Steam reforming; Thermodynamic analysis

1. Introduction

The demand for fossil fuel in electrical power generation has significantly increased in the past decade due to the rapid changes in global economic activities. This upsurge in fossil fuel consumption poses serious fuel supply insecurity and increases the amount of greenhouse gases accumulating in the environment. To alleviate these problems, several environmental-friendly fuels have been proposed alternatives to conventional fossil fuels. Biogas is an attractive fuel as it is derived renewably from biomass and it contains only trace amount of non-methane hydrocarbons. A common problem for biogas utilization is that most biogas is derived from small-scale sources, e.g. farm and municipal wastes. Hence, the use of biogas is applicable to a small-size power generation (5–100 kW) [1]. Moreover, the biogas composition fluctuates markedly, depending on its source [2]. Generally, biogas contains methane (40–65%), carbon dioxide (30–40%) and trace of nitrogen.

A solid oxide fuel cell (SOFC) is an appropriate technology for generating electricity from biogas due to its high efficiency (30–40%) for small-size power generations (<20 kW) [1]. Recently, a 100 kW class SOFC system fed by biogas has been proposed, and the electrical efficiency of almost 48.7% [3] was reported compared to 41.5% of a conventional system [4]. Additionally, its performance is still remarkable even at low methane contents in biogas. In laboratory test, the performance of SOFC drops only 5% when the biogas composition (CH_4:CO_2) is reduced from 70:30 to 30:70 [5].

An SOFC system can be divided into three main parts: (1) a fuel processor to reform the raw fuel into hydrogen gas, (2) SOFC stacks which subsequently generate electricity and useful heat from the reformed gas and (3) an afterburner where the residual fuel is combusted in order to supply heat to the preheaters and the fuel processor. Within the fuel processor, four main chemical reactions, namely steam reforming, dry

* Corresponding author. Tel.: +66 2 218 6868; fax: +66 2 218 6877.
E-mail address: Suttichai.A@chula.ac.th (S. Assabumrungrat).

1385-8947/$ – see front matter © 2007 Elsevier B.V. All rights reserved.
doi:10.1016/j.cej.2007.10.007

Please cite this article in press as: P. Piroonlerkgul, et al., Selection of appropriate fuel processor for biogas-fuelled SOFC system, Chem. Eng. J. (2007), doi:10.1016/j.cej.2007.10.007

Nomenclature

$D_{A–B}$	ordinary diffusivity of gas A versus gas B [$cm^2\ s^{-1}$]
$D_{A–B(eff)}$	ordinary diffusivity of gas A versus gas B [$cm^2\ s^{-1}$]
$D_{A,k}$	Knudsen diffusivity of gas A [$cm^2\ s^{-1}$]
$D_{A,k(eff)}$	effective Knudsen diffusivity of gas A [$cm^2\ s^{-1}$]
$D_{i(eff)}$	effective diffusion coefficient of species i (i = anode, cathode) [$cm^2\ s^{-1}$]
D_p	catalyst pore diameter [μm]
E	open circuit voltage [V]
$E_{act,a}$	activation energy at anode [$J\ mol^{-1}$]
$E_{act,c}$	activation energy at cathode [$J\ mol^{-1}$]
F	Faraday constant (9.6495×10^4) [$C\ mol^{-1}$]
ΔG_i	Gibb's free energy of reaction i [$J\ mol^{-1}$]
i	current density [$A\ cm^{-2}$]
$i_{0,i}$	exchange current density (i = anode, cathode) [$A\ cm^{-2}$]
$K_{eq,dry}$	equilibrium constant of dry reforming reaction [Pa^2]
$K_{eq,pox}$	equilibrium constant of partial oxidation reaction [$Pa^{3/2}$]
$K_{eq,RWGS}$	equilibrium constant of reverse water gas shift reaction (RWGS)
$K_{eq,steam}$	equilibrium constant of steam reforming reaction [Pa^2]
l_a	thickness of anode [μm]
l_c	thickness of cathode [μm]
L	thickness of electrolyte [μm]
M_A	molecular weight of gas A [g]
n	electrode porosity
p_i^I	inlet pressure of species i [Pa]
P	operating pressure [Pa]
P_i	partial pressure of species i [Pa]
r	average radius of the catalyst pore [μm]
R	gas constant (8.3145) [$J\ mol^{-1}\ K^{-1}$]
T	operating temperature [K]
V	cell voltage [V]

Greek letter

α_c	carbon activity
ε_{AB}	Lennard-Jones energy interaction parameter scaled with respect to the Boltzman constant
γ_a	pre-exponential factor for anode exchange current density [$A\ m^{-2}$]
γ_c	pre-exponential factor for cathode exchange current density [$A\ m^{-2}$]
$\eta_{act,a}$	activation overpotential at anode [V]
$\eta_{act,c}$	activation overpotential at cathode [V]
$\eta_{Conc,a}$	concentration overpotential at anode [V]
$\eta_{Conc,c}$	concentration overpotential at cathode [V]
η_{ohmic}	ohmic overpotential [V]
σ_{AB}	collision diameter [Å]
Ω_D	collision integral
ξ	electrode tortuosity

reforming, partial oxidation and autothermal reforming are possible [6]. Dry reforming is perhaps the most interesting option for the conversion of biogas since the major constituents of the biogas are carbon dioxide and methane. However, it gives less hydrogen yields compared with steam reforming reaction. For steam and dry reforming, an external heat source is required to supply the endothermic fuel processor and to preheat the reforming agent (steam and CO_2) and this reduces the overall efficiency of the fuel processor. This problem can be overcome by applying an exothermic partial oxidation reaction which utilizes air as the reforming agent. However, it is accompanied by a lower hydrogen yield. Moreover, the hydrogen partial pressure of the gas product obtained from the partial oxidation is low due to the dilution effect of nitrogen present in air. In order to circumvent this drawback, the partial oxidation can operate simultaneously with steam reforming to improve hydrogen yield in a route referred to as autothermal reforming. If methane is the fuel, autothermal reforming leads to a higher efficiency (93.9%) – defined as the lower heating value (LHV) of hydrogen generated divided by the LHV of the methane fuel – than that of the steam reforming (91.3%) even though the latter gives a higher hydrogen yield. This is because higher heating power is required to generate steam in the case of the steam reforming. In addition, steam reforming is more prone to carbon formation compared to the partial oxidation and autothermal reforming [7].

When biogas is considered as a feedstock for the reformer, dry reforming may become a co-reaction due to the large amount of CO_2 present in biogas. However, the quantity of carbon dioxide available is not sufficient to convert all methane in biogas into hydrogen. Air and steam are the common reforming agents to combine with CO_2 in the fuel processor. The combination of the dry reforming with partial oxidation helps reduce the reformer size and softens the operating conditions. Furthermore, the desired H_2/CO ratio can be achieved by tuning the composition of the reforming agent [8–10]. Combined steam and dry reforming gives a higher H_2:CO ratio compared to sole dry reforming, however, large amount of heat must be supplied to the fuel processor [11,12].

Although the advantages and disadvantages of the use of each reforming agent in the fuel processor have been widely reported [11,12], the determination of a suitable reforming agent when the fuel processor is integrated with an SOFC system is still a matter for further investigation. The performance analysis of integrated biogas-fed SOFC systems should provide better insights into proper selection guidelines and hence, the rationale for this study. Thermodynamic analysis was performed to compare the relevant performance indices (overall electrical efficiency and the power density) of the SOFC systems with different reforming agents.

2. Modeling

2.1. Fuel processors

The main reaction in the fuel processor fed by biogas is the dry reforming reaction (Eq. (1)) due to the high content of carbon dioxide in biogas. When this is supplemented with steam, Eq.

Please cite this article in press as: P. Piroonlerkgul, et al., Selection of appropriate fuel processor for biogas-fuelled SOFC system, Chem. Eng. J. (2007), doi:10.1016/j.cej.2007.10.007

(2) also takes place in the fuel processor. In a third option, air is fed along with biogas to the system so that the exothermic partial oxidation (Eq. (3)) occurs and provides the energy for the endothermic dry reforming.

$$CH_4 + CO_2 \rightarrow 2H_2 + 2CO \quad \text{(Dry reforming)} \tag{1}$$

$$CH_4 + H_2O \rightarrow 3H_2 + CO \quad \text{(Steam reforming)} \tag{2}$$

$$CH_4 + \tfrac{1}{2}O_2 \rightarrow 2H_2 + CO \quad \text{(Partial oxidation)} \tag{3}$$

It should be noted that the mildly endothermic reverse water gas shift reaction (RWGS) (Eq. (4)) always takes place in the fuel processor due to the present of CO_2 in biogas feed. This reaction inhibits the generation of hydrogen.

$$CO_2 + H_2 \rightarrow H_2O + CO \quad \text{(RWGS)} \tag{4}$$

The thermodynamics of dry and steam reforming are similar (since both are highly endothermic) while the methane partial oxidation is exothermic. However, carbon formation during dry reforming is more severe compared with that of steam reforming due to its lower H/C ratio [13]. In order to simplify the calculations, in this study the reformer is assumed to operate at isothermal condition and the exit gas reaches its equilibrium composition. The relationships of the thermodynamic equilibrium for the dry reforming, steam reforming, partial oxidation and RWGS are shown in Eqs. (5)–(8), respectively.

$$K_{\text{eq,dry}} = \frac{P_{H_2}^2 P_{CO}^2}{P_{CH_4} P_{CO_2}} \tag{5}$$

$$K_{\text{eq,steam}} = \frac{P_{H_2}^3 P_{CO}}{P_{CH_4} P_{H_2O}} \tag{6}$$

$$K_{\text{eq,pox}} = \frac{P_{H_2}^2 P_{CO}}{P_{CH_4} P_{O_2}^{1/2}} \tag{7}$$

$$K_{\text{eq,RWGS}\rightleftarrows} = \rightleftarrows \frac{P_{H_2O} P_{CO}}{P_{H_2} P_{CO_2}} \tag{8}$$

where $K_{\text{eq},i}$, the equilibrium constant of reaction i, can be calculated from this expression:

$$K_{\text{eq},i} = e^{-\Delta G_i/RT} \tag{9}$$

The possibility of carbon formation may be examined from the estimation of the carbon activity (α_c). The carbon formation is thermodynamically possible when $\alpha_c \geq 1$. The details of carbon activity calculations are described in our recent work [14]. In this study, the following carbon formation reactions are assumed to occur in the reformer.

$$2CO = CO_2 + C \tag{10}$$

$$CH_4 = 2H_2 + C \tag{11}$$

$$CO + H_2 = H_2O + C \tag{12}$$

where the carbon activities (α_c) for these carbon formation reactions can be calculated by Eqs. (13)–(15):

$$\alpha_{c,CO} = \frac{K_1 P_{CO}^2}{P_{CO_2}} \tag{13}$$

$$\alpha_{c,CH_4} = \frac{K_2 P_{CH_4}}{P_{H_2}^2} \tag{14}$$

$$\alpha_{c,CO\text{–}H_2} = \frac{K_3 P_{CO} P_{H_2}}{P_{H_2O}} \tag{15}$$

2.2. SOFC stack model

Electrochemical reaction takes place via the reaction between fuel and oxidizing agent. At the cathode section, oxygen in air is reduced to oxygen ions (Eq. (16)) which permeate via the solid electrolyte to react with the hydrogen fuel at the anode section (Eq. (17)). Only hydrogen is assumed to react electrochemically with oxygen ions. It was observed that the H_2 electro-oxidation is much faster than the CO electro-oxidation [15] and in addition the rate of WGS reaction is fast at high temperatures [16–18]. It is also assumed that little amount of methane remaining from the fuel processor is consumed via the steam reforming and that the anode compositions always reach their equilibrium along the cell length due to the fast kinetics at high temperature. For the SOFC stack, Ni-YSZ, YSZ and LSM-YSZ are used as the materials in the anode, electrolyte and cathode, respectively.

$$\tfrac{1}{2}O_2 + 2e^- \rightarrow O^{2-} \tag{16}$$

$$H_2 + 2O^{2-} \rightarrow H_2O + 2e^- \tag{17}$$

The open circuit voltage (E) of the cell can be calculated from the Nernst equation which is expressed as:

$$E = E^0 + \frac{RT}{2F} \ln\left(\frac{P_{H_2} P_{O_2}^{1/2}}{P_{H_2O}}\right) \tag{18}$$

The actual cell potential (V) is always less than the open circuit voltage (E) owing to the existence of overpotentials as shown in Eq. (19). The overpotentials can be categorized into three main sources: ohmic overpotential (η_{ohmic}), activation overpotential (η_{act}) and concentration overpotential (η_{Conc}).

$$V = E - \eta_{\text{act}} - \eta_{\text{ohmic}} - \eta_{\text{Conc}} \tag{19}$$

2.2.1. Ohmic overpotential (η_{ohmic})

This overpotential is the resistance to flow of electron through the electrodes and the interconnections as well as resistance to the flow of ions through electrolyte. This voltage drop is the vital one in all types of cells and is linearly proportional to current density (i). Due to the higher electronic conductivity of the electrodes compared to the electrolyte, only ohmic overpotential in the electrolyte is concerned. Hence, the ohmic overpotential of SOFC can be expressed by [19]:

$$\eta_{\text{ohmic}} = 2.99 \times 10^{-11} iL \exp\left(\frac{10300}{T}\right) \tag{20}$$

Please cite this article in press as: P. Piroonlerkgul, et al., Selection of appropriate fuel processor for biogas-fuelled SOFC system, Chem. Eng. J. (2007), doi:10.1016/j.cej.2007.10.007

2.2.2. Activation overpotential (η_{act})

Activation overpotential is controlled by the kinetics at the electrode surface. It is directly related to the activation barrier to be overcome by the reacting species in order to conduct the electrochemical reaction. The electrode reaction rate at high temperatures is fast, leading to low activation polarization as normally observed in SOFC.

These activation overpotentials in electrodes can be expressed by the Butler-Volmer equation,

$$i = i_0 \left[\exp\left(\frac{\alpha z F \eta_{\text{act}}}{RT}\right) - \exp\left(-\frac{(1-\alpha) z F \eta_{\text{act}}}{RT}\right)\right] \tag{21}$$

In case of SOFC, α and z are set to 0.5 and 2 [20]. Therefore, the activation potential at the anode and cathode can be explicitly written as:

$$\eta_{\text{act},j} = \frac{RT}{F} \sinh^{-1}\left(\frac{i}{2i_0}\right), \quad j = a, c \tag{22}$$

The exchange current density (i_0) for the cathode side depends on partial pressure of both hydrogen and water as well as the operating temperature [21,22]. For the anode side, i_0 depends on oxygen partial pressure and operating temperature as expressed in Eqs. (23)–(24) [23].

$$i_{0,\text{a}} = \gamma_{\text{a}} \left(\frac{P_{\text{H}_2}}{P_{\text{ref}}}\right)\left(\frac{P_{\text{H}_2\text{O}}}{P_{\text{ref}}}\right) \exp\left(-\frac{E_{\text{act,a}}}{RT}\right) \tag{23}$$

$$i_{0,\text{c}} = \gamma_{\text{c}} \left(\frac{P_{\text{O}_2}}{P_{\text{ref}}}\right)^{0.25} \exp\left(-\frac{E_{\text{act,c}}}{RT}\right) \tag{24}$$

2.2.3. Concentration overpotential (η_{Conc})

The concentration overpotential is the electrical loss owing to the difference between the reactant concentration on the reaction site and that in the bulk of the gas stream. This is due to the effect of the diffusion of the reactant gas into the pore of the electrochemical catalyst. It can be calculated by Eqs. (25) and (26):

$$\eta_{\text{Conc,a}} = \frac{RT}{2F} \ln\left[\frac{(1 + (RT/2F)(l_{\text{a}}/D_{\text{a(eff)}} p^{\text{I}}_{\text{H}_2\text{O}})i)}{(1 - (RT/2F)(l_{\text{a}}/D_{\text{a(eff)}} p^{\text{I}}_{\text{H}_2})i)}\right] \tag{25}$$

$$\eta_{\text{Conc,c}} = \frac{RT}{4F} \ln\left[\frac{p^{\text{I}}_{\text{O}_2}}{(p_{\text{c}} - \delta_{\text{O}_2}) - ((p_{\text{c}} - \delta_{\text{O}_2}) - p^{\text{I}}_{\text{O}_2}) \exp\left[(RT/4F)(\delta_{\text{O}_2} l_{\text{c}}/D_{\text{c(eff)}} p_{\text{c}})i\right]}\right] \tag{26}$$

where δ_{O_2}, $D_{\text{a(eff)}}$ and $D_{\text{c(eff)}}$ can be expressed by:

$$\delta_{\text{O}_2} = \frac{D_{\text{O}_2,k\text{(eff)}}}{D_{\text{O}_2,k\text{(eff)}} + D_{\text{O}_2-\text{N}_2\text{(eff)}}} \tag{27}$$

$$\frac{1}{D_{\text{c(eff)}}} = \frac{\xi}{n}\left(\frac{1}{D_{\text{O}_2,k}} + \frac{1}{D_{\text{O}_2-\text{N}_2}}\right) \tag{28}$$

$$D_{\text{a(eff)}} = \left(\frac{p_{\text{H}_2\text{O}}}{p_{\text{a}}}\right) D_{\text{H}_2\text{(eff)}} + \left(\frac{p_{\text{H}_2}}{p_{\text{a}}}\right) D_{\text{H}_2\text{O(eff)}} \tag{29}$$

$$\frac{1}{D_{\text{H}_2\text{(eff)}}} = \frac{\xi}{n}\left(\frac{1}{D_{\text{H}_2,k}} + \frac{1}{D_{\text{H}_2-\text{H}_2\text{O}}}\right) \tag{30}$$

$$\frac{1}{D_{\text{H}_2\text{O(eff)}}} = \frac{\xi}{n}\left(\frac{1}{D_{\text{H}_2\text{O},k}} + \frac{1}{D_{\text{H}_2-\text{H}_2\text{O}}}\right) \tag{31}$$

The correlation between the effective parameter and the normal parameter can be expressed by Eq. (32)

$$D_{\text{(eff)}} = \frac{n}{\xi} D \tag{32}$$

Knudsen diffusivity can be computed by the correlation below:

$$D_{\text{A,k}} = 9700 r \sqrt{\frac{T}{M_{\text{A}}}} \tag{33}$$

Ordinary diffusivity can be calculated by Chapman-Enskog equation (Eq. (34)) [24]:

$$D_{\text{A–B}} = 1.8583 \times 10^{-3} \left(\frac{T^{3/2}((1/M_{\text{A}})+(1/M_{\text{B}}))^{1/2}}{P\sigma^2_{\text{AB}}\Omega_{\text{D}}}\right) \tag{34}$$

where σ_{AB} is the collision diameter (Å) which is equal to $(\sigma_{\text{A}} + \sigma_{\text{B}})/2$. Ω_{D} is computed from [25]:

$$\Omega_{\text{D}} = \frac{A}{T^{\text{B}}_{\text{k}}} + \frac{C}{\exp(DT_{\text{k}})} + \frac{E}{\exp(FT_{\text{k}})} + \frac{G}{\exp(HT_{\text{k}})} \tag{35}$$

where T_{k} is equal to $T/\varepsilon_{\text{AB}}$ and A, C, E and G are constants for each gas.

2.3. Afterburner and heat exchanger

At the exit of the SOFC stack, the anode exit gas and the cathode exit gas are mixed for post combustion. Complete combustion is assumed to take place in the afterburner; hence methane, carbon monoxide and hydrogen contents in the exhaust gas become zero. The heat exchanger is assumed to operate without heat loss.

2.4. Calculation procedure for determining SOFC stack performance

For the SOFC operation, a constant operating voltage along the cell length is assumed as the current collector usually has high electrical conductivity. The operating voltage is kept at 0.7 V in this study. The current density inside the stack varies with the distance from the stack entrance due to the changes in gas compositions in the cathode and anode sections and therefore the open circuit voltage. Hence, the average current density and power density of the SOFC stack can be calculated. In this work, the calculation takes place for each small fuel utilization region employing the mathematical model presented in Section 2.2. The thermodynamic equilibrium is assumed for the anode gas in each region because the anode material is also active for the reactions and the operating temperature of the SOFC stack is high. In each region, the open circuit voltage, overpotentials,

Please cite this article in press as: P. Piroonlerkgul, et al., Selection of appropriate fuel processor for biogas-fuelled SOFC system, Chem. Eng. J. (2007), doi:10.1016/j.cej.2007.10.007

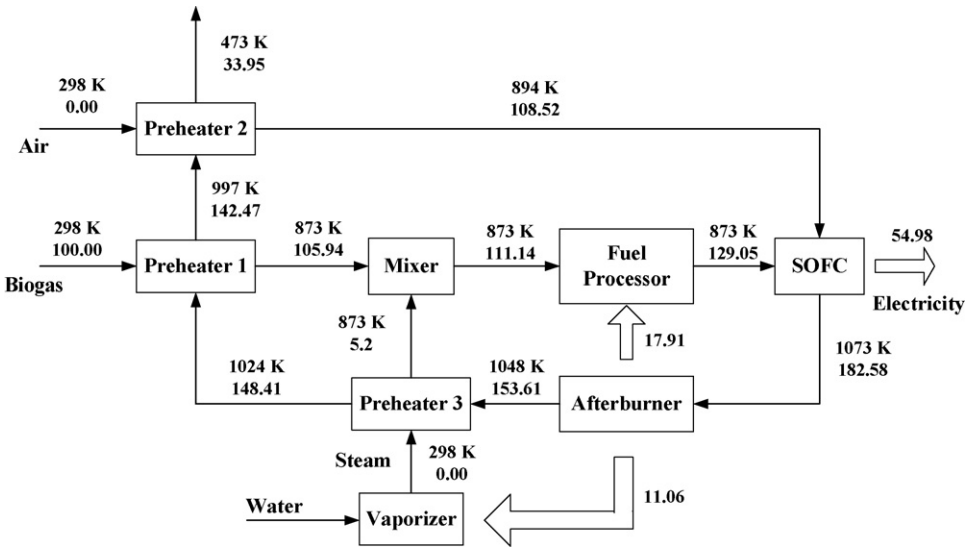

Fig. 1. The plant configuration and energy balance for the steam-fed SOFC system.

equilibrium composition of anode fuel, stack area and current density are computed. The stack areas calculated in each region are added up to yield the total stack area. Finally, the current calculated from the fuel utilized in the stack is divided by the total stack area to obtain the average current density and hence, the average power density is determined. The electrical efficiency may be computed from Eq. (36).

$$\text{SOFC plant efficiency} = \frac{\text{total electricity generated}}{\text{LHV of biogas feed}} \quad (36)$$

2.5. SOFC system configurations

Three biogas-fuelled SOFC systems are considered in this study, i.e. SOFC using steam as the reforming agent (steam-fed SOFC), SOFC using air as the reforming agent (air-fed SOFC) and SOFC using both air and steam as the reforming agents (co-fed SOFC). The plant configuration for the steam-fed SOFC is illustrated in Fig. 1. Several unit operations are included in this configuration consisting of a fuel processor, SOFC stack, an afterburner, a mixer, a vaporizer and preheaters. Steam is generated via the vaporizer, preheated and then mixed with biogas. The mixture gas is then fed into the fuel processor. In the fuel processor, the steam reforming, dry reforming and WGS take place to produce H_2-rich gas and the total heat consumed in these reactions is supplied from heat generated in the afterburner. The H_2-rich gas produced in the fuel processor is fed into the SOFC stack where the electrical energy is generated. The heat generated in the SOFC stack due to the irreversibility is utilized for air and H_2-rich gas preheating. The residue fuel gas released from the SOFC stack is burned up in the afterburner in order to supply heat to the vaporizer and the fuel processor. A high temperature flue gas which mainly contains carbon dioxide and steam released from the afterburner is used in preheating

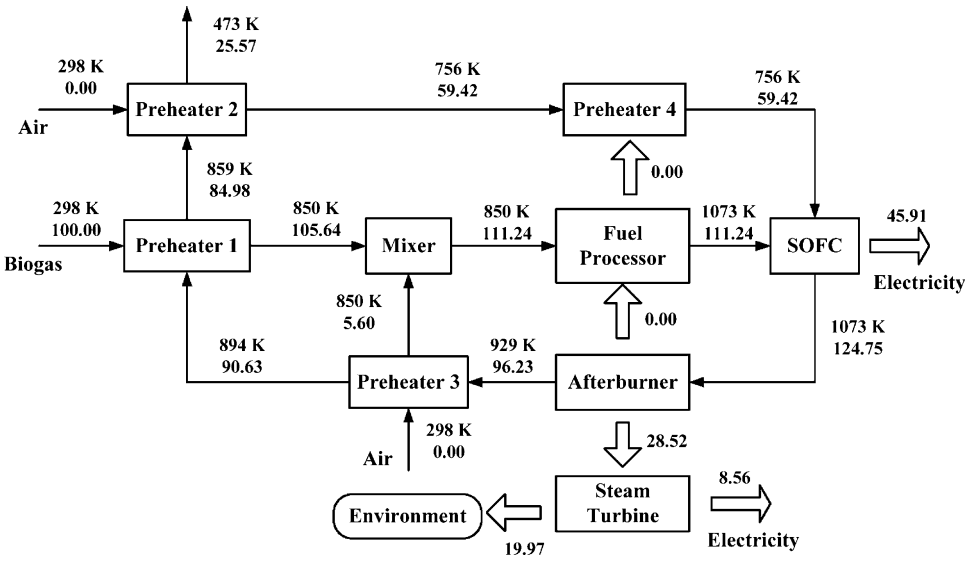

Fig. 2. The plant configuration and energy balance for the air-fed SOFC system.

Please cite this article in press as: P. Piroonlerkgul, et al., Selection of appropriate fuel processor for biogas-fuelled SOFC system, Chem. Eng. J. (2007), doi:10.1016/j.cej.2007.10.007

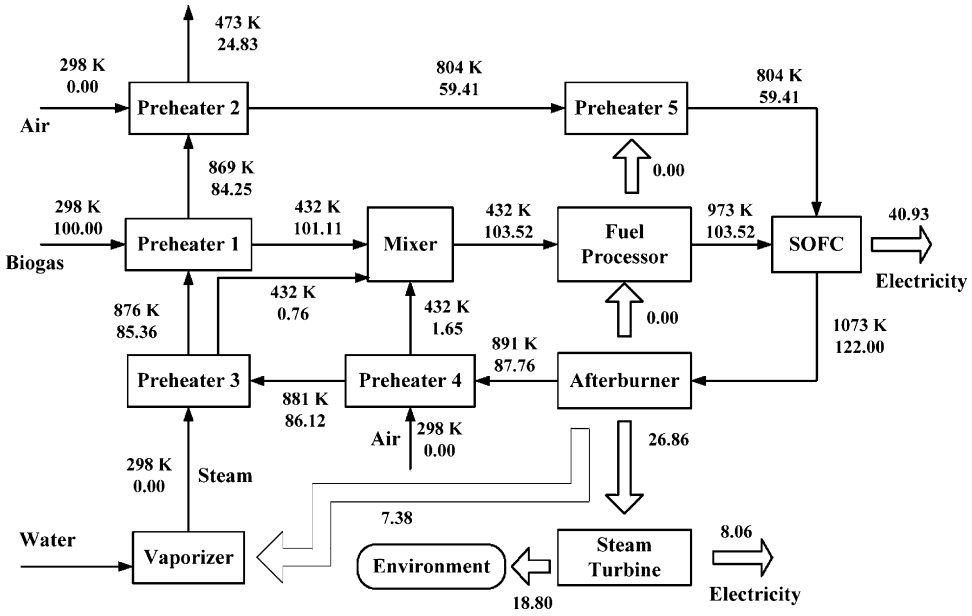

Fig. 3. The plant configuration and energy balance for the co-fed SOFC system.

biogas, steam and oxidizing agent (air) before being discharged to the environment at low temperature. For the calculation, the flue gas temperature released from the system is kept at 473 K. The total heating power used in preheating is computed and the afterburner outlet gas temperature and the quantity of the fuel combusted in the afterburner to achieve the required outlet gas temperature are then calculated. To achieve a desired temperature of the SOFC stack, an oxidizing agent (air) temperature is tuned up employing the energy balance in the SOFC stack. A trial-and-error is performed by tuning the fuel utilization until the total energy flowing into the afterburner is equal to the total energy flowing out of the afterburner. For the air-fed SOFC, its calculation procedure is similar to that of the steam-fed SOFC. However, the heating power used in preheating and the quantity of the fuel used in the afterburner of the former is extremely less than the latter. Therefore, almost all hydrogen in the anode gas can be utilized in the SOFC stack for the air-fed SOFC and the power density also reduces following to the increase in the fuel utilization. To achieve a reasonable power density, the hydrogen mole fraction of the SOFC anode output stream is controlled to be higher than 1.5 mol%. In this case, the heat residue from the afterburner is fed into the steam turbine to generate more electricity as illustrated in Fig. 2. The electrical efficiency of steam turbine is assumed to be 30%. The heat generated from the exothermic partial oxidation in the fuel processor is utilized in preheating the oxidizing agent.

According to the plant configuration of the co-fed SOFC, most of the configurations are identical to that of the air-fed SOFC as illustrated in Fig. 3; nevertheless, more heat is generated in the afterburner in order to generate steam. It should be noted that, in all cases, the quantities of air fed as the oxidant into the SOFC cathode are 5 times of theoretical air required to combust the biogas fuel. The excessive amount of air is required in order to avoid the overheating of the stack which would cause cell damages.

3. Results and discussion

The models of the SOFC systems are programmed in Visual Basic. The values of all parameters used in the calculations are summarized in Table 1. For model validation, the computed results are compared with the experimental results of Zhao and Virkar [26] and Tao et al. [27]. The feed compositions and the SOFC stack dimensions used in model validation are summarized in Table 2. As shown in Fig. 4, the simulation shows good agreement with the experimental data using pure hydrogen fuel [26] for all temperature levels particularly at the operating temperature of 1073 K which is used in the subsequent studies of this work. Moreover, with inlet gas containing various fuel types (CH_4–CO–H_2), the simulation could also predict the experimental data [27] well as illustrated in Fig. 5.

Table 1
Summary of model parameters [28]

Parameters	Value
γ_a	1.344×10^{10} A m^{-2}
γ_c	2.051×10^{9} A m^{-2}
$E_{act,a}$	1.0×10^{5} J mol^{-1}
$E_{act,c}$	1.2×10^{5} J mol^{-1}
n	0.48
ξ	5.4
D_p	1 μm
d_a	750 μm
d_c	50 μm
L	50 μm
V	0.7 V
T_{SOFC}	1073 K
Operating pressure (SOFC)	1 bar
Operating pressure (H_2 processor)	1 bar
$T_{Fuel\ processor\ (steam\ as\ reforming\ agent)}$	873 K
$T_{Fuel\ processor\ (air\ as\ reforming\ agent)}$	1073 K

Please cite this article in press as: P. Piroonlerkgul, et al., Selection of appropriate fuel processor for biogas-fuelled SOFC system, Chem. Eng. J. (2007), doi:10.1016/j.cej.2007.10.007

Table 2
Feed compositions and SOFC stack dimensions used in model validation

Parameters	Zhao and Virkar [26]	Tao et al. [27]
Fuel compositions (mole fraction)		
CH_4	–	0.21
H_2	0.97	0.4
CO	–	0.2
CO_2	–	0.18
N_2	–	0.01
H_2O	0.03	–
Stack dimensions		
Type of cell	Button cell	Planar SOFC with 100 cm^2 active surface area
n	0.48	0.48
ξ	5.4	5.4
D_p	1 μm	1 μm
d_a	1000 μm	500 μm
d_c	20 μm	50 μm
L	8 μm	10 μm
Stack average temperature	873–1073 K	1073 K

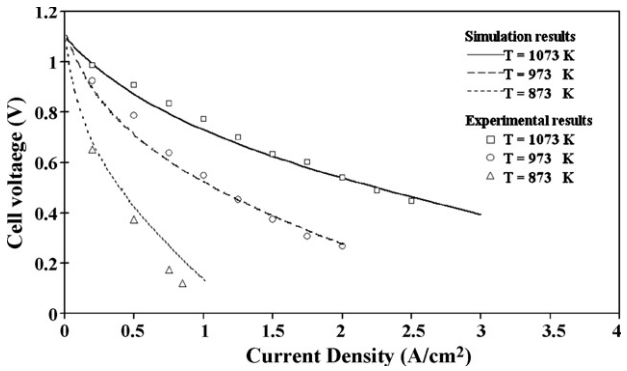

Fig. 4. Verification of the SOFC model.

The boundaries of carbon formation indicating the minimum amount of a reforming agent required to avoid the carbon formation for the biogas steam reforming and partial oxidation are illustrated in Fig. 6a and b, respectively. It is obvious that less reforming agent (steam or air) is required in order to inhibit the carbon formation when the reforming temperature increases. In fact, the moles of reforming agent per biogas required decreased almost hyperbolically with temperature attaining nearly constant value beyond about 1173 K. Biogas with a higher content of methane is more prone to carbon formation than that with a lower amount of methane. These trends are corresponding well with previous literatures [13,14,29]. Note that in the following studies the SOFC systems are always operated using a sufficient amount of the reforming agent to avoid the carbon formation.

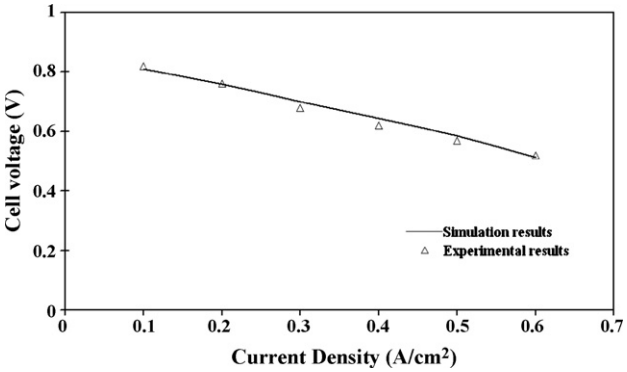

Fig. 5. Verification of SOFC model for the feed with CH_4, CO and H_2 mixtures.

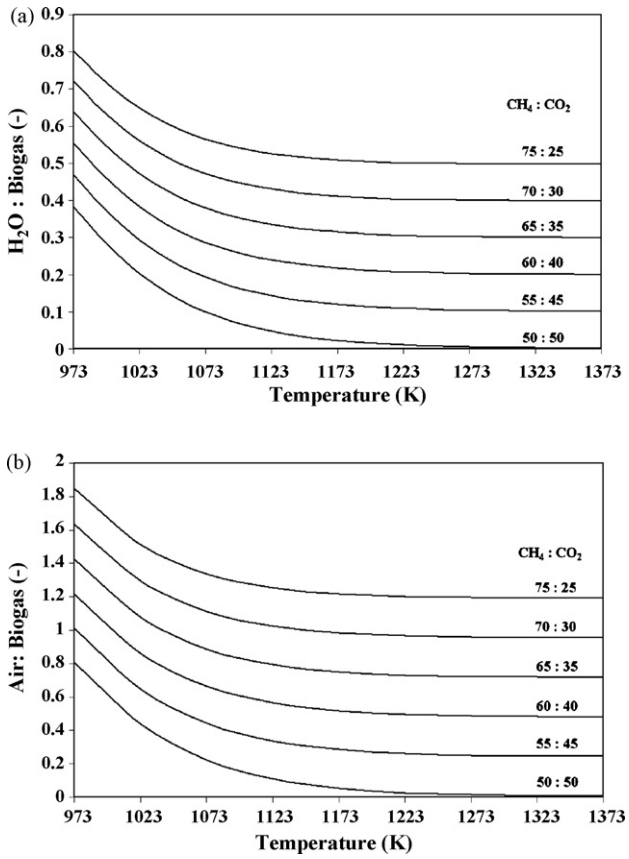

Fig. 6. Boundary of carbon formation for the biogas-fed fuel processors with different reforming agents: (a) steam and (b) air.

The electrical efficiency and power density of the steam-fed SOFC were first investigated. Energy value (lower number on each stream) and temperature (upper number) for different sections of the plant are shown in Fig. 1. The values of H_2O:biogas, CH_4:CO_2 in biogas and fuel processing temperature are 1.2, 60:40 and 873 K, respectively. It may be noted that the energy is given as a percentage of lower heating value of the biogas fuel. As seen in Fig. 1, large amounts of heat generated in afterburner, about 11.06 and 17.91% of biogas LHV, respectively, are supplied to the vaporizer and the fuel processor. An overall electrical efficiency of about 55% of biogas LHV was obtained for this SOFC system. Fig. 7 shows the plant electrical efficiency and power density of the steam-fed SOFC at various steam contents and CH_4:CO_2 ratios. As shown in Fig. 7, biogas with a higher CH_4:CO_2 ratio gives higher efficiency than that with a lower one. As the methane content in the biogas increases, the reformed gas contains hydrogen at a higher concentration and, therefore, a higher power density is achieved. The smaller content of CO_2 in the biogas reduces the energy loss by the exhaust gas of the system. Consequently, the electrical efficiency is improved. Inter-

Please cite this article in press as: P. Piroonlerkgul, et al., Selection of appropriate fuel processor for biogas-fuelled SOFC system, Chem. Eng. J. (2007), doi:10.1016/j.cej.2007.10.007

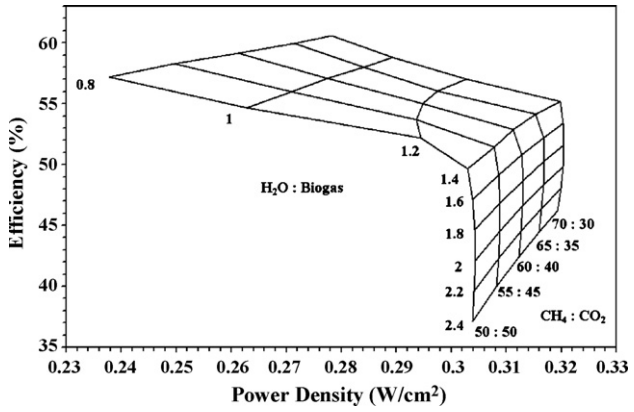

Fig. 7. Performance of the steam-fed SOFC at different H_2O:biogas and CH_4:CO_2 ratios (fuel processing temperature = 873 K).

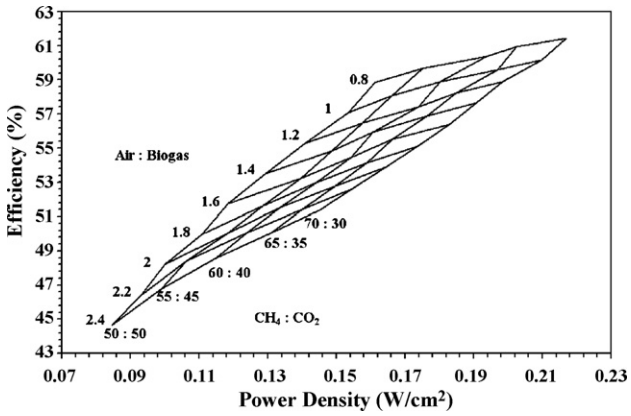

Fig. 8. Performance and current density of air-fed SOFC at different air:biogas and CH_4:CO_2 ratios in biogas (fuel processing temperature = 1073 K).

estingly, as the H_2O:biogas ratio increases, the plant electrical efficiency decreases. This is particularly pronounced when the H_2O:biogas ratio is higher than 1.6. Although excessive addition of steam in the system can increase the hydrogen yield from the reformer, significant amount of heat load is required to generate and preheat the excessive steam. Consequently, the SOFC cannot be operated at high fuel utilization, resulting in lower electrical efficiency. It is also observed that the power density increases initially, levels off and then slightly decreases. This behavior is most likely due to the fact that although steam is essential for promoting the production of hydrogen, it also acts as a diluent, leading to the decrease of hydrogen concentration and power density.

In the case of the air-fed SOFC, the plant configuration and its energy balance are illustrated in Fig. 2, the values of air:biogas, CH_4:CO_2 in biogas and fuel processing temperature are 1.6, 60:40 and 1073 K, respectively. Unlike the steam-fed SOFC, heating energy is not required for the steam generator and the fuel processor. However, hydrogen fuel cannot be used entirely in the SOFC stack, as some fuel must remain in the SOFC outlet stream in order to maintain a high power density for the SOFC. The residue gas combusted as well as the energy generated (28.52% of biogas LHV) is utilized in the steam turbine (assuming an electrical efficiency of 30%) to generate more electricity as shown in Fig. 2. Heat loss generated in the steam turbine (19.97% of biogas LHV) is released to the environment. The plant efficiency and power density for the air-fed SOFC with various air:biogas and CH_4:CO_2 ratios are illustrated in Fig. 8. Compared with the case of the steam-fed SOFC, the power density is much lower. This is due to the fact that the partial oxidation reaction (Eq. (2)) can produce only 2 moles of hydrogen per mole of methane compared with 3 moles of hydrogen per mole of methane in the case of the steam reforming reaction (Eq. (3)). In addition, the high proportion of nitrogen present in air also reduces the hydrogen concentration in the reformed gas. Consequently, the hydrogen partial pressure of the product gas derived from the partial oxidation is lower than that derived from the steam reforming, leading to a lower SOFC power density. However, the air-fed SOFC offers slightly higher electrical efficiency than the steam-fed system. This is due to the exothermicity of the partial oxidation route. Therefore, heat energy from the afterburner is not required to supply to the fuel processor unlike the steam-fed SOFC. Moreover, energy is not required for steam generation which usually consumes large amount of heat. These features help to annul the effect of reduced hydrogen yield in the partial oxidation route. Similar to the case of the steam-fed SOFC, both plant efficiency and power density improve as the quantity of methane in biogas increases as illustrated in Fig. 8. The effect of variation in the air:biogas ratio was also investigated. The results indicate that both power density and overall efficiency decrease with increasing the air content. The decrease in power density is mainly due to the significant increase in inert nitrogen in the inlet stream (anode). The decrease in the electrical efficiency may be ascribed to the excessive air fed to the reformer, occasioning higher energy loss from the increased amount of exhaust gas.

As a third option, the co-fed SOFC is also investigated and its energy balance is illustrated in Fig. 3. The values of H_2O:biogas, air:biogas, CH_4:CO_2 in biogas and fuel processing temperature are 0.8, 2, 60:40 and 973 K, respectively. Unlike the steam-fed SOFC, there is no energy supplied to the fuel processor due to the participation of exothermic partial oxidation reaction; however, some heating energy produced in the afterburner (7.38% of biogas LHV) must be supplied to the vaporizer to generate steam. Furthermore, the residue heat from the co-fed SOFC system (26.86% of biogas LHV) is supplied to the steam turbine to generate more electricity like in the case of the air-fed SOFC. The heat loss from the gas turbine (18.8% of biogas LHV) is released to the environment. The plant electrical efficiency and the power density at different air:biogas and H_2O:biogas ratios are illustrated in Fig. 9. In this study, the biogas composition (CH_4:CO_2) is kept at 60:40. From the foregoing analysis, the electrical efficiency of the co-fed SOFC decreases with the increase in the reforming agent content. The power density decreases as the air:biogas ratio increases due to the presence of large amount of nitrogen in air. However, an optimum H_2O:biogas ratio which provides a maximum power density is observed. This is due to the competing effects between the promotion of hydrogen production and the dilution effect by the addition of more water.

In order to select a suitable reforming agent, the performance of the SOFC systems with different reforming agents is com-

Please cite this article in press as: P. Piroonlerkgul, et al., Selection of appropriate fuel processor for biogas-fuelled SOFC system, Chem. Eng. J. (2007), doi:10.1016/j.cej.2007.10.007

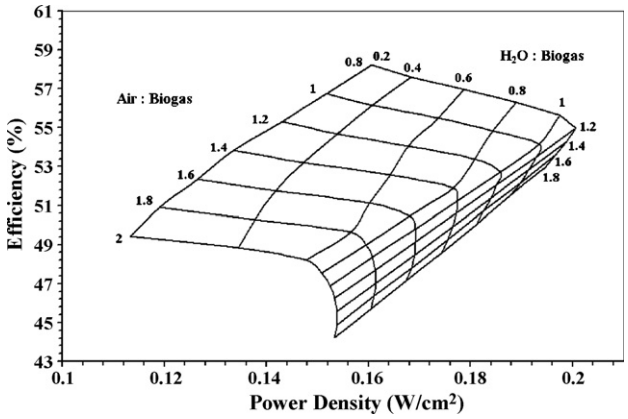

Fig. 9. Performance and current density of co-fed SOFC at different air:biogas and H_2O:biogas ratios (fuel processing temperature = 973 K).

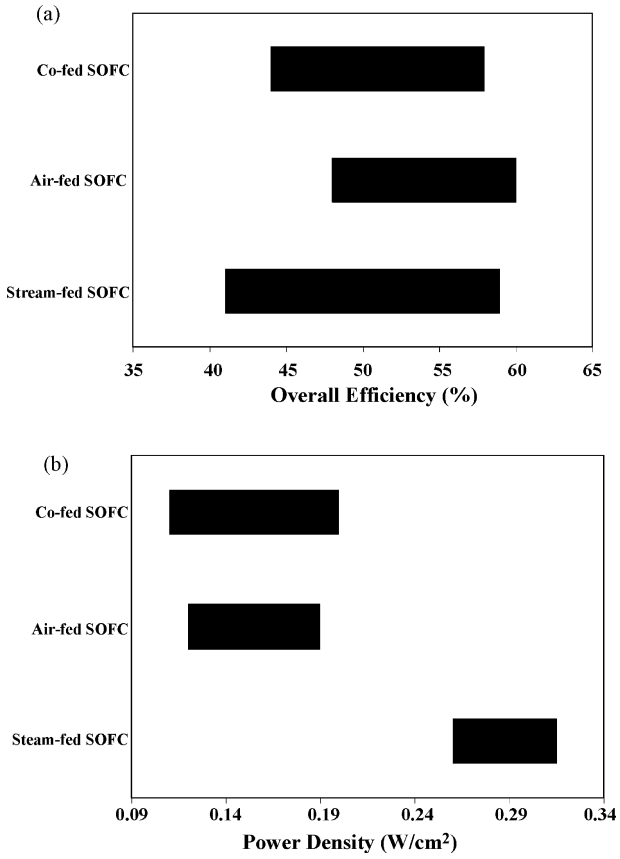

Fig. 10. SOFC performance: (a) overall electrical efficiency and (b) power density (CH_4:CO_2 = 60:40).

pared as shown in Fig. 10. It is obvious that steam is the most attractive reforming agent for the biogas-fed SOFC regarding the power density. Although the air-fed SOFC can provide slightly higher electrical efficiency than the steam-fed SOFC, the power density is much lower due to the high content of nitrogen in air. By adding steam to the air-fed SOFC, the power density can be improved but with the reduction of the electrical efficiency. Because the stack is among the most expensive part of the SOFC system, it is likely that the use of steam as the reforming agent is the most suitable for the biogas-fed SOFC although the electrical efficiency is slightly lower than the use of air.

In order to improve the efficiency of the steam-fed SOFC, the biogas split option is proposed as illustrated in Fig. 11. For this operation, part of biogas is split from the fuel processor and directly fed to the afterburner. This diminishes the heat load in the SOFC system due to the decrease in the quantities of steam added. Moreover, the extent of the endothermic steam reforming reaction is also diminished. As seen in Fig. 11, the heat load in steam generator and H_2 processor for the steam-fed SOFC with 9% of biogas split are 10.1 and 16.3% of biogas LHV, respectively, which are lower compared with those for the steam-fed SOFC without the biogas split (11.1 and 17.9% of biogas LHV for the heat load in steam generator and H_2 processor, respectively). The heating power and the heat exchanger area required in preheating are also reduced. Consequently, the electrical efficiency can be increased while the capital cost is also reduced. The results of the biogas split option shown in Fig. 12 indicate

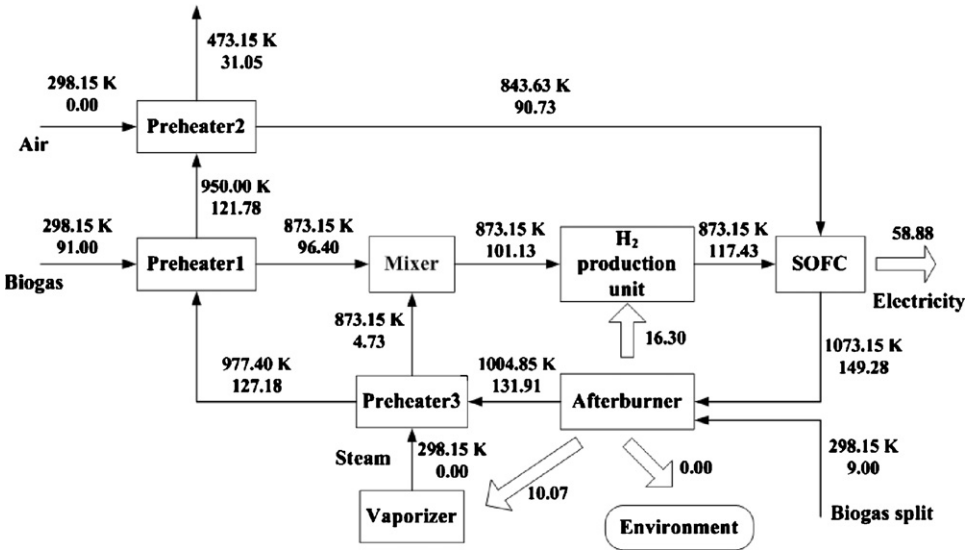

Fig. 11. The SOFC configuration with the biogas split operation.

Please cite this article in press as: P. Piroonlerkgul, et al., Selection of appropriate fuel processor for biogas-fuelled SOFC system, Chem. Eng. J. (2007), doi:10.1016/j.cej.2007.10.007

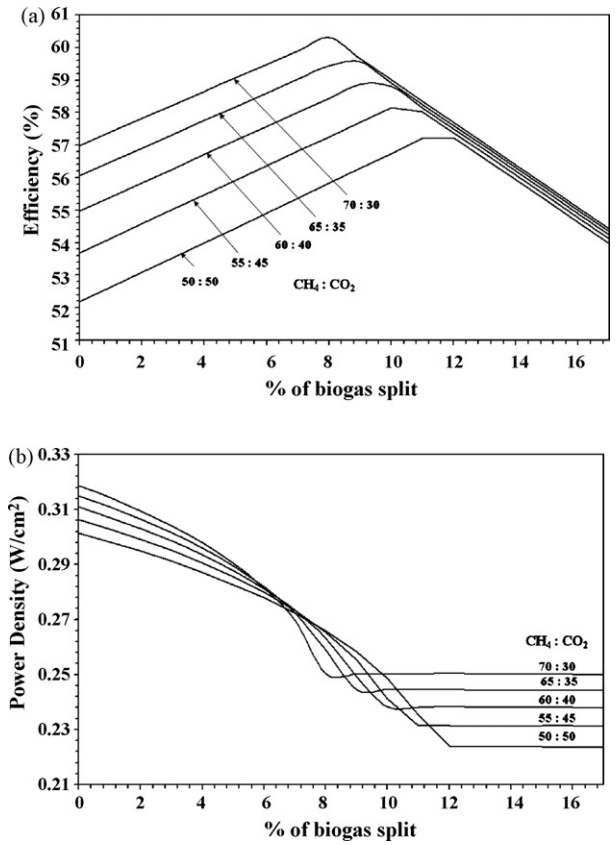

Fig. 12. The effect of %biogas split on (a) overall electrical efficiency and (b) power density at different biogas compositions (fuel processing temperature = 873 K, H_2O:biogas = 1.2).

that the increase in the percentage of biogas split can improve the plant efficiency. However, there is an optimal point at which the SOFC achieves a maximum electrical efficiency. For the operation over this point, the plant efficiency decreases with increasing the percentage of biogas split since the heat released from the afterburner is higher than that required in the vaporizer and the fuel processor. With the installation of biogas split operation, 59% of overall electrical efficiency can be achieved compared to 55% for the normal case with the CH_4:CO_2 ratio of 60:40. Although the biogas split can improve the plant electrical efficiency, the power density always decreases with the increasing biogas split, implying that more SOFC stack area is required for the higher percentage of biogas split. However, it should be noted that the use of steam-fed SOFC with biogas split still offers higher power density than the air-fed SOFC while the electrical efficiency becomes comparable.

4. Conclusions

Performance of the biogas-fed SOFC systems with different reforming agents (steam, air and combined steam/air) was determined in order to find a suitable reforming agent. The boundary of carbon formation was firstly calculated to specify a minimum amount of each reforming agent necessary to avoid carbon formation. Within the range of operating variables examined (chosen to avoid debilitating carbon formation), it seems that when the amount of reforming agent increases, the electrical efficiency always decreases. For the steam-fed SOFC, there is an optimal amount of steam which provides a maximum power density. However, for the air-fed SOFC, the power density always decreases with the increased amount of air due to the dilution effect of nitrogen in air. Steam is considered to be the most suitable reforming agent in this study as the steam-fed SOFC offers much higher power density than the air-fed SOFC although its electrical efficiency is slightly lower due to the high energy requirement in the steam generation. When steam is added in the air-fed SOFC as in the case of the co-fed SOFC, the power density can be improved but the electrical efficiency becomes lower compared with the case of the air-fed SOFC. In order to improve the electrical efficiency of the steam-fed SOFC, the biogas split option was considered. It was found that a higher electrical efficiency can be achieved. In addition, although the power density is lowered by this operation, the value is still higher than the case of the air-fed SOFC.

Acknowledgements

This research is financially supported by the Thailand Research Fund and Commission on Higher Education.

References

[1] J. Van Herle, Y. Membrez, O. Bucheli, Biogas as a fuel source for SOFC co-generators, J. Power Sources 127 (2004) 300–312.
[2] D.C. Dayton, Fuel cell integration—a study of the impacts of gas quality and impurities, NREL Final Report, 2001.
[3] J. Van herle, F. Maréchal, S. Leuenberger, Y. Membrez, O. Bucheli, D. Favrat, Process flow model of solid oxide fuel cell system supplied with sewage biogas, J. Power Sources 131 (2004) 127–141.
[4] R. Layi Fagbenle, A.B.C. Oguaka, O.T. Olakoyejo, A thermodynamic analysis of a biogas-fired integrated gasification steam injected gas turbine (BIG/STIG) plant, Appl. Therm. Eng. 27 (2005) 2220–2225.
[5] M. Jenne, T. Dörk, A. Schuler, in: U. Bossel (Ed.), Proceedings of the Fifth European Solid Oxide Fuel Cell Forum, Lucerne, Switzerland, July 2002, European Forum Secretariat, CH 5442 Oberrohrdorf, Switzerland, 2002, pp. 460–466.
[6] P. Ferreira-Aparicio, M.J. Benito, J.L. Sanz, New trends in reforming technologies: from hydrogen industrial plants to multifuel microreformers, Catal. Rev. 47 (2005) 491–588.
[7] S. Ahmed, M. Krumpelt, Hydrogen from hydrocarbon fuels for fuel cells, Int. J. Hydrogen Energy 26 (2001) 291–301.
[8] J.R. Rostrup-Nielsen, Syngas in perspective, Catal. Today 71 (2002) 243–247.
[9] P.D.F. Vernon, M.L.H. Green, A.K. Cheetham, A.T. Ashcroft, Partial oxidation of methane to synthesis gas, and carbon dioxide as an oxidising agent for methane conversion, Catal. Today 13 (1992) 417–426.
[10] A.M. O'Connor, J.R.H. Ross, The effect of O_2 addition on the carbon dioxide reforming of methane over Pt/ZrO_2 catalysts, Catal. Today 46 (1998) 203–210.
[11] G.F. Froment, Production of synthesis gas by steam- and CO_2-reforming of natural gas, J. Mol. Catal. A: Chem. 163 (2000) 147–156.
[12] J.R. Rostrup-Nielsen, J. Sehedsted, J.K. Norskov, Hydrogen and synthesis gas by steam- and CO_2 reforming, Adv. Catal. 47 (2002) 65–139.
[13] J.H. Edwards, A.M. Maitra, The chemistry of methane reforming with carbon dioxide and its current and potential applications, Fuel Proc. Technol. 42 (1995) 269–289.
[14] S. Assabumrungrat, N. Laosiripojana, P. Piroonlerkgul, Determination of the boundary of carbon formation for dry reforming of methane in a solid oxide fuel cell, J. Power Sources 159 (2006) 1274–1282.

Please cite this article in press as: P. Piroonlerkgul, et al., Selection of appropriate fuel processor for biogas-fuelled SOFC system, Chem. Eng. J. (2007), doi:10.1016/j.cej.2007.10.007

[15] M.A. Khaleel, Z. Lin, P. Singh, W. Surdoval, A finite element analysis modeling tool for solid oxide fuel cell development: coupled electrochemistry, thermal and flow analysis in MARC, D. Collin, J. Power Sources 130 (2004) 136–148.
[16] M.C.J. Bradford, M.A. Vannice, Catalytic reforming of methane with carbon dioxide over nickel catalysts. II: Reaction kinetics, Appl. Catal. A: Gen. 142 (1996) 97–122.
[17] H.M. Swaan, V.C.H. Kroll, G.A. Martin, C. Mirodatos, Deactivation of supported nickel catalysts during the reforming of methane by carbon dioxide, Catal. Today 21 (1994) 571–578.
[18] R. Blom, I.M. Dahl, A. Slagtem, B. Sortland, A. Spjelkavik, E. Tangstad, Carbon dioxide reforming of methane over lanthanum-modified catalysts in a fluidized-bed reactor, Catal. Today 21 (1994) 535–543.
[19] J.R. Ferguson, J.M. Fiard, R. Herbin, Three-dimensional numerical simulation for various geometries of solid oxide fuel cells, J. Power Sources 58 (1996) 109–122.
[20] S.H. Chan, K.A. Khor, Z.T. Xia, A complete polarization model of a solid oxide fuel cell and its sensitivity to the change of cell component thickness, J. Power Sources 93 (2001) 130–140.
[21] S.P. Jiang, S.P.S. Badwal, H_2 Oxidation reactions at the Ni and Pt electrodes on Y-TZP electrolytes, J. Electrochem. Soc. 144 (1997) 3777–3784.
[22] S.P. Jiang, S.P.S. Badwal, An electrode kinetics study of H_2 oxidation on Ni/Y_2O_3–ZrO_2 cermet electrode of the solid oxide fuel cell, Solid State Ionics 123 (1999) 209–224.
[23] J. Fleig, Solid oxide fuel cell cathodes: polarization mechanisms and modeling of the electrochemical performance, Annu. Rev. Mater. Res. 33 (2003) 361–382.
[24] W.J. Massman, A review of the molecular diffusivities of H_2O, CO_2, CH_4, CO, O_3, SO_2, NH_3, N_2O, NO, and NO_2 in air, O_2 and N_2 near STP, Atmos. Environ. 32 (1998) 1111–1127.
[25] H. Yakabe, M. Hishinuma, M. Uratani, Y. Matsuzaki, I. Yasuda, Evaluation and modeling of performance of anode-supported solid oxide fuel cell, J. Power Sources 86 (2000) 423–431.
[26] F. Zhao, A.V. Virkar, Dependence of polarization in anode-supported solid oxide fuel cells on various cell parameters, J. Power Sources 141 (2005) 79–95.
[27] G. Tao, T. Armstrong, A. Virkar, Intermediate temperature solid oxide fuel cell (IT-SOFC) research and development activities at MSRI, in: Nineteenth Annual ACERC&ICES Conference, Utah, 2005.
[28] M. Ni, M.K.H. Leung, D.Y.C. Leung, Parametric study of solid oxide fuel cell performance, Energy Convers. Manage. 48 (2007) 1525–1535.
[29] S.H. Lee, W. Cho, W.S. Ju, B.H. Cho, Y.C. Lee, Y.S. Baek, Tri-reforming of CH_4 using CO_2 for production of synthesis gas to dimethyl ether, Catal. Today 87 (2003) 133–137.

Please cite this article in press as: P. Piroonlerkgul, et al., Selection of appropriate fuel processor for biogas-fuelled SOFC system, Chem. Eng. J. (2007), doi:10.1016/j.cej.2007.10.007

Appendix 9

Elsevier Editorial System(tm) for Chemical Engineering Journal
Manuscript Draft

Manuscript Number:

Title: Performance improvement of solid oxide fuel cell system using palladium membrane reactor with different operation modes

Article Type: Original Article

Section/Category: Chemical Reaction Engineering

Keywords: SOFC; membrane reactor; palladium membrane; performance

Corresponding Author: Dr. Suttichai Assabumrungrat, PhD

Corresponding Author's Institution: Chulalongkorn University

First Author: Supawat Vivanpatarakij , BEng

Order of Authors: Supawat Vivanpatarakij , BEng; Suttichai Assabumrungrat, PhD; Navadol Laosiripojana , PhD; Amornchai Arpornwichanop , DEng

Abstract: The performance improvement of a solid oxide fuel cell (SOFC) system by replacing a conventional reformer with a palladium membrane reactor was investigated. When pure hydrogen was extracted from the reaction mixture via the palladium membrane, the power density of the SOFC was improved, depending on the value of hydrogen recovery (□). Three operation modes of membrane reactors; i.e., high pressure compressor (MR-HPC), vacuum pump (MR-V) and combined high pressure compressor and vacuum pump (MR-HPC-V) were considered. Their overall SOFC system characteristics were compared with those of the SOFC system with the conventional reformer. The economic analysis revealed that the total capital cost/net electrical power was dependent on hydrogen recovery, net electrical efficiency and operation mode. At high electrical efficiency, the replacement of the conventional reformer with the membrane reactor became attractive. Finally, it was demonstrated that the MR-HPC-V was the best operation mode for integration with the SOFC system.

Suggested Reviewers:

Opposed Reviewers:

Department of Chemical Engineering
Faculty of Engineering
Chulalongkorn University

December 1, 2007

Dear the editor of Chemical Engineering Journal,

I would like to submit a research article entitled "Performance improvement of solid oxide fuel cell system using palladium membrane reactor with different operation modes" for your consideration for inclusion in Chemical Engineering Journal. The article is original and unpublished and is not being considered for publication elsewhere.

If you have any query, please do not hesitate to contact me. I am looking forward to hearing from you.

Sincerely yours,

(Associate Professor Suttichai Assabumrungrat)
Department of Chemical Engineering, Faculty of Engineering,
Chulalongkorn University, Bangkok 10330, Thailand
Tel: 662-2186878-82; fax:662-2186877
E-mail: Suttichai.A@chula.ac.th

List of Suggested Reviewers

1. Professor E. Croiset
   Department of Chemical Engineering, University of Waterloo, Canada
   Email: ecroiset@cape.uwaterloo.ca

2. Professor S.H. Chan
   Fuel Cell Strategic Research Programme, School of Mechanical and Aerospace Engineering, 50, Nanyang Avenue, Nanyang Technological University, Singapore 639798, Singapore
   Email: mshchan@ntu.edu.sg

*** Manuscript**

Submitted to Chemical Engineering Journal

Type of contribution: Full length article

Performance improvement of solid oxide fuel cell system using palladium membrane reactor with different operation modes

S. Vivanpatarakij [a], S. Assabumrungrat [a, *], N. Laosiripojana [b] and A. Arpornwichanop [c]

[a] *Center of Excellence in Catalysis and Catalytic Reaction Engineering, Department of Chemical Engineering, Faculty of Engineering, Chulalongkorn University, Bangkok 10330, THAILAND*

[b] *The Joint Graduate School of Energy and Environment, King Mongkut's University of Technology Thonburi, Bangkok 10140, THAILAND*

[c] *Control and Systems Engineering, Department of Chemical Engineering, Faculty of Engineering, Chulalongkorn University, Bangkok 10330, THAILAND*

[*] Corresponding author. fax: 662-218-6877,

E-mail address: Suttichai.A@chula.ac.th (S. Assabumrungrat)

Abstract

The performance improvement of a solid oxide fuel cell (SOFC) system by replacing a conventional reformer with a palladium membrane reactor was investigated. When pure hydrogen was extracted from the reaction mixture via the palladium membrane, the power density of the SOFC was improved, depending on the value of hydrogen recovery (ξ). Three operation modes of membrane reactors; i.e., high pressure compressor (MR-HPC), vacuum pump (MR-V) and combined high pressure compressor and vacuum pump (MR-HPC-V) were considered. Their overall SOFC system characteristics were compared with those of the SOFC system with the conventional reformer. The economic analysis revealed that the total capital cost/net electrical power was dependent on hydrogen recovery, net electrical efficiency and operation mode. At high electrical efficiency, the replacement of the conventional reformer with the membrane reactor became attractive. Finally, it was demonstrated that the MR-HPC-V was the best operation mode for integration with the SOFC system.

Keywords: SOFC; membrane reactor; palladium membrane; performance improvement

1. Introduction

A solid oxide fuel cell (SOFC) is a promising electrical power generator compared to conventional systems as it offers a wide range of applications, low emissions, fuel flexibility and high system efficiency. Although hydrogen is a main fuel for most type of fuel cells, the uses of various alternative fuels such as methane, methanol, ethanol, gasoline and other oil derivatives are possible in the presence of a reformer. To date, methane is a promising fuel as it is an abundant component in natural gas and the methane steam reforming technology is relatively well established. Therefore, it is the fuel of interest in this study.

A number of researches have been carried out aiming to improve performance of SOFCs. Novel cell components with better characteristics have been explored [1-3]. Some researchers have focused on the integration of SOFCs with other units such as a gas turbine for the efficient utilization of energy within the combined system [4-7]. A non-uniform cell potential operation (or multi-stage operation) has been proposed [8, 9, 10, 11]. Another attractive approach is to replace a conventional reformer with a palladium membrane reactor which has been successfully applied to many hydrogen-generating reactions [12]. As the fuel cell performance is dependent on hydrogen partial pressure in the anode feed [13], it was expected that by using the palladium membrane, pure hydrogen is extracted from the reaction mixture and, therefore, the performance of SOFC is improved.

Our preliminary study investigated a methanol-fueled SOFC system integrated with a palladium membrane reactor. The driving force for hydrogen separation was introduced by using a high pressure compressor which required high electrical power for the operation. It was demonstrated that the SOFC cells could be operated at a higher power density, resulting in a cost reduction of the SOFC cells. However, the

required large and expensive palladium membrane made the proposed system uneconomical [14].

Theoretically, a membrane reactor can be operated under different modes of driving force introduction, resulting in the differences in the required membrane area and power consumption. Therefore it is likely that the SOFC system integrated with a palladium membrane reactor may become economical than the system with a conventional reformer when appropriate choices of the operation mode of membrane reactor and operating condition are selected.

In this paper, the characteristics of the methane-fueled SOFC systems integrated with a palladium membrane reactor with different operation modes (i.e., high pressure compressor (MR-HPC), vacuum pump (MR-V) and combined high pressure compressor and vacuum pump (MR-HPC-V)) were investigated. Their economic analysis was compared with that of the SOFC system integrated with a conventional reformer in order to find a suitable operation mode of the membrane reactor for integrating with the SOFC system.

2. Theory

2.1 Methane steam reforming (MSR)

Methane steam reforming is a conventional method of hydrogen production. The major reactions taking place in the reactor are methane steam reforming (Eq.(1)), water gas shift reaction (Eq.(2)) and carbon dioxide methanation (Eq.(3)).

$$CH_4 + H_2O = CO + 3H_2 \quad (1)$$

$$CO + H_2O = CO_2 + H_2 \quad (2)$$

$$CH_4 + 2H_2O = CO_2 + 4H_2 \quad (3)$$

In order to avoid carbon formation problem, the feed containing a H_2O:CH_4 molar ratio of 2.5 (or high) is usually employed [15].

Mathematical models of methane steam reforming were reported by Xu and Froment (1989) [16]. The kinetic rates on Ni/$MgAl_2O_4$ catalyst were derived based on the Langmuir-Hinshelwood reaction mechanism. The rate expressions for reactions (1)-(3) are given by the following expressions:

$$r_1 = \frac{\frac{k_1}{p_{H_2}^{2.5}}\left(p_{CH_4}p_{H_2O} - \frac{p_{H_2}^3 p_{CO}}{K_1}\right)}{(DEN)^2} \tag{4}$$

$$r_2 = \frac{\frac{k_2}{p_{H_2}}\left(p_{CO}p_{H_2O} - \frac{p_{H_2}p_{CO_2}}{K_2}\right)}{(DEN)^2} \tag{5}$$

$$r_3 = \frac{\frac{k_3}{p_{H_2}^{3.5}}\left(p_{CH_4}p_{H_2O}^2 - \frac{p_{H_2}^4 p_{CO_2}}{K_3}\right)}{(DEN)^2} \tag{6}$$

where $DEN = 1 + K_{CO}p_{CO} + K_{H_2}p_{H_2} + K_{CH_4}p_{CH_4} + K_{H_2O}p_{H_2O}/p_{H_2}$ (7)

$$k_i = A_i \exp\left(\frac{-E_i}{RT}\right) ;\ i = 1, 2, 3 \tag{8}$$

$$K_j = B_j \exp\left(\frac{-\Delta H_j}{RT}\right) ;\ j = \mathrm{CO}, \mathrm{H_2}, \mathrm{CH_4}, \mathrm{H_2O} \tag{9}$$

The kinetic parameters for the methane steam reforming are summarized in Table 1.

2.2 Palladium membrane

A palladium membrane is well-known as a highly selective membrane for hydrogen separation. The ability of hydrogen transfer through the membrane is typically quantified in term of permeability. The hydrogen flux (N_{H_2}) is inversely proportional to the membrane thickness **(** δ **)** and directly proportional to the product of the hydrogen permeability (Q_0 **)** and the driving force (the difference in the square root of hydrogen partial pressure across the membrane).

$$N_{H_2} = \frac{Q_0}{\delta} exp(\frac{-E_D}{RT})(p_{H_2,r}^{0.5} - p_{H_2p}^{0.5}) \quad (10)$$

In order to achieve a high hydrogen flux, a thin film of palladium membrane is generally coated on a porous support with good mechanical property. In addition, the driving force is enhanced by installing a compressor and/or a vacuum pump. The required power (P_{pump}) for the compressor and vacuum pump can be calculated by using the Aspen Plus program. In this study, the efficiencies of both the compressor and the vacuum pump are assumed to be 85%.

2.3 Membrane reactor

A membrane reactor (MR) is a reaction system where separation unit and chemical reactors are combined together. The use of a palladium membrane reactor (Pd-MR) is a promising approach for methane steaming reforming (MSR). As the reactions are limited by equilibrium; the separation of hydrogen product via the selective palladium membrane can increase the conversion of methane and achieve a high-purity hydrogen product at the same time. To calculate the palladium membrane area, the membrane was divided into small increments represented by $dz_{Pd,i}$. The

corresponding hydrogen recovery ($H_{2,permeate_i}$) at each element can be computed by Eq. (11) and the total hydrogen recovery ($H_{2,permeate}$) obtained from the membrane reactor was the summation of hydrogen recovery at each element (Eq.(12)). The length of the membrane reactor ($z_{Pd,\ total}$) was extended until the hydrogen recovery reaches the target value ($H_{2,\ require}$) (Eq.(13)). The final membrane area which corresponds to the target hydrogen recovery represents the required membrane area (A_{Pd}) for the operation (Eq.(14)).

$$H_{2,permeate_i} = 2 \cdot \pi \cdot r_{ext} \cdot dz_{Pd,i} \cdot N_{H_2,i} \tag{11}$$

$$H_{2,permeate} = \sum_{i=1}^{n} H_{2,permeate_i} \tag{12}$$

$$z_{Pd,total} = \sum_{H_{2,permeate}=0}^{H_{2,permeate}=H_{2,require}} dz_{Pd,i} \tag{13}$$

$$A_{Pd} = 2 \cdot \pi \cdot r_{ext} \cdot z_{Pd,total} \tag{14}$$

2.4 SOFC

An SOFC unit consists of two porous ceramic electrodes (i.e. an anode and a cathode) and a solid ceramic electrolyte. In theory, both hydrogen and CO can react electrochemically with oxygen ions at the anode of the SOFC cells. However, it was reported that about 98% of current is produced by H_2 oxidation in common situations [17]. It is therefore assumed in this study that the CO electro-oxidation is neglected. The theoretical open-circuit voltage of the cell (E), which is the maximum voltage under specific operating conditions, can be calculated from the following equations [18]:

$$E = E_0 + \frac{RT}{2F}\ln\left(\frac{P_{H_2}P_{O_2}^{0.5}}{P_{H_2O}}\right) \quad (15)$$

$$E_0 = 1.253 - 2.4516\times10^{-4}T \quad (16)$$

The actual voltage (Eq.(17)) is usually lower than the open-circuit voltage due to the presence of polarization losses: ohmic polarization (Eq.(18)-(19)), activation polarization (Eq.(20)-(23)) and concentration polarization (Eq.(24)) [19].

$$V = E - (\eta_{ohm} + \eta_{Act} + \eta_{Conc}) \quad (17)$$

The ohmic polarization is the resistance of electron through electrode and electrolyte. The activation polarization is mostly illustration of a loss for driving the electrochemical reaction to completion. The concentration polarization occurs due to the mass transfer limitation through the porous electrodes.

Ohmic polarization:

$$\eta_{Ohm} = \sum \rho_j \delta_j \quad (18)$$

$$\rho_j = a_j \exp(b_j T) \quad (19)$$

Activation polarization:

$$i = i_0\left[\exp\left(\frac{\alpha n_e F \eta_{Act}}{RT}\right) - \exp\left(-\frac{(1-\alpha)n_e F \eta_{Act}}{RT}\right)\right] \quad (20)$$

$$\eta_{Act} = \frac{2RT}{n_e F}\sinh^{-1}\left(\frac{i}{i_0}\right); \text{ where } \alpha = 0.5 \quad (21)$$

$$i_{0,A} = 5.5\times10^{8}\left(\frac{p_{H_2}}{p}\right)\left(\frac{p_{H_2O}}{p}\right)\exp\left(\frac{-100\times10^{3}}{RT}\right) \quad (22)$$

$$i_{0,C} = 7.0\times10^{8}\left(\frac{p_{O_2}}{p}\right)^{m}\exp\left(\frac{-120\times10^{3}}{RT}\right) \quad (23)$$

Concentration polarization:

$$\eta_{Conc} = -\frac{2RT}{n_e F}\ln\left(\frac{y_{H_2}y^{I}_{H_2O}}{y^{I}_{H_2}y_{H_2O}}\right) \quad (24)$$

To simplify the calculation of the SOFC performance, it is assumed that both fuel and oxidant are well-diffused through the electrodes. Therefore, the concentration polarization losses ($\eta_{Conc,\ A}$ and $\eta_{Conc,\ C}$) are neglected. This assumption is valid when the current density is not very high [20]. Table 2 summarizes the values of the parameters of the ohmic polarization.

2.5 Configurations of different SOFC systems

The diagrams of different SOFC systems are illustrated in Figure 1. In a conventional system (Figure 1a.), methane and steam are fed to a reformer where they are converted to CO, CO_2 and H_2. The product gas containing hydrogen at a low concentration is directly introduced to the SOFC stack where electrical power is generated. The SOFC exhaust gases are combusted in a burner whose heat can be utilized for energy-demanding units in the system. When the conventional reformer is replaced by a membrane reactor, pure hydrogen is extracted from the reaction mixture and fed to the SOFC stacks. The term "hydrogen recovery (ξ)" is defined as the mole of hydrogen extracted by the membrane divided by the mole of hydrogen theoretically

produced based on the mole of methane feed (4 mol of H_2: 1 mol of CH_4). The term "fuel utilization (U_f)" represents the mole of hydrogen electrochemically consumed within the stack divided by the mole of hydrogen theoretically produced based on the mole of methane feed.

Three operation modes of a membrane reactor are considered in this study. For the membrane reactor with a high pressure compressor (MR-HPC) (Figure 1b.), the pressure of the permeation is kept at 1 atm while the driving force for hydrogen permeation is enhanced by using the high pressure compressor. In the second case (Figure 1c.), the permeation side is kept at below atmospheric pressure by using a vacuum pump. It is noted that the low pressure compressor is still required at the inlet of the conventional reformer and the membrane reactor in order to feed the reactants to the system. In the last configuration (Figure 1d.), both the high pressure compressor and the vacuum pump are used. In all SOFC systems with the membrane reactor, the residue gas in the reaction gas mixture and the exhausted gas from the SOFC stacks are combusted in the burner similar to the case with the conventional reformer. Table 3 summarizes the standard condition of the SOFC system in this study.

2.6 Economic analysis

Economic analysis was carried out to compare the costs of the SOFC systems incorporated with palladium membrane reactors of different operation modes with that of the system with the conventional reformer. The total capital cost includes the costs of compressor, vacuum pump, SOFC stack (1500 \$/m^2) [21] and Pd membrane (746 \$/m^2) [22]. The compressor cost and vacuum pump cost (\$) were described by the following expressions, Eq.25 and Eq.26 [23].

$$\text{Cost of compressor}\,(\$) = 1.49 \cdot HP^{0.71} \times 10^3 \qquad (25)$$

where: $10 < HP < 800$

$$\text{Cost of vacuum pump (\$)} = 2.59 \cdot X^{1.03} \times 10^5 \quad (26)$$

where: $0.01 < X < 0.52$ (lbs H_2/h)/(suction Torr)

3. Results and Discussion

The study began with the model validation of the methane steam reforming in a conventional reformer. The calculations were based on the condition reported in the literature [19]; i.e., H_2O:CH_4 ratio = 3, GHSV = 1067 h^{-1} and reformer pressure = 1 atm. As shown in Figure 2, it is obvious that our calculation results are in good agreement with those reported earlier [19] for all temperature ranges (723-773 K). The deviations are in the range between 3-5%. Then, the SOFC model was verified. Figure 3 shows the relationship between the power density and current density at three temperature levels; i.e., 1023, 1073 and 1123 K. In the simulation, pure hydrogen was fed to the SOFC and the fuel utilization (U_f) was kept at 80%. Again, our calculations show good agreement with those reported in the previous literature [18].

In order to demonstrate the benefit from replacing of the conventional reformer with the membrane reactor, the plots of the power density and electrical efficiency against the current density of different systems are compared (Figure 4). The fuel utilization and operating temperature were kept at 80% and 1073 K, respectively. It is obvious that the SOFC system with the membrane reactor offers higher power density and electrical efficiency than that with the conventional reformer, particularly at higher values of hydrogen recovery (ξ). At ξ = 95%, the increase of the maximum power density of 25% can be achieved. However, when the membrane reactor is operated at too low hydrogen recovery (e.g., ξ = 80.6%), the use of the palladium membrane reactor can not compete the use of the conventional

reactor due to the fuel depletion in the anode of the SOFC. Therefore, the membrane reactor has to be operated at a sufficiently high hydrogen recovery (ξ).

According to the operation of membrane reactors, various operation modes are possible for enhancing the driving force of hydrogen permeation through the membrane. The selection of suitable operation mode and operating condition should be based on the consideration of the required membrane area and power consumption. Figure 5 shows the effect of the compressor pressure on the required palladium membrane area and the required power for the case of the membrane reactor with a high pressure compressor (MR-HPC). The pressure in the permeation side was always kept at 1 atm. The results indicate that when the compressor is operated at higher pressures, the membrane reactor requires less membrane area but higher compressor power. For the membrane reactor with a vacuum pump (MR-V), the results shown in Figure 6 indicate that when the vacuum pump pressure is reduced, the required membrane area decreases initially and then levels off but the overall power consumption for operating the vacuum pump and the low pressure compressor continuously increases. Comparison between the MR-HPC and the MR-V reveals that the MR-V generally requires less membrane area but higher power consumption. The other operation mode of the membrane reactor considered in this study is the combination of both high pressure compressor and vacuum pump (MR-HPC-V). Figure 7 shows the effects of the compressor pressure (between 2-5 atm) and the vacuum pump pressure (between 0.01-0.2 atm) on the required membrane area and the power consumption for ξ = 90%. Similar trends as the effects of the compressor pressure and the vacuum pump pressure on the required membrane area and the power consumption are observed. For comparison among the three operation modes, considering the case with the required membrane area of 25 m^3 and the hydrogen

recovery of 90%, it is obvious that within the range of pressure studied in the MR-HPC, even with the highest pressure (30 atm), the hydrogen recovery of 90% can not be achieved. For the MR-V, the required vacuum pump pressure and power consumption are about 0.035 atm and 50 kW, respectively. For the MR-HPC-V, the power consumption also depends on the choice of the operating pressure of the high pressure compressor. At P_R = 2, 3, 4 and 5 atm, the vacuum pump pressures are 0.088, 0.127, 0.162 and 0.198 atm, respectively while the required power consumptions are 50, 52.5, 54 and 55 kW, respectively. It is therefore obvious for the MR-HPC-V that the load of the vacuum pump can be reduced by using the high pressure compressor.

It is clear from the previous paragraph that the operation modes of the membrane reactor and the operating condition (pressure) play an important role on the membrane area and the power requirement. The economic analysis is essential for selecting a suitable operation mode of the membrane reactor for the SOFC system. Table 4 provides an example of the economic analysis of the SOFC systems with different operation modes. In all systems, the hydrogen recovery (ξ) and the fuel utilization (U_f) were set at 90% and 80%, respectively. The compressor was operated at 30 atm for the MR-HPC while the vacuum pump was operated at 0.035 atm for the MR-V. For the MR-HPC-V, the compressor and the vacuum pump were operated at 5 and 0.135 atm, respectively. The net electrical power was 371.4 kW corresponding to the overall electrical efficiency of 45.3%. However, the actual electrical power to be generated for the cases with the conventional reformer, MR-HPC, MR-V and MR-HPC-V are 373.7, 429.8, 426.8 and 427.5 kW, respectively. The additional powers are required to operate the compressor and/or vacuum pump in the systems. It should be noted that for all cases the heat obtained from the burner and the SOFC is sufficient to provide to all heat-demanding units in the systems. Regarding the required SOFC

area, it is clear that the uses of membrane reactors could reduce the requirement of the overall SOFC area; however, they require additional cost on the palladium membrane and the compressor and/or vacuum pump. The total capital cost of each system could be calculated. The values of the total capital cost followed the order: MR-HPC-V < MR-HP-C < MR-V < conventional. Obviously, based on the same net electrical power output, the total capital costs of the SOFC systems with the membrane reactors were lower than that of the conventional SOFC system. The MR-V was the most expensive among different operation modes due to the expensive vacuum pump. The MR-HPC-V was found to be the most attractive operation mode under this condition.

The economic analysis at various values of hydrogen recovery (85, 90 and 95%) and overall electrical efficiency (40.7, 45.3 and 47.7%) were considered and the corresponding values of the total capital cost/net electrical power were calculated for the cases with the conventional reformer, MR-HPC, MR-V and MR-HPC-V. As shown in Figure 8, the total capital cost/net electrical power is dependent on the hydrogen recovery, electrical efficiency and operation mode. In all systems, the values of the total capital cost/net electrical power increases with the increase of the electrical efficiency because the SOFC needs to operate at a lower power density to achieve the high electrical efficiency, resulting in the higher SOFC area and consequently the higher total capital cost. When the system is operated at a higher hydrogen recovery, the value of the total capital cost/net electrical power decreases due to the improved power density of the SOFC as demonstrated earlier in Figure 4. It is observed that for η = 40.7%, the replacement of the conventional reformer with the membrane reactor is not attractive at ξ = 85%. However, it becomes quite comparable at ξ = 90% and attractive at ξ = 95%. At high electrical efficiency, the use of membrane reactor offers lower total capital cost/net electrical power than the

use of the conventional reformer. Comparison between the different operation modes of the SOFC systems with membrane reactor reveals that the MR-HPC-V is the most attractive operation mode in all ranges of hydrogen recovery and electrical efficiency.

4. Conclusion

Performance of the SOFC systems fed by methane was analyzed to investigate the potential benefit from replacing the conventional reformer with the palladium membrane reactor. Obviously, the use of the palladium membrane reactor can improve the power density of the SOFC. Three operation modes of membrane reactors; i.e., MR-HPC, MR-V and MR-HPC-V were considered. The economic analysis of the different systems revealed that the total capital cost/net electrical power is dependent on hydrogen recovery, electrical efficiency and operation mode of the membrane reactor. The use of the palladium membrane reactor becomes attractive over the conventional reformer when the system is operated at high values of electrical efficiency and hydrogen recovery. Finally, it was demonstrated that the MR-HPC-V was the best operation mode for integration with the SOFC system.

Acknowledgment

The supports from The Thailand Research Fund and Commission on Higher Education are gratefully acknowledged.

References

[1] S.P. Yoon, J. Han, S.W. Nam, T.H. Lim, S.A. Hong, J. Power Sources 136 (2004) 30-36.

[2] S.D. Kim, S.H. Hyun, J. Moon, J.H. Kim, R.H. Song, J. Power Sources 139 (2005) 67-72.

[3] S.P. Simner, J.F. Bonnett, N.L. Canfield, K.D. Meinhardt, J.P. Shelton, V.L. Sprenkle, J.W. Stevenson, J. Power Sources 113 (2003) 1-10.

[4] P. Kuchonthara, S. Bhattacharya, A. Tsutsumi, J. Power Sources 124 (2003) 65-75.

[5] J. Palsson, A. Selimovic, L. Sjunnesson, J. Power Sources 86(2000) 442-448.

[6] B. Fredriksson Möller, J. Arriagada, M. Assadi, I. Potts, J. Power Sources 131 (2004) 320-326.

[7] Y. Inui, T. Matsumae, H. Koga, K. Nishiura, Energy Conversion and Management 46 (2005) 1837-1847.

[8] A. Selimovic, J. Palsson, J. Power Sources 106 (2002) 76-82.

[9] S.F. Au, N. Woudstra, K. Hemmes, J. Power Sources. 122 (2003) 28-36.

[10] S.M. Senn, D. Poulikakos, Electrochemistry Communications 7 (2005) 773-780.

[11] S. Vivanpatarakij, S. Assabumrungrat, N. Laosiripojana, J. Power Sources 167 (2007) 139-144,

[12] E. Kikuchi, Catalysis Today 56 (2000) 97-101.

[13] S.H. Chan, O.L. Ding, Int. J. Hydrogen Energy. 30 (2005) 167-179.

[14] W. Sangtongkitcharoen, S. Vivanpatarakij, N. Laosiripojana, A. Arpornwichanop, S. Assabumrungrat, Chemical Engineering Journal.2007, doi:10.1016/ j.cej.2007.06.021

[15] H.J. Renner, R. Marschner, Catalytic reforming of natural gas and other hydrocarbon, Ullmann's Encyclopedia of Industrial Chemistry fifth edition, VCH Verlagsgesellschaft, Weinheim, Germany. A2 (1985) 186–204.

[16] J. Xu, G.F. Froment, AICHE Journal 35 (1989) 88-96.

[17] M.A. Khaleel, Z. Lin, P. Singh, W. Surdoval, D. Collin, J. Power Sources 130 (2004) 136-148.

[18] E. Hernandez-Pacheco, M.D. Mann, P.N. Hutton, D. Singh, K.E. Martin, Inter J. Hydrogen Energy 30 (2005) 1221-1233.

[19] M. Pfafferodt, P. Heidebrecht, M. Stelter, K. Sundmacher, J. Power Sources 149 (2005) 53-62.

[20] J. Shu, B.P.A. Grandjean, S. Kaliaguine, Applied Catalysis A 119 (1994) 305-325.

[21] E. Riensche, U. Stimming, G. Unverzagt, J. Power Sources 73 (1998) 251-256.

[22] A. Criscuol, A. Basile, E. Drioli, O. Loiacono, J. Membr. Sci. 181 (2001) 21-27.

[23] S.M. Walas, Chemical Process Equipment Selection and Design. Butterworth, Inc. 1988 665-668.

Nomenclature

a	Constant in Eq.19	(Ω m)
A_{Pd}	Pd membrane area	(m^2)
b	Constant in Eq.19	(K)
E	Open circuit voltage (OCV)	(V)
E_0	Reversible potential	(V)
E_D	Activation energy for diffusion through membrane (1.57)	(kJ mol^{-1})
F	Faraday constant (96485.34)	(C mol^{-1})
$H_{2,permeate}$	Permeation hydrogen	(mol)
HP	Horse power in Eq.25	(HP)
i	Current density	(A m^{-2})
i_0	Exchange current density	(A m^{-2})
k	Adsorption parameters	(-)
K	Equilibrium constant	(-)
n_e	Electron transfer	(-)
N_{H_2}	Hydrogen flux	(mol s^{-1} m^{-2})
P_i	Partial pressure	(atm)
P_{com}, P_{vac}	Power requirement of compressor, vacuum pump	(kW)
P	Total pressure	(atm)
Q_0	Pre-exponential constant for membrane permeability (4.40×10^{-7})	(mol m^{-1} s^{-1} $Pa^{-0.5}$)
Q_{MR}	Heat of membrane reactor	(kW)
Q_R	Heat of reformer	(kW)
r_{ext}	External radius tube reactor	(m)

r_{int}	Internal radius tube reactor	(m)
R	Universal gas constant (8.31447×10^{-3})	(kJ mol^{-1} K^{-1})
T	Absolute temperature	(K)
U_f	Fuel utilization	(%)
W	Electrical work	(W)
X	Parameter in Eq.26	(lbs.H_2/h/suction Torr)
y_i^I	Mole faction of component *i* in bulk phase	(-)
z_{Pd}	Length of Pd membrane reactor	(m)

Greeks letters

α	electron transfer coefficient	(-)
η_i	Overpotential	(Ω m^2)
η	Electrical efficiency	(%)
δ	Thickness	(m)
ρ	Specific ohmic resistance	(Ω m)
ξ	Hydrogen recovery	(%)

Figure(s)

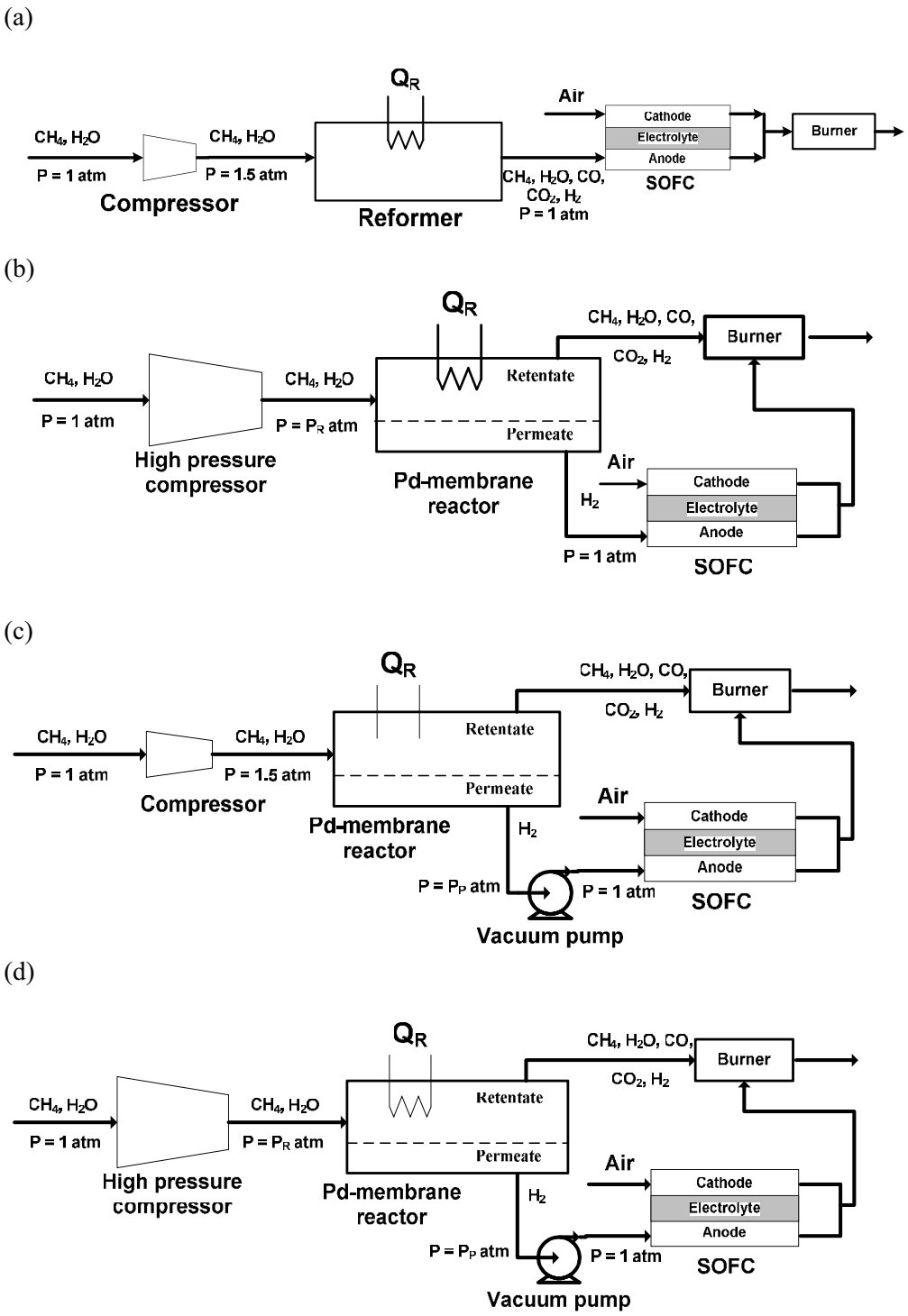

Fig. 1. Schematic diagrams of SOFC systems with different operation modes: (a) conventional reformer, (b) MR-HPC, (c) MR-V, (d) MR-HPC-V.

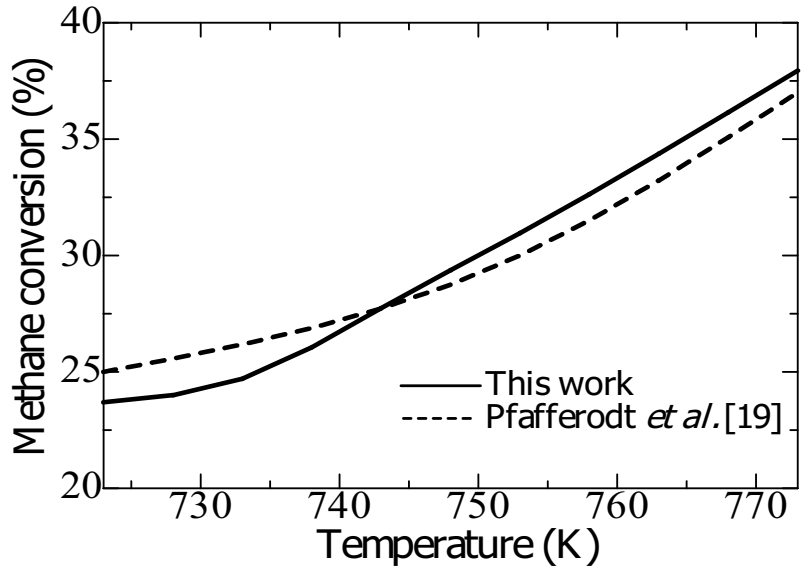

Fig. 2. Validation of the reformer model with experimental results from the literature [19] (P = 1 atm and H_2O:CH_4 = 3).

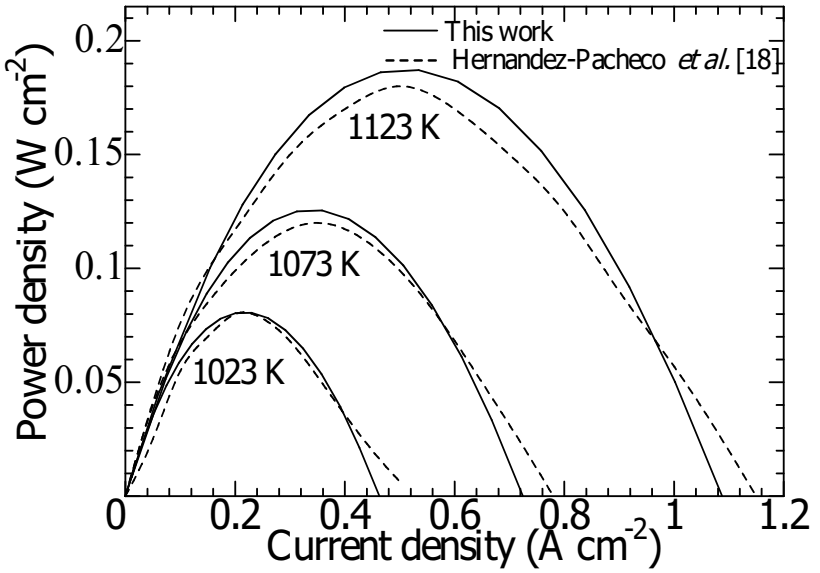

Fig. 3. Validation of SOFC model with results from the literature [18] (pure H_2 feed and U_f = 80%).

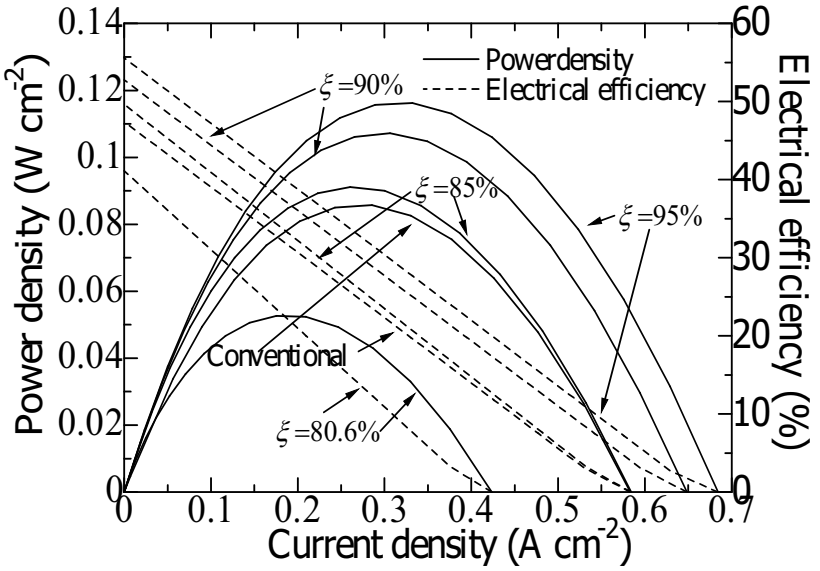

Fig. 4. Improvement of SOFC performance by using Pd membrane reactor (U_f =80% and T = 1073 K).

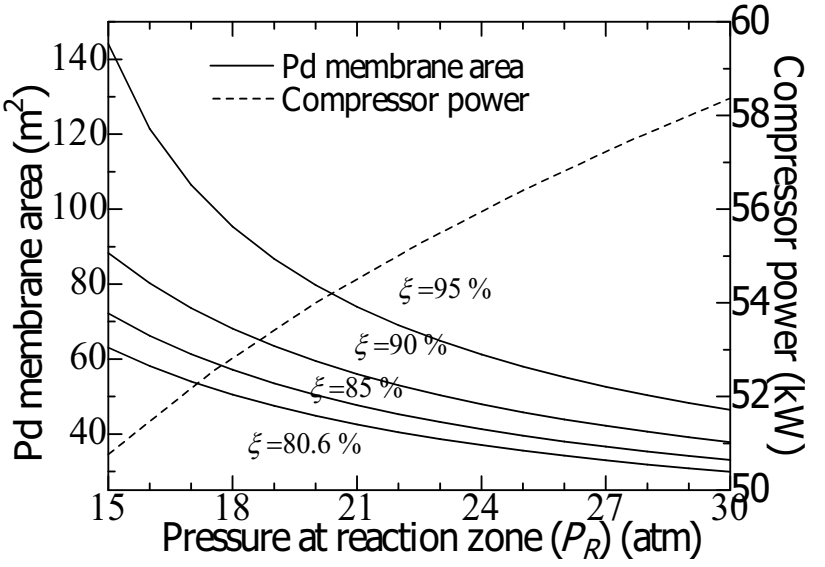

Fig. 5. Effect of reaction pressure on required Pd membrane area and compressor power (T = 773 K, P_R = 1 atm and H_2O:CH_4 = 3).

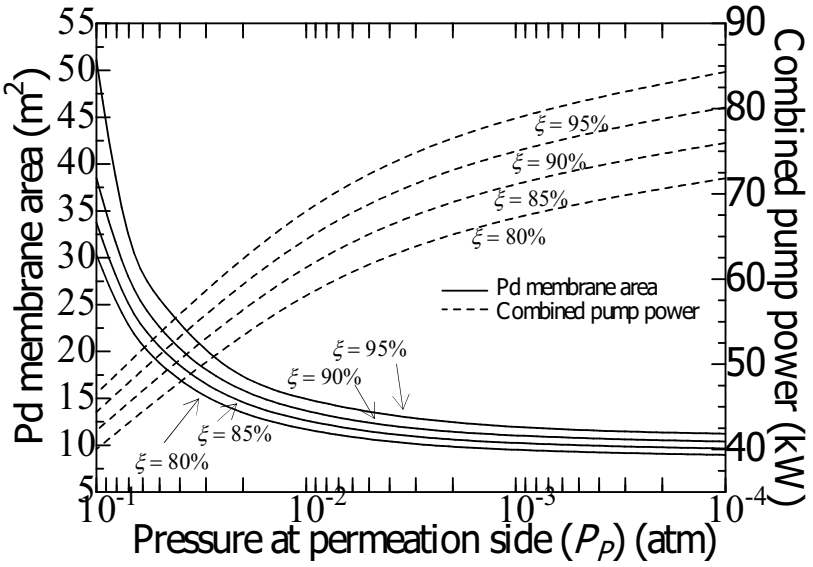

Fig. 6. Effect of permeation pressure on required Pd membrane area and vacuum pump power (T = 773 K, P_P = 1 atm and H_2O:CH_4 = 3).

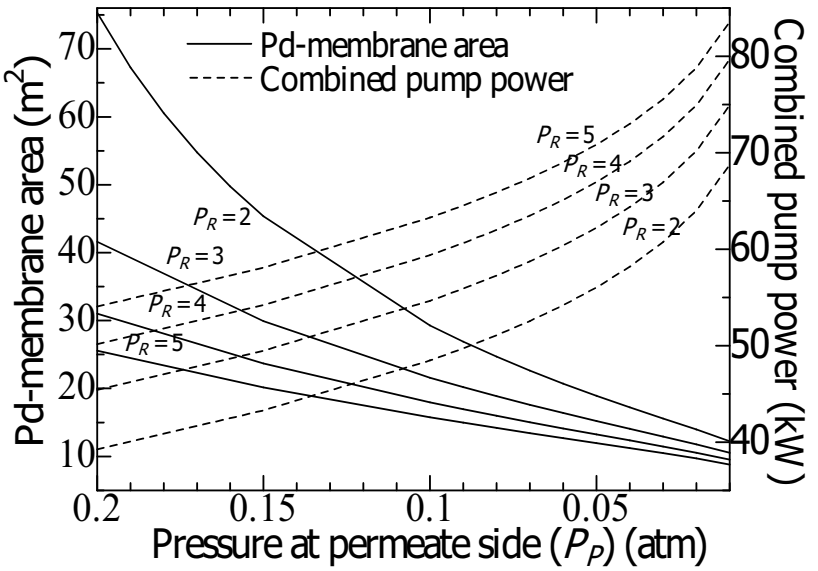

Fig. 7. Effect of reaction and permeation pressure on required Pd membrane area and power consumption (ξ = 90%, T = 773 K and H_2O:CH_4 = 3).

(a)

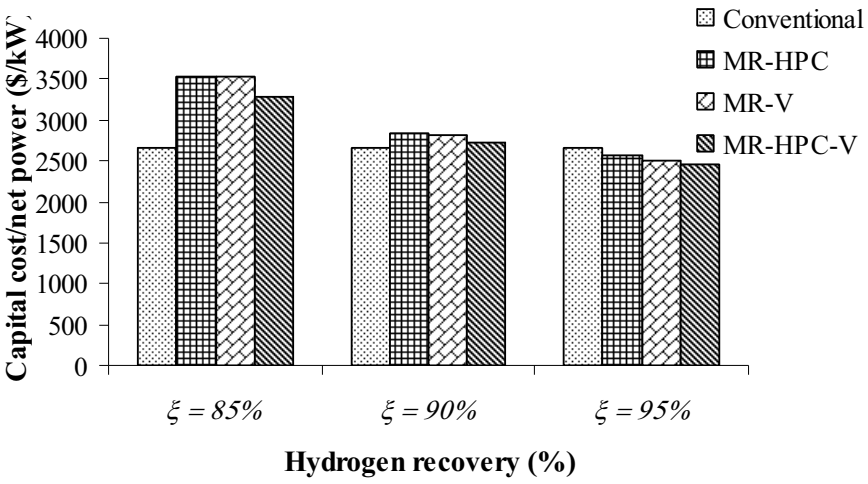
Capital cost/net power ($/kW)
4000
3500
3000
2500
2000
1500
1000
500
0
Conventional
MR-HPC
MR-V
MR-HPC-V
ξ = 85%
ξ = 90%
ξ = 95%
Hydrogen recovery (%)

(b)

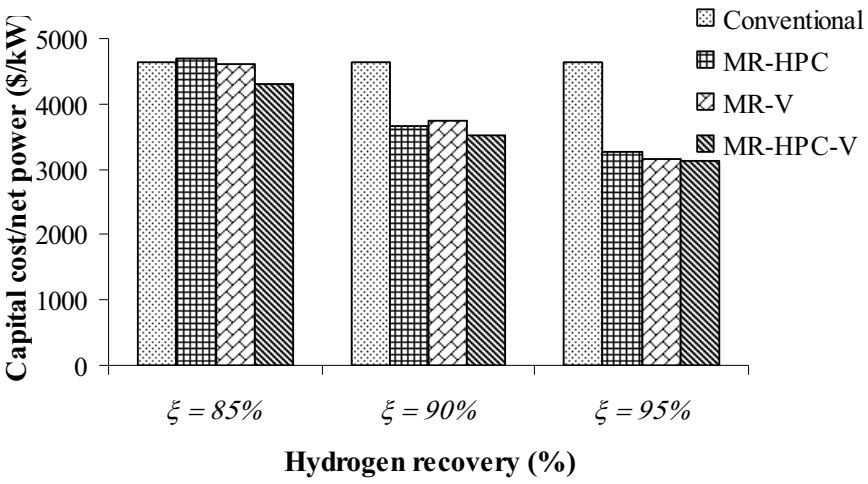
Capital cost/net power ($/kW)
5000
4000
3000
2000
1000
0
Conventional
MR-HPC
MR-V
MR-HPC-V
ξ = 85%
ξ = 90%
ξ = 95%
Hydrogen recovery (%)

(c)

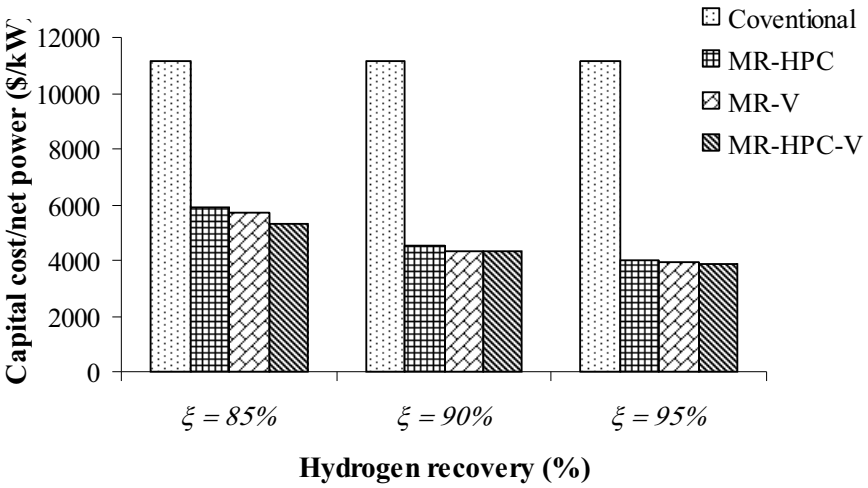

Fig. 8. Economic analysis of different SOFC systems: (a) $\eta = 40.7\%$, (b) $\eta = 45.3\%$ and (c) $\eta = 47.7\%$ (U_f= 80% and T = 1073 K).

Table(s)

Table 1 Kinetic parameters for methane steam reforming [16].

Parameter	Pre-exponential factor (A or B)	E or ΔH (kJ.mol^{-1})
k_1	4.225×10^{15} (mol atm$^{0.5}$ (g h)$^{-1}$)	240.10
k_2	1.955×10^{6} (mol (g h)$^{-1}$)	67.13
k_2	1.020×10^{15} (mol atm$^{0.5}$ (g h)$^{-1}$)	243.9
K_{CO}	6.65×10^{-4} (atm^{-1})	-38.28
K_{H2}	1.77×10^{5} (-)	88.68
K_{H2O}	6.12×10^{-9} (atm^{-1})	-82.90
K_{CH4}	8.23×10^{-5} (atm^{-1})	-70.65

Table 2 Ohmic polarization constants for Eqs.(18) and (19).

	a	b	δ (μm)
Anode	2.98×10^{-5}	-1392	50
Cathode	8.11×10^{-5}	600	50
Electrolyte	2.94×10^{-5}	10350	140

Table 3 Standard condition.

Parameter	Value
CH_4 input	1 (mol/s)
Reformer input H_2O:CH_4 ratio	3 (-)
U_f (fuel utilization)	80 (%)
Temperature of SOFC	1073 (K)
SOFC input Air:CH_4 ratio	15 (-)
Temperature of conventional reformer	973 (K)
Temperature of membrane reactor	773 (K)
Pressure of conventional reformer	1.5 (atm)
Pressure of SOFC	1 (atm)

Table 4 Economic analysis of the SOFC systems with different operation modes.

	Conventional	MR-HPC	MR-V	MR-HPC-V
Temperature of reformer (K)	923	773	773	773
Fuel utilization (U_f) (%)	80	80	80	80
H_2 Recovery (%)	-	90	90	90
Operating voltage (V)	0.610	0.696	0.691	0.692
Electrical power (kW)	376.7	429.9	426.8	427.5
Pressure at reaction side (P_R) (atm)	1.5	30	1.5	5
Compressor Power (kW)	5.3	58.4	5.3	20.3
Pressure at permeation side (P_P) (atm)	-	1.00	0.035	0.135
Vacuum pump power (kW)	-	-	50.	35.9
Net electrical power (kW)	371.4	371.4	371.4	371.4
Efficiency (%)	45.26	45.26	45.26	45.26
Pd membrane area (m^2)	-	38.17	19.12	18.76
SOFC area (m^2)	1143	866.72	877.86	843.34
Cost of Pd membrane (746 \$/m^2)	-	28,476	14,260	13,995
Cost of SOFC (1500 \$/m^2)	1,714,500	1,300,080	1,316,790	1,265,010
Saving cost on SOFC (\$)	-	414,420	397,710	449,490
Capital cost of compressor (\$)	5,979	32,194	5,979	17,200
Capital cost of vacuum pump (\$)	-	-	51,700	13,652
Saving cost of SOFC over Pd membrane (\$)	-	385,944	383,450	435,495
Total capital cost (\$)	1,720,479	1,360,750	1,388,729	1,309,857
Total capital cost/electrical energy (\$/kW)	4,568	3,166	3,254	3,064
Total Capital cost /net power (\$/kW)	4,633	3,664	3,739	3,527

Appendix 10

Elsevier Editorial System(tm) for Chemical Engineering and Processing: Process Intensification

Manuscript Draft

Manuscript Number:

Title: Performance of biogas-fed solid oxide fuel cell systems integrated with membrane module for CO2 removal

Article Type: Full Text Article

Keywords: Biogas; CO2-selective membrane; Solid oxide fuel cell; Thermodynamic analysis; Economic analysis

Corresponding Author: Professor Suttichai Assabumrungrat, Ph.D.

Corresponding Author's Institution: Chulalongkorn University

First Author: Pakorn Piroonlerkgul , B.Eng.

Order of Authors: Pakorn Piroonlerkgul , B.Eng.; Suttichai Assabumrungrat, Ph.D.; Navadol Laosiripojana , PhD; Adesoji A Adesina, PhD

Abstract: Two SOFC systems with CO2 capture, i.e., SOFC with CO2 capture from biogas feed (biogas-cap SOFC) and SOFC with CO2 capture from reformed gas (reformed gas-cap SOFC) have been investigated. Employing the sweep gas to increase the gas separation capability, both systems offered higher power density but lower electrical efficiency than those of the SOFC without CO2 capture (non-cap SOFC). The installation of a vacuum pump can improve the electrical efficiency of the biogas-cap SOFC but not for the reformed gas-cap SOFC. Economic analysis revealed that the biogas-cap SOFC with sweep gas is superior to the other SOFC systems.

Department of Chemical Engineering
Faculty of Engineering
Chulalongkorn University

Professor A. Górak
Technische Universität Dortmund, Chair of Fluid Separations,
Department of Biochemical and Chemical Engineering,
Emil-Figge-Strasse 70, D-44227 Dortmund,
Germany,
Email: Gorak.CEP@ct.uni-dortmund.de

April 2, 2008

Dear Professor Górak,

I would like to submit a research article entitled "Performance of biogas-fed solid oxide fuel cell system integrated with membrane module for CO_2 removal" for your consideration for inclusion in Chemical Engineering and Processing: Process Intensification. The article is original and unpublished and is not being considered for publication elsewhere.

The paper investigates improvement in the performance of SOFC system by incorporation of a CO_2-selective membrane separation unit via engineering and economic analyses. Different integration configurations have been considered in order to explore an appropriate choice and benefits of the integration.

If you have any query, please do not hesitate to contact me. I am looking forward to hearing from you.

Sincerely yours,

(Professor Suttichai Assabumrungrat)
Department of Chemical Engineering, Faculty of Engineering,
Chulalongkorn University, Bangkok 10330, Thailand
Tel: 662-2186878-82; fax:662-2186877
E-mail: Suttichai.A@chula.ac.th

List of Suggested Reviewers

1. Professor You, H.-X.; Chemical Engineering College, Dalian University of Technology, Dalian 116012, China; email:youhx@sina.com

2. Professor Diwekar, U.M.; Vishwamitra Research Institute, Center for Uncertain Systems, Tools for Optimization and Management, 34, N.Cass Ave., Westmont, IL 60607, United States; email:urmila@vri-custom.org

Submitted to Chemical Engineering and Processing: Process Intensification

Type of contribution: Full text article

Performance of biogas-fed solid oxide fuel cell systems integrated with membrane module for CO_2 removal

P. Piroonlerkgul [a], S. Assabumrungrat [a,*], N. Laosiripojana [b] and A.A. Adesina [c]

[a] Center of Excellence in Catalysis and Catalytic Reaction Engineering,
Department of Chemical Engineering, Faculty of Engineering, Chulalongkorn University,
Bangkok 10330, THAILAND

[b] The Joint Graduate School of Energy and Environment,
King Mongkut's University of Technology Thonburi, Bangkok 10140, THAILAND

[c] Reactor Engineering & Technology Group,
School of Chemical Sciences & Engineering, University of New South Wales,
Sydney, NSW, Australia 2052

Corresponding author (FAX: 662-218-6877, Email: Suttichai.A@chula.ac.th)

Abstract

Two SOFC systems with CO_2 capture, i.e., SOFC with CO_2 capture from biogas feed (biogas-cap SOFC) and SOFC with CO_2 capture from reformed gas (reformed gas-cap SOFC) have been investigated. Employing the sweep gas to increase the gas separation capability, both systems offered higher power density but lower electrical efficiency than those of the SOFC without CO_2 capture (non-cap SOFC). The installation of a vacuum pump can improve the electrical efficiency of the biogas-cap SOFC but not for the reformed gas-cap SOFC. Economic analysis revealed that the biogas-cap SOFC with sweep gas is superior to the other SOFC systems.

Key words: Biogas; CO_2-selective membrane; Solid oxide fuel cell; Thermodynamic analysis; Economic analysis

1. Introduction

In view of current and foreseeable energy shortage and environmental scenario, the exploitation of a renewable energy sources has attracted much attention in recent literature. Biogas is one of the renewable energy sources derived from the processing of the waste streams with variable nature, e.g. farm residues, industrial effluents and landfill. Compared to fossil fuel, biogas offers advantages of being renewable and free of non-methane hydrocarbon. A general problem found in the utilization of biogas for electricity generation is that most of biogas is derived from small-scale sources, e.g. farm and municipal wastes, therefore, biogas can only be employed in a small size power generator (5-100 kW) [1]. Furthermore, the biogas composition fluctuates markedly depending on its sources [2]; it generally contains methane (40-65%) and carbon dioxide (30-40%) with small amount of H_2S as an impurity.

The solid oxide fuel cell (SOFC) is a promising electricity generation technology owing to its high performance and environmentally-friendly operation. SOFC fuelled by biogas can offer high efficiency (30-40%) even in small size power generations (< 20 kW) [1]. Additionally, it can achieve reasonable performance even at low methane contents in biogas. Laboratory tests suggest that, the SOFC electrical efficiency drops only 5% when the methane contents in biogas diminish from 70 mol% to 30 mol% [3]. Moreover, biogas can be internally-reformed in SOFC stack due to the typical high stack temperature (1073-1273 K). However, if biogas is directly fed into the SOFC stack, carbon deposition can easily occur [4], in addition, a large temperature gradient is also a major problem for the SOFC stack fed directly by biogas due to a strong cooling effect caused by the fast reforming reaction [5, 6]. A fuel processor is normally installed in the biogas-fuelled SOFC system to relieve these problems. Our recent work has shown that the addition of excess steam, CO_2 or air can inhibit the carbon formation in the fuel

processor [7]. The use of steam as the reforming agent in the fuel processor (steam reforming) offers higher performance for SOFC system compared with the use of air (partial oxidation) [8]. Nevertheless, with an increase in CO_2 content in biogas, the H_2 yield of the pre-reformer reduces due to the reaction between CO_2 and H_2 generated from the steam reforming reaction via Reverse water gas shift reaction, RWGS. The decrease in H_2 concentration in the reformed gas can diminish the power density and the investment cost also increase due to the enlargement in the SOFC stack size [9]. Furthermore, the presence of large amounts of CO_2 in the pre-reforming product can decrease the cell potential. Suwanwarangkul et al. [10] studied the performance of SOFC fuelled by the mixture of H_2 and CO_2 gases with several H_2/CO_2 ratios. They reported that when H_2 concentration decreases from 100% to 20%, the SOFC cell potential decreases by 20% due to the impact of the RWGS reaction. Hence, the separation of CO_2 from the biogas feed or from the reformed gas is the interesting way to increase the biogas-fuelled SOFC system performance.

Currently, there are various available CO_2 separation technologies e.g. chemical absorption, adsorption and membrane technology. Membrane technology has been widely tested and presently applicable in the capture of CO_2 in natural gas [11]. Compared with CO_2 absorption technology which is conventionally used, membrane technology offers the advantages of operational flexibility in handling feed streams with variable flow rates and compositions. Polymeric membrane is one of the interesting choices due to its low capital investment costs compared with other types of membrane [12]. Moreover, the process equipment for the polymeric membrane operation is also simple and easy to handle. Selection of polymeric membrane for gas separation is based on two parameters; permeability and permselectivity. Polyimide membrane is the more attractive gas separator because it offers higher permselectivity and permeability

compared to membranes derived from other polymers [13]. The use of capillary module with polyimide membrane for the CH_4 enrichment in biogas mixtures (CH_4, CO_2 and H_2S) was also investigated and the results showed that CH_4 concentration in biogas increases from 55-85% up to 91-94.4% [14]. Poly(dimethylsiloxane) (PDMS) and poly(1-trimethylsilyl-1-propyne) (PTMSP) can be utilized in the separation of acid gases (CO_2 and H_2S) from syngas at room temperature due to their high CO_2/H_2 selectivity. Nonetheless, H_2 permeance increases at elevated temperature [15]. It should be noted that a common problem arising from the use of these polymeric membranes is the instability of the membranes at high operating temperature [16].

In the present study, an integration of a biogas-fuelled SOFC system and CO_2-selective membrane technology was investigated. The improvement in the SOFC power density following to the installation of CO_2-selective membrane was considered. Two configurations are applied in this study: 1) SOFC with the capture of CO_2 from the biogas feed (biogas-cap SOFC) and 2) SOFC with the capture of CO_2 from the reformed gas (reformed gas-cap SOFC). Furthermore, two available operation modes in the permeation side of membrane i.e. the exploitation of sweep gas and the exploitation of vacuum pump were also investigated. Thermodynamic analysis was performed to evaluate the performance indicators (overall electrical efficiency and power density) of these configurations and operations and to compare them with those of the SOFC system without CO_2-selective membrane installation. Lastly, an economic analysis was employed to identify whether the CO_2-selective membrane should be installed into the SOFC system.

2. Modeling

2.1 Fuel processor

The key steps are the dry reforming (Eq.(1)) and the steam reforming (Eq.(2)) reactions.

$$CH_4 + CO_2 \leftrightarrow 2H_2 + 2CO \quad (1)$$

$$CH_4 + H_2O \leftrightarrow 3H_2 + CO \quad (2)$$

Due to the high CO_2 concentration in biogas feed, the mildly endothermic reverse water gas shift reaction (RWGS) (Eq.(3)) also takes place in the fuel processor inhibiting the generation of hydrogen.

$$CO_2 + H_2 \leftrightarrow H_2O + CO \quad (3)$$

To simplify the calculations, the fuel processor is assumed to operate isothermally with the exit gas reaching equilibrium composition. The relevant thermodynamic equilibrium constants for the dry reforming, steam reforming and RWGS are provided in Eqs. (4), (5) and (6), respectively.

$$K_{eq,dry} = \frac{P_{H_2}^2 P_{CO}^2}{P_{CH_4} P_{CO_2}} \quad (4)$$

$$K_{eq,steam} = \frac{P_{H_2}^3 P_{CO}}{P_{CH_4} P_{H_2O}} \quad (5)$$

$$K_{eq,RWGS} = \frac{P_{H_2O} P_{CO}}{P_{H_2} P_{CO_2}} \quad (6)$$

where $K_{eq,i}$ is the equilibrium constant of reaction i and may be calculated from:

$$K_{eq,i} = e^{-\frac{\Delta G_i}{RT}} \quad (7)$$

2.2 SOFC stack model

Electrochemical reactions taking place in the SOFC stack convert the chemical energy of the fuel directly to electricity. At the cathode section, oxygen is reduced to oxygen ions (Eq.(8)) which migrates through the solid electrolyte to react with the fuel (Eq.(9)) at the anode section. Only hydrogen is assumed to react electrochemically with oxygen ions since the H_2 electro-oxidation is much faster than the CO electro-oxidation [17] and the rate of WGS reaction is fast at high temperatures [18-20]. It is also assumed that methane remaining from the fuel processor is consumed via the steam reforming and that the anode gas compositions are always at their equilibrium along the cell length due to the fast kinetics particularly at high temperature of SOFC. It is noted that Ni-YSZ, YSZ and LSM-YSZ are chosen as the materials for the anode, electrolyte and cathode of the SOFC stack, respectively.

$$\frac{1}{2}O_2 + 2e^- \longrightarrow O^{2-} \quad (8)$$

$$H_2 + 2O^{2-} \longrightarrow H_2O + 2e^- \quad (9)$$

The open circuit voltage (E) of the cell can be calculated from the following Nernst equation:

$$E = E^0 + \frac{RT}{2F}\ln\left(\frac{P_{H_2}P_{O_2}^{\frac{1}{2}}}{P_{H_2O}}\right) \quad (10)$$

The actual cell potential (V) (Eq. (11)) is always less than the open circuit voltage (E) due to the existence of various overpotentials; i.e., ohmic overpotential (η_{ohm}), activation overpotential (η_{act}) and concentration overpotential (η_{conc}).

$$V = E - \eta_{ohm} - \eta_{act} - \eta_{conc} \quad (11)$$

2.2.1 Ohmic overpotential (η_{Ohm})

The ohmic overpotential is the resistance to flow of electron through the electrodes and the interconnectors as well as resistance to the flow of ions through electrolyte. This voltage drop is the vital one in all types of cells and is linearly proportional to current density (*i*). Due to the higher electronic conductivity of the electrodes and interconnectors compared to the electrolyte, only ohmic overpotential in the electrolyte is considered. The ohmic overpotential of SOFC may be expressed as [21]:

$$\eta_{ohmic} = 2.99 \times 10^{-11} iL \exp\left(\frac{10300}{T}\right) \quad (12)$$

2.2.2 Activation overpotential (η_{Act})

Activation overpotential is controlled by the kinetics at the electrode surface. It is directly related to the activation barrier and to be overcome by the reacting species in order to conduct the electrochemical reaction. For SOFC, due to the high temperature, the electrode reaction rate is fast, resulting in low activation polarization. The activation overpotentials in electrodes can be expressed by the Butler-Volmer equation,

$$i = i_0\left[\exp\left(\frac{\alpha z F \eta_{act}}{RT}\right) - \exp\left(-\frac{(1-\alpha) z F \eta_{act}}{RT}\right)\right] \quad (13)$$

In case of SOFC, α and *z* are set to 0.5 and 2 [22]. Therefore, the activation potential at the anode and cathode can be explicitly written as:

$$\eta_{act,j} = \frac{RT}{F} \sinh^{-1}\left(\frac{i}{2i_0}\right), \qquad j = a, c \quad (14)$$

It should be noted that the exchange current density (i_0) for the cathode side depends on partial pressure of both hydrogen and water as well as the operating temperature [23, 24]. For the anode side, i_0 depends on oxygen partial pressure and operating temperature as expressed in Eqs. (15)-(16) [25].

$$i_{0,a} = \gamma_a \left(\frac{P_{H_2}}{P_{ref}}\right)\left(\frac{P_{H_2O}}{P_{ref}}\right)\exp\left(-\frac{E_{act,a}}{RT}\right) \quad (15)$$

$$i_{0,c} = \gamma_c \left(\frac{P_{O_2}}{P_{ref}}\right)^{0.25}\exp\left(-\frac{E_{act,c}}{RT}\right) \quad (16)$$

2.2.3 Concentration overpotential (η_{Conc})

The concentration overpotential is the electrical loss arising from the difference between the reactant concentration on the reaction site and that in the bulk of the gas stream. It may be calculated from Eqs. (17) and (18):

$$\eta_{Conc,a} = \frac{RT}{2F}\ln\left[\frac{\left(1+\left(\frac{RT}{2F}\right)\left(\frac{l_a}{D_{a(eff)}p^I_{H_2O}}\right)i\right)}{\left(1-\left(\frac{RT}{2F}\right)\left(\frac{l_a}{D_{a(eff)}p^I_{H_2}}\right)i\right)}\right] \quad (17)$$

$$\eta_{Conc,c} = \frac{RT}{4F}\ln\left[\frac{p^I_{O_2}}{\left(p_c-\delta_{O_2}\right)-\left(\left(p_c-\delta_{O_2}\right)-p^I_{O_2}\right)\exp\left[\left(\frac{RT}{4F}\right)\left(\frac{\delta_{O_2}l_c}{D_{c(eff)}p_c}\right)i\right]}\right] \quad (18)$$

where δ_{O_2}, $D_{a(eff)}$ and $D_{c(eff)}$ are given as:

$$\delta_{O_2} = \frac{D_{O_2,k(eff)}}{D_{O_2,k(eff)}+D_{O_2-N_2(eff)}} \quad (19)$$

$$\frac{1}{D_{c(eff)}} = \frac{\xi}{n}\left(\frac{1}{D_{O_2,k}}+\frac{1}{D_{O_2-N_2}}\right) \quad (20)$$

$$D_{a(eff)} = \left(\frac{p_{H_2O}}{p_a}\right) D_{H_2(eff)} + \left(\frac{p_{H_2}}{p_a}\right) D_{H_2O(eff)} \quad (21)$$

$$\frac{1}{D_{H_2(eff)}} = \frac{\xi}{n}\left(\frac{1}{D_{H_2,k}} + \frac{1}{D_{H_2-H_2O}}\right) \quad (22)$$

$$\frac{1}{D_{H_2O(eff)}} = \frac{\xi}{n}\left(\frac{1}{D_{H_2O,k}} + \frac{1}{D_{H_2-H_2O}}\right) \quad (23)$$

The relationship between the effective diffusivity and the molecular diffusivity, $D_{A\text{-}B}$, is:

$$D_{(eff)} = \frac{n}{\xi} D_{A-B} \quad (24)$$

Knudsen diffusivity, $D_{A,K}$, may be estimated from:

$$D_{A,K} = 9700 r_p \sqrt{\frac{T}{M_A}} \quad (25)$$

The molecular diffusivity may be obtained from Chapman-Enskog equation (Eq. (26)) [26]:

$$D_{A-B} = 1.8583 \times 10^{-3} \left(\frac{T^{\frac{3}{2}} \left(\frac{1}{M_A} + \frac{1}{M_B}\right)^{\frac{1}{2}}}{P \sigma_{AB}^2 \Omega_D} \right) \quad (26)$$

where σ_{AB} is the collision diameter (Å) which is equal to $\frac{\sigma_A + \sigma_B}{2}$. Ω_D is computed from Eq. (27) below [27]:

$$\Omega_D = \frac{A}{T_k^B} + \frac{C}{\exp(D \cdot T_k)} + \frac{E}{\exp(F \cdot T_k)} + \frac{G}{\exp(H \cdot T_k)} \quad (27)$$

where T_k is equal to $\frac{T}{\varepsilon_{AB}}$ and A, C, E and G are constants for each gas.

2.3 Membrane Module

A membrane module for CO_2 removal is installed in the SOFC system. Fig. 1 shows the configuration of the membrane tube. Feed gas containing CO_2 is introduced to the inner side of the membrane, where pressure is maintained at 1.5 atm and negligible axial pressure gradient is assumed. To enhance the rate of CO_2 removal, the partial pressure of CO_2 was reduced by introducing a sweep gas (air) or using a vacuum pump at the shell side of the membrane. Steady-state mass balances in both tube and shell sides of the membrane provide:

$$\frac{dR_i}{dA} = -\frac{p_i}{\delta}\left(P_R x_i - P_P y_i\right) \quad (28)$$

$$\frac{dPe_i}{dA} = \frac{p_i}{\delta}\left(P_R x_i - P_P y_i\right) \quad (29)$$

In this study, 6FDA-DAT polyimide is chosen for the separation of CO_2 from the biogas feed due to its high CO_2/CH_4 selectivity [28], whereas PDMS (polydimethylsiloxane) membrane is employed to separate CO_2 from the reformed gas due to its high CO_2/H_2 selectivity [29]. According to the high-temperature instability of membrane, the operating temperature of 298 K is assumed for these membrane modules. The values of parameter used in the calculation for the membrane module are summarized in Table 1.

2.4 Afterburner and heat exchanger

At the outlets of the SOFC stack, the anode and cathode exhaust gases are mixed for the post combustion. Total combustion is presumed in the afterburner; hence methane, carbon monoxide and hydrogen contents in the flue gas are assumed to be zero. The heat obtained is then supplied to several heat-demanding units in the SOFC system such as

feed preheaters and fuel processor. All the heat exchangers are assumed to operate without heat loss in this study.

2.5 Vacuum pump and compressor

For the calculations of vacuum pump and compressor, the outlet gas temperature (T_{out}) and power consumption ($\dot{W}_{comp}$) can be estimated by employing Eqs. (30) and (31), respectively [30]. The efficiency (η_c) of 75% is assumed in this study.

$$T_{out} = T_{in}\left(1+\frac{1}{\eta_c}\left(\left(\frac{P_{out}}{P_{in}}\right)^{\frac{\gamma-1}{\gamma}}-1\right)\right) \tag{30}$$

$$\dot{W}_{comp} = -\dot{m}\int_{T_{in}}^{T_{out}} C_p dT \tag{31}$$

where $$\gamma = \frac{C_p}{C_p - R}. \tag{32}$$

2.6 Calculation procedure for determining SOFC stack performance

For the SOFC operation, a constant operating voltage (V) along the cell length is assumed due to the high electrical conductivity of the current collector. The operating voltage is kept at 0.7 V in this study. The quantity of air fed as the oxidant into the SOFC cathode is 4 times that of theoretical amount required to combust the biogas fuel. Due to the changes in gas compositions along the cathode and anode sections, the open circuit voltage and consequently the current density vary with the distance from the stack entrance. In this work, the calculation takes place for each small fuel utilization region employing the mathematical model presented in Section 2.2. The thermodynamic equilibrium is assumed for the anode gas in each region because the anode material is also active for the reactions and the operating temperature of the SOFC stack is high. In each region, the open circuit voltage, overpotentials, equilibrium composition of anode fuel, stack area and current density are calculated. The stack areas calculated in each region are added up to yield the total stack area. Finally, the current calculated from the fuel utilized in the stack is divided by the total stack area to obtain the average current density, and the average power density can be then determined. The electrical efficiency and the fuel utilization are computed from Eqs. (33) and (34), respectively.

$$SOFC\ plant\ efficiency = \frac{net\ electricity\ generated}{LHV\ of\ biogas\ feed} \quad (33)$$

$$Fuel\ utilization = \frac{total\ H_2\ consumed\ in\ SOFC\ stack}{Inlet\ molar\ flow\ rate\ of\ H_2\ and\ CO} \quad (34)$$

2.7 SOFC system configurations

Two biogas-fed SOFC systems with CO_2 capture unit are proposed in this study, i.e. the SOFC system with the CO_2 capture from the biogas (biogas-cap SOFC) and the SOFC system with the CO_2 capture from the reformed gas (reformed gas-cap SOFC). The SOFC system without CO_2 capture unit (non-cap SOFC) is also considered as a base case for comparison. Fig. 2 shows the plant configuration of the non-cap SOFC. Several unit operations such as pre-reformer, SOFC stack, an afterburner, a mixer, a vaporizer and preheaters are included in this configuration. Steam is generated in the vaporizer, preheated and then mixed with biogas. The gas mixture is fed into the fuel processor where the steam reforming, dry reforming and WGS take place. The obtained H_2-rich gas is then fed into the SOFC stack where the electrical energy is generated. The isothermal condition is assumed for the SOFC stack to simplify the computation. The heat generated in the SOFC stack from the irreversibility is utilized for air and H_2-rich gas preheating. To achieve a desired temperature of the SOFC stack, an oxidizing agent (air) temperature is tuned up, employing the energy balance of the SOFC stack. The residue fuel gas released from the SOFC stack is burned up in the afterburner in order to supply heat to the pre-heaters, fuel processor and vaporizer. The flue gas is set to be released from the system at 473 K. The total heat requirement for the SOFC system is computed and a trial-and-error is performed by tuning the fuel utilization until the total heat requirement for the system is equal to the total heat generation from the system ($\sum_i Q_{endo,i} = \sum_j Q_{exo,j}$).

Considering the SOFC systems with CO_2 capture unit, their configurations are almost identical to that of the non-cap SOFC system. However, for the biogas-cap SOFC (Fig. 3), biogas is compressed and then fed into the polyimide membrane module where CO_2 is captured. The sweep gas (air) is also fed into the permeate side in order to decrease the gas partial pressure. The retentate gas is preheated and then fed into the fuel

processor whereas the permeate gas is fed into the selective oxidation unit prior to being released into the environment. For the reformed gas-cap SOFC (Fig. 4), biogas is compressed and fed into the fuel processor. The reformed gas is cooled down to the membrane operating temperature (298 K) at which water is condensed and removed from the gas stream. In the membrane module, CO_2 is captured and the retentate gas is heated and then fed into the SOFC stack, while the permeate gas (CO_2-rich gas) is burned in selective oxidation unit (this unit is not considered in this study) before being released into the environment.

The exploitation of a vacuum pump as another alternative for improving driving force of CO_2 removal is also investigated and its basic working is illustrated in Fig. 5. The high temperature permeate gas released from the vacuum pump can be fed directly into the afterburner, while the retentate gas is fed into the SOFC stack. The advantage of this operation mode is that the permeate gas can be subsequently utilized to generate heat in the afterburner regardless of the dilution effect of the sweep gas.

3. Results and Discussion

In the present work, all models of the SOFC systems are written in Visual Basic. The values of all parameters used in the calculations are given in Table 2. The study starts with the model validation of the SOFC stack. Our previous work [8] demonstrated that the model is a good predictor of the performance curves of the SOFC stack fed by a mixture of hydrogen (97%) and water (3%). In this work, the model is further verified with the simulation results for the case with a lower concentration of hydrogen. Based on the condition listed in Table 3, the results shown in Table 4 indicate that the calculation results from our model are in good agreement with those from the literature [31]. This strengthens confidence in the reliability of the model for SOFC. Then, the model of CO_2

separation by membrane is verified. The feed conditions and the parameters used in the model are summarized in Table 5. Again, our results show good agreement with those reported in the literature [29] as illustrated in Fig. 6.

Prior to the SOFC system investigation, the performance of membrane modules for CO_2 separation was examined. The flow rates and compositions of the feed gases are summarized in Table 6. The feed gas composition for the polyimide membrane is based on a raw biogas, whereas that for the PDMS membrane is based on a reformed gas after water removal. The $\%CO_2$ removal and $\%CH_4$ or H_2 loss at different membrane areas and sweep gas to feed gas ratios are summarized in Fig. 7. It is obvious that the increases in membrane area and sweep gas to feed gas ratio can raise the extent of CO_2 removal. At membrane area of 50 m^2 and sweep gas to feed gas ratio of 4, polyimide and PDMS membranes can remove 80 and 90% of CO_2 in the feed gases, respectively. However, some CH_4 (4%) and a large extent of H_2 (55%) also permeate together with CO_2 through polyimide and PDMS membrane, respectively, into the permeate side. It should be noted that the permeate gases cannot be fed into the afterburner for heat utilization due to the dilution of sweep gas (air); and a selective oxidation unit is required before releasing the gas to the environment. Subsequently, the sweep gas to feed gas ratio was fixed at 4.

Following these preliminary runs, the performance of the biogas-fed SOFC systems is then investigated. Figs. 8(a) and 8(b) show the electrical efficiency and power density of the biogas-cap SOFC system and reformed gas-cap SOFC system, respectively. It is clear that the electrical efficiency decreases with increasing membrane area due to the high loss of CH_4 or H_2 in the permeate gas. However, it is evident that the increase in membrane area for CO_2 removal can improve the power density of the SOFC stack since higher H_2 concentration in the SOFC feed gas is achieved. Compared to the non-cap SOFC system (dashed lines), both biogas-cap SOFC and reformed gas-cap

SOFC offer lower electrical efficiency due to the CH_4 or H_2 loss; however, their power densities are always higher. The electrical efficiency of the reformed gas-cap SOFC is lower than that of the biogas-cap SOFC because the CO_2/H_2 selectivity of PDMS membrane is much lower than the CH_4/H_2 selectivity of the polyimide membrane, resulting in higher loss of fuel in the SOFC feed for the reformed gas-cap SOFC.

To improve the electrical efficiency of the biogas-cap SOFC and reformed gas-cap SOFC, the benefit from the installation of vacuum pump is then studied in order to reduce the operating pressure at the membrane permeate side. The basic working scheme of the membrane module with a vacuum pump is shown in Fig. 5. Under this operation mode, the sweep gas is not required because the partial pressure of each gas component is sufficiently low. Hence, without the dilution by the sweep gas, the permeate gas can be fed into the afterburner and produced more heating energy for the system. It should be noted that as described earlier in Section 2.7, the fuel utilized in the SOFC stack is adjusted to meet the condition at which the endothermic heat required in the system is satisfied by the exothermic heat obtained from the afterburner. Therefore, it is expected that the use of the vacuum pump would offer a higher electrical efficiency. Nevertheless, large amount of electrical energy consumption for operating with the vacuum pump needs to be taken into account.

Fig. 9 shows the $\%CO_2$ removal and $\%CH_4$ or H_2 loss for different membrane areas and different pressures at the permeate side. The lowering of pressure at the permeate side offers similar effect as the increase of the sweep gas to feed gas ratio. Compared with Fig. 7, it is observed that when operated with the vacuum pump at 0.1 bar, the values of $\%CO_2$ removal and $\%CH_4$ or H_2 loss are similar to those of the case with the sweep gas to feed gas ratio of 4 for the same membrane area. Considering the biogas-cap SOFC with vacuum pump installation, the increase in membrane area and

decrease in membrane permeate side pressure can improve the electrical efficiency as illustrated in Fig. 10. This result is in good agreement with that of our recent work [8] indicating that the split of a part of biogas feed from the fuel processor for direct feeding to the afterburner can improve the electrical efficiency by reducing the heat load in the SOFC system. The results also reveal that within some operating ranges, the electrical efficiency of the biogas-cap SOFC operating with high membrane area becomes higher than that of the non-cap SOFC. The power density of the biogas-cap SOFC with vacuum pump installation is always higher than that of the non-cap SOFC. The increase in membrane area diminishes the power density at high values of permeate side pressure (> 0.3 bar) since the effect of methane loss overshadows the benefit of CO_2 removal. An optimum membrane area which provides a maximum power density is observed at low permeate side pressure due to competing effects between the increase in the methane loss and the promotion in CO_2 removal. With the identical membrane area, the biogas-cap SOFC offers the lowest power density when the permeate side pressure is at 0.7 bar. As membrane permeate side pressure is lower than 0.7, the decrease in permeate side pressure can improve the power density due to the significant increase in CO_2 removal.

Considering the reformed gas-cap SOFC with vacuum pump installation, the operation at which the endothermic energy is equal to the exothermic energy cannot be achieved at high membrane area and low membrane permeate side pressure because the heating energy generated is higher than the heat load in SOFC system as shown in Fig. 11a. It should be noted that the fuel utilization is always controlled to be lower than 95% to achieve reasonable power density. The maximum electrical efficiency that the reformed gas-cap SOFC can achieve is 49.37% which is lower than that of the non-cap SOFC. Considering only the condition that the optimal operation can be achieved, the increase in membrane area and the decrease in permeate side pressure do not improve the

power density, implying that the effect of H_2 loss always overshadows the effects of CO_2 removal. However, it still offers higher power density than the non-cap SOFC; probably due to the effect of water removal which increases the H_2 concentration in the SOFC feed gas.

In summary, the operation of the reformed gas-cap SOFC offers extremely lower electrical efficiency (less than 40%) compared with that of the non-cap SOFC. Moreover, large heat exchanger area is also required to cool down the reformed product to the membrane operating temperature and reheat to the SOFC operating temperature. In addition, there is no benefit obtained from the installation of vacuum pump in the reformed gas-cap SOFC system. These clearly indicate that the reformed gas-cap SOFC is not a good choice for the SOFC system. For the biogas-cap SOFC, even if it can offer higher power density compared with the non-fed SOFC, its electrical efficiency is lower than that of the non-fed SOFC when operating with the sweep gas mode. The installation of the vacuum pump to the biogas-cap SOFC can offer comparable or even higher electrical efficiency compared to that of the non-cap SOFC; however, the improvement of the power density over that of the non-cap SOFC becomes smaller compared to the case with the sweep gas mode. Therefore, it is difficult to identify which operation mode can provide utmost performance for the SOFC system among non-cap SOFC, biogas-cap SOFC with sweep gas and biogas-cap SOFC with vacuum pump installation.

In order to determine a suitable SOFC system, the economic analysis called "incremental analysis" is employed for the investigation. This method considers only the cost difference between the base case and the interested case. The non-cap SOFC is considered as the base case in this study. There are five costs considered in this study: SOFC stack cost, membrane module and replacement cost, compressor cost, vacuum pump cost and biogas fuel cost. Other costs of the interested case are assumed to be

similar to those of base case. The parameters utilized in the economic analysis and the costing models for each unit operation are summarized in Tables 7 and 8, respectively. The incremental net present value (INPV) (Eq. 35) for each operation is computed as the indicator. A positive value of INPV represents that the interested case is more economically feasible than the non-cap SOFC.

$$INPV = -(capital\cos t - capital\cos t_{base}) - (annual\cos t - annual\cos t_{base})\frac{\left(1-\left(\frac{1}{1+r}\right)^{y}\right)}{r} \quad (35)$$

As shown in Fig. 12, the biogas-cap SOFC system offers the optimum INPV at a membrane area of 4 m^2 and is superior to the non-cap SOFC system when the area of polyimide membrane is less than 30 m^2 even if it can offer high power density (low SOFC active area) at high membrane area. This is due to the effect of the electrical efficiency drop and more biogas feed required for maintaining identical electrical power. Moreover, high capital cost for compressor and membrane module also reduce the possibility of the biogas-cap SOFC for operation at high membrane area. Considering the biogas-cap SOFC with vacuum pump installation, the effect of the increase in biogas feed and additional investment on the compressor, vacuum pump and membrane modules also overshadow the decrease in SOFC stack size at high polyimide membrane area. Moreover, it is not feasible to operate at very low pressure of membrane permeate side as illustrated in Fig. 13. The biogas-cap SOFC with vacuum pump installation is more feasible than the non-cap SOFC at the membrane area less than 12 m^2 for the permeate side pressure between 0.3-0.9 bar. At extremely low permeate side pressure (< 0.1 bar), the biogas-cap SOFC with vacuum pump installation is not feasible to operate at

membrane area higher than 6 m^2. This can be explained by the fact that the decrease in permeate side pressure increases the vacuum pump load and also the investment cost of vacuum pump. The economic comparison between the biogas-cap SOFC and that with vacuum pump installation is shown in Table 9. The optimum condition of each operation mode is chosen for this comparison. Both of these cases offer INPV higher than 0, indicating that they are more attractive to operate compared with the non-cap SOFC. The biogas-cap SOFC with sweep gas offers higher INPV ($5,320.21) than the biogas-cap SOFC with vacuum pump installation ($4,359.18). Even if the biogas-cap SOFC with vacuum pump installation can offer higher electrical efficiency compared with the biogas-cap SOFC, the cost of vacuum pump suppresses this effect. It therefore seems that the biogas-cap SOFC is a preferred economic option to the biogas-cap SOFC with vacuum pump installation.

4. Conclusion

Performance of biogas-fed SOFC system was analyzed to investigate the benefit of CO_2-selective membrane installation. The two configurations, namely; biogas-cap SOFC and reformed gas-cap SOFC were examined in terms of both engineering and economic models. It was observed that the power density improves when the SOFC was integrated with a CO_2-selective membrane. However, due to low CO_2/H_2 or CO_2/CH_4 selectivity of membrane separator, there was significant H_2 (or CH_4) loss and electrical efficiency also dropped especially in case of reformed gas-cap SOFC. In particular, it was found that the installation of vacuum pump (replacing the use of sweep gas) to the biogas-cap SOFC can offer comparable electrical efficiency to the non-cap SOFC. Unfortunately, this advantage has detrimental effect on the power density. For the reformed gas-cap SOFC, although the installation of vacuum pump can improve the

electrical efficiency, the increase in membrane area and the decrease in membrane permeate pressure did not improve the power density. This implies that there is no benefit in the installation of vacuum pump for the reformed gas-cap SOFC. It may therefore be concluded that the reformed gas-cap SOFC is not a good alternative for the SOFC system owing to its extremely low efficiency (less than 40 percent) and the large heat exchanger area required. Economic assessment via the "incremental analysis" method was then employed to evaluate the feasibility study of biogas-cap SOFC operation. The results showed that the biogas-cap SOFC with sweep gas and that with vacuum pump installation were more superior to the non-cap SOFC at low membrane area. The biogas-cap SOFC with vacuum pump installation is, however, economically less attractive than the biogas-cap SOFC with sweep gas due to high vacuum pump cost.

Acknowledgement

This research is financially supported by the Thailand Research Fund and Commission on Higher Education.

References

[1] J. Van herle, Y. Membrez, O. Bucheli, Biogas as a fuel source for SOFC co-generators, Journal of Power Sources 127 (2004) 300-312.

[2] D.C. Dayton, Fuel cell integration-a study of the impacts of gas quality and impurities, NREL final report, 2001.

[3] M. Jenne, T. Dörk, A. Schuler, Proceedings of the Fifth European Solid Oxide Fuel Cell Forum, Lucerne, Switzerland, European Forum Secretariat, CH 5442-Oberrohrdorf, Switzerland, 2002, pp. 460-466.

[4] K. Kendall, C.M. Finnerty, G. Saunders, J.T. Chung, Effects of dilution on methane entering an SOFC anode, Journal of Power Sources 106 (2002) 323-327.

[5] E. Achenbach, E. Riensche, Methane/steam reforming kinetics for solid oxide fuel cells, Journal of Power Sources 52 (1994) 283-288.

[6] J. Meusinger, E. Riensche, U. Stimming, Reforming of natural gas in solid oxide fuel cell systems, Journal of Power Sources 71 (1998) 315-320.

[7] S. Assabumrungrat, N. Laosiripojana, P. Piroonlerkgul, Determination of the boundary of carbon formation for dry reforming of methane in a solid oxide fuel cell, Journal of Power Sources 159 (2006) 1274-1282.

[8] P. Piroonlerkgul, S. Assabumrungrat, N. Laosiripojana, A.A. Adesina, Selection of appropriate fuel processor for biogas-fuelled SOFC system, Chemical Engineering Journal In Press, Corrected Proof.

[9] W. Sangtongkitcharoen, S.Vivanpatarakij, N. Laosiripojana, A. Arpornwichanop, S. Assabumrungrat, Performance analysis of methanol-fueled solid oxide fuel cell system incorporated with palladium membrane reactor, Chemical Engineering Journal 138 (2008) 436-441.

[10] R. Suwanwarangkul, E. Croiset, E. Entchev, S. Charojrochkul, M.D. Pritzker, M.W. Fowler, P.L. Douglas, S. Chewathanakup, H. Mahaudom, Experimental and modeling study of solid oxide fuel cell operating with syngas fuel, Journal of Power Sources 161 (2006) 308-322.

[11] E.J. Granite, T. O'Brien, Review of novel methods for carbon dioxide separation from flue and fuel gases, Fuel Processing Technology 86 (2005) 1423-1434.

[12] S. Alexander Stern, Polymers for gas separations: the next decade, Journal of Membrane Science 94 (1994) 1-65.

[13] D. Shekhawat, D.R. Luebke, H. Pennline, A review of carbon dioxide selective membranes; U.S. Department of Energy Topical Report, DOE/NETL-2003/1200., 2003.

[14] M. Harasimowicz, P. Orluk, G. Zakrzewska-Trznadel, A.G. Chmielewski, Application of polyimide membranes for biogas purification and enrichment, Journal of Hazardous Materials 144 (2007) 698-702.

[15] T.C. Merkel, R.P. Gupta, B.S. Turk, B.D. Freeman, Mixed-gas permeation of syngas components in poly(dimethylsiloxane) and poly(1-trimethylsilyl-1-propyne) at elevated temperatures, Journal of Membrane Science 191 (2001) 85-94.

[16] M. Amelio, P. Morrone, F. Gallucci, A. Basile, Integrated gasification gas combined cycle plant with membrane reactors: Technological and economical analysis, Energy Conversion and Management 48 (2007) 2680-2693.

[17] M.A. Khaleel, Z. Lin, P. Singh, W. Surdoval, D. Collin, A finite element analysis modeling tool for solid oxide fuel cell development: coupled electrochemistry, thermal and flow analysis in MARC(R), Journal of Power Sources 130 (2004) 136-148.

[18] R. Blom, I.M. Dahl, A. Slagtem, B. Sortland, A. Spjelkavik, E. Tangstad, Carbon dioxide reforming of methane over lanthanum-modified catalysts in a fluidized-bed reactor, Catalysis Today 21 (1994) 535-543.

[19] M.C.J. Bradford, M.A. Vannice, Catalytic reforming of methane with carbon dioxide over nickel catalysts II. Reaction kinetics, Applied Catalysis A: General 142 (1996) 97-122.

[20] H.M. Swaan, V.C.H. Kroll, G.A. Martin, C. Mirodatos, Deactivation of supported nickel catalysts during the reforming of methane by carbon dioxide, Catalysis Today 21 (1994) 571-578.

[21] J.R. Ferguson, J.M. Fiard, R. Herbin, Three-dimensional numerical simulation for various geometries of solid oxide fuel cells, Journal of Power Sources 58 (1996) 109-122.

[22] S.H. Chan, K.A. Khor, Z.T. Xia, A complete polarization model of a solid oxide fuel cell and its sensitivity to the change of cell component thickness, Journal of Power Sources 93 (2001) 130-140.

[23] S.P. Jiang, S.P.S. Badwal, Hydrogen oxidation at the nickel and platinum electrodes on yttria-tetragonal zirconia electrolyte, Journal of the Electrochemical Society 144 (1997) 3777-3784.

[24] S.P. Jiang, S.P.S. Badwal, An electrode kinetics study of H2 oxidation on Ni/Y2O3-ZrO2 cermet electrode of the solid oxide fuel cell, Solid State Ionics 123 (1999) 209-224.

[25] J. Fleig, Solid Oxide Fuel Cell Cathodes: Polarization Mechanisms and Modeling of the Electrochemical Performance, Annual Review of Materials Research 33 (2003) 361-382.

[26] W.J. Massman, A review of the molecular diffusivities of H2O, CO2, CH4, CO, O3, SO2, NH3, N2O, NO, and NO2 in air, O2 and N2 near STP, Atmospheric Environment 32 (1998) 1111-1127.

[27] H. Yakabe, M. Hishinuma, M. Uratani, Y. Matsuzaki, I. Yasuda, Evaluation and modeling of performance of anode-supported solid oxide fuel cell, Journal of Power Sources 86 (2000) 423-431.

[28] L. Wang, Y. Cao, M. Zhou, S.J. Zhou, Q. Yuan, Novel copolyimide membranes for gas separation, Journal of Membrane Science 305 (2007) 338-346.

[29] A. Corti, D. Fiaschi, L. Lombardi, Carbon dioxide removal in power generation using membrane technology, Energy 29 (2004) 2025-2043.

[30] T. Kaneko, J. Brouwer, G.S. Samuelsen, Power and temperature control of fluctuating biomass gas fueled solid oxide fuel cell and micro gas turbine hybrid system, Journal of Power Sources 160 (2006) 316-325.

[31] L. Petruzzi, S. Cocchi, F. Fineschi, A global thermo-electrochemical model for SOFC systems design and engineering, Journal of Power Sources 118 (2003) 96-107.

[32] M. Ni, M.K.H. Leung, D.Y.C. Leung, Parametric study of solid oxide fuel cell performance, Energy Conversion and Management 48 (2007) 1525-1535.

[33] F. Palazzi, N. Autissier, F.M.A. Marechal, D. Favrat, A methodology for thermo-economic modeling and optimization of solid oxide fuel cell systems, Applied Thermal Engineering 27 (2007) 2703-2712.

[34] S.M. Walas, Chemical Process Equipment Selection and Design. Butterworth, Inc., 665-668, 1988.

[35] A.K. Datta, P.K. Sen, Optimization of membrane unit for removing carbon dioxide from natural gas, Journal of Membrane Science 283 (2006) 291-300.

Nomenclature

A	membrane area, m^2
A_{cell}	SOFC stack active area, m^2
C_p	specific heat capacity, J mol^{-1} K^{-1}
C_{cell}	cost of one SOFC cell, $
$C_{compressor}$	cost of compressor, $
C_{stack}	cost of SOFC stack, $
$C_{Vacuum\ pump}$	cost of vacuum pump, $
$D_{i(eff)}$	effective diffusion coefficient of species i (i = anode, cathode), cm^2 s^{-1}
$D_{A,k(eff)}$	effective Knudsen diffusivity of gas A, cm^2 s^{-1}
$D_{A-B(eff)}$	ordinary diffusivity of gas A versus gas B, cm^2 s^{-1}
$D_{A,k}$	Knudsen diffusivity of gas A, cm^2 s^{-1}

D_{A-B}	ordinary diffusivity of gas A versus gas B, $cm^2\ s^{-1}$
D_p	catalyst pore diameter, μm
E	open circuit voltage, V
$E_{act,a}$	activation energy at anode, $J\ mol^{-1}$
$E_{act,c}$	activation energy at cathode, $J\ mol^{-1}$
F	Faraday constant (9.6495×10^4), $C\ mol^{-1}$
ΔG_i	Gibb's free energy of reaction i, $J\ mol^{-1}$
i	current density, $A\ cm^{-2}$
$i_{0,i}$	exchange current density (i = anode, cathode), $A\ cm^{-2}$
$K_{eq,dry}$	equilibrium constant of dry reforming reaction, Pa^2
$K_{eq,steam}$	equilibrium constant of steam reforming reaction, Pa^2
$K_{eq,pox}$	equilibrium constant of partial oxidation reaction, $Pa^{3/2}$
$K_{eq,RWGS}$	equilibrium constant of reverse water gas shift reaction, dimensionless
l_a	thickness of anode, μm
l_c	thickness of cathode, μm
L	thickness of electrolyte, μm
$\dot{m}$	total gas molar flow rate, $mol\ s^{-1}$
M_A	molecular weight of gas A, g
n	electrode porosity, dimensionless
N_{cell}	number of cells, dimensionless
N_{stack}	number of stack, dimensionless
p_i	permeability of component i, barrer
p_a	operating pressure at the SOFC anode, Pa
p_c	operating pressure at the SOFC cathode, Pa

p_i^I	inlet pressure of species *i*, Pa
P	operating pressure, Pa
P_i	partial pressure of species *i*, Pa
P_P	operating pressure at permeate side of membrane, Pa
P_{ref}	reference pressure (10^5), Pa
P_R	operating pressure at retentate side of membrane, Pa
Pe_i	molar flow rate of component *i* at permeate side of membrane, mol s^{-1}
Q_{endo}	heat demand in the SOFC system, kW
Q_{exo}	heat generated in the SOFC system, kW
r_p	average radius of the catalyst pore, μm
R	gas constant (8.3145), J $mol^{-1}K^{-1}$
R_i	molar flow rate of component *i* at retentate side of membrane, mol s^{-1}
r	interest rate, dimensionless
T	operating temperature, K
V	cell voltage, V
$\dot{W}_{comp}$	electricity consumed in the compressor, kW
x_i	mole fraction of component *i* at retentate side of membrane, dimensionless
y_i	mole fraction of component *i* at permeate side of membrane, dimensionless
y	plant life time, year
z	the number of electrons involved per reaction, dimensionless

Greek letters

α	symmetrical factor, dimensionless
δ	membrane thickness, μm

ξ	electrode tortuosity, dimensionless
$\eta_{act,a}$	activation overpotential at anode, V
$\eta_{act,c}$	activation overpotential at cathode, V
$\eta_{Conc,a}$	concentration overpotential at anode, V
$\eta_{Conc,c}$	concentration overpotential at cathode, V
η_c	compressor or pump efficiency, dimensionless
η_{ohmic}	ohmic overpotential, V
σ_{AB}	collision diameter, Å
Ω_D	collision integral, dimensionless
ε_{AB}	Lennard-Jones energy interaction parameter scaled with respect to the Boltzman constant, dimensionless
γ_a	pre-exponential factor for anode exchange current density, A m^{-2}
γ_c	pre-exponential factor for cathode exchange current density, A m^{-2}

Figure Caption

Fig. 1. The configuration of membrane module.

Fig. 2. The plant configuration of non-cap SOFC system.

Fig. 3. The plant configuration of biogas-cap SOFC system.

Fig. 4. The plant configuration of the reformed gas-cap SOFC system.

Fig. 5. The basic working of membrane module with vacuum pump installation.

Fig. 6. Verification of the membrane separation model.

Fig. 7. The percentage of CO_2 removal and the percentage of CH_4 or H_2 loss at different membrane area and sweep gas to feed gas ratio: (a) polyimide membrane and (b) PDMS membrane.

Fig. 8. The electrical efficiency and power density at different membrane area: (a) biogas-cap SOFC and (b) reformed gas-cap SOFC.

Fig. 9. The percentage of CO_2 removal and the percentage of CH_4 or H_2 loss at different membrane area and permeate side pressure: (a) polyimide membrane with vacuum pump installation and (b) PDMS membrane with vacuum pump installation.

Fig. 10. The electrical efficiency and power density of biogas-cap SOFC with vacuum pump installation at different membrane area and permeate side pressure.

Fig. 11. Performance of the reformed gas-cap SOFC with vacuum pump installation at different membrane areas and membrane permeate side pressures: (a) Excess energy released to the environment, (b) electrical efficiency and (c) power density.

Fig. 12. Incremental net present value of biogas-cap SOFC operated at different membrane areas (sweep gas to feed gas ratio = 4).

Fig. 13. Incremental net present value of the biogas-cap SOFC with vacuum pump installation operated at different membrane areas and permeate side pressure.

List of Table

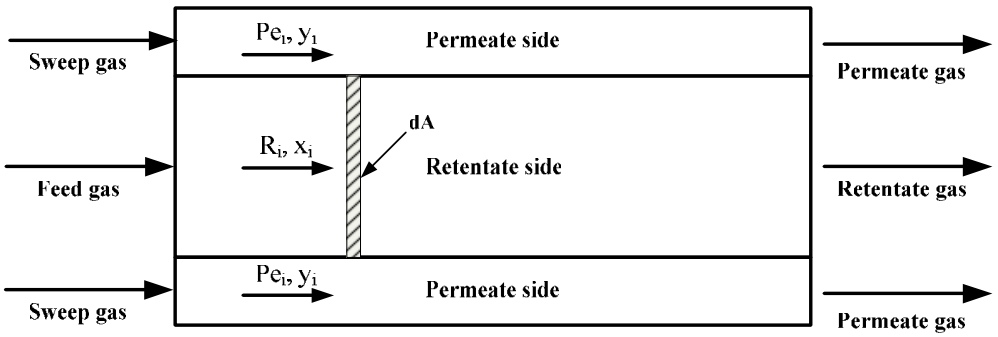

Fig. 1. The configuration of membrane module.

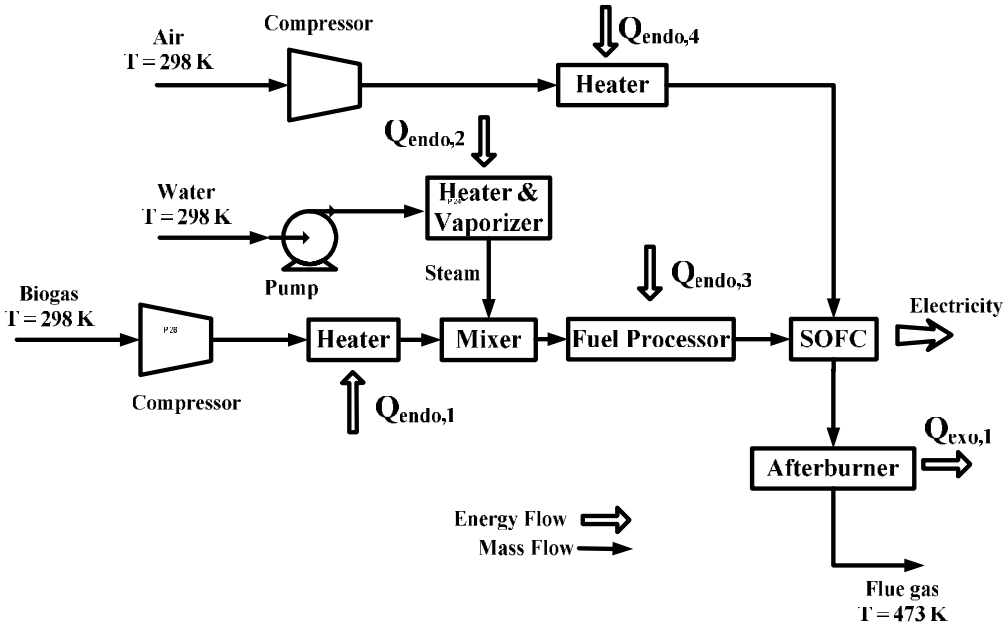

Fig. 2. The plant configuration of the non-cap SOFC system.

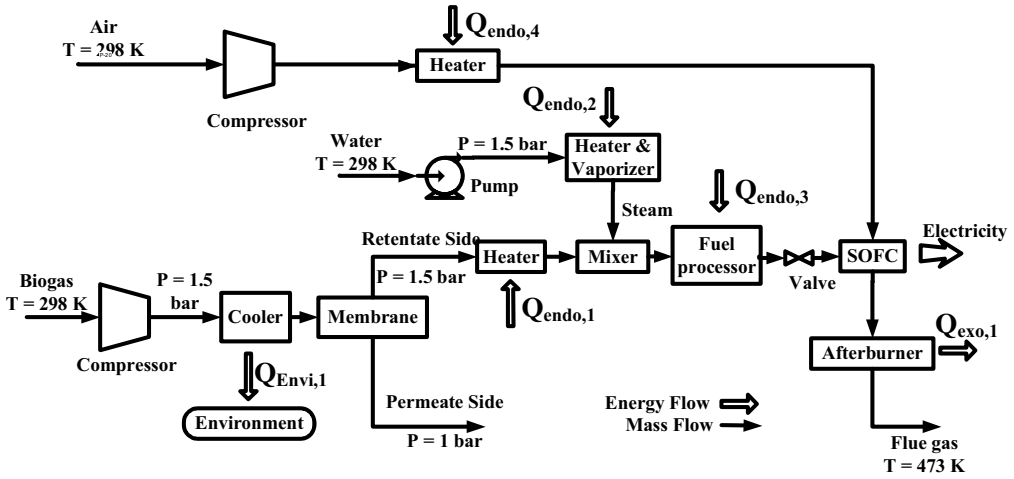

Fig. 3. The plant configuration of biogas-cap SOFC system.

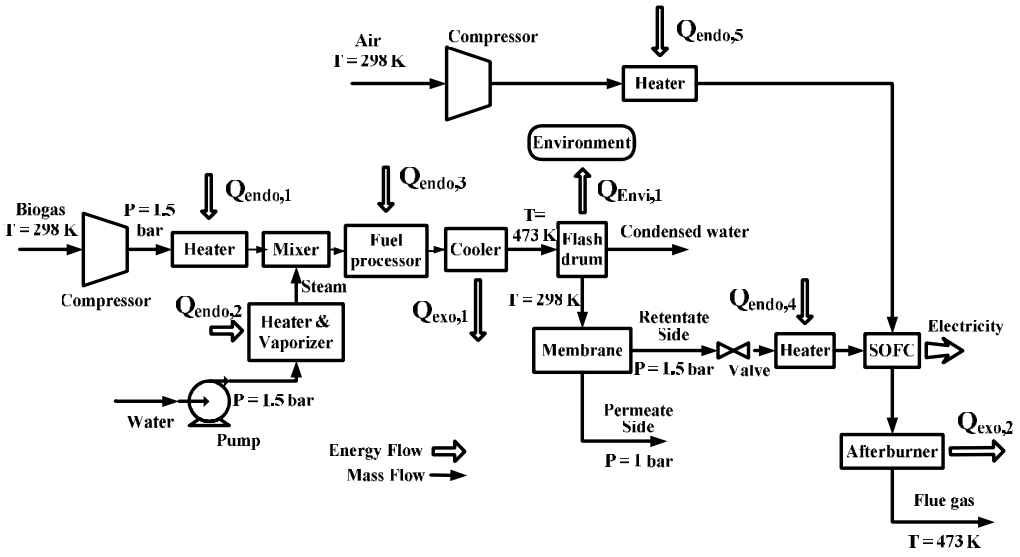

Fig. 4. The plant configuration of the reformed gas-cap SOFC system.

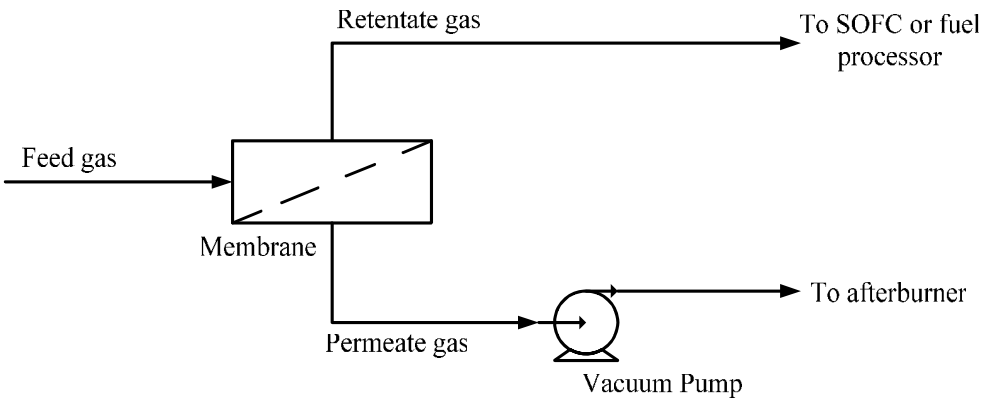

Fig. 5. The basic working of membrane module with vacuum pump installation.

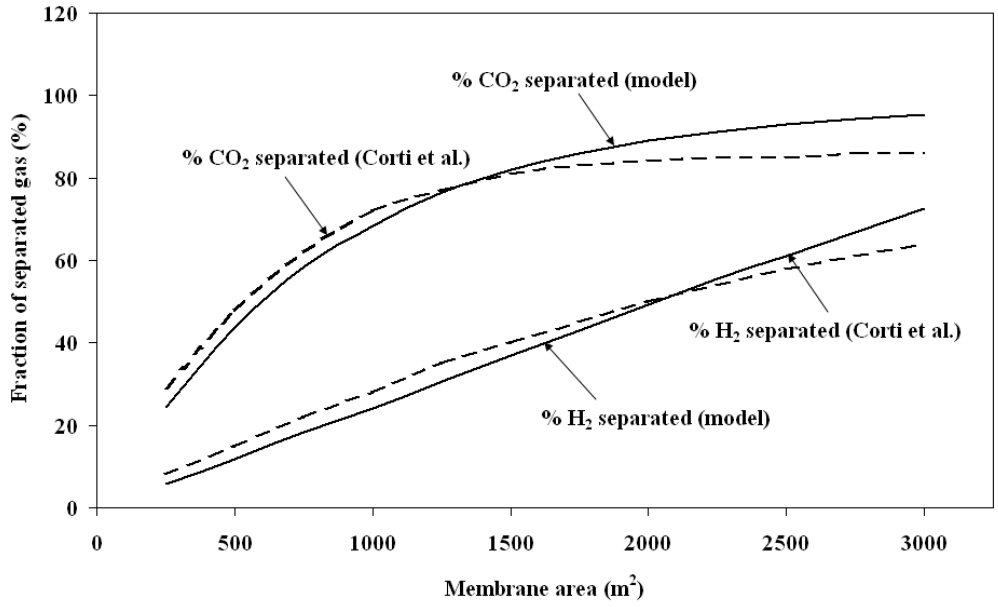

Fig. 6. Verification of the membrane separation model.

a

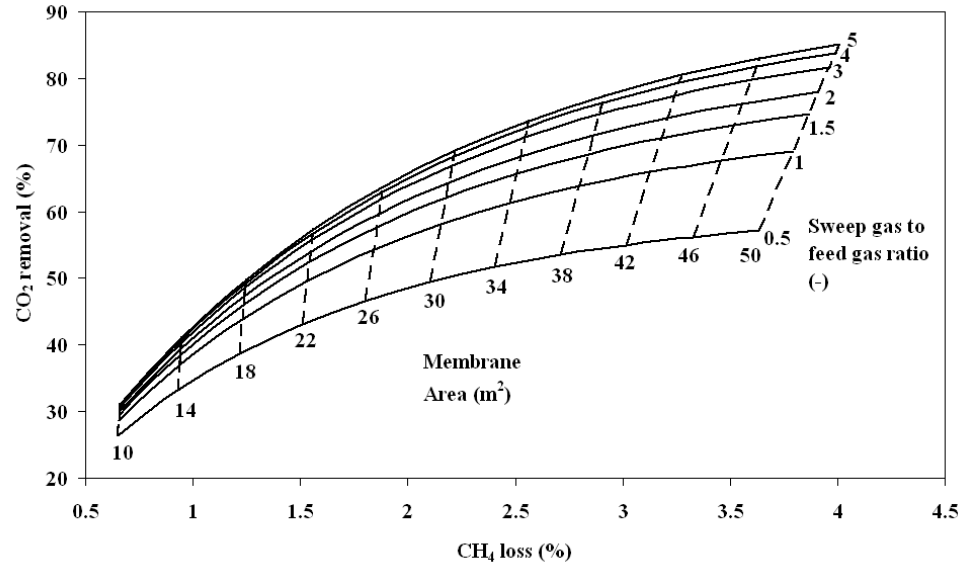

b

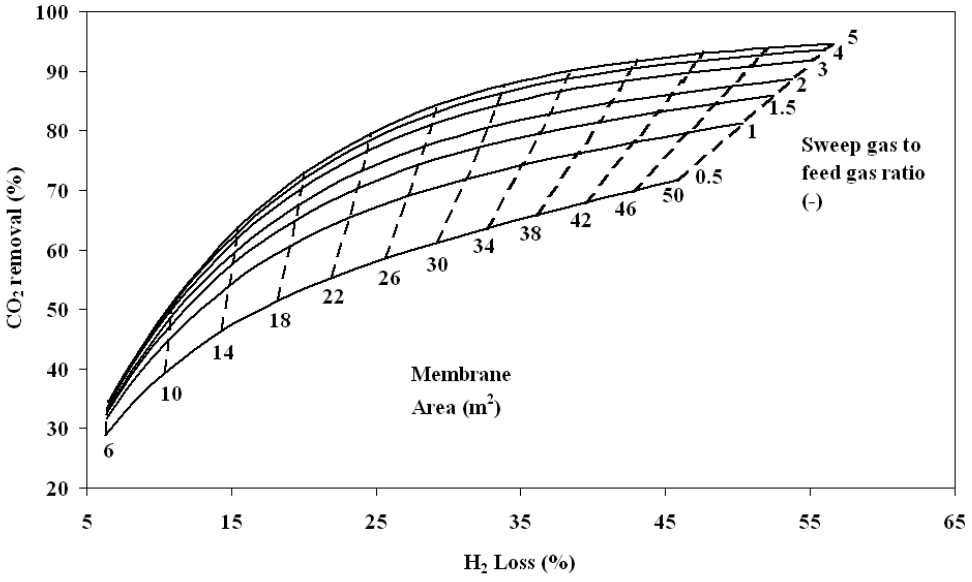

Fig. 7. The percentage of CO_2 removal and the percentage of CH_4 or H_2 loss at different membrane area and sweep gas to feed gas ratio: (a) polyimide membrane and (b) PDMS membrane.

a

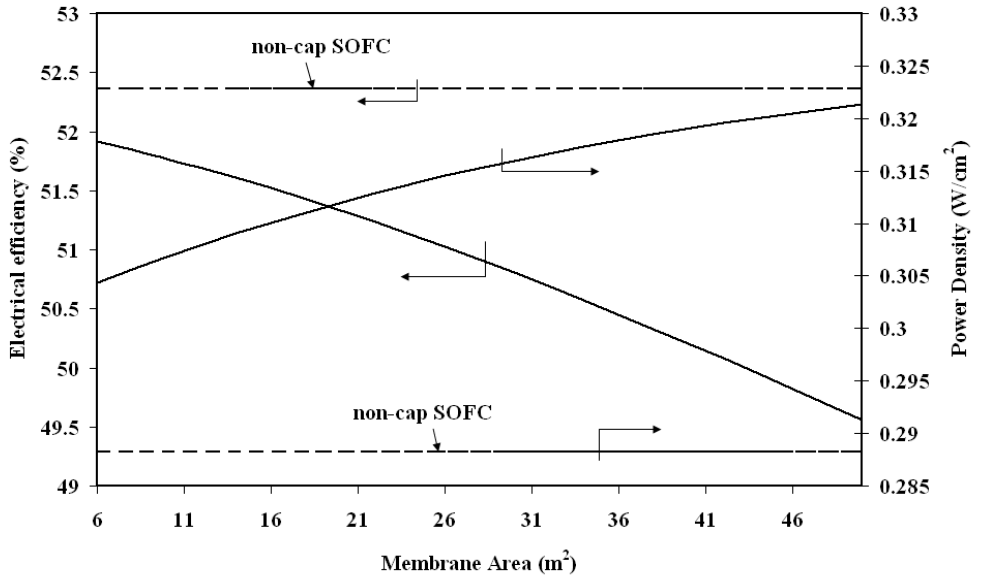

b

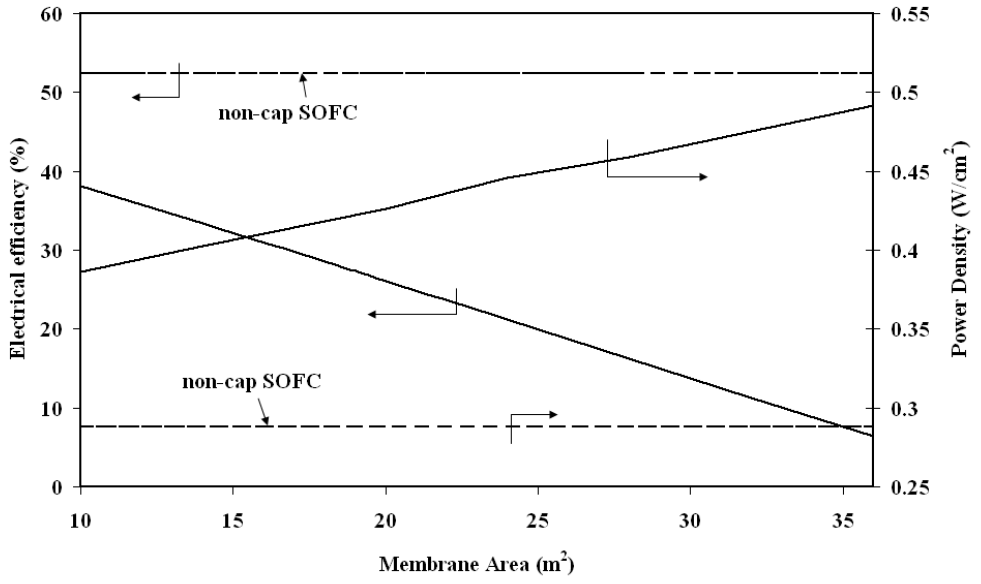

Fig. 8. The electrical efficiency and power density at different membrane area: (a) biogas-cap SOFC and (b) reformed gas-cap SOFC.

a

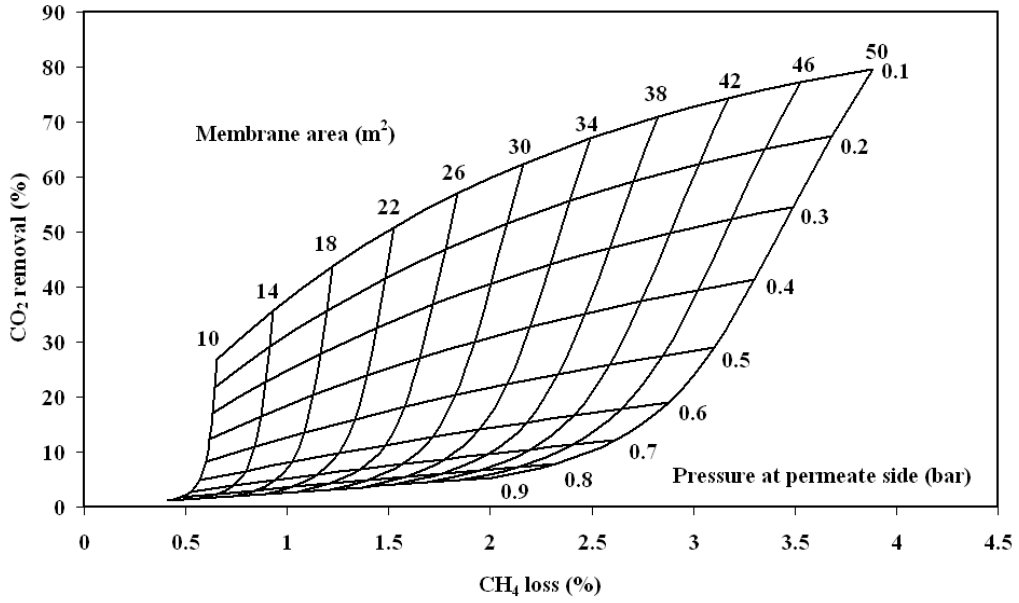

b

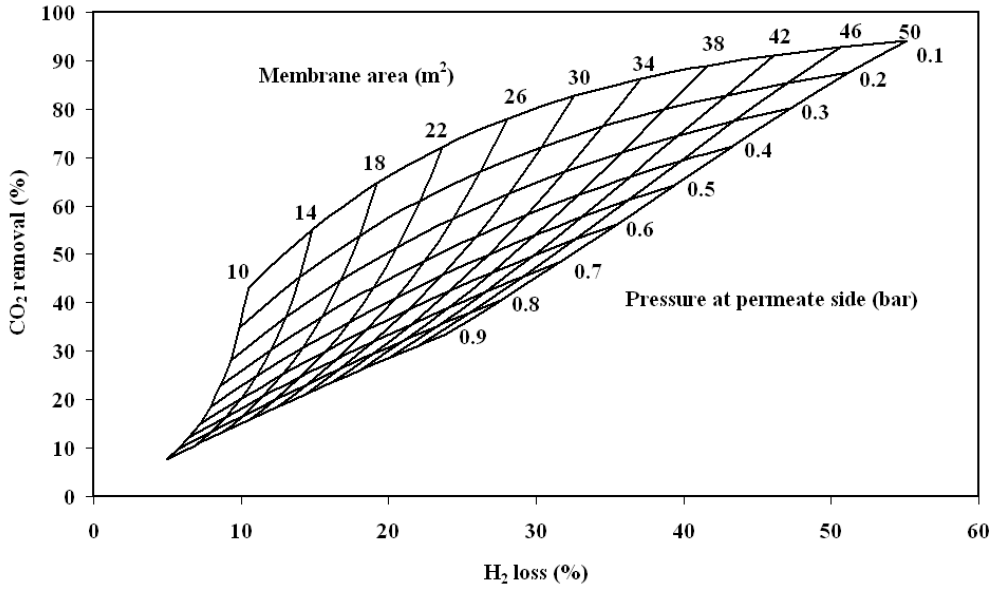

Fig. 9. The percentage of CO_2 removal and the percentage of CH_4 or H_2 loss at different membrane area and permeate side pressure: (a) polyimide membrane with vacuum pump installation and (b) PDMS membrane with vacuum pump installation.

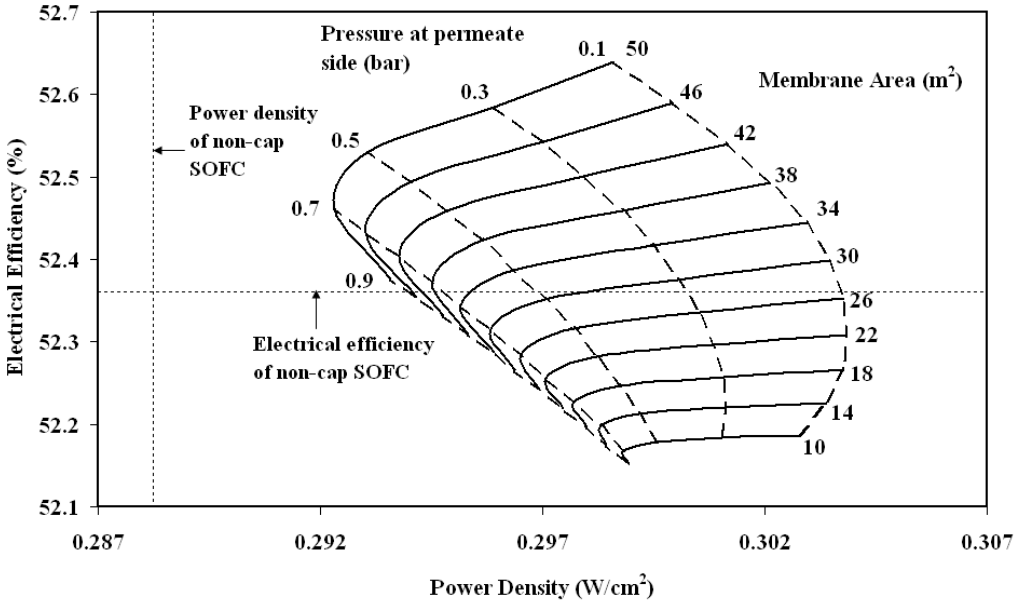

Fig. 10. The electrical efficiency and power density of biogas-cap SOFC with vacuum pump installation at different membrane area and permeate side pressure.

a

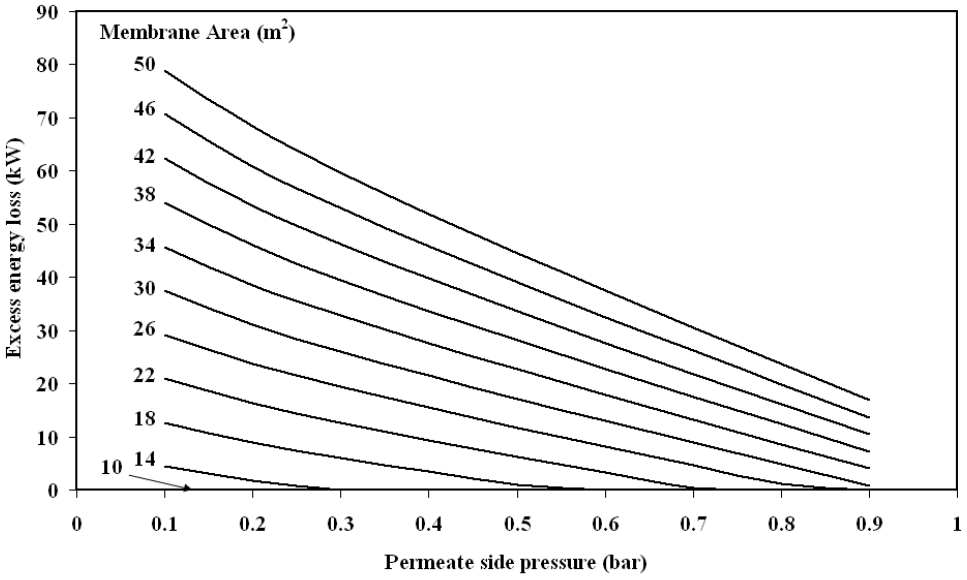

b

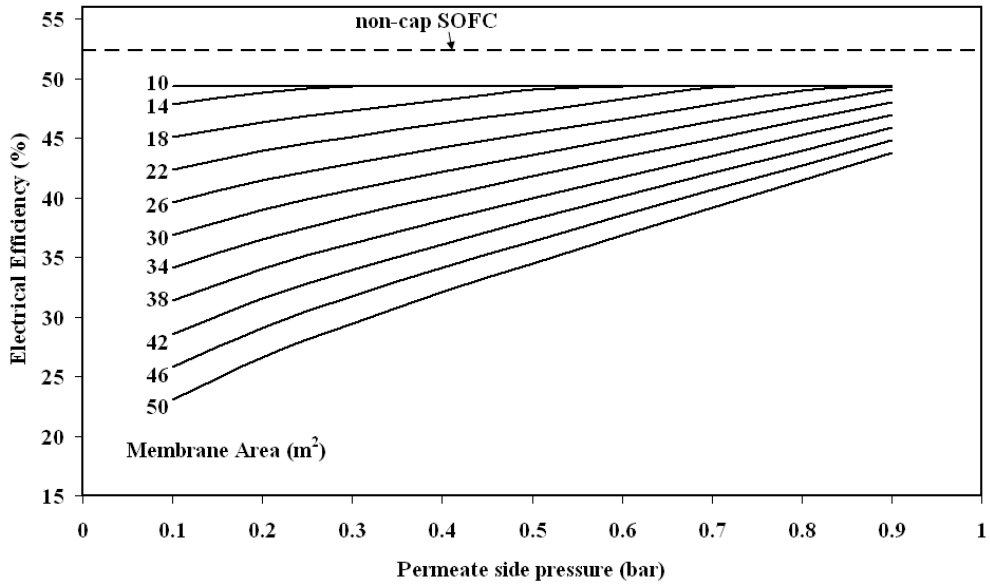

c

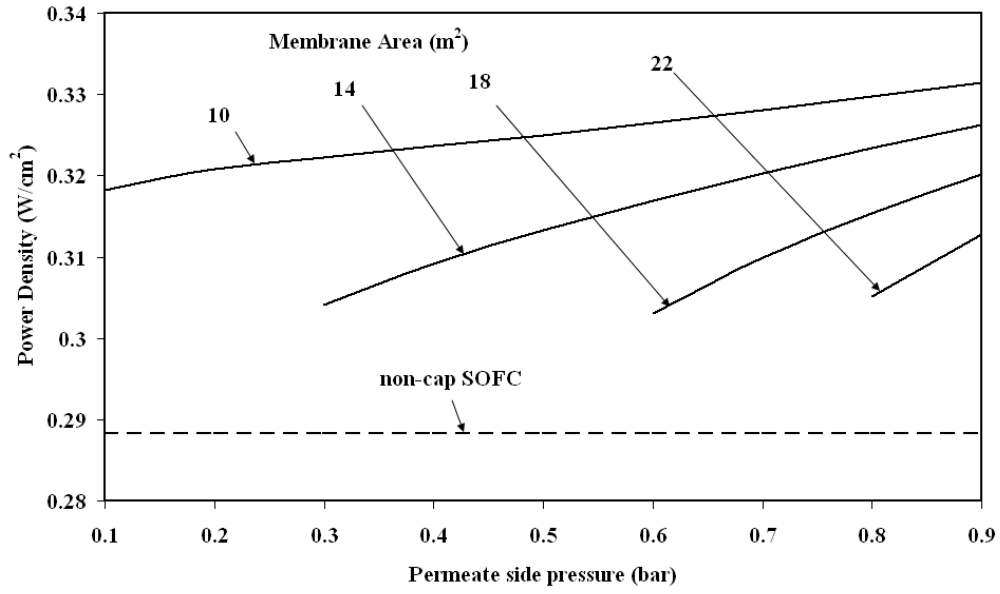

Fig. 11. Performance of the reformed gas-cap SOFC with vacuum pump installation at different membrane areas and membrane permeate side pressures: (a) Excess energy released to the environment, (b) electrical efficiency and (c) power density.

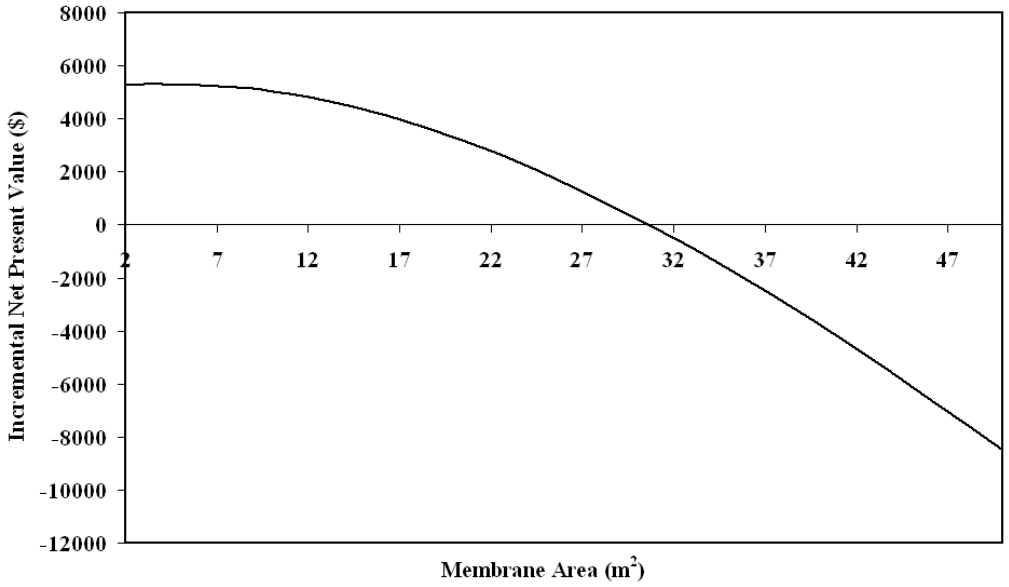

Fig. 12. Incremental net present value of biogas-cap SOFC operated at different membrane areas (sweep gas to feed gas ratio = 4).

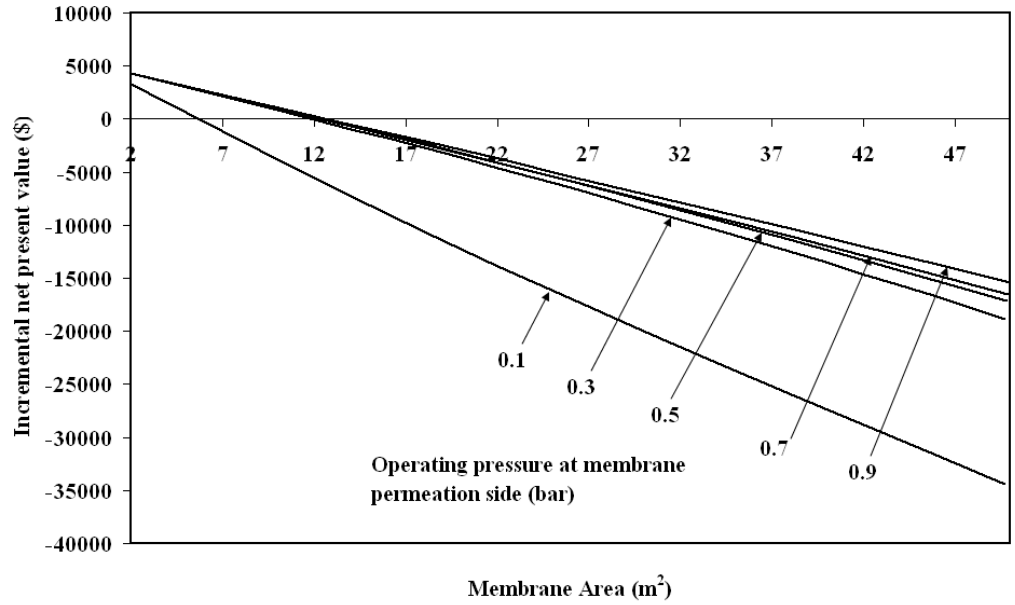

Fig. 13. Incremental net present value of the biogas-cap SOFC with vacuum pump installation operated at different membrane areas and permeate side pressure.

Table 1

Membrane thickness and permeability of each gas component

	Polyimide membrane [28]	PDMS membrane [29]
Membrane Thickness (μm)	0.1	1.5
Permeability (barrer)		
CH_4	0.69	940
CO_2	39.59	3200
CO	-	400
H_2O	-	10
H_2	-	500

1 barrer = [10^{-10} cm^3 (STP) cm]/[cm^2 s cmHg]

Table 2

Summary of model parameters [32].

Parameters	*Value*
γ_a	1.344×10^{10} A/m^2
γ_c	2.051×10^{9} A/m^2
$E_{act,a}$	1.0×10^{5} J/mol
$E_{act,c}$	1.2×10^{5} J/mol
n	0.48
ξ	5.4
D_p	3 μm
l_a	750 μm
l_c	50 μm
L	50 μm
V	0.7 V
T_{SOFC}	1073 K
Operating pressure (SOFC)	1 bar
$T_{fuel\ processor}$	973 K

Table 3

Feed compositions and SOFC stack dimensions used in model validation.

Parameters	Values [31]
Fuel compositions (Mole fraction):	
CH_4	-
H_2	0.26
CO	0.24
CO_2	0.025
N_2	0.46
H_2O	0.015
Stack dimensions:	
Type of cell	Planar SOFC with 225 cm^2 active surface area
n	0.48
ξ	5.4
D_p	3 μm
l_a	40 μm
l_c	40 μm
L	70 μm
Stack average temperature	1073 K

Table 4

Model validation of the SOFC model.

T = 1073 K	Petruzzi et al., 2003	Model	Error (%)	Petruzzi et al., 2003	Model	Error (%)
Cell Voltage (V)	0.8	0.8	0	0.75	0.77	2.67
Electrical Power (W)	62.9	63	0.16	70	71.6	2.29
Fuel Utilization (%)	70	70	-	80	80	-

Table 5

Summary of feed characteristics and parameters used in the model verification of membrane separation.

Parameters	*Values*
Fuel mass flow rate (kg/s)	5.89
Fuel compositions (Mole fraction):	
CH_4	0.068
H_2	0.6714
CO	0.0068
CO_2	0.1627
N_2	-
H_2O	0.0911
Membrane parameters:	
Material used	PDMS
Membrane thickness (μm)	1.3
Operating pressure (bar):	
Permeate side	1
Retentate side	10
Permeability (barrer) at 298 K:	
CH_4	940
CO	400
CO_2	3200
H_2	500
H_2O	10

1 barrer = $[10^{-10}$ cm^3 (STP) cm] / [cm^2 s cmHg].

Table 6

Flow rates and compositions of the membrane feed gases.

	Polyimide membrane	PDMS membrane
Molar flow rate (mol/s)	0.56028	0.56028
Pressure (bar)	1.5	1.5
Temperature (K)	298	298
Mole Fraction		
CH_4	0.6	0.0035
CO_2	0.4	0.1563
CO	0	0.1961
H_2O	0	0
H_2	0	0.6441

Table 7

Economic parameters used in the calculations.

Parameter	Value
Biogas price ($/MMBTU)	7.85 (Natural gas price is assumed.)
Membrane module cost ($/m^2)	108 [35]
Membrane replacement cost ($/m^2)	54 [35]
Interest rate (%)	7
Plant load time (h/a)	7,000
Plant life time (year)	5

Table 8

Costing models of SOFC [33], compressor and vacuum pump [34].

Costing model	
Cell cost ($)	$C_{cell} = A_{cell} \times 0.1442$
Number of cells	$N_{cell} = A_{cell}/200$
Number of stacks	$N_{stack} = N_{cell}/100$
Fuel cell stacks cost ($)	$C_{stack} = 2.7 \times (C_{cell} \times N_{cell} + 2 \times N_{stack} \times A_{cell} \times 0.46425)$
Compressor ($)	$C_{compressor} = 1.49 \times HP^{0.71} \times 10^3$
Vacuum pump ($)	$C_{Vacuum\ pump} = 2.59 \times X^{1.03} \times 10^5$ where: $0.01 < X < 0.52$ (lbs/h)/(suction Torr)

Table 9

The economic comparison between the biogas-cap SOFC with different modes.

	Biogas-cap SOFC (Sweep gas)	Biogas-cap SOFC (Vacuum pump)
Power produced (kW)	156.72	156.72
Membrane area (m^2)	4.03	2
Operating pressure at permeate side (bar)	1	0.5
Sweep gas to feed gas ratio	4	0
Feed rate of biogas (mol/s)	0.5644	0.5629
Electrical efficiency (%)	51.98	52.11
Power density (W/cm^2)	0.303	0.3
SOFC area (m^2)	51.98	52.5
Decrease in capital cost from base case ($)	7,903.48	5,901.02
Increase in operating and fuel cost from base case ($/year)	630.04	376.04
Incremental net present value ($)	5,320.21	4,359.18

Appendix 11

Fe(III), Cu(II), V(V)/TiO_2 for Hydroxylation of Benzene to Phenol with Hydrogen Peroxide at Room Temperature

Garun TANARUNGSUN[1], Worapon KIATKITTIPONG[2], Suttichai ASSABUMRUNGRAT[1], Hiroshi YAMADA[3], Tomohiko TAGAWA[3] and Piyasan PRASERTHDAM[1]

[1]*Center of Excellence in Catalysis and Catalytic Reaction Engineering, Department of Chemical Engineering, Faculty of Engineering, Chulalongkorn University, Bangkok 10330, Thailand*

[2]*Department of Chemical Engineering, Faculty of Engineering and Industrial Technology, Silpakorn University, Nakhon Pathom 73000, Thailand*

[3]*Department of Chemical Engineering, Nagoya University, Chikusa-ku, Nagoya-shi, Aichi 464-8603, Japan*

Keywords: Hydroxylation, Benzene, Hydrogen Peroxide, Phenol, TiO_2

The hydroxylation of benzene to phenol with hydrogen peroxide catalyzed by transition metal (Fe(III), Cu(II), and V(V)) on a TiO_2 support was performed at room temperature. The Fe(III) catalyst gave the highest conversion and yield but showed the lowest selectivity. At room temperature, the phenol yield was quite low and therefore modifying the system by solvent addition or operation under UV light was examined. Among the various solvents studied, i.e., acetone, acetronitrile and pyridine, acetone gave the highest conversion and yield; however, the selectivity was low. Acetonitrile is a suitable solvent in terms of improved selectivity and yield. Operation under UV light significantly improved the yield with comparatively high selectivity. Ascorbic acid, as a reducing agent, was able to improve the phenol yield. In some solvent systems, an optimum amount of ascorbic acid was observed.

Introduction

Phenol is an important intermediate for the synthesis of various petrochemical and agrochemical products. More than 90% of the world's phenol production is produced from the cumene process (Schmidt, 2005). The process is composed of three steps and produces acetone as a co-product, which will be an oversupplied product in the future. In addition, the cumene hydroperoxide intermediate can decompose aggressively. Therefore, an alternative process could be developed.

The direct oxidation of benzene to phenol is one of the alternative routes. There are two main pathways for the direct oxidation of benzene to phenol; i.e., gas and liquid phase reactions.

Gas phase hydroxylation of benzene with nitrous oxide has been conducted in a pilot facility (Uriarte *et al.*, 1998). However, it is efficient only when the supply of nitrous oxide is available, for example, as a by-product from the adipic acid synthesis. Major problems of an industrial application are deactivation of the catalyst by heavy coke formation and the low phenol selectivity of nitrous oxide (Uriarte *et al.*, 1998; Lemke *et al.*, 2003). The other disadvantages are that it is operated at an elevated temperature of higher than 573 K and yields marginal conversion, resulting in an unduly high cost.

Liquid phase hydroxylation of benzene to phenol is operated at room temperature or normally not higher than 353 K. H_2O_2 or O_2 is employed as an oxidant. High selectivity can be obtained at a lower oxidant cost compared with the gas phase operation using N_2O as an oxidant. Therefore many researchers have focused on this route and aimed at developing a suitable catalyst for the reaction. Several kinds of metals such as Fe, Cu and V were loaded on supports such as SiO_2, Al_2O_3, HZSM-5, MCM-41, and TiO_2 (Seo *et al.*, 1995; Okamura *et al.*, 1998; Chen and Lu 1999; Kanzaki *et al.*, 2004).

The solvent is usually added to the reaction system for dissolving hydrogen peroxide and benzene into one phase for the oxidation of benzene to phenol. Several solvents such as acetone, acetonitrile, acetic acid, pyridine and dichloromethane have been employed (Stockmann *et al.*, 2001; Xiao *et al.*, 2001; Miyake *et al.*, 2002; Choi *et al.*, 2005; Dubey and Kannan 2005; Liu *et al.*, 2005; Zhang *et al.*, 2005). However, there are only a few works comparing the effect of solvent types. Stockmann *et al.* (2001) studied the oxidation

Received on June 6, 2006; accepted on January 16, 2007.
Correspondence concerning this article should be addressed to S. Assabumrungrat (E-mail address: Suttichai.A@chula.ac.th).

Table 1 Materials and chemicals

Metal source	Iron (III) acetylacetonate 97% (Sigma-Aldrich Co.) Cupric (II) nitrate 99% (Sigma-Aldrich Co.) Ammonium metavanadate (V) 99.5% (Carlo Erba reagenti Co.)
Support	TiO_2 (JRC-TIO1) (Catalysis Society of Japan)
Solvent	99.8% Acetone (Carlo Erba Reagenti Co.) 99.8% Acetonitrile (Merck Co.) 99.7% Pyridine (Merck Co.)
Reducing agent	99.7% Ascorbic acid (Polskic Odczynniki Chemiczne S.A. Co.)
Substrate	99.7% Benzene (Merck Co.)
Oxidant	30 wt% Hydrogen peroxide (Merck Co.)
By product	99.9% Biphenyl (Sigma-Aldrich Co.)
Reference	98% Catechol (Sigma-Aldrich Co.) 99% Phenol (Panreac Sintesis Co.) 99.8% Quinol (APS Co.) 98% 1,4-Benzoquinone (ACROS Co.)

of benzene to phenol using amorphous microporous mixed oxides catalyst. The acetonitrile solvent showed the highest yield among several solvents; i.e., 2-propanol, dimethyl glycol, and propylene glycol. On the other hand, there are some researchers, who study a solvent free system from the environmental viewpoint but low conversion and yield are usually obtained. The liquid-phase oxidation of benzene to phenol in a benzene–water bi-phase system was studied (Mizuno *et al.*, 2005). The catalyst was dissolved in water that was saturated with benzene. Therefore benzene was oxidized to phenol in the water phase. By extracting the produced phenol into the organic phase, products were easily separated from the catalyst, preventing the consecutive oxidation of phenol.

It is widely accepted that OH• radicals can also be generated on photo-irradiated TiO_2 surfaces (Park and Choi, 2005). TiO_2 photocatalyst has been applied to the hydroxylation of benzene to phenol but the conversion efficiency in photocatalysis was lower than that of the Fenton process. Therefore, surface modifications of TiO_2 should be performed. The presence of electron acceptors, i.e., Fe(III), Ag(I) and O_2, enhanced the photocatalytic reaction (Park and Choi, 2005). In the addition, the recent works found that Cu-, Fe-, and V-containing catalysts gave high yield of phenol (Choi *et al.*, 2005; Liu *et al.*, 2005). It should be noted that the comparison of reaction performance of different systems published in the literature is rather difficult due to the differences in various parameters such as types and amounts of catalyst, support, oxidant and solvent and also the differences in operating condition such as the operating temperature and pressure.

In this study, we have mainly investigated the catalytic behavior of Fe(III), Cu(II) and V(V) catalysts impregnated with a TiO_2 commercial support for the hydroxylation of benzene to phenol at room temperature. Various reaction systems such as solvent free systems with and without UV for photooxidation and a system with a solvent were investigated. In addition, the influences of the solvent type and the amount of ascorbic acid as a reducing agent have also been studied.

1. Experimental

1.1 Materials and chemicals

The details of materials and chemicals employed in this work were summarized in **Table 1**. All chemicals were used without prior purification.

1.2 Catalyst preparation

Metal oxide/TiO_2 catalyst was prepared by impregnation of support powder in an aqueous solution of a metal salt at 353 K followed by evaporation and drying over night. The dry catalysts were calcined in an air stream with a heating rate of 10 K/min from room temperature to 773 K and left for 5 h to remove the organic template. After calcination, the catalysts were stored in a dessicator.

1.3 Characterization

XRD patterns of the TiO_2 support and metal supported catalysts were obtained by using X-ray diffractrometer, D 5000 (Siemens AG) using Cu Kα radiation equipped with Ni filter with a range of detection of 2θ 20–80 and a resolution of 0.04.

BET surface area and porosity of the catalysts were measured by Micromeritics ASAP 2020 (Micromeritics Instrument Corp.). The sample of 0.3 g was degassed at 573 K for 3 h and the amount of N_2 adsorption was observed.

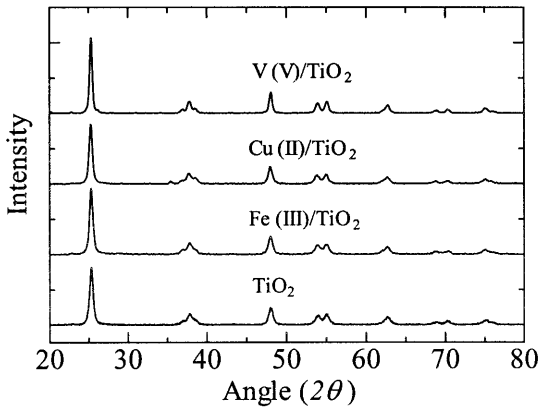

Fig. 1 XRD patterns of the TiO_2 support and supported metal catalysts

XPS surface analysis was performed using a Kratos Amicus X-ray photoelectron spectroscope (Shimadzu Corp.). The XPS spectra were measured using the following conditions: Mg Ka X-ray source at the current of 20 mA and 12 keV, resolution of 0.1 eV/step, and pass energy of 75 eV. The operating pressure was approximately 1×10^{-6} Pa. A wide-scan survey spectrum was collected for each sample in order to determine the elements present on the surface. All the binding energies were calibrated internally with the carbon C 1s photoemission peak at 285.0 eV. Photoemission peak areas were determined after smoothing and background subtraction using a linear routine. Deconvolution of complex spectra were done by fitting with Gaussian (70%)–Lorentzian (30%) shapes using the VISION 2 software equipped with the XPS system (Shimadzu Corp.).

1.4 Experimental setup and product analysis

The oxidation of benzene by H_2O_2 was carried out in a 125-cm^3 round flat bottomed flask at 303 K and 1 atm with a high speed stirrer. The reaction system consisted of two liquid phases: an organic phase containing a substrate and a solvent, and an aqueous phase containing acetone and 30% H_2O_2.

In a typical experiment, 0.2 g of catalyst (metal loading 5 wt%) in a metal oxide form was added in a liquid mixture containing 40 cm^3 of solvent, 30 cm^3 of H_2O_2 (0.32 mol) and 11 cm^3 of benzene (0.16 mol). For the photooxidation system, the ultraviolet light source is a black light blue fluorescent bulb (8 W).

The feed and products were analyzed by a gas chromatogragh (GC 9A, Shimazu Corp.) with a packed column of GP 10% SP-2100. The operating conditions of GC are as follows: the injection temperature of 523 K, detector temperature of 523 K, initial column temperature of 383 K, final column temperature of 443 K and temperature programmed rate of 10 K/min. The products were also analyzed by GC-MS especially for some product species which cannot be detected by the FID detector. The metal loading of catalyst was calculated as (the weight of metal)/(the weight of TiO_2 added metal).

Table 2 BET surface area and pore volume of support and synthesized catalysts and metal/Ti atomic ratio on surface analyzed by XPS

Catalyst	BET surface [m^2/g]	Pore volume [cm^3/g]	Metal/Ti atomic ratio on surface
TiO_2 (JRC-TIO-1)	76.56	0.29	—
V/TiO_2 5%	60.62	0.24	0.31
Cu/TiO_2 5%	62.33	0.23	0.32
Fe/TiO_2 5%	68.52	0.25	0.35

2. Results and Discussion

2.1 Catalyst characterization

From our preliminary study, metal loading at 5 wt% was selected for this study because it showed the optimum value for obtaining a reasonable yield and turnover number. The characteristics of the catalyst were investigated to identify its crystal structure, surface area and pore size volume and metal loading on the surface which were analyzed by XRD, BET and XPS, respectively. Due to a low loading, no obvious peaks of V, Cu and Fe metal were observed, similar XRD patterns with a blank TiO_2 anatase phase were obtained as shown in **Figure 1**. However, it should be noted that from the other sets of our data, the metal oxide peaks were observed obviously at metal loadings of higher than 10 wt% (not shown). The XPS results shown in **Table 2** suggest that the metal species were deposited at least on the surface of the support.

The BET surface area and pore volume of various metal-supported catalysts were shown in Table 2. As metals were loaded on the TiO_2 support, the surface area and pore volume decreased compared with those of the blank TiO_2 support.

2.2 Effect of metal species on the reaction performance in the solvent free system

The byproducts from the reactions were CO_2, hydroquinone, cresol, biphenyl and catechol. However, CO_2 went out from our open system, the analysis of sampled exit gas showed a neglected amount of CO_2 and, therefore, the amount of CO_2 was not measured in the routine experiments. As for the oxidation of the solvent, a blank test was done in the system consisting of an only solvent, TiO_2 and H_2O_2 without benzene. As an example, only a small amount of acetic acid and CO_2 were detected from the blank test with the acetone solvent. Because the system was operated at room temperature, only a small amount of solvent could be oxidized. Therefore, this effect could be negligible.

The effect of metal species on the reaction performance in the solvent free system was summarized

Table 3 Catalytic performances for hydroxylation of benzene to phenol of Fe(III), Cu(II), V(V)/TiO_2 catalysts under a solvent free condition

Catalyst	Conversion[a] [%]	Selectivity[b] [%]	Yield[c] [%]	TOF[d] [h^{-1}]	TON[e]
Fe/TiO_2 5%	0.5	46	0.23	0.53	2.14
Cu/TiO_2 5%	0.29	80	0.23	0.61	2.44
V/TiO_2 5%	0.21	90	0.19	0.4	1.62

[a]Conversion [%] = (moles of benzene reacted)/(initial moles of benzene) × 100
[b]Selectivity [%] = (moles of phenol)/(moles of benzene reacted) × 100
[c]Yield [%] = (moles of phenol)/(initial moles of benzene) × 100
[d]Turnover frequency = (moles of phenol)/(moles of metal × h)
[e]Turnover number = (moles of phenol)/(moles of metal)

in **Table 3**. The operating condition and the terms of reaction performance were shown below the table. The activity of metal catalysts was ordered as Fe(III) > Cu(II) > V(V), however, the phenol selectivity was in the reverse order. It should be noted that the differences of surface area and pore volume among three metal species were insignificant (as shown in Table 2). In addition, the impregnation method does not usually change the structure or morphology of the support. The characterization study of Navio *et al.* (1996) showed that the structure of TiO_2 was similar to that of TiO_2 impregnated with Fe(III) from Iron(III) acetylacetonate. Therefore, the differences in catalytic activity should be mainly affected by the difference in type of metal ion species. The formation of phenol proceeds through a similar mechanism as that of Fenton chemistry by replacing the redox of Fe(III)/Fe(II) to that of Cu(II)/Cu(I) (Sasaki *et al.*, 1983; Ito *et al.*, 1988; Yamanaka *et al.*, 2002) as well as V(V)/V(IV). Even though the solvent free system is environmental friendly, the obtained yields are very low. In this case Cu/TiO_2 was highest of TON and TOF. The system should be modified in several ways such as by adding solvent or operating in photooxidation with a UV light as studied in the following sections.

2.3 Effect of solvent on the reaction performance

A solvent was used to reduce the mass transfer resistance for dissolving H_2O_2 into the benzene phase. It should be noted that 40 cm^3 of various solvents were added. In this amount, the system stills consisted of three phases (i.e., organic, aqueous and catalyst). Using a high-speed stirrer for well mixing was preferable than adding more solvent for obtaining two-phase mixture to avoid the dilution effect. The effects of several solvent species, i.e., acetone, acetronitrile and pyridine, on the reaction performance in various metal catalysts were summarized in **Table 4**.

The effect of the operation with a UV light was also provided in the table and will be described in the next section.

In the case of acetone and acetonotrile solvents, the addition of a solvent obviously improved conversion, the yield and also turnover number and turnover frequency for all metal catalysts. The Fe(III) show the highest of TON and TOF in the solvent system. These solvents are effective to prevent the decomposition of H_2O_2, which leads to an increase of TON (total activity). On the other hand, in the case of the pyridine solvent, conversion and the yield decreased when adding solvent.

These agree with the necessity of the acidic environment around the catalyst (Seo *et al.*, 1993). Acetone gave the highest conversion in all metal catalysts but, unfortunately, the selectivity was low. The acetonitrile showed a good alternative, offering a slightly lower yield with significantly higher phenol selectivity.

2.4 Effect of UV light on the reaction performance

Comparison of the results shown in Tables 3 and 4 for the cases of solvent free with and without UV light indicated that higher conversion and yield can be obtained by applying the UV light. Selectivity slightly increased in the case of an Fe catalyst while slightly decreased in the cases of Cu and V catalysts.

It should be noted that the activity of metal catalyst was ordered as Fe(III) > Cu(II) > V(V) and in the reverse order of the selectivity, which is the same trend as the cases of solvent free and solvent added both in the previous sections.

In the case of using acetone as a solvent, UV light improved the conversion but with an insignificant effect on selectivity for all metal catalysts.

In this study only a simple comparison was done on the photocatalytic oxidation of benzene. No apparent change on the selectivity was observed but strong promotion in conversion.

The primary and principal step of the UV/H_2O_2 degradation has been postulated as the initial attack by photon to hydrogen peroxide and the formation of hydroxyl free radicals (OH•) (De *et al.*, 1999).

$$H_2O_2 + h\nu \rightarrow 2OH\bullet$$

The UV light enhances the decomposition of H_2O_2 to increase the hydroxyl radicals for the reaction to phenol. However, if the amount of the hydroxyl radicals was excessive, it can convert phenol to hydroquinone and benzoquinone.

In the UV light system, TiO_2 enhanced the decomposition of H_2O_2 to hydroxyl free radicals and hydroxyl ions by generating electrons (Hong and Kang, 2006).

$$TiO_2 + h\nu \rightarrow h^+ + e^-$$

$$H_2O_2 + e^- \rightarrow OH\bullet + OH^-$$

Table 4 Catalytic performances for hydroxylation of benzene to phenol of Fe(III), Cu(II), $V(V)/TiO_2$ catalysts in a solvent-added systems and solvent free system with UV

Catalyst	Solvent	Conversion[a] [%]	Selectivity[b] [%]	Yield[c] [%]	TOF[d] [h^{-1}]	TON[e]
Fe	Acetone	4.5	32	1.44	3.35	13.39
	Acetronitrile	1.2	90	1.08	2.51	10.04
	Pyridine	0.2	95	0.19	0.44	1.77
	Solvent free with UV	2.4	51	1.22	2.85	11.35
	Acetone with UV	5.6	30	1.68	3.91	15.62
Cu	Acetone	3.1	32	0.99	2.62	10.48
	Acetronitrile	1	88	0.88	2.33	9.31
	Pyridine	0.2	92	0.18	0.49	1.91
	Solvent free with UV	1.5	72	1.08	2.86	11.43
	Acetone with UV	4.5	32	1.44	3.81	15.24
V	Acetone	2.1	39	0.82	1.74	6.97
	Acetronitrile	0.9	84	0.76	1.61	6.46
	Pyridine	0.1	100	0.1	0.21	0.85
	Solvent free with UV	1.2	82	0.98	2.09	8.33
	Acetone with UV	3.9	37	1.44	3.06	12.27

(Benzene, 11 cm^3; catalyst weight, 0.2 g; benzene/H_2O_2 mole ratio, 0.5; solvent, 40 cm^3; temperature, 303 K; pressure, 1 atm; reaction time, 4 h)
[a]Conversion [%] = (moles of benzene reacted)/(initial moles of benzene) × 100
[b]Selectivity [%] = (moles of phenol)/(moles of benzene reacted) × 100
[c]Yield [%] = (moles of phenol)/(initial moles of benzene) × 100
[d]Turnover frequency = (moles of phenol)/(moles of metal × h)
[e]Turnover number = (moles of phenol)/(moles of metal)

The hydroxyl radical reacts directly with benzene to produce a hydroxycyclohexadienyl (CHD) radical, which subsequently undergoes an H^+ abstraction by metal catalyst as follows (Bremmer *et al.*, 2000; Gao and Hua, 2004).

$$OH\bullet + \text{benzene} \rightarrow \text{CHD}$$

$$\text{CHD} + Fe(III) \rightarrow \text{phenol} + Fe(II) + H^+$$

However, the CHD radical intermediate can react with H^+ and collapse to benzene as follows.

$$\text{CHD} + Fe(II) + H^+ \rightarrow \text{benzene} + Fe(III) + \text{water}$$

Although photocatalytic activity could be modified by adding metal species rather than the promotion of OH radicals, Park and Choi (2005) suggested the effect of Fe species to oxidize CHD radicals. They have also suggested the "photo-Fenton reaction" in the presence of $Fe^{3+} + H_2O_2 + h\nu$. On the other hand, Shimizu *et al.* (2002) reported that Fe^{3+} and Cu^{2+} were selective for dihydroxybenzene while TiO_2 was likely to oxidize dihydroxybenzene to CO_2. Thus, further studies are needed on the photocatalytic promotion of added metal ions.

The side reaction of hydroxyl radicals reacted with H_2O_2 to water can occur and therefore, the concentration of H_2O_2 possibly decreased faster than the system without UV light (De *et al.*, 1999).

$$H_2O_2 + OH\bullet \rightarrow HO_2\bullet + H_2O$$

$$OH\bullet + H_2O_2 \rightarrow O_2\bullet + H + H_2O$$

$$HO_2\bullet + H_2O_2 \rightarrow OH\bullet + O_2 + H_2O$$

The species of hydrogen oxidant compound affected the generation of phenol and other aromatic compounds. Moreover, when increasing the temperature, the hydrogen oxidant compound can be decomposed faster than the decomposition at room temperature.

Comparing with the case of using acetone as a solvent, the obtained yields are similar while phenol selectivities are significantly higher in the case of solvent-free with UV light.

2.5 Effect of reducing agent

The ascorbic acid was used as a reducing agent for changing the metal ion state, such as Fe(III) to Fe(II), V(V) to V(IV) and Cu(II) to Cu(I) (Seo *et al.*, 1997). **Figure 2** shows the effects of the amount of ascorbic acid and types of solvent on the phenol yield and selectivity of the $Fe(III)/TiO_2$ catalyst.

In the case of a solvent added system, the phenol yield increased while selectivity slightly decreased with

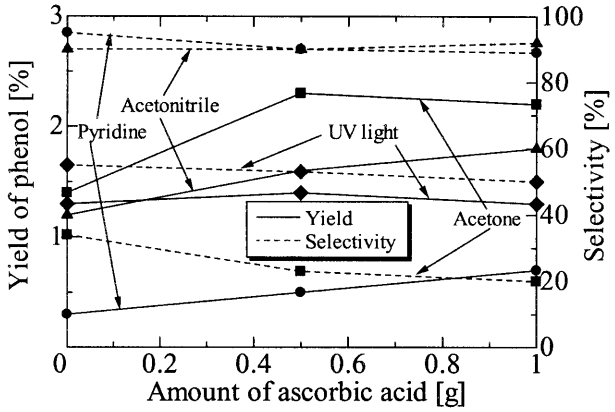

Fig. 2 Effect of the amount of ascorbic acid on the phenol yield and selectivity for different systems catalyzed by the Fe(III)/TiO_2 catalyst

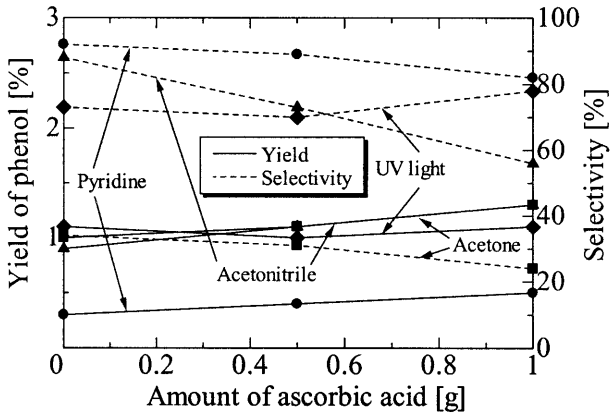

Fig. 3 Effect of the amount of ascorbic acid on the phenol yield and selectivity for different systems catalyzed by the Cu(II)/TiO_2 catalyst

an increasing amount of ascorbic acid for all solvent types. A similar tendency can be obtained for the systems catalyzed by Cu(II) and V(V) metal catalysts as shown in **Figures 3** and **4**, respectively.

The mechanism of Fenton's method is widely accepted as follows.

$$Fe(II) + H_2O_2 \rightarrow Fe(III) + OH\bullet + OH^-$$

The ascorbic acid is well known as a good reducing agent. It changes the state of metal catalyst from Fe(III) to Fe (II).

$$2Fe(III) + \text{ascorbic acid} + 0.5O_2 \rightarrow 2Fe(II) + \text{dehydroascorbic acid} + H_2O$$

$$2Fe(II) + O_2 + 2H^+ \rightarrow 2Fe(III) + H_2O_2$$

$$Fe(III) + H_2O_2 + H^+ \rightarrow Fe(II) + OH\bullet + H_2O$$

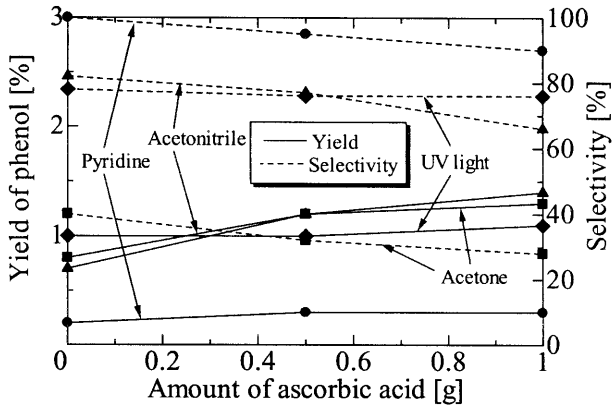

Fig. 4 Effect of the amount of ascorbic acid on the phenol yield and selectivity for different systems catalyzed by the V(V)/TiO_2 catalyst

Both Fe(III) and Fe(II) play important roles in the reaction system. Fe(III) reacts with a CHD radical intermediate to form phenol while Fe(II) promotes the decomposition of hydrogen peroxide to a hydroxyl free radical. The amount of generated hydroxyl radicals which affects the phenol formation could be controlled by the amounts of ascorbic acid and metal catalyst added.

It is worthwhile to note that the formation of phenol proceeds through the similar mechanism of that of Fenton chemistry by replacing the redox of Fe(III)/Fe(II) to that of Cu(II)/Cu(I) and V(V)/V(IV).

However, as shown in Figures 2–4, further addition of ascorbic acid caused a lower effect on the yield enhancement. In some cases, a drop of the yield was observed. It can be explained that too the much ascorbic acid, which functions as a reducing agent, suppressed the formation of Fe(III) which resulted in a decrease in the formation of phenol via the H^+ abstraction of CHD. It should be noted that phenol can be produced even though no ascorbic acid was added. These results were not the same as those reported by Miyahara *et al.* (2001) that no phenol was produced in the absence of ascorbic acid.

In the case of a solvent-free with UV light condition, the increase in the amount of ascorbic acid insignificantly affected the conversion and selectivity for all metal catalysts as shown in Figures 2–4. As the formation of active OH• species in the photocatalytic reactions does not include the oxidation of metal ions, only a retardation effect of ascorbic acid might be observed.

Conclusions

The hydroxylation of benzene to phenol with hydrogen peroxide was performed at room temperature using various transition metals, Fe(III), Cu(II) and

V(V) impregnated on TiO_2 support. The activity was ordered as follows: Fe(III) > Cu(II) > V(V); however, the phenol selectivity was in the reverse order. Among various solvents studied, i.e., acetone, acetronitrile and pyridine, acetone showed the highest conversion and yield but low in selectivity. However, acetronitrile may be an attractive solvent because of its high selectivity. Operation with UV light can significantly the improve the yield and selectivity. Addition of ascorbic acid can enhance the phenol yield; however, too much ascorbic acid can retard the yield improvement.

Acknowledgments

Financial supports from the Thailand Research Fund and Commission on Higher Education are gratefully acknowledged. The authors also would like to thank Assistant Professor Okorn Mekasuwandamrong and Assistant Professor Varong Pavarajarn for useful discussion.

Literature Cited

Bremmer, D. H., A. E. Burgess and F. B. Li; "Coupling of Chemical, Electrochemical and Ultrasonic Energies for Controlled Generation of Hydroxyl Radicals Direct Synthesis of Phenol by Benzene Hydroxylation," *Appl. Catal. A*, **203**, 111–120 (2000)

Chen, Y. W. and Y. H. Lu; "Characteristics of V-MCM-41 and Its Catalytic Properties in Oxidation of Benzene," *Ind. Eng. Chem. Res.*, **38**, 1893–1903 (1999)

Choi, J. S., T. H. Kim, K. Y. Choo, J. S. Sung, M. B. Saidutta, S. O. Ryu, S. D. Song, B. Ramachandra and Y. W. Rhee; "Direct Synthesis of Phenol from Benzene on Iron-Impregnated Activated Carbon Catalysts," *Appl. Catal. A*, **290**, 1–8 (2005)

De, A. K., B. Chaudhuri, S. Bhattacharjee and B. K. Dutta; "Estimation of (·)OH Radical Reaction Rate Constants for Phenol and Chlorinated Phenols Using UV/H_2O_2 Photo-Oxidation," *J. Hazard Mater.*, **64**, 91–104 (1999)

Dubey, A. and S. Kannan; "Liquid Phase Hydroxylation of Benzene over Cu-Containing Ternary Hydrotalcites," *Catal. Commum.*, **6**, 394–398 (2005)

Gao, F. and R. Hua; "Highly Efficient K7NiV13O38-Catalyzed Hydroxylation of Aromatics with Aqueous Hydrogen Peroxide (30%)," *Appl. Catal. A*, **270**, 223–226 (2004)

Hong, W. J. and M. Kang; "The Super-Hydrophilicities of Bi-TiO_2, V-TiO_2, and Bi-V-TiO_2 Nano-Sized Particles and Their Benzene Photodecompositions with H_2O Addition," *Mater. Lett.*, **60**, 1296–1305 (2006)

Ito, S., H. Okada, R. Katayama, A. Kunai and K. Sasaki; "Direct Conversion of Benzene to Hydroquinone Mediated with Cu(I)/Cu(II) Redox System," *J. Electrochem. Soc.*, **135**, 2996–3000 (1988)

Kanzaki, H., T. Kitamura, R. Hamada, S. Nishiyama and S. Tsuruya; "Activities for Phenol Formation Using Cu Catalysts Supported on Al_2O_3 in the Liquid-Phase Oxidation of Benzene in Aqueous Solvent with High Acetic Acid Concentration," *J. Mol. Catal. A: Chem.*, **208**, 203–211 (2004)

Lemke, K., H. Ehrich, U. Lohse, H. Berndt and K. Jahnisch; "Selective Hydroxylation of Benzene to Phenol over Supported Vanadium Oxide Catalysts," *Appl. Catal. A*, **243**, 41–51 (2003)

Liu, Y., K. Murata and M. Inaba; "Liquid-Phase Oxidation of Benzene to Phenol by Molecular Oxygen over Transition Metal Substituted Polyoxometalate Compounds," *Catal. Commun.*, **6**, 679–683 (2005)

Miyahara, T., H. Kanzaki, R. Hamada, S. Kuroiwa, S. Nishiyama and S. Tsuruya; "Liquid-Phase Oxidation of Benzene to Phenol by CuO–Al_2O_3 Catalysts Prepared by Co-Precipitation Method," *J. Mol. Catal. A: Chem.*, **176**, 141–150 (2001)

Miyake, T., M. Hamada, H. Niwa, M. Nishizuka and M. Oguri; "Effect of Vanadium Compound on the Synthesis of Phenol by Hydroxylation of Benzene with Oxygen and Hydrogen on Platinum Catalyst," *J. Mol. Catal. A: Chem.*, **178**, 199–204 (2002)

Mizuno, T., H. Yamada, T. Tagawa and S. Goto; "Partial Oxidation Benzene in Benzene–Water Bi-Phase System," *J. Chem. Eng. Japan*, **38**, 849–853 (2005)

Navio, J. A., G. Colon, M. I. Litter and G. N. Bianco; "Synthesis, Characterization and Photocatalytic Properties of Iron-Doped Titania Semiconductors Prepared from TiO_2 and Iron(III) Acetylacetonate," *J. Mol. Catal. A: Chem.*, **106**, 267–276 (1996)

Okamura, J., S. Nishiyama, S. Tsuruya and M. Masai; "Formation of Cu-Supported Mesoporous Silicates and Aluminosilicates and Liquid-Phase Oxidation of Benzene Catalyzed by the Cu-Mesoporous Silicates and Aluminosilicates," *J. Mol. Catal. A: Chem.*, **135**, 133–142 (1998)

Park, H. and W. Choi; "Photocatalylytic Conversion of Benzene to Phenol Using Midified TiO_2 and Polyoxometalates," *Catal. Today*, **101**, 291–297 (2005)

Sasaki, K., A. Kunai, J. Harada and S. Nakabori; "Electrolytic Hydrogenation of Phenols in Aqueous Acid Solutions," *Electrochimica. Acta*, **28**, 671–674 (1983)

Schmidt, R. J.; "Industrial Catalytic Processes-Phenol Production," *Appl. Catal. A*, **280**, 89–103 (2005)

Seo, Y. J., T. Tagawa and S. Goto; "Liquid Phase Oxidation of Benzene to Phenol over Supported $FeCl_3$ Catalyst," *J. Mol. Catal.*, **78**, 201–210 (1993)

Seo, Y. J., T. Tagawa and S. Goto; "Effect of Supports for the Direct Cxidation of Benzene to Phenol over Supported $FeCl_3$ Catalyst," *React. Kinet. Catal. Lett.*, **54**, 265–271 (1995)

Shimizu, K., T. Kaneko, T. Fujishima, T. Kodama, H. Yoshida and Y. Kitayama; "Selective Oxidation of Liquid Hydrocarbons over Photoirradiated TiO_2 Pillared Clays," *Appl. Catal. A*, **225**, 185–191 (2002)

Stockmann, M., F. Konietzni and J. U. Notheis; "Selective Oxidation of Benzene to Phenol in Liquid Phase with Amorphous Microporous Mixed Oxides," *Appl. Catal. A*, **225**, 343–358 (2001)

Uriarte, A. K., M. A. Rodkin, M. J. Gross, A. S. Kharitonov and G. I. Panov; "Direct Hydroxylation of Benzene to Phenol by Nitrous Oxide," *Stud. Surf. Sci. Catal.*, **110**, 857–864 (1998)

Xiao, F. S., J. Sun, X. Meng and R. Yu; "A Novel Catalyst of Copper Hydroxyphosphate with High Activity in Wet Oxidation of Aromatics," *Appl. Catal. A*, **207**, 267–271 (2001)

Yamanaka, H., R. Hamada, H. Nibuta, S. Nishiyama and S. Tsuruya; "Gas-Phase Catalytic Oxidation of Benzene over Cu-Supported ZSM-5 Catalysts: An Attempt of One-Step Production of Phenol," *J. Mol. Catal. A: Chem.*, **178**, 89–95 (2002)

Zhang, J., Y. Tang, G. Li and C. Hu; "Room Temperature Direct Oxidation of Benzene to Phenol Using Hydrogen Peroxide in the Presence of Vanadium-Substituted Heteropolymolybdates," *Appl. Catal. A*, **278**, 251–261 (2005)

Appendix 12

J. Ind. Eng. Chem., **Vol. 13**, No. 3, (2007) 444-451

Liquid Phase Hydroxylation of Benzene to Phenol with Hydrogen Peroxide Catalyzed by Fe(III)/TiO_2 Catalysts at Room Temperature

Garun Tanarungsun, Worapon Kiatkittipong*, Suttichai Assabumrungrat†, Hiroshi Yamada, Tomohiko Tagawa**, and Piyasan Praserthdam**

Center of Excellence in Catalysis and Catalytic Reaction Engineering, Department of Chemical Engineering, Faculty of Engineering, Chulalongkorn University, Bangkok 10330, Thailand
**Department of Chemical Engineering, Faculty of Engineering and Industrial Technology, Silpakorn University, Nakhon Pathom 73000, Thailand*
***Department of Chemical Engineering, Nagoya University, Chikusa, Nagoya, 464-8603, Japan*

Received November 15, 2006; Accepted February 2, 2007

Abstract: Liquid phase hydroxylation of benzene to phenol with hydrogen peroxide on Fe(III)/TiO_2 catalysts was examined at room temperature. The catalytic performances of various TiO_2 supports were tested. The TiO_2 (JRC-TIO-1, anatase) having the highest surface area and pore volume appeared to be the most suitable support because it offered the highest activity and selectivity. The effects of the Fe(III) precursor and Fe(III) loading were investigated. The catalyst prepared from iron(III) acetylacetonate with 5 wt% Fe(III) loading was selected as a suitable catalyst. From tests of seven solvents, it was found that acetone gave the highest conversion and yield; however, acetonitrile may also be attractive because it offered high selectivity. Biphasic operation, introduced by adding more amount of solvent, did not show a potential improvement because the dilution effect seemed to play an important role in the reaction system. Finally, it was revealed that increasing the amount of ascorbic acid helped increase the conversion by enhancing the decomposition of H_2O_2 to hydroxyl radicals. However, it suppressed the formation of Fe(III), which resulted in a decrease in the degree of phenol formation. In addition, phenol can be further reacted with excess hydroxyl radicals to yield hydroquinone, benzoquinone, and catechol, resulting in a decreased selectivity.

Keywords: *hydroxylation of benzene, phenol production, hydrogen peroxide, Fe(III), TiO_2*

Introduction

Phenol is an important intermediate for the synthesis of various petrochemical and agrochemical products. Commercial phenol production is mainly based on the cumene process [1]. Because this process produces acetone as a co-product, which will be oversupplied in the future, and the cumene hydroperoxide intermediate can decompose violently, the development of an alternative process is desired. A number of studies have been focused on the direct oxidation of benzene to phenol.

There are two main pathways for the direct oxidation of benzene to phenol; i.e., gas phase and liquid phase reactions. Gas phase hydroxylation of benzene with nitrous oxide has been conducted in a pilot facility [2]. However, this process is suitable only when a supply of nitrous oxide is available, for example, as a by-product from adipic acid synthesis. Major problems arise when adapting this process to industrial applications because of catalyst deactivation by heavy coke formation and the low phenol selectivity of nitrous oxide [2]. In addition, the process is operated at an elevated temperature (higher than 573 K) and results in marginal conversion, resulting in undue high costs. Liquid phase hydroxylation of benzene to phenol is operated at room temperature or temperatures normally not higher than 353 K. H_2O_2 or O_2 is employed as an oxidant. High selectivity can be obtained with lower oxidant cost when compared with the gas phase operation. Therefore, many researchers have focused on this route and have aimed to develop suitable catalysts for the reaction.

† To whom all correspondence should be addressed.
(e-mail: suttichai.A@chula.ac.th)

Table 1. Materials and Chemicals

Metal source	Iron(III) acetylacetonate, 97 % (Aldrich)
	Iron(III) nitrate monohydrate, 98 % (SIGMA)
	Iron(III) chloride hexahydrate, 99 % (MERCK)
Support	TiO_2 (JRC-TIO1, JRC-TIO4) (Catalysis Society of Japan)
	TiO_2, 99 % (Fluka)
	Titanium(IV) dioxide, powder, 99.8 % (Aldrich)
Solvent	Acetone, 99.8 % (Carlo Erba)
	Acetonitrile, 99.8 % (MERCK)
	1- Butyl alcohol, 99 % (Fluka)
	tert-Butyl alcohol, 99 % (Fluka)
	Dichloromethane, 99 % (Carol Erba reagenti)
	Ethyl alcohol, 99.9 % (Carol Erba reagenti)
	Pyridine, 99.7 % (MERCK)
Reducing agent	Ascorbic acid, 99.7 % (Polskic Odczynniki Chemiczne S.A.)
Substrate	Benzene, 99.7 % (MERCK)
Oxidant	Hydrogen peroxide, 30 % wt. (MERCK)
By-product reference	Biphenyl, 99.9 % (Fluka)
	Catechol, 98 % (Fluka)
	Phenol, 99 % (Panreac Sintesis)
	Quinol, 99.8 % (APS)
	1,4 Benzoquinone, 98 % (ACROS)

Several kinds of metal, such as Fe, Cu, and V, were loaded on various supports, such as SiO_2, Al_2O_3, HZSM-5, MCM-41, and TiO_2 [3-6]. Fe-containing catalysts have drawn some attention from researchers for the hydroxylation of benzene to phenol because of its low cost and acceptable yield. Seo and coworkers [3,7] studied the use of Fe(II) and Fe(III) on SiO_2. Various Fe precursors, i.e., $FeCl_3$, $FeCl_2$, and $Fe(NO_3)_3$, were investigated. Fe(III) from $FeCl_3$ as precursor showed good performance for the hydroxylation of benzene to phenol; the addition of acidic compounds strongly affected the catalytic performance.

The solvent is usually added to the reaction system to dissolvs hydrogen peroxide and benzene into one phase for the oxidation of benzene to phenol. Several solvents, such as acetone, acetonitrile, acetic acid, pyridine and, dichloromethane, have been employed [8-14]. However, there are only a few studies that have compared the effects of various solvent types. Stockmann and coworkers [10] studied the oxidation of benzene to phenol using amorphous microporous mixed-oxide catalyst. Acetonitrile showed the highest yield among several solvents; i.e., 2-propanol, dimethyl glycol, and propylene glycol. On the other hand, some researchers have studied solvent-free systems from an environmental viewpoint. Low conversion and yield are usually reported.

TiO_2 has been used extensively as a catalyst and support for oxidation and photooxidation reactions [15-19]. It is widely accepted that OH^o radicals can also be generated on illuminated TiO_2 surfaces [20]. TiO_2 photocatalysis has been applied to the hydroxylation of benzene to phenol, but the conversion efficiency in this photocatalysis was lower than that of the Fenton process. Therefore, surface modifications of TiO_2 should be performed. The presence of electron acceptors, i.e., Fe and O_2, enhanced the photocatalytic reaction [20]. In addition, recent studies have found that Cu-, Fe-, and V-containing catalysts gave high yields of phenol [12,13]. It should be noted that comparison of the reaction performance of different systems published in the open literature is rather difficult because of differences in various parameters, such as the types and amounts of catalysts, supports, oxidants, and solvents and also differences in operating conditions such as the operating temperature and pressure.

In this study, the liquid phase hydroxylation of benzene to phenol with hydrogen peroxide on various Fe(III)/TiO_2 catalysts at room temperature was investigated. Several TiO_2 supports were tested. TiO_2 has been used as a support for many oxidation reactions. It was also reported to offer high performance for the oxidation of benzene to phenol [20]. The effects of the type of Fe(III) precursor and the Fe(III) loading were studied to find a suitable catalyst. The catalytic performances of the systems with different types of solvent and under biphasic/triphasic operations were compared. In addition, the influence of the amount of ascorbic acid as a reducing agent was considered.

Experimental

Materials and Chemicals

Table 1 summarizes the materials and chemicals employed in this work. All chemicals were used without prior purification. Four types of TiO_2 supports, i.e., TiO_2 (JRC-TIO-1), TiO_2 (JRC-TIO-4), TiO_2 (Fluka), and TiO_2 (Aldrich), and three types of Fe(III) precursors, i.e., iron(III) acetylacetonate, iron(III) chloride hexahydrate, and iron(III) nitrate monohydrate, were used in the study.

Catalyst Preparation

Fe(III)/TiO_2 catalysts were prepared by impregnation of TiO_2 support powder in a solution of Fe(III) precursor at 353 K, followed by evaporation and drying overnight. The catalysts obtained were calcined in a furnace continuously fed with air (flow: 60 cm^3/min). The temperature was increased from room temperature to 773 K at a heating rate of 10 K/min and then held for 5 h to remove organic residues. After calcination, the catalysts were stored in a dessicator.

Table 2. Catalytic Performance of Commercial TiO_2 Supports

Catalyst	Conversion [a] (%)	Selectivity [b] (%)	BET surface area (m^2/g)	Pore volume (cm^3/g)
TiO_2 (JRC-TIO1, anatase)	0.8	100	76.6	0.29
TiO_2 (JRC-TIO4, anatase)	0.2	72	51.8	0.11
TiO_2 (Fluka, anatase)	0.4	100	16.5	0.03
TiO_2 (Aldrich, anatase)	0.1	70	8.0	0.02
TiO_2 (JRC-TIO1, rutile)	0.03	100	1.8	0.003
TiO_2 (Fluka, rutile)	0.01	100	1.7	0.002

(Benzene = 11 cm^3; catalyst weight = 0.2 g; benzene/H_2O_2 mole ratio = 0.5; temperature = 303 K; pressure = 1 atm; reaction time = 4 h)
[a] Conversion calculated as moles of benzene reacted per initial moles of benzene*100 %
[b] Selectivity calculated as moles of phenol per mole of benzene reacted*100 %

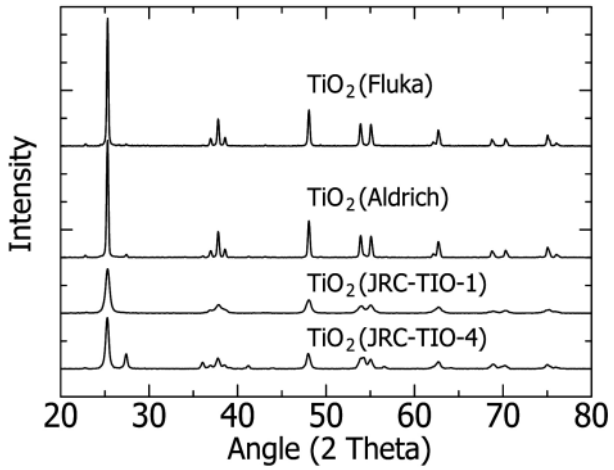

Figure 1. XRD patterns of TiO_2 supports.

Characterization

XRD patterns of the TiO_2 supports and Fe(III)/TiO_2 catalysts were obtained by using a SIEMENS D 5000 X-ray diffractrometer, with Cu Ka radiation and equipped with a Ni filter; range of detection (2θ): 20～80; resolution 0.04.

The BET surface areas and porosities of the catalysts were measured by a Micromeritics ASAP 2020 instrument. A sample of 0.3 g was degassed at 573 K for 3 h and the amount of N_2 adsorbed was observed.

XPS surface analysis was performed using Kratos Amicus X-ray photoelectron spectroscopy. The XPS spectra were measured using the following conditions: Mg Ka X-ray source at current of 20 mA and 12 keV, resolution of 0.1 eV/step, and pass energy of 75 eV. The operating pressure was ca. 1×10^{-6} Pa. A wide-scan survey spectrum was collected for each sample to determine the elements present on the surface. All the binding energies were calibrated internally with the carbon C 1s photoemission peak at 285.0 eV. Photoemission peak areas were determined after smoothing and background subtraction using a linear routine. Deconvolution of complex spectra was done by fitting with Gaussian (70 %)-Lorentzian (30 %) shapes using the VISION 2 software that came with the XPS system.

Experimental Setup and Product Analysis

The hydroxylation of benzene by H_2O_2 was carried out in a 125-cm^3 round-flat-bottomed flask at 303 K and 1 atm with high-speed stirring at 600 rpm. In a typical experiment, 0.5 g of ascorbic acid (2.8 mmol) was added in a liquid mixture containing 40 cm^3 of solvent, 30 cm^3 of H_2O_2 (0.32 mol), and 11 cm^3 of benzene (0.16 mol). It should be noted that the typical experiment was operated in a triphasic system consisting of solid catalyst, solvent phase, and aqueous phase. When more solvent was added to the system, the reaction might have occurre in the biphasic system comprising the solid catalyst and solvent phase.

The feed and products were analyzed by a gas chromatogragh (SHIMADZU 9A) equipped with a packed column of GP 10 % SP-2100. The operating conditions of the GC were as follows: injection temperature of 523 K, detector temperature of 523 K, initial column temperature of 383 K, final column temperature of 443 K, and temperature programmed rate of 10 K/min. The products were also analyzed by GC-MS, especially for some product species that could not be detected by the FID detector. The benzene conversion is defined as the number of moles of benzene consumed by the reaction divided by the initial unmber of moles of benzene, while the phenol selectivity is defined as the nuber of moles of generated phenol divided by the number of moles of benzene consumed.

Results and Discussion

Selection of TiO_2 Supports

TiO_2 was used as a catalyst support for the hydroxylation of benzene to phenol. TiO_2 supports were characterized by XRD. The similar XRD patterns shown in Figure 1 indicate that all of the supports were of the anatase phase [21]. The blank reaction tests of the TiO_2 supports were performed under solvent-free conditions. The results shown in Table 2 reveal that TiO_2 (JRC-TIO-1) offered the highest conversion, which corresponded with it also having the highest BET surface area and pore

Table 3. Effects of %Fe(III) Loading and Type of Fe(III) Precursor on Catalytic Performance

Precursor	Fe loading (%)	Conversion[a]	Selectivity[b]	Yield[c]	TOF[d]	TON[e]	BET[f]	Pore volume [g]
Fe(III) aca	1	4.7	25	1.19	13.83	55.34	74.4	0.26
	5	10.8	21	2.29	5.32	21.30	68.5	0.25
	10	13.2	20	2.65	3.08	12.32	64.3	0.22
	20	14.8	18	2.63	1.53	6.11	57.9	0.19
Fe(III) Cl	1	4.2	29	1.23	14.26	57.03	72.4	0.27
	5	9.2	23	2.16	5.02	20.09	69.1	0.24
	10	11.2	20	2.21	2.57	10.28	64.8	0.23
	20	12.8	18	2.24	1.30	5.21	58.5	0.2
Fe(III) N	1	5.1	24	1.23	14.29	57.15	70.1	0.26
	5	11.2	19	2.13	4.95	19.81	65.4	0.23
	10	13.7	16	2.16	2.51	10.04	59.9	0.22
	20	16.1	14	2.20	1.28	5.12	54.2	0.18

(Benzene = 11 cm^3; catalyst weight = 0.2 g; benzene/H_2O_2 mole ratio = 0.5; acetone solvent = 40 cm^3; ascorbic acid = 0.5 g; temperature = 303 K; pressure = 1 atm; reaction time = 4 h)

[a] Conversion calculated as moles of benzene reacted per initial moles of benzene*100 %

[b] Selectivity calculated as moles of phenol per mole of benzene reacted*100 %

[c] Yield calculated as moles of phenol per initial moles of benzene*100 %

[d] Turnover frequency calculated as moles of phenol per mole of Fe per h

[e] Turnover number calculated as moles of phenol per mole of Fe

[f] BET surface area (m^2/g)

[g] Pore size volume (cm^3/g)

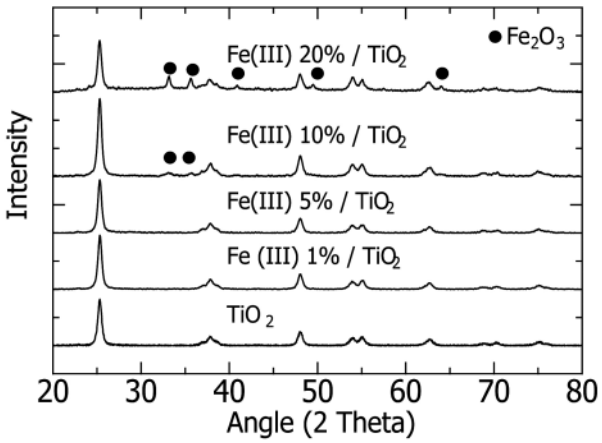

Figure 2. XRD patterns of Fe(III)/TiO_2 at various % loading (Fe(III) acetylacetonate as precursor).

volume. TiO_2 (JRC- TIO-1) and TiO_2 (Fluka) were further converted to the rutile phase by calcination at 773 K for 20 h. The reaction tests reveal that although TiO_2 in the rutile phase still maintained high selectivity (100 %), the conversion became much lower, which corresponded with the significant reduction of its BET surface area and pore volume. It should be noted that the obtained conversion was significantly low and, therefore, loading with metal catalyst was needed. Thus, TiO_2 (JRC-TIO-1) in the anatase phase was selected as a support for all of the following experiments.

Effects of Fe(III) Precursor and Fe(III) Loading

Fe(III)/TiO_2 catalysts were prepared from three precursors: Fe(III) acetylacetonate, Fe(III) chloride hexahydrate, and Fe(III) nitrate monohydrate, abbreviated as Fe (III) acac, Fe(III) Cl, and Fe(III) N, respectively. Because the TiO_2 surface is hydrophilic, the precursors in hydrate form or having water as a solvent should allow the uniform distribution of Fe metal in the catalysts. The XRD patterns of samples with various percentages of Fe(III) loadings (in the case of Fe(III) acac as precursor) are shown in Figure 2. The obvious peaks of Fe(III) in Fe_2O_3 crystallize were observed only at a Fe(III) loading of 20 %. The relationship between the Fe(III) loading at surface determined by XPS and the Fe(III) loading is shown in Figure 3. The results indicate that the metal was located more at the surface of TiO_2 than in the pores. In addition, it is clear that the type of precursor influenced the metal distribution in the catalysts. The accessibility of Fe(III) into the catalyst pores followed the order Fe(III) Cl > Fe(III) acac $\approx$ Fe(III) N.

The effects of the Fe(III) loading on the benzene conversion, phenol selectivitiy, and yield for different catalysts are summarized in Table 3. The values of the turnover frequency, turnover number, BET surface area, and pore volume are also provided. The byproducts from the reaction system were hydroquinone, benzoquinone, and catechol. The experimental results indicated that the conversion increased with increasing Fe(III) loading, while the selectivity decreased, thus an optimum yield was ob-

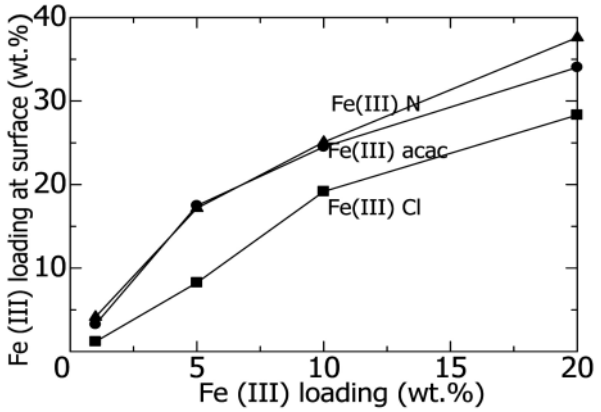

Figure 3. Relationship between %Fe on surface and %Fe(III) loading for different Fe precursors.

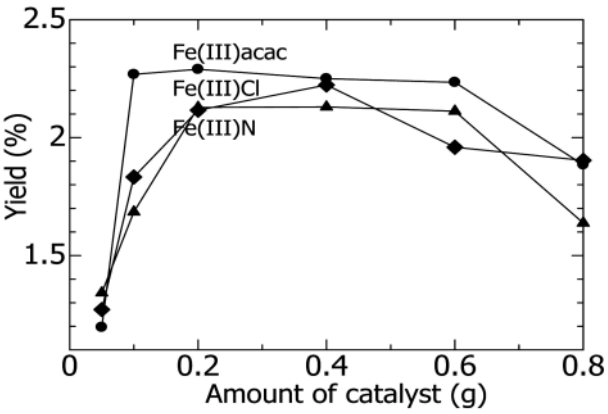

Figure 5. Effect of catalyst weight on phenol yield for different Fe(III) precursors.

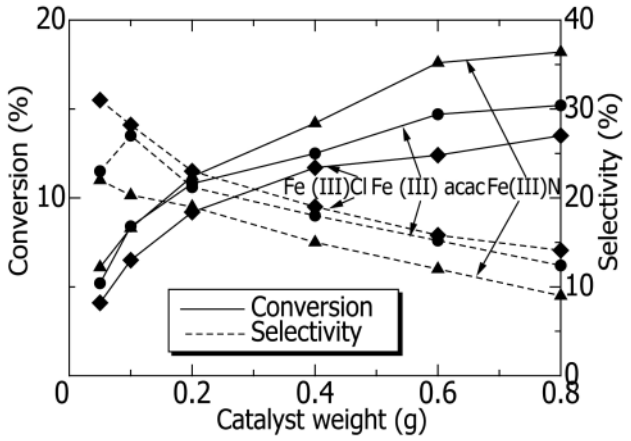

Figure 4. Effect of catalyst weight on benzene conversion and phenol selectivity for different Fe(III) precursors.

served. The increases in conversion were obtained as a result of the increased amount of metal active species. However, when considering the values of TOF and TON, it is noticed that the metal active sites were utilized less efficiently at high Fe(III) loadings. This situation is likely to be due to the reduced BET surface area and pore volume. The increase in yield was less pronounced when the Fe(III) loading was higher than 5 wt%. Therefore, this value was selected as an optimum Fe(III) loading for all precursors.

Figure 4 shows the catalytic performances of Fe(III)/TiO_2 catalysts prepared from the three precursors at different catalyst weights. The Fe(III) loading of the catalysts was 5 wt%. The benzene conversion increased, but the phenol selectivity decreased, upon increasing the amount of catalyst. This situation because phenol can be further reacted to give catechol, benzoquinone, and hydroquinone, which are undesirable by products. The catalytic activity followed the order Fe(III) N > Fe(III) acac > Fe(III) Cl; however, the selectivity followed the opposite order. From the corresponding yields (Figure 5), the most suitable precursor and catalyst weight were Fe(III) acac and 0.2 g, respectively.

It should be noted that the type of Fe(III) precursor influenced the metal distribution of the catalyst and its catalytic performance. It is likely that the reaction took place mainly at the catalyst surface because the rank of the catalytic activity observed from the benzene conversion in Table 3 followed the same trend as that shown in Figure 3 for all values of catalyst loading. In addition, the type of catalyst precursor may not significantly govern the selectivity. As shown in Figure 4, for example, when the conversion was ca. 12.5 %, the corresponding values of selectivity of Fe(III) N, Fe(III) acac, and Fe(III) Cl were ca. 15.5, 17, and 15 %, respectively, i.e., the were essentially equivalent. However, further studies are required to consider this situation in more detail.

Effect of Type of Solvent and Biphasic/Triphasic Operation

Solvent was used to reduce the mass transfer resistance by helping dissolve H_2O_2 into the benzene phase. Under the standard conditions with a solvent volume of 40 cm^3, the reaction was performed in a triphasic system comprising the solid catalyst, organic phase, and aqueous phase. The oxidation performances of the system with different solvents are summarized in Table 4. High yields were obtained for acetone, dichloromethane, and acetonitrile, respectively. Acetone offered the highest benzene conversion and phenol yield, but low selectivity. Acetonitrile might be a good alternative solvent because it provided very high selectivity with a yield as high as that obtained when using dichloromethane as solvent. From these observations, acetone and acetonitrile were further considered to compare the catalytic performance in biphasic and triphasic operations.

Figure 6 shows the catalytic performance of the reaction system using different amounts of solvent; i.e., 40, 60, and 80 cm^3. In the case of acetone, the system changed

Table 4. Effect of Solvent Type on the Catalytic Performance of Fe(III)/TiO_2 Catalysts

Solvent	Conversion[a] (%)	Selectivity[b] (%)	Yield[c] (%)	TOF[d] (1/h)	TON[e] (-)
Acetone	10.8	21.2	2.3	5.32	21.3
Dichloromethane	2.2	62	1.4	3.18	12.7
Acetonitrile	1.3	97	1.3	2.93	11.7
Pyridine	0.8	92	0.7	1.73	6.9
tert-Butyl alcohol	1.5	47	0.7	1.65	6.6
1-Butyl alcohol	1.5	10	0.2	0.35	1.4
Ethyl alcohol	1.3	8	0.1	0.25	1

(Benzene = 11 cm^3; % Fe(III) loading = 5 wt%; catalyst weight = 0.2 g; benzene/H_2O_2 mole ratio = 0.5; solvent = 40 cm^3; ascorbic acid = 0.5 g; temperature = 303 K; pressure = 1 atm; reaction time = 4 h)

[a] Conversion calculated as moles of benzene reacted per initial moles of benzene*100 %

[b] Selectivity calculated as moles of phenol per mole of benzene reacted*100 %

[c] Yield calculated as moles of phenol per initial mole of benzene*100 %

[d] Turnover frequency calculated as moles of phenol per mole of Fe per h

[e] Turnover number calculated as moles of phenol per mole of Fe

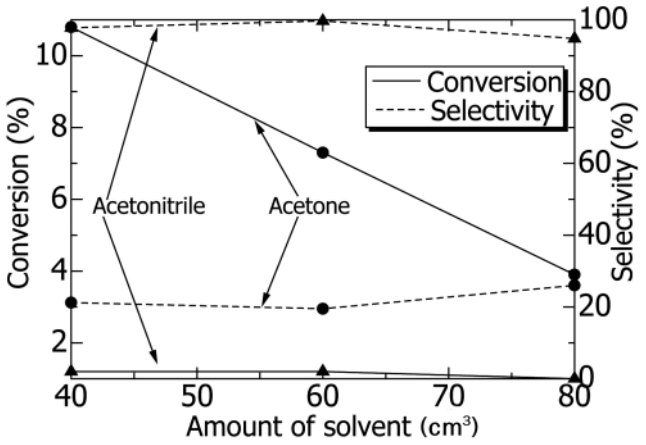

Figure 6. Effect of amount of solvent on benzene conversion and phenol selectivity.

from triphasic to biphasic at 60 cm^3. The benzene conversion dramatically decreased, while the selectivity increased slightly, when the system changed to biphasic and when more solvent was added in the biphasic system. In the case of acetonitrile, the system remained triphasic at 60 cm^3 and became biphasic at 80 cm^3. An almost insignificant effect of the amount of acetonitrile on the conversion and selectivity was observed, at least within the range of this study. Although it was expected that operation in biphasic systems would eliminate the presence of interfacial mass transfer resistance and, consequently, improve the catalytic performance of the reaction system, the dilution effect, as well as the poor mixing induced by the addition of extra solvent, retarded any such improvement. For both solvent cases, biphasic operation did not have a beneficial effect on the catalytic performance. This situation was particularly obvious in the case of acetone as solvent, which offered much lower performance. It should be noted that for the case of acetonitrile, which is not an inert solvent but participates directly in the reaction [10], no significant drop in the catalytic performance was observed upon increasing the amount of solvent. This study suggest that selection of a suitable amount of solvent is important, but operation in a biphasic system is not always advantageous.

Effect of the Amount of Ascorbic Acid

The amount of ascorbic acid was varied between 0.5 and 5 g using two types of solvent; i.e., acetone and acetonitrile.

The mechanism of Fenton's method is widely accepted as follows:

$$Fe(II) + H_2O_2 \rightarrow Fe(III) + OH^{o} + OH^{-} \quad (1)$$

The hydroxyl radical reacts directly with benzene to produce cyclohexadienyl (CHD) radical, which subsequently undergoes an H^+ abstraction as follows [22,23]:

$$OH^{o} + \text{benzene} \rightarrow CHD \quad (2)$$

$$CHD + Fe(III) \rightarrow \text{phenol} + Fe(II) + H^{+} \quad (3)$$

However, the CHD radical intermediate can react with H^+ and collapse to benzene as follows:

$$CHD + Fe(II) + H^{+} \rightarrow \text{benzene} + Fe(III) + \text{water} \quad (4)$$

Ascorbic acid is well known as a good reducing agent. It changes the state of the metal catalyst from Fe(III) to Fe(II).

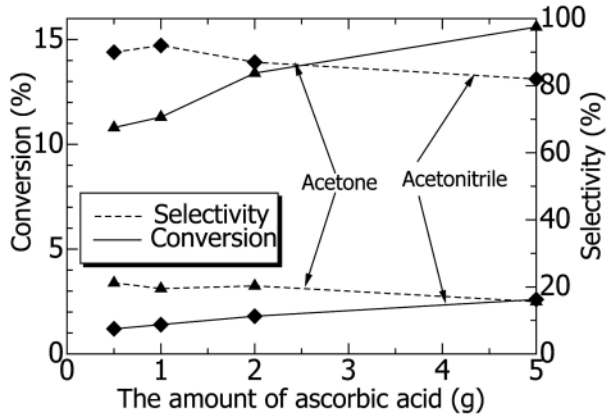

Figure 7. Effect of amount of ascorbic acid on benzene conversion and phenol selectivity.

2 Fe(III) + ascorbic acid + 0.5 O_2 → 2 Fe(II) + Dehydroascorbic acid + H_2O

2 Fe(II) + O_2+ 2H^+ → 2Fe(III) + H_2O_2

Fe(III) + H_2O_2 + H^+ → Fe(II) + OH^o + H_2O

Both Fe(III) and Fe(II) play important roles in the reaction system. Fe(III) helps to catalyze the conversion of the CHD radical intermediate to phenol, while Fe(II) promotes the decomposition of hydrogen peroxide to hydroxyl free radicals. The amount of generated hydroxyl radicals which affects phenol formation, could be controlled by the amounts of ascorbic acid and metal catalyst added.

As shown in Figure 7 the benzene conversion increased with increasing the amount of ascorbic acid, while the selectivity decreased slightly, in both the acetone and acetonitrile systems.

This situation can be explained by considering that increasing the amount of ascorbic acid activated the state change from Fe(III) to Fe(II), which enhanced the decomposition of H_2O_2 to hydroxyl radicals (as shown in Eq. 1) and, consequently, increased the benzene conversion (Eq. 2). However, too much ascorbic acid, which functioned as a reducing agent, suppressed the formation of Fe(III), which resulted in a decrease in the formation of phenol via the H^+ abstraction of CHD (Eq. 3). In addition, CHD can easily collapse to benzene when the Fe(II) content increased (Eq. 4) and also phenol can be further reacted with excess hydroxyl radicals to yield catechol, hydroquinone, and benzoquinone, resulting in the decrease of selectivity.

It is should be noted that ascorbic acid was highly soluble in the aqueous phase, but not in the organic phase. The addition of solvent was necessary to promote the reaction in this system by dissolving H_2O_2, ascorbic acid, and benzene into one phase.

Conclusion

The liquid phase hydroxylation of benzene to phenol with hydrogen peroxide catalyzed by Fe(III)/TiO_2 catalysts was investigated. The most suitable Fe(III) precursor and %Fe(III) loading were iron(III) acetylacetonate and 5 wt%, respectively. Among the solvents studied (acetone, dichloromethane, acetronitrile, pyridine, *tert*-butyl alcohol, 1-butyl alcohol, and ethyl alcohol), acetone showed the highest conversion and yield, but low selectivity. However, acetronitrile may be an attractive solvent because of its high selectivity. Biphasic operation was not attractive compared to triphasic operation because of the dilution effect. Benzene conversion increased with increasing the amount of ascorbic acid; however, too much ascorbic acid retarded the yield improvement because of lower phenol selectivity.

Acknowledgment

Financial support from the Thailand Research Fund and Commission on Higher Education are gratefully acknowledged.

References

1. R. J. Schmidt, *Appl. Catal. A*, **280**, 89 (2005).
2. G. I. Panov, A. K. Uriarte, M. A. Rodkin, and V. I. Sobolev, *Catal. Today*, **41**, 365 (1998).
3. Y. J. Seo, T. Tagawa, and S. Goto, *React Kinet. Catal. Lett.*, **54**, 265 (1995).
4. H. Kanzaki, T. Kitamura, R. Hamada, S. Nishiyama, and S. Tsuruya, *J. Mol. Catal. A*., **208**, 203 (2004).
5. Y. W. Chen and Y. H. Lu, *Ind. Eng. Chem. Res*., **38**, 1893 (1999).
6. J. Okamura, S. Nishiyama, S. Tsuruya, and M. Masai, *J. Mol. Catal. A*, **135**, 133 (1998).
7. Y. J. Seo, T. Tagawa, and S. Goto, *J. Mol. Catal. A*, **78**, 201 (1993).
8. T. Miyake, M. Hamada, H. Niwa, M. Nishizuka, and M. Oguri, *J. Mol. Catal. A*, **178**, 199 (2002).
9. J. Zhang, Y. Tang, G. Li, and C. Hu, *Appl. Catal. A*, **278**, 251 (2005).
10. M. Stockmann, F. Konietzni, and J. U. Notheis, *Appl. Catal. A*, **208**, 343 (2001)
11. F. S. Xiao, J. Sun, X. Meng, and R. Yu, *Appl. Catal. A*, **20**, 267 (2001).
12. Y. Liu, K. Murata, and M. Inaba, *Catal. Commun*., **6**, 679 (2005).
13. A. Dubey and S. Kannan, *Catal. Commun.*, **6**, 394 (2005).
14. J. S. Choi, T. H. Kim, K. Y., J. S. Sung, M. B.

Saidutta, S. O. Ryu, S. D. Song, B. Ramachandra, and Y. W. Rhee, *Appl. Catal. A*, **290**, 1 (2005).
15. K. D. Kim, L. B. Kim, J. B. Lee, and H. T. Kim, *J. Ind. Eng. Chem.*, **7**, 153 (2001).
16. M. S. Lee, G. D. Lee, S. S. Park, and S. S. Hong, *J. Ind. Eng. Chem.*, **9**, 89 (2003).
17. S. S. Hong, M. S. Lee, J. H. Kim, B. H. Ahn, K. T. Lim, and G. D. Lee, *J. Ind. Eng. Chem.*, **8**, 150 (2002).
18. H. H. Chung, M. J. Lee, J. Jung, and S. W. Choi, *J. Ind. Eng. Chem.*, **8**, 483 (2002).
19. H. H. Chungm and J. S. Rho, *J. Ind. Eng. Chem.*, **5**, 261 (1999).
20. H. Park and W. Choi, *Catal. Today*, **101**, 291 (2005).
21. S. S. Hong, C. S. Ju, C. G. Lim, B. H. Ahn, K. T. Lim, and G. D. Lee, *J. Ind. Eng. Chem.*, **7**, 99 (2001).
22. F. Gao and R. Hua, *Appl. Catal. A*, **270**, 223 (2004).
23. D. H. Bremmer, A. E. Burgess, and F. B. Li, *Appl. Catal. A*, **203**, 111 (2000).

Appendix 13

J. Ind. Eng. Chem., **Vol. 13**, No. 5, (2007) 870-877

Multi Transition Metal Catalysts Supported on TiO_2 for Hydroxylation of Benzene to Phenol with Hydrogen Peroxide

Garun Tanarungsun, Worapon Kiatkittipong*, Suttichai Assabumrungrat†, Hiroshi Yamada, Tomohiko Tagawa**, and Piyasan Praserthdam**

Center of Excellence in Catalysis and Catalytic Reaction Engineering, Department of Chemical Engineering, Faculty of Engineering, Chulalongkorn University, Bangkok 10330, THAILAND
**Department of Chemical Engineering, Faculty of Engineering and Industrial Technology, Silpakorn University, Nakhon Pathom 73000, THAILAND*
***Department of Chemical Engineering, Nagoya University, Chikusa, Nagoya, 464-8603, JAPAN*

Received April 24, 2007; Accepted June 13, 2007

Abstract: Liquid phase hydroxylation of benzene to phenol with hydrogen peroxide catalyzed by multi transition metals (Fe (III), V (V), and Cu (II)) supported on TiO_2 at room temperature was investigated. Particular focus was on the effects of second and third metal loading on the reaction performance. Bi- and tri-metal oxide catalysts showed obviously higher benzene conversion and phenol yield than single metal Fe supported on TiO_2. Among various solvents studied, i.e., acetone, acetonitrile, pyridine and water, acetonitrile was the most suitable solvent in terms of selectivity and yield. Operation with UV light in $FeVCu/TiO_2$ tri-metal catalyst could improve phenol yield without reduction of selectivity. The reactions could be explained as the Fenton-type mechanism for Fe (III), Cu (II), and V (V) metal catalysts. The effect of types of support on reaction performance was also investigated and their performances were ordered as follows: $TiO_2 > SiO_2 > \alpha$ - Al_2O_3.

Keywords: *oxidation of benzene, bi- and tri-metal, phenol production, hydrogen peroxide, Fe (III), V (V), Cu (II), TiO_2*

Introduction

Nowadays approximately 95 % of phenol production was produced by cumene process and the other 5 % by toluene oxidation process [1]. However, the cumene process is quite complicated as it consists of three main reaction steps, firstly, alkylation of benzene with propylene to cumene, secondly, oxidation of cumene to cumene hydroperoxide and finally, decomposition to phenol and propanone (acetone) co-product, which would be an oversupplied product in the future. The direct oxidation of benzene to phenol, a shortcut to one step reaction, is one of the attractive processes under investigation nowadays.

Many transition metal catalysts have been employed for catalyzing many oxidation reactions. However, most recent works revealed that Cu, Fe, and V containing catalysts are among the most desirable metal active species for the hydroxylation of benzene to phenol [2,3]. Stockmann and coworkers [4] used microporous mixed oxide catalysts with the transition metals (Cu, V, and Fe) whose catalytic activity was reported to follow the order of Fe > V > Cu. Acetonitrile solvent gave the best results with respect to phenol yield. Choi and coworkers [2] studied the transition metals (V (V), Fe (III), Cu (II)) supported on activated carbon. The activity of transition metals for the production of phenol was ordered as follow: V > Fe > Cu. It was found that iron and vanadium containing catalysts (with 5.0 wt% loading) gave phenol yield of over 15 %. Liu and coworkers [3] studied the transition metal substituted polyoxometalate compound for oxidation of benzene by O_2 with ascorbic acid as a reducing agent in an acetone/sulfolane/water mixed solvent. The catalytic performance of the metal species was ordered as follow: Cu > V > Fe. These transition metals

† To whom all correspondence should be addressed.
(e-mail: Suttichai.A@chula.ac.th)

Table 1. Details of Materials and Chemicals

Metal source	Iron (III) acetylacetonate 97 % (Aldrich)
	Cupric (II) nitrate 99 % (SIGMA)
	Ammonium metavanadate (V) 99.5 % (Carlo Erba reagenti)
Support	TiO_2 (JRC-TIO1) (Catalysis Society of Japan)
Solvent	Acetone 99.8 % (Carlo Erba)
	Acetonitrile 99.8 % (MERCK)
	Pyridine 99.7 % (MERCK)
Reducing agent	Ascorbic acid 99.7 % (Polskic Odczynniki Chemiczne S.A.)
Substrate	Benzene 99.7 % (MERCK)
Oxidant	Hydrogen peroxide 30 % wt. (MERCK)
Byproduct reference	Biphenyl 99.9 % (Fluka)
	Catechol 98 % (Fluka)
	Phenol 99 % (Panreac Sintesis)
	Quinol 99.8 % (APS)
	1,4 Benzoquinone 98 % (ACROS)

were recently investigated by loading on clay support. The reactivity of metal species for phenol production was ordered as follow: V > Fe > Cu [5]. The differences in the order of metal activity were mainly arisen from the different supports. One of the interesting supports was TiO_2. When TiO_2 was photo-irradiated, its surfaces could generate OH・radicals [6] which were important for phenol production from benzene. However, the hydroxylation of benzene to phenol with TiO_2 photocatalyst gave much lower conversion than that of the Fenton process. Therefore, TiO_2 could be used as a support accompanying with metal surface modification. In our previous works [7,8], the catalytic behavior of Fe (III), Cu (II), and V (V) catalysts impregnated on TiO_2 commercial support for the hydroxylation of benzene to phenol at room temperature was investigated. The activity of metal catalysts was ordered as follow: Fe (III) > Cu (II) > V (V); however, the phenol selectivity was in the reverse order [7]. The effect of second or third metal loading is yet to be examined in this study.

It should be noted that there are quite limited works focusing on the use of multi transition metals for direct hydroxylation of benzene to phenol. Dubey and coworkers [9] studied the multi transition metals over Cu-containing hydrotalcites with general formula of CuM(II)M(III)-HT. The ternary catalyst system offered higher activity than the binary systems; however, it was significantly influenced by the nature of bivalent metal ions as well as trivalent metal ions of HT-like lattice. Among the catalysts screened, CuCoAlHT and CuNiAlHT with (Cu + Co(or Ni))/Al = 3.0 and Cu/Co(or Ni) = 3.0 showed maximum activity with improved phenol selectivity. However, in their study low conversion of benzene was still obtained and it showed that the catalyst can catalyze phenol to catechol and hydroquinone [10]. Many researchers used titanium dioxide for photooxidation reaction and oxidation reaction [11-14].

In this study, the catalytic behaviors of Fe (III) impregnated on the TiO_2 support doped with Cu (II) and/or V (V) in bi- and tri-metal oxide catalyst systems on the hydroxylation of benzene to phenol were investigated. The influences of solvent species and UV light were studied. In addition, the effect of support type, i.e. TiO_2, -Al_2O_3 and SiO_2, was examined.

Experimental

Materials and Chemicals

Table 1 summarizes the details of materials and chemicals employed in this work. All chemicals were used without prior purification. Three supports; i.e., TiO_2 (JRC-TIO-1), α-Al_2O_3 (Aldrich), and SiO_2 (Aldrich), and three types of metal precursors; i.e., iron (III) acetylacetonate, Cupric (II) nitrate 99 % (SIGMA) and Ammonium metavanadate (V) 99.5 % (Carlo Erba reagenti) were used in the study.

Catalyst Preparation

Catalysts were prepared by impregnating a solution of metal precursor (Fe, Cu or V metal) on TiO_2, SiO_2, α-Al_2O_3 support powder at 353 K followed by evaporation and drying for overnight. The obtained catalysts were calcined in a furnace which was continuously fed with air flow (60 cm^3/min). The temperature was increased from room temperature to 773 K at a heating rate of 10 K/min and held for 5 h to remove the organic residues. After calcinations, the catalysts were stored in a dessicator. Percent loading of Fe (III) on TiO_2 was 5 wt% and loading of V (V) and Cu (II) was 2.5 wt% in the FeV/TiO_2 and FeCu/TiO_2. FeVCu/TiO_2 was 5 wt% loading of Fe (III) and 2.5 wt% loading of V (V) and Cu (II) each.

Characterization

XRD patterns of the metal supported catalysts were obtained by using X-ray diffractrometer, D 5000 (SIEMENS AG) using Cu Kα radiation equipped with Ni filter with a range of detection of (2θ) 20～80 and a resolution of 0.04.

BET surface area and porosity of the catalysts were measured by Micromeritics ASAP 2020. A sample of 0.3 g was degassed at 573 K for 3 h and the amount of N_2 adsorption was recorded.

XPS surface analysis was performed using a Kratos Amicus X-ray photoelectron spectroscopy. The XPS spectra were measured using the following conditions: Mg Ka X-ray source at current of 20 mA and 12 keV, resolution of 0.1 eV/step, and pass energy of 75 eV. The operating pressure was approximately 1×10^{-6} Pa. A

Table 2. Summary of BET Surface Area and Pore Volume of Supports and Catalysts

Catalyst	BET surface area (m^2/g)	Pore volume (cm^3/g)
TiO_2	76.6	0.29
α-Al_2O_3	2.1	0.001
SiO_2	257.3	1.50
Fe/TiO_2	68.5	0.25
FeV/TiO_2	57.5	0.19
FeCu/TiO_2	58.7	0.23
FeVCu/TiO_2	54.2	0.22
FeV/ α-Al_2O_3	2.0	0.0009
FeCu/ α-Al_2O_3	2.0	0.001
FeVCu/ α-Al_2O_3	2.1	0.001
FeV/SiO_2	239.4	1.24
FeCu/SiO_2	240.2	1.30
FeVCu/SiO_2	230.2	1.22

wide-scan survey spectrum was collected for each sample in order to determine the elements present on the surface. All the binding energies were calibrated internally with the carbon C 1s photoemission peak at 285.0 eV. Photoemission peak areas were determined after smoothing and background subtraction using a linear routine. Deconvolution of complex spectra were done by fitting with Gaussian (70 %) - Lorentzian (30 %) shapes using VISION 2 software equipped with the XPS system.

Experimental Setup and Product Analysis

The hydroxylation of benzene by H_2O_2 was carried out in a 125 cm^3 round flat bottomed flask at 303 K and 1 atm with a high speed stirrer at 600 rpm. In a typical experiment, 0.5 g of ascorbic acid (2.8 mmol) was added in a liquid mixture containing 40 cm^3 of solvent, 30 cm^3 of H_2O_2 (0.32 mol) and 11 cm^3 of benzene (0.16 mol). It should be noted that with this amount of solvent, the experiments were operated in a triphasic system consisting of solid catalyst, solvent phase and aqueous phase. For the photooxidation system, the ultraviolet light source of a black light blue fluorescent bulb (8 Watts) was included to the system which was kept in the black box.

The products were analyzed by a gas chromatogragh (SHIMADZU 9A) with a packed column of GP 10 % SP-2100. The operating conditions of GC were as follows: injection temperature of 523 K, detector temperature of 523 K, initial column temperature of 383 K, final column temperature of 443 K and temperature programmed rate of 10 K/min. The products were also analyzed by GC-MS especially for some product species which cannot be detected by the FID detector.

The terms of reaction performance were defined as follows.

Table 3. Results of % Metal Loading on TiO_2 Support Measured by XPS.

Catalyst	% metal loading*	Ratio of Fe/V or Fe/Cu
V/TiO_2 5 wt%	15.61	-
Cu/TiO_2 5 wt%	16.04	-
Fe/TiO_2 5 wt%	17.48	-
Fe, V/TiO_2 5 and 2.5 wt%	13.59, 5.73	2.37
Fe, Cu/TiO_2 5 and 2.5 wt%	13.39, 4.88	2.74
Fe, V, Cu/TiO_2 5, 2.5, and 2.5 wt%	12.20, 5.91, 5.47	2.06, 2.23

*% loading of metal calculated weight of metal / (TiO_2 added metal) × 100

$$\text{Conversion of benzene} = \frac{\text{mole of benzene reacted}}{\text{initial mole of benzene}}$$

$$\text{Yield of phenol} = \frac{\text{mole of phenol produced}}{\text{initial mole of benzene}}$$

$$\text{Selectivity of phenol} = \frac{\text{mole of phenol produced}}{\text{mole of benzene reacted}}$$

$$\text{Turn over number (TON)} = \frac{\text{mole of phenol produced}}{\text{mole of metal catalyst}}$$

$$\text{Turn over frequency (TOF)} = \frac{\text{mole of phenol produced}}{\text{mole of metal catalyst} \times \text{reaction time}}$$

Results and Discussion

Catalyst Characterization

XRD patterns of different catalysts supported on TiO_2 and the blank TiO_2 support were determined (not shown). However, no obvious peaks of Fe, Cu, and V metals were observed when compared with the pattern of the blank anatase TiO_2. This is probably due to low metal loading on the support. The values of BET surface area and pore volume of various supports and metal supported catalysts were summarized in Table 2. As metals were loaded on the supports, the surface area and pore volume decreased compared to those of the blank supports. The surface area and pore volume were ordered as follow: $SiO_2 > TiO_2 > \alpha$-Al_2O_3. The amount of metal loading on TiO_2 surface was studied by XPS and the results are shown in Table 3. The amount of metal loading (Fe (III), Cu (II), and V (V)) on the TiO_2 surface were higher than percent metal loading on the support, suggesting that the metal species were deposited more on the surface of the support. For the single metal catalysts, Fe showed the

Table 4. Catalytic Performances for Hydroxylation of Benzene to Phenol of Single Metal Fe (III), Cu (II), V (V)/TiO_2 Catalysts and bi-metal FeCu/TiO_2 and FeV/TiO_2 in Various Solvent-added Systems

Catalyst	Solvent	Conversion (%)[a]	Selectivity (%)	Yield (%)[b]	TOF (h^{-1})[c]	TON (-)[d]
5 wt%Fe/TiO_2	acetone	4.5	32	1.44	3.35	13.39
5 wt%Fe/TiO_2	acetonitrile	1.2	90	1.08	2.51	10.04
10 wt%Fe/TiO_2	acetone	13.2	20	2.65	3.08	12.32
5 wt%Cu/TiO_2	acetone	3.1	32	0.99	2.62	10.48
5 wt%Cu/TiO_2	acetonitrile	1	88	0.88	2.33	9.31
5 wt%V/TiO_2	acetone	2.1	39	0.82	1.74	6.97
5 wt%V/TiO_2	acetonitrile	0.9	84	0.76	1.62	6.46
FeCu/TiO_2*	acetone	10.5	62	6.51	10.53	42.10
FeCu/TiO_2*	acetonitrile	8.5	75	6.34	10.25	41.00
FeCu/TiO_2*	pyridine	3.6	83	2.99	4.84	19.34
FeCu/TiO_2*	Water	0.5	90	0.45	0.73	2.91
FeV/TiO_2**	acetone	8.8	70	6.16	9.26	37.04
FeV/TiO_2**	acetonitrile	7.8	85	6.63	9.97	39.86
FeV/TiO_2**	pyridine	2.4	95	2.28	3.43	13.71
FeV/TiO_2**	Water	0.3	100	0.30	0.45	1.80

Benzene: 11 cm^3 catalyst 0.2 g; benzene/H_2O_2 mole ratio: 0.5; acetone solvent 40 cm^3; ascorbic cid 0.5 g; temperature 303 K; pressure 1 atm; Reaction time 4 h;

[a]Conversion calculated as moles of benzene reacted per initial moles of benzene × 100

[b]Yield calculated as moles of phenol per initial moles of benzene × 100

[c]Turn over frequency calculated as moles of product per mole of metal per h

[d]Turn over number calculated as moles of phenol per mole of metal

* loading 5 wt%Fe and 2.5 wt%Cu

** loading 5 wt%Fe and 2.5 wt%V

highest metal dispersion on the surface. This result was corresponding well with the binary and ternary metal oxide catalysts whose Fe/Cu and Fe/V ratios were higher than 2.

Effects of Second Metal (Cu or V) and Solvent Type on the Reaction Performance

From our previous work [7], among three single metal catalysts, i.e., Fe (III), Cu (II), and V (V) supported on TiO_2, Fe showed the best performance for phenol production in terms of conversion and yield. Therefore, in this study, the effects of second metal (and third metal as will be mentioned later) on Fe-containing TiO_2 catalyst was investigated.

Some data of phenol production performances of single metal catalysts supported on TiO_2 from our previous work [7] were compared with those of bi-metal oxide catalysts from this study as shown in Table 4.

Considering the case with acetone as a solvent, the addition of a second metal, i.e., Cu, and V at 2.5 wt% on 5 wt% Fe/TiO_2 catalyst resulted in higher benzene conversion and phenol yield compared to those of Fe/TiO_2 with Fe loading of 5 wt%. Their obtained yields were also higher than those of Fe/TiO_2 with Fe loading of 10 wt%, indicating the improvement of catalytic performance by the presence of the second metal. As the kind and amount of active metals are different, discussions based on turnover frequency (TOF) should provide a better insight. At 5 wt% loading, the TOFs for Fe, Cu, and V are 3.35, 2.62, and 1.74 h^{-1}, respectively for the case of acetone solvent. It is clear that Fe is superior to Cu and V. At a higher metal loading, 10 wt% Fe/TiO_2 showed slightly lower TOF than did the 5 wt% Fe/TiO_2. It is likely due to the poorer metal dispersion at higher metal loading. With the binary metal system, the values of TOF significantly increased to 10.5 and 9.3 h^{-1} for Fe-Cu and Fe-V, respectively, compared to those of the single metal catalysts. Similar trend was observed on TON; i.e. the value increased from 13.39 (5 wt% Fe/TiO_2) to 42.1 (FeCu/TiO_2) and 37.04 (FeV/TiO_2). These higher values suggest the synergistic effect from the addition of the second components on the catalyst. The synergistic effect has been reported in some other systems. For example, Chou and coworkers [28] reported that small amount of Al loading to Cu-MCM-41 improved the conversion and selectivity of 2,3,6-trimethylphenol hydroxylation to 2,3,5-trimethylbenzoquinone; however, the selectivity decreased with high Al loading, leading to lower obtained yield.

Considering the bi-metal oxide catalyst system with different solvents, i.e., acetone, acetonitrile, pyridine and water, acetone and acetonitrile showed the substantial re-

Table 5. Catalytic Performances for Hydroxylation of Benzene to Phenol of Tri-metal FeVCu/TiO_2 Catalysts in Various Solvent-added Systems with and Without UV

Condition	Catalyst*	Solvent	Conversion (%)[a]	Selectivity (%)	Yield (%)[b]	TOF (h^{-1})[c]	TON (-)[d]
Without UV	FeVCu/TiO_2	acetone	16.5	45	7.2	8.43	33.72
	FeVCu/TiO_2	acetonitrile	10.2	70	7.14	8.36	33.44
	FeVCu/TiO_2	dichloromethane	5.2	90	4.68	5.48	21.92
	FeVCu/TiO_2	pyridine	3.9	95	3.71	4.34	17.37
	FeVCu/TiO_2	-	2.5	60	1.5	1.76	7.02
	FeVCu/TiO_2	water	0.9	100	0.9	1.05	4.21
	FeVCu/TiO_2	Ethanol	7.5	4	0.3	0.35	1.40
With UV	FeVCu/TiO_2	acetone	18.61	52	9.68	11.33	45.31
	FeVCu/TiO_2	acetonitrile	14.27	68	9.7	11.36	45.43
	FeVCu/TiO_2	pyridine	7.9	90	7.11	8.32	33.29

Benzene: 11 cm^3 catalyst 0.2 g; benzene/H_2O_2 mole ratio: 0.5; solvent 40 cm^3; ascorbic cid 0.5 g; Temperature 303 K; pressure 1 atm; Reaction time 4 h;

[a]Conversion (%) calculated as moles of benzene reacted per initial moles of benzene × 100

[b]Yield (%) calculated as moles of phenol per initial moles of benzene × 100

[c]Turn over frequency calculated as moles of phenol per mole of metal per h

[d]Turn over number calculated as moles of phenol per mole of metal

* loading 5 wt%Fe (III), 2.5 wt%V (V), and 2.5 wt%Cu (II)

action performance. In the case of acetone solvent, loading with the second metal significantly increased conversion and phenol selectivity, as discussed in the last paragraph. In the case of acetonitrile solvent, Fe/TiO_2 catalyst showed very high selectivity (~90%), and loading with the second metal increased conversion without a pronounced reduction of the selectivity. Even though pyridine and water solvents gave high selectivity, they were not attractive due to the poor benzene conversion and phenol yield. Their TOF and TON are much lower than those of the system with acetone and acetonitrile solvents.

FeVCu/TiO_2 Ternary-metal Catalyst for Hydroxylation of Benzene to Phenol with and Without UV in Various Solvents

The reaction performances of FeVCu/TiO_2 tri-metal catalyst with and without UV in various solvents were shown in Table 5. Comparing with Table 4 when using the same operating condition (without UV), FeCuV/TiO_2 tri-metal catalyst showed the improvement in terms of conversion and yield but it gave lower selectivity than the bi-metal catalysts, FeCu/TiO_2, and FeV/TiO_2, in both acetone and acetonitrile solvents. Although, the TOF value of the tri-metal catalyst was lower than those of the bi-metal catalysts, the value was still higher than those of the single-metal systems, indicating that the second and third components are still effective to promote the catalytic performance. It was further observed that acetone gave a yield as high as acetonitrile; however, the selectivity was lower. Therefore, acetonitrile was considered as the best solvent in this system.

Like the bi-metal catalysts, the selectivity achieved in the tri-metal catalyst system with pyridine and water solvents was still very high (almost 100 %). Compared to the case without solvent, pyridine gave higher benzene conversion but the value was still small. For the case of water as the solvent, the decrease of H_2O_2 concentration according to the increase of the aqueous phase volume may lead to a dilution effect. Therefore, phenol yield was lower than that of the case without solvent. It can be concluded that the performance of the solvent can be ordered as follow: acetonitrile > acetone > dichloromethane > pyridine > water > ethanol. It is probably because the polarity index of acetonitrile (5.8) was higher than that of acetone (5.1), and therefore, acetonitrile can dissolve more hydroxyl peroxide to react with benzene in the organic phase than does the acetone. The increased ratio of benzene per oxidant in the benzene phase results in a higher catalytic reaction in the system. The results showed a similar tendency with the study of Zhang and coworkers [29] which showed an order as: acetonitrile > acetone > alcohol for the system catalyzed by $NaVO_3$ catalyst.

The mechanism of Fenton's method is widely accepted as follows [16,31].

$$Fe(II) + H_2O_2 \rightarrow Fe(III) + OH^{o} + OH^{-} \quad (1)$$

The hydroxyl radical reacts directly with benzene to produce cyclohexadienyl (CHD) radical, which subsequently undergoes an H^+ abstraction as follows.

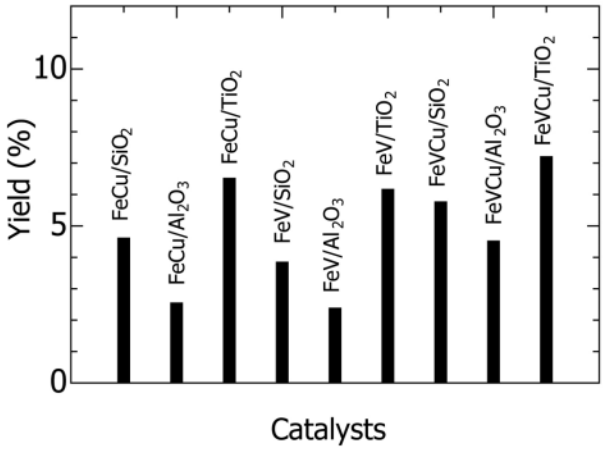

Figure 1. Comparison of phenol yield of different catalysts.

$$OH^{o} + \text{benzene} \rightarrow \text{CHD} \quad (2)$$

$$\text{CHD} + \text{Fe (III)} \rightarrow \text{phenol} + \text{Fe (II)} + H^{+} \quad (3)$$

However, the CHD radical intermediate can react with H^+ and collapse to benzene as follows.

$$\text{CHD} + \text{Fe (II)} + H^{+} \rightarrow \text{benzene} + \text{Fe (III)} + \text{water} \quad (4)$$

The ascorbic acid is well known as a good reducing agent. It changes the state of metal catalyst from Fe (III) to Fe (II).

$$2\ \text{Fe (III)} + \text{ascorbic acid} + 0.5\ O_2 \rightarrow 2\ \text{Fe (II)} + \text{Dehydroascorbic acid} + H_2O$$

$$2\ \text{Fe (II)} + O_2 + 2H^{+} \rightarrow 2\text{Fe (III)} + H_2O_2$$

$$\text{Fe (III)} + H_2O_2 + H^{+} \rightarrow \text{Fe (II)} + OH^{o} + H_2O$$

In the cases of Cu and V, the formation of phenol proceeds through the similar mechanism as that of Fenton chemistry by replacing the redox of Fe (III)/Fe (II) to that of Cu (II)/Cu (I) as well as V (V)/V (IV) [7,16,20]. The synergistic effect of Cu and V might be arisen from: a) increasing redox rate of Fe to increase the rate reaction (1), b) increasing the oxidation of Fe (II) to prevent the reverse reaction (4) and c) stabilizing phenol to prevent the further oxidation of phenol. More detailed studies should be carried in order to elucidate this effect.

The effect of UV light was also provided in Table 5. The use of UV light obviously improved conversion for all solvent systems. In this study, only a simple comparison was done on the photocatalytic oxidation of benzene. Selectivity slightly increased in the case of acetone while slightly decreased in the cases of acetonitrile and pyridine. The UV light enhanced the decomposition of H_2O_2 by increasing the hydroxyl radicals which reacted with benzene [21]; however, if the amount of the hydroxyl radicals was excessive, it can convert phenol to hydroquinone and benzoquinone. The optimum of UV intensity may be further studied for each case of different solvent and catalyst.

Effect of Support on the Reaction Performance

Three types of metal doping, i.e., FeCu, FuV, and FeVCu were loaded on three supports, i.e., SiO_2, α-Al_2O_3 and TiO_2. The results of the obtained yields were compared as shown in Figure 1. The orders of the performance of the support are the same for all three types of metal doping, i.e., $TiO_2 > SiO_2 > \alpha$-Al_2O_3. The results of BET measurement summarized in Table 2 showed that the values of specific surface area of the supported catalysts followed the order of $SiO_2 > TiO_2 > \alpha$-Al_2O_3, indicating that the surface area is not the only major influencing factor on the catalytic performance and, therefore, the interaction between the metal-support should be an important issue. It was reported in some studies that in the case of supporting acidic Fe species, SiO_2 is preferred to give strong surface acidity. However, in this case with neutral Fe species, rather polar support (TiO_2) gave better results. Also TiO_2 support is essential for the photocatalytic reactions [32]. It was also reported that difference in metal species loading provided a different support behavior. With 5 wt% Cu loading, the catalytic activity of benzene oxidation with respect to support was ordered as follows: γ-$Al_2O_3 > TiO_2 > SiO_2$ [21] and that of 0.5 wt% V was $ZrO_2 > \alpha$-$Al_2O_3 > SiO_2$ [23].

Comparison with other Results from Literatures

Many researchers have studied the hydroxylation of benzene to phenol in different reaction conditions, i.e., solvent and oxidant species, active catalyst and support, reaction temperature, reaction time, etc. Therefore, it is difficult to compare their performance of each parameter directly. The ratios of benzene per catalyst and oxidant type are ones of the most important parameters. As shown in Table 6, although our system was operated with comparatively moderate benzene per catalyst, low residence time and low temperature (room temperature), the obtained yields are relatively high compared with others.

Conclusion

The liquid phase hydroxylation of benzene to phenol with hydrogen peroxide catalyzed by multi transition metal (Fe-) containing TiO_2 catalyst was investigated. Doping with 2.5 wt% Cu or V as a second metal loading to 5 wt% Fe component for bi-metal oxide catalyst obviously improved phenol yield and selectivity. FeVCu/TiO_2 tri-metal catalyst showed higher benzene conver-

Table 6. Comparison of Experimental Results from Different Literatures

Catalyst	Benzene/catalyst (mol/g)	Oxidant	Reaction Temperature (K)	Solvent	Reaction time (h)	Yield (%)	Reference
TBA-$PW_{11}Cu$	3.54×10^{-3}	O_2	323	acetone, water, sulfolane	12	8.4	[9]
Cu/Al_2O_3	4.20×10^{-3}	O_2	303	acetic acid	24	2.5	[21]
$CsPMoV_2$	6.96×10^{-3}	O_2	353	acetic acid	24	7.2	[27]
V/Al_2O_3	7.14×10^{-1}	O_2	303	acetic acid	24	8.2	[22]
Fe/Activated carbon	NA	H_2O_2	338	acetonitrile	5	7	[2]
Cu/Activated carbon	NA	H_2O_2	338	acetonitrile	5	3.6	[2]
V/Activated carbon	NA	H_2O_2	338	acetonitrile	5	13.2	[2]
5.0Fe/NACH-600N	NA	H_2O_2	338	acetonitrile	3	20	[25]
Cu/TiO_2	9.43×10^{-4}	H_2O_2	303	acetone	4	1.3	[7]
Fe/TiO_2	1.08×10^{-3}	H_2O_2	303	acetone	4	2.3	[7]
V/TiO_2	1.18×10^{-3}	H_2O2	303	acetone	4	1.3	[7]
$PMO_{11}V$	1.25×10^{-3}	H_2O_2	338	acetonitrile	2	11.5	[24]
$FeCu/TiO_2$	1.55×10^{-3}	H_2O_2	303	acetone	4	6.5	this work
FeV/TiO_2	1.66×10^{-3}	H_2O_2	303	acetonitrile	4	6.6	this work
$FeVCu/TiO_2$	2.13×10^{-3}	H_2O_2	303	acetone	4	7.2	this work
$FeVCu/TiO_2$+ Photo	2.13×10^{-3}	H_2O_2	303	acetonitrile	4	9.7	this work
V/Clay	1.75×10^{-2}	H_2O_2	313	acetonitrile	4	10.6	[5]
TS-1	1.75×10^{-2}	H_2O_2	313	acetonitrile	4	5.2	[5]
VO_x/SiO_2	3.06×10^{-2}	H_2O_2	343	acetic acid	20	8.3	[26]
V-MCM-41	4.00×10^{-1}	H_2O_2	333	acetonitrile	3	9	[23]

sion and phenol yield; however, it slightly decreased in selectivity and also TOF. Acetonitrile was the most suitable solvent since the highest phenol yield with high selectivity were obtained. Operation with UV light in $FeVCu/TiO_2$ tri-metal catalyst improved also phenol yield without selectivity change. The performances of the support were ordered as follows: $TiO_2 > SiO_2 > \alpha$-Al_2O_3.

Acknowledgments

Financial supports from the Thailand Research Fund and Commission on Higher Education are gratefully acknowledged.

References

1. R. J. Schmidt, *Appl. Catal. A*., **280**, 89 (2005).
2. J. S. Choi, T. H. Kim, K. Y. Choo, J. S. Sung, M. B. Saidutta, S. D. Song, and Y. W. Rhee, *J. Porous Mater*., **12**, 301 (2005).
3. Y. Liu, K. Murata, and M. Inaba, *Catal. Com.*, **6**, 679 (2005).
4. M. Stockmann, F. Konietzni, and J. U. Notheis, *Appl. Catal. A.*, **208**, 343 (2001)
5. X. Gao and J. Xu, Appl. *Clay Sci.*, **33**, 1 (2006).
6. H. Park and W. Choi, *Catal. Today*, **101**, 291 (2005).
7. G. Tanarungsun, W. Kiatkittipon, S. Assabumrungrat, H. Yamada, T. Tagawa, and P. Prasertdam, *J. Chem. Eng. Japan*, **40**, 415 (2007).
8. G. Tanarungsun, W. Kiatkittipon, S. Assabumrungrat, H. Yamada, T. Tagawa, and P. Prasertdam, *J. Ind. Eng. Chem*., **13**, 444 (2007).
9. A. Dubey and S. Kannan, *Catal. Com.*, **6**, 394 (2005).
10. A. Dubey, V. Rives, and S. Kannan , *J. Mol. Catal. A*, **181**, 151 (2002).
11. H. H. Chungm and J. S. Rho, *J. Ind. Eng. Chem*., **5**, 261 (1999).
12. H. H. Chungm and J. S. Rho, *J. Ind. Eng. Chem.*, **5**, 81 (1999).
13. S. S. Hong, C. S. Ju, C. G. Lim, B. H. Ahn, K. T. Lim, and G. D. Lee, *J. Ind. Eng. Chem*., **7**, 99 (2001).
14. S. B. Kim, H. T. Jang, and S. C. Hang, *J. Ind. Eng. Chem.*, **8**, 156 (2002).
15. Y. J. Seo, Y. Mukai, T. Tagawa, and S. Goto, *J. Mol. Catal. A*, **120**, 149 (1997).
16. T. Miyahara, H. Kanzaki, R. Hamada, S. Kuroiwa, S. Nishiyama, and S. Tsuruya, *J. Mol. Catal. A*., **176**, 141 (2001).
17. K. D. Asim, B. Chaudhuri, S. Bhattacharjee, and B. K. Dutta, *J. Hazard. Mater.*, **64**, 91 (1999).
18. S. C. Kim, *J. Hazard. Mater*., **91**, 285 (2002).
19. K. Murata, R. Yanyong, and M. Inaba, *Catal. Lett*.,

102, 143 (2005).
20. H. Kanzaki, T. Kitamura, R. Hamada, S. Nishiyama, and S. Tsuruya, *J. Mol. Catal. A*., **208**, 203 (2004).
21. Y. K. Masumoto, R. Hamada, K. Yokota, S. Nishiyama, and S. Tsuruya, *J. Mol. Catal. A.*, **184**, 215 (2002).
22. Y. W. Chen and Y. H. Lu, *Ind. Eng. Chem. Res.*, **38**, 1893 (1999).
23. N. A. Alekar, V. Indira, S. B. Halligudi, D. Srinvas, S. Gopinathan, and C. Gopinathan, *J. Mol. Catal. A.*, **164**, 181 (2000).
24. J. S. Choi, T. H. Kim, K. Y. Choo, J. S. Sung, M. B. Saidutta, S. O. Ryu, S. D. Song, B. Ramachndra, and Y. W. Rhee, *Appl. Catal. A.*, **290**, 1 (2005).
25. K. Lemke, H. Ehrich, U. Lohse, H. Berndt, and K. Jahnisch, *Appl. Catal. A.*, **243**, 41 (2003).
26. S. T. Yamaguchi, S. Sumimoto, Y. Ichihashi, S. Nishiyama, and S. Tsuruya, *Ind. Eng. Chem. Res.*, **44**, 1 (2005).
27. K. I. Shimizu, H. Akahane, T. Kodama, and Y. Kitayama, *Appl. Catal. A*, **269**, 75 (2004).
28. B. Chou, J. L. Tsai, and S. Cheng, *Micropor. Mesopor. Mater.*, **48**, 309 (2001)
29. J. Zhang, Y. Tang, G. Li., and C. Hu, *Appl. Catal. A*, **278**, 251 (2005).
30. T. Mizuno, H. Yamada, T. Tagawa, and S. Goto, *J. Chem. Eng. Japan*, **38**, 849 (2005).
31. Y. J. Seo, T. Tagawa, and S. Goto, *J. Mol. Cat.*, **78**, 201 (1993).
32. Y. J. Seo, T. Tagawa, and S. Goto, *React. Kinet. Catal. Letters*, **54**, 265 (1995)

Appendix 14

Catalysis Communications 9 (2008) 1886–1890

Contents lists available at ScienceDirect

Catalysis Communications

journal homepage: www.elsevier.com/locate/catcom

Hydroxylation of benzene to phenol on Fe/TiO_2 catalysts loaded with different types of second metal

Garun Tanarungsun [a], Worapon Kiatkittipong [b], Piyasan Praserthdam [a], Hiroshi Yamada [c], Tomohiko Tagawa [c], Suttichai Assabumrungrat [a,*]

[a] Center of Excellence in Catalysis and Catalytic Reaction Engineering, Department of Chemical Engineering, Faculty of Engineering, Chulalongkorn University, Bangkok 10330, Thailand
[b] Department of Chemical Engineering, Faculty of Engineering and Industrial Technology, Silpakorn University, Nakhon Pathom 73000, Thailand
[c] Department of Chemical Engineering, Nagoya University, Chikusa, Nagoya 464-8603, Japan

ARTICLE INFO

Article history:
Received 26 October 2007
Received in revised form 23 February 2008
Accepted 4 March 2008
Available online 18 March 2008

Keywords:
Hydroxylation
Phenol production
Hydrogen peroxide
Metal oxide
TiO_2

ABSTRACT

This paper investigated the liquid phase hydroxylation of benzene to phenol with hydrogen peroxide over Fe/TiO_2-based catalysts. Various types of second metal (i.e., Ni, Co, Pd and Pt) were loaded together with Fe on the TiO_2 support and the catalytic performance of the obtained catalysts was compared. It was found that the presence of the second metal can improve the phenol production of the typical Fe/TiO_2 catalyst. The yield of phenol follows the order: Pt > Pd >> Co ≈ Ni. Various techniques (NH_3-TPD, XRD, BET surface area, SEM-EDX and XRF) were employed to characterize the Fe/TiO_2, $FePt/TiO_2$ and $FePd/TiO_2$ catalysts. The acid property of the catalyst was found to be influenced by the addition of the second metal. Finally the effects of some operating variables (reaction time, H_2O_2/benzene ratio and amount of ascorbic acid) on the catalytic performance were investigated.

1. Introduction

Phenol is an important intermediate for the synthesis of petrochemicals, agrochemicals and plastics. Nowadays approximately 95% of phenol production was produced by cumene process consisting of three main reaction steps (alkylation of benzene with propylene to cumene, oxidation of cumene to cumene hydroperoxide and decomposition to phenol and acetone). The direct oxidation of benzene to phenol, a one-step reaction, is an attractive process under investigation nowadays due to the potential simplification of the production process. Various oxidants, such as nitrous oxide [1,2], hydrogen peroxide [3–8], oxygen [9,10], or mixture of oxygen and hydrogen [11,12] have been employed for the direct oxidation of benzene to phenol. Among them, the hydroxylation of benzene to phenol with hydrogen peroxide was probably the most effective route to achieve high conversion and yield [13]. Hydrogen peroxide, besides molecular oxygen, is the most attractive oxidant because it is of comparatively low cost and gives only water as a byproduct [13].

Many transition metal catalysts have been employed for catalyzing the hydroxylation of benzene to phenol but so far no appreciable success has been achieved. It has been reported that Fe, Cu and V catalysts are effective for the oxidation of benzene by O_2 or H_2O_2 with ascorbic acid as a reducing agent [14–20]. Liu et al. [21] reported that the performance of the substituted transition metal in the polyoxometalate compounds (TMSP) on the benzene conversion followed the order: Cu > V > Fe. The reaction mechanisms over Fe, Cu and V catalysts were proposed to follow Fenton reaction.

The Fenton reaction has been well-known as the reaction for oxidation of aromatic compounds. Many researchers studied the oxidation reaction with Fe due to its low cost. Although high conversion can be obtained, the selectivity was rather low because the reaction is frequently accompanied by the formation of byproducts such as biphenyl and further oxidation compounds of phenol [13]. To improve catalytic performance of a catalyst, it is customary to add a second metal on the catalyst to alter its catalytic properties. Noble metals, such as Pt, Pd, and Au, have been applied to improve the activity of transition metal oxide catalysts. Pd and Pt are well-known for the hydrogenation reaction [7]. Some researchers have employed Pt and Pd as a co-catalyst to improve the activity of a based metal oxide catalyst. Because Pt and Pd changed the oxidation state of metal oxide catalyst and converted O_2 and H_2 to H_2O_2, the activity for the oxidation reaction is therefore improved [11].

* Corresponding author. Tel.: +662 2186868; fax: +662 2186877.
E-mail address: Suttichai.A@chula.ac.th (S. Assabumrungrat).

1566-7367/$ - see front matter © 2008 Elsevier B.V. All rights reserved.
doi:10.1016/j.catcom.2008.03.008

In this study, we attempted to improve the catalytic properties of the Fe/TiO_2 catalyst for the liquid phase hydroxylation of benzene to phenol with hydrogen peroxide at room temperature. Fe is selected as the main catalyst due to its low cost. Various types of second metals (i.e., Ni, Co, Pd and Pt) were loaded together with Fe on the catalysts for selecting suitable metals for this reaction system. Different characterization techniques were performed to understand the role of the second metal. Finally, the effects of some operating variables such as reaction time, ratio of H_2O_2: benzene and amount of reducing agent on the phenol yield were investigated.

2. Experimental

2.1. Catalyst preparation

Catalysts were prepared by impregnating TiO_2 (JRC-TIO1) support powder in a solution of mixture of metal precursors at 353 K followed by evaporation and drying for overnight. The metal precursors were palladium (II) nitrate, platinum (II) diamine dichloride, cobolt (II) nitrate, nickel (II) nitrate hexahydrate and iron (III) acetylacetonate. The obtained catalysts were then calcined in a furnace whose temperature was increased from room temperature to 773 K at a heating rate of 10 K/min and held for 5 h to remove the organic residues. After calcinations, the catalysts were stored in a dessicator.

2.2. Characterization

XRD patterns of the TiO_2 support and metal supported catalysts were obtained by using X-ray diffractrometer, D 5000 (Siemens AG) using Cu Kα radiation equipped with Ni filter with a range of detection of 2θ 20–80 and a resolution of 0.04.

BET surface area and porosity of the catalysts were measured by Micromeritics ASAP 2020. A sample of 0.3 g was degassed at 573 K for 3 h and the amount of N_2 adsorption was recorded.

X-ray fluorescence analysis (XRF) was performed to determine composition in the bulk of catalysts. The analysis was performed using Siemens SRS3400.

Ammonia-temperature programmed desorption (NH_3-TPD) was carried out using a Micromeritics 2000 TPD/TPR instrument. A catalyst sample (0.1 g) was treated in a helium flow for 1 h at 523 K for removing water and degassing of the catalyst. Then it was saturated in a flow of 15% NH_3/He mixture after cooling to room temperature. After purging with helium at room temperature for 1 h to remove weakly physisorbed NH_3, the sample was heated to 1023 K at a rate of 10 K/min in a helium flow (30 cm^3/min).

Scanning electron microscopy (SEM) and Energy dispersive X-ray spectroscopy (EDX) techniques were used to determine the catalyst granule morphology and elemental distribution of the catalyst particles using JEOL JSM-5800LV scanning electron microscope. The SEM was operated in the back scattering electron (BSE) mode at 20 kV. EDX was performed to determine the elemental concentration distribution on the catalyst granules using Link Isis Series 300 software.

2.3. Experimental setup and product analysis

The oxidation of benzene by H_2O_2 was carried out in a 125 cm^3 round flat bottomed flask at 303 K and 1 atm with a high speed stirrer. The reaction system consisted of two liquid phases: an organic phase containing a substrate (benzene) and solvent (acetonitrile), and an aqueous phase containing 30 wt% H_2O_2 and some acetonitrile.

In a typical experiment, 0.2 g of catalyst was added in a liquid mixture containing 40 cm^3 of acetonitrile, 30 cm^3 (0.32 mol) of H_2O_2 and 11 cm^3 (0.16 mol) of benzene.

The feed and products were analyzed by a gas chromatograph (GC 9A, Shimazu Corp.) with a packed column of GP 10% SP-2100. The injection temperature of 523 K, detector temperature of 523 K, initial column temperature of 383 K, final column temperature of 443 K and temperature programmed rate of 10 K/min were employed. The products were also analyzed by GC–MS especially for some product species which cannot be detected by the FID detector.

The metal loadings of catalyst were calculated as the weight of metal divided by the weight of metal added TiO_2.

The terms of reaction performance were defined as follows:

$$\text{Conversion of benzene} = \frac{\text{mole of benzene reacted}}{\text{initial mole of benzene}}$$

$$\text{Selectivity of phenol} = \frac{\text{mole of phenol produced}}{\text{mole of benzene reacted}}$$

$$\text{Yield of phenol} = \frac{\text{mole of phenol produced}}{\text{initial mole of benzene}}$$

3. Results and discussion

3.1. Catalyst screening and catalyst characterization

Table 1 shows the catalytic performance in the hydroxylation of benzene on several TiO_2-supported binary metal oxide catalysts (Fe/TiO_2, FeNi/TiO_2, FeCo/TiO_2, FePd/TiO_2 and FePt/TiO_2), together with TiO_2 without metal oxides. Note that the values in the blanket represent the weight percentages of the metals. The BET surface area and pore volume were slightly decreased by adding Fe and second metal in the support.

For the Ni and Co co-catalysts, slightly higher yields than that of the single iron oxide catalyst were obtained. The results may confirm the catalytic behavior of Ni and Co metals reported earlier by Dubey et al. [22–24] that from the selection of different metals, Ni and Co as bivalent cations on ternary hydrotalcite catalyst showed high activity for hydroxylation of phenol. It may be concluded that catalysts containing Ni and Co were not suitable for hydroxylation of benzene to phenol but suitable for hydroxylation of phenol.

On the contrary, significant improvement of phenol yield can be achieved by doping small amount of Pd or Pt. The activities of the co-catalysts were ordered as: Pt > Pd >> Co ≈ Ni. It should be noted that, all of the mentioned metals were reported to offer the same degree for decomposition reaction of hydrogen peroxide. Rufus et al. [25] investigated the in situ deposition of various metals on CdS during the photocatalytic decomposition of aqueous sulfide. The order of reactivity was: Rh > Pt > Pd > Ru = Ir > Co ≈ Ni. Therefore, the Pt and Pd were selected for further characterization and reaction study.

Table 1
Summary of catalytic performance and some physical properties of different catalysts

Catalyst	Conversion (%)	Selectivity (%)	Yield (%)	BET (m^2/g)	Pore volume (cm^3/g)
TiO_2	N.D.	N.D.	0.19	74.5	0.26
Fe/TiO_2 (5%)	N.D.	N.D.	1.36	71.0	0.26
FeNi/TiO_2 (5%,1%)	2.2	65	1.43	70.2	0.24
FeNi/TiO_2 (5%,2.5%)	3.0	56	1.68	69.3	0.26
FeCo/TiO_2 (5%,2.5%)	3.3	58	1.91	67.5	0.24
FePd/TiO_2 (5%,1%)	6.7	80	5.36	65.4	0.23
FePt/TiO_2 (5%,1%)	6.5	91	5.92	65.1	0.22

N.D. = Not determined. (Benzene = 11 cm^3;%Fe (III) loading = 5 wt%; catalyst weight = 0.2 g; H_2O_2/benzene mole ratio = 2; acetronitrile solvent 40 cm^3; ascorbic acid = 0.5 g; temperature = 303 K; pressure = 1 atm; reaction time = 4 h).

The chemical composition of the catalyst on the surface and bulk composition of Fe/TiO_2, $FePd/TiO_2$ and $FePt/TiO_2$ were determined by SEM-EDX and XRF, respectively. The comparable results obtained from SEM-EDX and XRF suggest that the metal species were deposited at least on the surface of the support. However, it should be noted that the amounts of iron, platinum, palladium of the catalysts are not quite in good agreement with the applied metal loading (not shown).

The XRD patterns of the support and the catalysts were determined; however, there are no significant changes in XRD spectra between Fe supported on TiO_2 and binary metal oxide supported on TiO_2. It is probably because the amount of Pt or Pd in the catalyst was low.

The results of NH_3-TPD showed that the second metal loading of Pt or Pd influenced the acid property of the catalyst. As shown in Fig. 1, only one peak at $T \approx 443$ K was observed for Fe/TiO_2. However, by loading Pt or Pd, a peak at a lower temperature ($T \approx 373$ K) and an additional peak at higher temperature (623–723 K) were observed. The presence of the second metal obviously altered the acid property of the catalysts. As it was reported that the acidic condition was necessary for the system of ferrous and ferric ions in the liquid phase hydroxylation of benzene to phenol [3], it is likely that the use of the second metal helped increase the activity of the Fenton reaction of iron oxide in the catalyst by altering the acid property of the catalyst. The strong acid site (at high temperature) was more pronounced in the case of Pt. This may be the reason why Pt gives higher phenol yield than that of Pd. It was reported that Pt might promote the reducibility of iron oxide (FeO_x) and probably could act together with reduced FeO_x species in a concert mechanism in benzene oxidation. Pt is well-known for the hydrogenation reaction [7] while iron oxide is well-known for oxidation. Therefore the interaction between iron or Pt and H_2O_2 would be expected. H_2O_2 was decomposed to hydroxyl radical on the precious metal, i.e., Pt [12].

3.2. Effect of reaction time

Fig. 2 shows the influence of reaction time on the phenol yield. The reaction occurs similar to Fenton chemistry, through the participation of hydroxyl radical in activating benzene toward the formation of phenol. Increasing the reaction time directly increased the benzene conversion. It should be noted that the catalyst deactivation was not checked in this study. The obtained results indicated that after 4 h the phenol selectivity decreased as observed by the increase of byproducts in the system. In the H_2 and O_2 system, H_2O_2 was formed from both gases on the platinum and this H_2O_2 was decomposed to hydroxyl radical on the platinum. It is likely that the platinum and palladium could increase the amount of hydroxyl radical and form water due to the decomposition of H_2O_2.

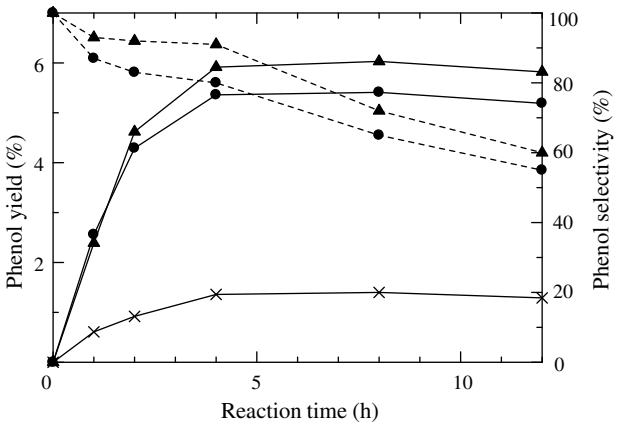

Fig. 2. Effect of reaction time on phenol yield (—) and selectivity (---) for different catalyst i.e., × Fe/TiO_2, ● $FePd/TiO_2$, ▲ $FePt/TiO_2$.

The mechanism of Fenton's method is widely accepted as follows [26]:

$$Fe^{2+} + H_2O_2 \rightarrow Fe^{3+} + OH^0 + OH^- \quad (1)$$

The hydroxyl radical reacts directly with benzene to produce cyclohexadienyl (CHD) radical, which subsequently undergoes an H^+ abstraction as follows:

$$OH^0 + \text{benzene} \rightarrow \text{CHD} \quad (2)$$

$$\text{CHD} + Fe^{3+} \rightarrow \text{phenol} + Fe^{2+} + H^+ \quad (3)$$

However, the CHD radical intermediate can react with H^+ and collapse to benzene as follows:

$$\text{CHD} + Fe^{2+} + H^+ \rightarrow \text{benzene} + Fe^{3+} + H_2O \quad (4)$$

3.3. Effect of the amount of H_2O_2 for the hydroxylation of benzene

The effect of the ratio of H_2O_2: benzene on yield of phenol was shown in Fig. 3. In the cases of Pt and Pd modified catalysts, phenol yield increased with increasing the ratio of H_2O_2 per benzene up to 2 and then decreased. It can be explained that further oxidation of phenol to hydroquinone, benzoquinone and other products can be

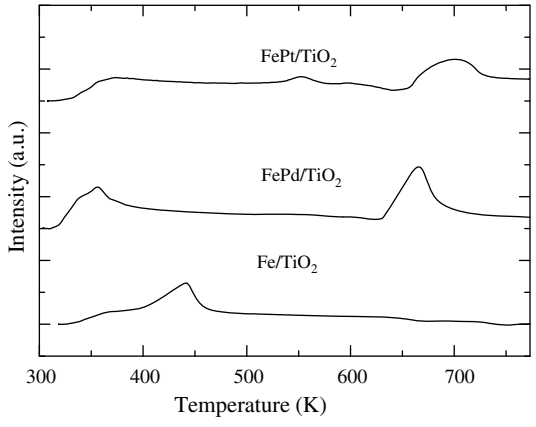

Fig. 1. NH_3-TPD results of different catalysts.

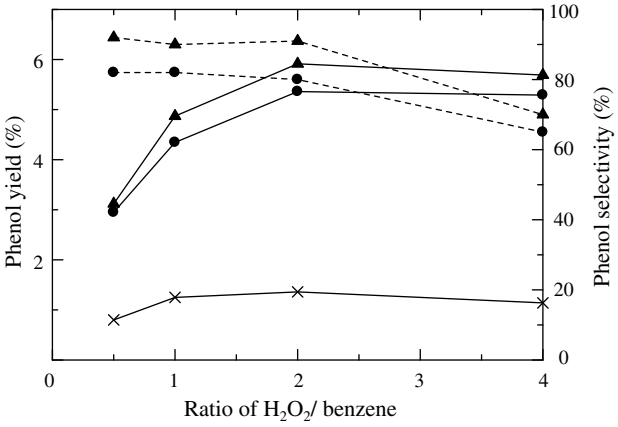

Fig. 3. Effect of H_2O_2/benzene ratio on phenol yield (—) and selectivity (---) for different catalyst i.e., × Fe/TiO_2, ● $FePd/TiO_2$, ▲ $FePt/TiO_2$ (4 h reaction time).

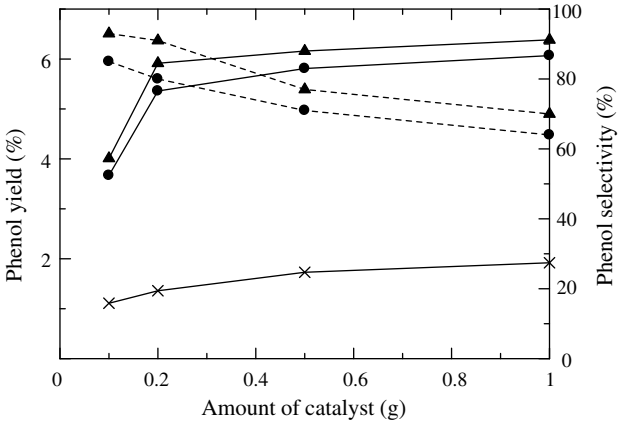

Fig. 4. Effect of amount of catalyst on phenol yield (—) and selectivity (---) for different catalyst i.e., × Fe/TiO_2, ● $FePd/TiO_2$, ▲ $FePt/TiO_2$ (4 h reaction time).

occurred with the presence of excessive amount of H_2O_2 oxidant. At a high oxidant concentration, it was difficult to control the selective oxidation to produced phenol. The benzene conversion was increased by the high concentration of oxidant but it decreased the phenol selectivity.

3.4. Effect of the amount of catalyst

The influence of the amount of catalyst on the yield of phenol over binary metal oxide supported on TiO_2 catalyst at room temperature is illustrated in Fig. 4. The yield of phenol increased with increasing the amount of catalyst.

The catalyst concentration has the effect on the decomposition of hydrogen peroxide and the amount of hydroxyl radical for the reaction. Increasing the amount of catalyst increased the conversion and yield but decreased phenol selectivity. The phenol was easy to oxidize to other products (hydroquinone, benzoquinone and cresol). Therefore, phenol yield did not increase at high concentration of catalyst.

3.5. Effect of the amount of ascorbic acid

The dependence of the phenol yield on the amount of ascorbic acid was investigated at room temperature as shown in Fig. 5. The yield of phenol increased with increasing the amount of ascorbic acid up to 1 g. Further increase in the amount of ascorbic acid insignificantly affected the phenol yield. The use of excessive amount of ascorbic acid, which functioned as a reducing agent, led to the reductive decomposition of hydrogen peroxide. In this case, increasing the amount of ascorbic acid increased the benzene conversion and decreased the selectivity of phenol.

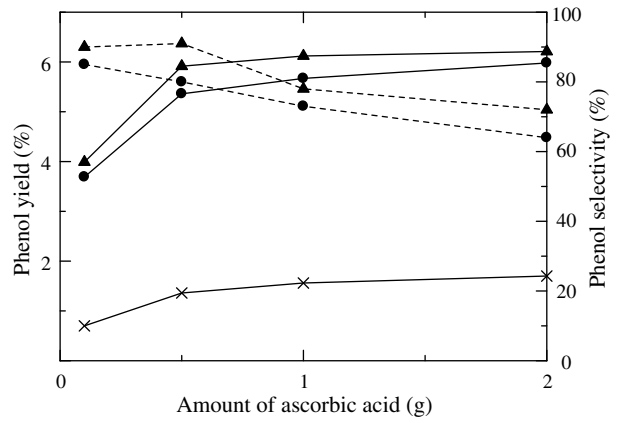

Fig. 5. Effect of amount of ascorbic acid on phenol yield (—) and selectivity (---) for different catalyst i.e., × Fe/TiO_2, ● $FePd/TiO_2$, ▲ $FePt/TiO_2$ (4 h reaction time).

The ascorbic acid is well-known as a good reducing agent. It changes the state of metal catalyst from Fe (III) to Fe (II) [4–6].

$$2Fe^{3+} + \text{ascorbic acid} + 0.5O_2 \rightarrow 2Fe^{2+} + \text{dehydroascorbic acid} + H_2O \quad (5)$$

$$2Fe^{2+} + O_2 + 2H^+ \rightarrow 2Fe^{3+} + H_2O_2 \quad (6)$$

$$Fe^{3+} + H_2O_2 + H^+ \rightarrow Fe^{2+} + OH^0 + H_2O \quad (7)$$

As the active species (Fe^{2+}) was regenerated by ascorbic acid, the effect of ascorbic acid was similar to the case of increasing the amount of catalyst.

4. Conclusion

The liquid phase hydroxylation of benzene to phenol with hydrogen peroxide catalyzed by Fe-containing binary metal oxide catalysts supported on TiO_2 was investigated. The second metal can improve the phenol production of the typical Fe/TiO_2 catalyst in the order of Pt > Pd >> Co ≈ Ni. Doping with 1 wt% Pt or Pd obviously improved phenol yield. The presence of the Pt or Pd obviously altered the acid property of the catalyst which is favorable for the Fenton reaction. At too long reaction time or too large amount of H_2O_2 oxidant or catalyst or ascorbic acid, byproducts (benzoquinone, hydroquinone and cresol) could be produced. The optimum condition for the system is 4 h of reaction time with the ratio of 2 moles of H_2O_2, 1.25 g of catalyst and 6.25 g of ascorbic acid per mole of benzene.

Acknowledgements

Financial support from the Thailand Research Fund and Commission on Higher Education is gratefully acknowledged.

References

[1] H. Yamanaka, R. Hamada, H. Nibuta, S. Nishiyama, S. Tsuruya, J. Mol. Catal. A: Chem. 178 (2002) 89.
[2] J.L. Motz, H. Heinichen, W.F. Holderich, J. Mol. Catal. A: Chem. 136 (1998) 175.
[3] Y.J. Seo, Y. Mukai, T. Tagawa, S. Goto, J. Mol. Catal. A: Chem. 120 (1997) 49.
[4] G. Tanarungsun, W. Kiatkittipong, S. Assabumrungrat, H. Yamada, T. Tagawa, P. Prasertdam, J. Chem. Eng. Jpn. 40 (2007) 415.
[5] G. Tanarungsun, W. Kiatkittipong, S. Assabumrungrat, H. Yamada, T. Tagawa, P. Prasertdam, J. Ind. Eng. Chem. 13 (2007) 444.
[6] G. Tanarungsun, W. Kiatkittipong, S. Assabumrungrat, H. Yamada, T. Tagawa, P. Prasertdam, J. Ind. Eng. Chem. 13 (2007) 870.
[7] X. Gao, J. Xu, Appl. Clay Sci. 33 (2006) 1.
[8] Y.K. Masumoto, R. Hamada, K. Yokota, S. Nishiyama, S. Tsuruya, J. Mol. Catal. A: Chem. 184 (2002) 215.
[9] H. Kanzaki, T. Kitamura, R. Hamada, S. Nishiyama, S. Tsuruya, J. Mol. Catal. A: Chem. 208 (2004) 203.
[10] T. Ohtani, S. Nishiyama, S. Tsuruya, M. Masai, J. Catal. 155 (1995) 158.
[11] N.I. Kuznetsova, L.I. Kuznetsova, V.A. Likholobov, G.P. Pez, Catal. Today 99 (2005) 193.
[12] T. Miyake, M. Hamada, Y. Sasaki, M. Oguri, Appl. Catal. A: Gen. 131 (1995) 33.
[13] H.H. Monfared, Z. Amouei, J. Mol. Catal. A: Chem. 217 (2004) 161.
[14] K. Fujushima, A. Fukuoka, A. Yamagishi, S. Inagaki, Y. Fukushima, M. Ichikawa, J. Mol. Catal A: Chem. 166 (2000) 211.
[15] C.W. Lee, W.J. Lee, Y.K. Park, S.E. Park, Catal. Today 61 (2000) 137.
[16] K. Teramura, T. Tanaka, T. Hosokawa, T. Ohuchi, M. Kani, T. Funabiki, Catal. Today 96 (2004) 205.
[17] K. Lemke, H. Eric, U. Lohse, H. Berndt, K. Jahnisch, Appl. Catal. A: Gen. 243 (2003) 41.
[18] R.S.G. Ferreira, P.G.P. de Oliveira, F.B. Noronha, Appl. Catal. B: Environ. 50 (2004) 243.
[19] J. Zhang, Y. Tang, G. Li, C. Hu, Appl. Catal. A: Gen. 278 (2005) 251.
[20] V. Parvulescu, B.L. Su, Catal. Today 69 (2001) 315.

[21] Y. Liu, K. Murata, M. Inaba, Catal. Commun. 6 (2005) 679.
[22] A. Dubey, V. Rives, S. Kannan, J. Mol. Catal. A 181 (2002) 151.
[23] A. Dubey, V. Rives, S. Kannan, Phys. Chem. Chem. Phys. 3 (2001) 4826.
[24] A. Dubey, S. Kannan, S. Velu, K. Suzuki, Appl. Catal. A: Gen. 238 (2003) 319.
[25] I.B. Rufus, B. Viswanathan, V. Ramakrishnan, J.C. Kuriacose, J. Photochem. Photobiol. A: Chem. 91 (1995) 63.
[26] T. Miyahara, H. Kanzaki, R. Hamada, S. Kuroiwa, S. Nishiyama, S. Tsuruya, J. Mol. Catal. A: Chem. 176 (2001) 141.

Appendix 15

Journal of the Japan Petroleum Institute, **51**, (2), 114–117 (2008)

[Research Note]

Catalyst Regenerator for Partial Oxidation of Benzene in Reaction-extraction System

Hiroshi YAMADA[†1]*, Tomoaki MIZUNO[†1], Tomohiko TAGAWA[†1], Garun TANARUNGSUN[†2], Piyasan PRASERTHDAM[†2], and Suttichai ASSABUMRUNGRAT[†2]

[†1] Dept. of Chemical Engineering, Nagoya University, Chikusa-ku, Nagoya 464-8603, JAPAN
[†2] Center of Excellence in Catalysis and Catalytic Reaction Engineering, Dept. of Chemical Engineering, Chulalongkorn University, Bangkok 10330, THAILAND

(Received November 19, 2007)

The liquid-phase oxidation of benzene to phenol was investigated in the biphasic benzene-water system using VCl_3 and molecular oxygen as the catalyst and oxidant, respectively. Benzene was dissolved in the aqueous catalyst phase and reacted with oxygen to form phenol. Phenol was preferentially extracted into the benzene phase, thus suppressing the formation of over-oxidized byproducts. During the reaction, the catalyst was oxidized and deactivated. To regenerate the catalyst, a regenerator was installed into the system. Hydrogen was fed to the regenerator to reduce the deactivated catalyst, but no significant improvement of the system performance was observed without the presence of a second catalyst. Pd sheet in the regenerator allowed the system to run very stably, and the system was easy to shut down and start up.

Keywords
Benzene, Phenol, Partial oxidation, Bi-phase system, Reaction-extraction system

1. Introduction

Commercial production of phenol generally depends on the indirect-multistage cumene process which produces equimolar amounts of acetone as a byproduct. Therefore, methods for direct oxidation of benzene to phenol under mild conditions are desirable. Many catalysts such as Cu[1], V[2),3)], Pd[4),5)] and Pt[5)] have been investigated for direct oxidation with molecular oxygen. However, a few efforts have focused on the design of reactors or reaction systems for the direct oxidation of benzene. A stirring batch reactor was used in a bi-phase system[6)]. Benzene and hydrogen peroxide were separated by a membrane which allowed benzene to permeate across the membrane to the aqueous phase whereas phenol permeated back to the organic phase. The system had high selectivity for phenol, and minimized over-oxidation to form byproducts. Selectivity for phenol of 99.94% could be achieved with a hydrophobic porous polypropylene membrane. A palladium membrane reactor was used in a gas phase reaction[7)]. Hydrogen was activated during permeation across the membrane. The active hydrogen atoms reacted with oxygen molecules to form active species like O or OH radicals, which then attacked benzene to produce phenol. The yield of phenol was 20%. We previously proposed the liquid-phase oxidation of benzene to phenol in a biphasic benzene-water system[8)]. Catalyst deactivation was found to be a major problem in the process.

The present study improved the liquid-phase oxidation of benzene to phenol in the biphasic benzene-water system by incorporating a regenerator into the reactor-extractor system. **Figure 1** shows the concept of the proposed system consisting of a reactor, an extractor, and a regenerator. The reactor contains both benzene phase and aqueous phase. Benzene dissolved into the aqueous phase is oxidized to phenol which is then extracted into the benzene phase. Further oxidation of phenol does not take place in the benzene phase because the catalyst is selectively dissolved in the aqueous phase. However, further oxidation of phenol can occur in the aqueous phase. Therefore, phenol dissolved in the benzene phase is removed from the reactor by the extractor. Benzene phase is pumped by a circulation pump from the reactor to the extractor which contains aqueous NaOH solution, where phenol is extracted into the alkaline solution as phenoxide. Only benzene is returned to the reactor. The regenerator is used to regenerate the deactivated catalyst. The aqueous phase containing the catalyst is pumped from the reactor to the regenerator where hydrogen gas is used to reactivate the catalyst.

* To whom correspondence should be addressed.
* E-mail: yamada@nuce.nagoya-u.ac.jp

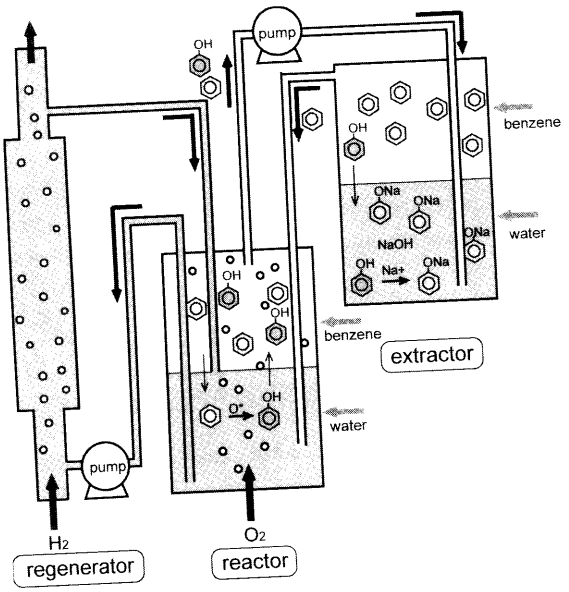

Fig. 1 Reactor System

2. Experimental

Figure 1 shows the all glass apparatus used in this study. Two jacketed stirred tank reactors were used as the reactor and the extractor and a bubble column reactor as the regenerator. Benzene (6.0×10^{-5} m^3) and water (1.0×10^{-4} m^3) were placed in the reactor and oxygen (2.5×10^{-5} m^3/min) was continuously introduced. VCl_3 catalyst was dissolved in the aqueous phase at a concentration of 10 mol/m^3-aq. Benzene (1.4×10^{-4} m^3) and aqueous NaOH solution (1.0×10^{-4} m^3 with a concentration of 1.2 mol/m^3-aq) were placed in the extractor. Benzene phase was circulated between the reactor and the extractor using a circulation pump. The flow rate was controlled at 3.5×10^{-5} m^3/min. The temperature of the reactor and the extractor was fixed at 313 K in all experiments. The regenerator containing the aqueous catalyst solution (1.0×10^{-4} m^3) was continuously fed with hydrogen (2.5×10^{-5} m^3/min). Another circulation pump was used to circulate the aqueous solution between the reactor and the regenerator. The flow rate was set at 3.7×10^{-5} m^3/min. The regenerator was operated at 313 or 333 K.

All chemicals used in this study were purchased from Wako Pure Chemical Industries, Ltd. No further purification was carried out. A small amount of sample was periodically analyzed with a gas chromatograph (GC-353B, GL Sciences, Inc.) equipped with a 25 m column (CP-Sil 8CB, J&W Scientific, Inc.) operated at 393 K. GC-MS (gas chromatograph-mass spectrometer, HP6890GC-HP5972A, Hewlett Packard Co., Ltd.) with a 60 m column (HP-INNOWAX, Hewlett Packard Co., Ltd.) was used to identify any byproduct.

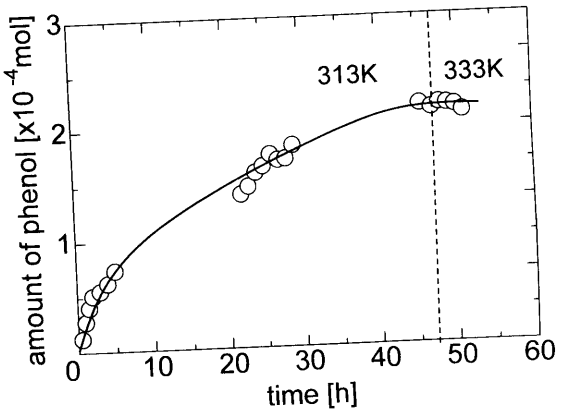

Fig. 2 Reaction Profile Using Regenerator without Reduction Catalyst

3. Results and Discussion

Hydroquinone, byproduct, was detected when the extractor was not used. However, no byproduct was detected after including the extractor into the system.

In this benzene and aqueous biphasic reaction system, the reaction occurs in the aqueous phase which contains the catalyst. The benzene dissolved in the aqueous phase was consumed by the reaction but it is supplied from benzene phase where far excess amount of benzene is charged as an extracting solvent. The benzene concentration depends only on the solubility of benzene in water. As excess benzene is charged into the reaction system, conversion based on charged benzene does not show the catalytic performance. Therefore, the time course of phenol formation is mainly discussed.

At first the regenerator was operated without reducing catalyst. The operation temperature was 313 K, the same temperature as those of the reactor and extractor. The reaction profile shown in **Fig. 2** indicated that after running the system for 45 h, the production of phenol apparently stopped due to catalyst deactivation. To promote regeneration of the catalyst by hydrogen, the temperature of the regenerator was increased to 333 K. However, no significant improvement was detected.

A new experiment was then carried out with reducing catalyst packed in the regenerator. To reduce the over-oxidized vanadium species with hydrogen, 30 g of 0.5 wt% Pd/Al_2O_3 (Sigma Aldrich, Inc.) was packed into the regenerator which was operated at 333 K. **Figure 3** clearly shows that the use of Pd/Al_2O_3 improved the performance of the reaction system, but phenol formation stopped within 50 h. The same amount of VCl_3 catalyst as used in the initial experiment was added to the system. The system then began to produce phenol again and continued until 190 h. The color of the catalyst (aqueous) phase changed during the reaction from the initial brownish green to pale blue after 1 h, which faded with time and finally became color-

Table 1 Investigation of Vanadium Adsorption

sample	initial conc. [ppm]	3 days after [ppm]	adsorption ratio [%]
V	10.33	10.33	0
V + Zr	10.33	8.75	15.3
V + Pd/Al_2O_3	10.33	0.023	99.8

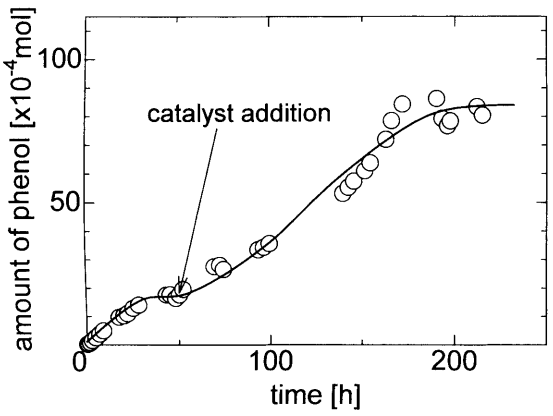

Fig. 3 Reaction Profiles Using Regenerator with Pd/Al_2O_3

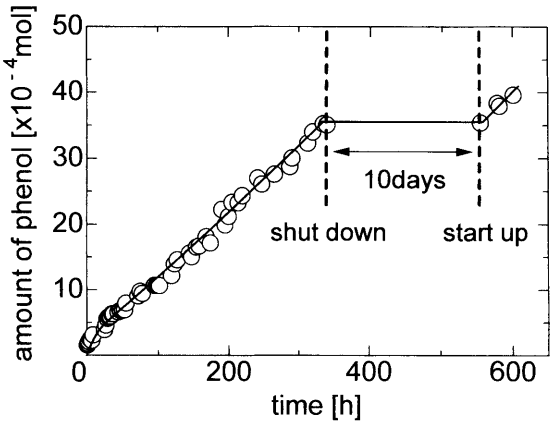

Fig. 4 Reaction Profiles Using Regenerator with Pd/sheet

less and transparent. Phenol formation rate decreased and became zero as the catalyst phase became colorless.

After new catalyst was added, the color cycle was repeated. V^{2+}, V^{3+}, V^{4+} and V^{5+} ions are colored purple, green, blue, and transparent, respectively. We used VCl_3 as a catalyst precursor, so the catalyst phase was dark green at first. The catalyst phase became pale blue showing V^{3+} was oxidized to blue V^{4+}. At this stage, the main vanadium species in the reactor was V^{4+}. This oxidation process activated molecular oxygen as in Fenton's method. There are two hypotheses for the declining performance of the system: oxidation of the catalyst from V^{4+} to V^{5+}, and adsorption of vanadium ion onto the Pd/Al_2O_3 catalyst in the regenerator. In both cases, the color of the catalyst phase eventually becomes transparent.

A set of experiments was carried out to investigate the adsorption of vanadium on the Pd/Al_2O_3 catalyst. VCl_3 0.063 g was dissolved into 30 cm^3 water. Pd/Al_2O_3 6.0 g was stood in the solution for 3 days at 333 K. As ZrO_2 balls were packed on top of the Pd/Al_2O_3 layer to fix the catalyst in the regenerator, adsorption of VCl_3 onto ZrO_2 balls (10 g) was also tested under the same conditions. **Table 1** summarizes the results. Concentrations were determined by ICP (inductively coupled plasma) atomic emission spectrometer. Pd/Al_2O_3 preferentially adsorbed vanadium ions whereas ZrO_2 balls slightly adsorbed vanadium ions. Therefore, the loss of the catalytic activity shown in **Fig. 3** was caused by adsorption of the vanadium species on the Pd/Al_2O_3 catalyst in the regenerator. Al_2O_3 is porous and has high surface area, so is likely to be a good medium for adsorbing metal ions. **Figure 3** also shows that added vanadium catalyst could produce much larger amounts of phenol than the initial vanadium charge, because the adsorption of initial vanadium retarded the adsorption rate of the added vanadium. This resulted in the prolonged apparent catalyst life of the added vanadium. A supported catalyst in the regenerator may not be a good choice unless a large excess of vanadium catalyst is involved in this system. Therefore, a palladium metal bulk catalyst was tested.

Bulk regeneration catalyst formed of palladium sheet (12.3 g, 100 × 100 × 0.1 mm, Nilaco Co.) was inserted in the regenerator. **Figure 4** shows that phenol could be produced in the system without deactivation for more than two weeks. Therefore, adsorption of active vanadium species onto the regeneration catalyst was avoided. The formation rate of phenol was smaller than that of Pd/Al_2O_3 as expected because of the difference in surface area between the Pd sheet and the supported Pd catalyst.

An experiment was continued to test the shut-down and start-up operation. To shut down the system, the temperature was decreased to room temperature and gaseous feed was stopped at 340 h. After 10 days, the system was started up again. As shown in **Fig. 4**, phenol was produced again and the formation rate of phenol was almost same as in the previous run. Therefore, the system was very stable, and easy to shut down and start up.

4. Conclusion

The combined reactor, extractor and regenerator system for the organic-aqueous liquid-phase oxidation of

benzene to phenol with gaseous oxygen under water soluble vanadium catalyst could reactivate the deactivated catalyst for continuous operation. Although Pd/Al_2O_3 catalyst could regenerate the catalyst, operation suffered from the adsorption of vanadium ion on the Al_2O_3 support. Use of palladium sheet in the regenerator allowed the system to run very stably, and allowed easy shut down and start up.

References

1) Miyahara, T., Kanzaki, H., Hamada, R., Kuroiwa, S., Nishiyama, S., Tsuruya, S., *J. Mol. Catal. A*, **176**, 141 (2001).
2) Masumoto, Y., Hamada, R., Yokota, K., Nishiyama, S., Tsuruya, S., *J. Mol. Catal. A*, **184**, 215 (2002).
3) Lemke, K., Ehrich, H., Lohse, U., Berndt, H., Jaehnisch, K., *Appl. Catal. A: General*, **243**, 41 (2003).
4) Burton, H. A., Kozhevnikov, I. V., *J. Mol. Catal. A*, **184**, 285 (2002).
5) Kuznetsova, N. I., Kuznetsova, L. I., Likholobov, V. A., Pez, G. P., *Catal. Today*, **99**, 193 (2005).
6) Molinari, R., Poerio, T., Argurio, P., *Catal. Today*, **118**, 52 (2006).
7) Itoh, N., Niwa, S., Mizukami, F., Inoue, T., Igarashi, A., Namba, T., *Catal. Commun.*, **4**, 243 (2003).
8) Mizuno, T., Yamada, H., Tagawa, T., Goto, S., *J. Chem. Eng. Japan*, **38**, 849 (2005).

要　　旨

反応抽出を用いたベンゼン部分酸化反応システム用触媒再生器の検討

山田　博史[†1)]，水野　友章[†1)]，田川　智彦[†1)]，Garun TANARUNGSUN[†2)]，
Piyasan PRASERTHDAM[†2)]，Suttichai ASSABUMRUNGRAT[†2)]

[†1)] 名古屋大学大学院工学研究科化学生物工学専攻分子化学工学分野，464-8603 名古屋市千種区不老町

[†2)] Center of Excellence in Catalysis and Catalytic Reaction Engineering, Dept. of Chemical Engineering, Chulalongkorn University, Bangkok 10330, THAILAND

ベンゼンの部分酸化反応によるフェノールの合成をベンゼン-水液2相系で行った。触媒としてVCl_3，酸化剤として気体酸素を用いた。反応システムは反応器，抽出器，触媒再生器の三つの装置からなる。反応器中において，ベンゼンは触媒の溶けている水相に溶け込みフェノールへと酸化される。生成したフェノールはベンゼン相に抽出され，それ以上の逐次酸化が抑制される。ベンゼン相に抽出されたフェノールはそのままではフェノールの蓄積に伴い水相に分配されて逐次酸化が進行してしまうので，抽出器において再度抽出され反応器系外に送られる。反応中に酸化されて失活した触媒を水素で還元し再生する触媒再生器について検討を行った。触媒再生器において還元触媒がない条件では触媒は再生されなかった。還元触媒としてPdはくを用いるとベンゼンの部分酸化反応は安定して進行した。また，停止-再起動も簡単に行うことができた。

Appendix 16

Submitted to Journal of Industrial and Engineering Chemistry

Type of Contribution: Research paper

Subject Area: - CHEMICAL REACTION ENGINEERING - REACTIONS

Ternary metal oxide catalysts for selective oxidation of benzene to phenol

Garun Tanarungsun [a], Worapon Kiatkittipong [b], Piyasan Praserthdam [a],

Hiroshi Yamada [c], Tomohiko Tagawa [c] and Suttichai Assabumrungrat [a,*]

[a] *Center of Excellence in Catalysis and Catalytic Reaction Engineering, Department of Chemical Engineering, Faculty of Engineering, Chulalongkorn University, Bangkok 10330, THAILAND*

[b] *Department of Chemical Engineering, Faculty of Engineering and Industrial Technology, Silpakorn University, Nakhon Pathom 73000, THAILAND*

[c] *Department of Chemical Engineering, Nagoya University, Chikusa, Nagoya, 464-8603, JAPAN*

* Corresponding author Tel.: +66 2 2186868; Fax: +66 2 2186877

E-mail address: Suttichai.A@chula.ac.th (S. Assabumrungrat)

Abstract

This paper studied the liquid phase hydroxylation of benzene to phenol with hydrogen peroxide catalyzed by ternary metal oxide catalysts (Fe(III), V(V) and Cu(II)) supported on TiO_2 at room temperature. The effects of V(V) and Cu(II) metal oxide loading were investigated. The catalysts were prepared by co-impregnation method and characterized by BET, XRD, XRF, SEM-EDX, NH_3-TPD techniques. It was reported that the presence of V(V) and Cu(II) influenced the acid property on the catalyst. The increase of the metal loading increased the acidity of the catalyst. TiO_2 loaded with Fe, V and Cu of 5, 2.5 and 2.5 wt%, respectively offered the highest yield of phenol. Although the increase of the metal loading improved the yield of phenol, the TOF reduced due to the reduction of dispersion of the catalyst metal. The optimum condition for the system is a reaction time of 4 h, catalyst weight of 0.2 g, the H_2O_2: benzene molar ratio of 2 and 6.25 g of ascorbic acid per mole of benzene.

Keywords*: Oxidation of benzene; Phenol production; Hydrogen peroxide; Fe(III); V(V); Cu(II); TiO_2*

Introduction

Phenol is an important chemical used in many industries. More than 90% of phenol has been produced from the cumene process [1]. However, the industrial cumene process has several significant shortcomings: it is a multistage synthesis; the intermediate cumene hydroperoxide is explosive; there are ecological problems, and the production rate of the co-product acetone exceeds market demand [2]. The direct hydroxylation of benzene to phenol is an attractive alternative for phenol production.

Some homogeneous and heterogeneous catalytic systems consisting of Fenton's reagent have been investigated for the hydroxylation of benzene using H_2O_2 [3-7] or O_2 as an oxidant [7-9]. Oxygen gas is a more environmental-friendly oxidant than H_2O_2 but it still offers low conversion and yield of phenol. The use of homogeneous liquid phase oxidation catalyst like Fenton catalysts, Fe^{2+}/ Fe^{3+}, or other dissolved transition metal cations, such as Cu^{2+}, Mn^{2+}, V^{3+}, V^{5+} and Co^{2+} [10] has proven to be quite efficient. However, it necessitates a tight pH control to prevent precipitation and extra steps for the recuperation and the reuse of the catalyst. The alternative approach has been based on the development of solid catalysts, which feature efficiency as well as stability under the reaction conditions. For industrial processes, heterogeneous catalysts have some advantages over homogeneous catalysts such as catalyst recovery and recycling.

Many researchers studied the oxidation of benzene to phenol by using the transition metal oxide catalysts supported on TiO_2 [11-13], SiO_2 [13], Al_2O_3 [13,14], MCM-41 [1,6,15,16], SBA-15 [17], activated carbon [1,18], clay [10], heteropolyacid [19,20] and amorphous microporous mixed oxides [21]. The most popular transition metal oxides for the oxidation of aromatics are Fe, Cu and V. Miyahara *et al*. [8] studied liquid phase oxidation of benzene by various supported Cu. Among the

supported Cu catalysts studied i.e., Cu/SiO_2, Cu/Al_2O_3, Cu/SiO_2-Al_2O_3, Cu/MCM-41, Cu/HMCM-41, Cu-NaY, CuO-SiO_2 and CuO-Al_2O_3, the $CuO–Al_2O_3$ catalyst prepared by a co-precipitation method was found to be an effective catalyst for phenol production. However, the results showed relatively low phenol yield.

Phenol production from benzene and H_2O_2 was carried out using Fe, Cu, V supported on TiO_2 [11,12], activated carbon [1,18] and MCM 41 [1]. The conversion and selectivity of the metal oxide catalyst could be improved by adding second and third metal oxides to Fe/TiO_2 [13].

The development of new catalysts for the direct oxidation of benzene to phenol remains an attractive and important subject for the success of this process. In this study, the focus was on the improvement of the catalytic performance of Fe/TiO_2 catalyst by adding second and third metal oxides (V and Cu) at different compositions to the catalysts. In addition, various techniques were employed to characterize the synthesized catalysts. Finally, the effects of various operating parameters; i.e., the reaction time, the ratio of H_2O_2 to benzene, the amount of catalyst, the amount of ascorbic acid, were investigated.

Experimental

Materials and chemicals

Table 1 summarizes the details of materials and chemicals employed in this work. All chemicals were used without further purification.

Catalyst preparation

Catalysts were prepared by impregnating TiO_2 with a mixed solution of metal precursors at 353 K. For example, 5 wt.% Fe, 2.5 wt.% V and 2.5 wt.% Cu loaded on TiO_2 (abbreviated as $Fe_5V_{2.5}Cu_{2.5}/TiO_2$) were prepared by mixing 9 g of TiO_2, 0.5 g of Fe (i.e. 3.17 g of iron (III) acetylacetonate), 0.25 g of V (i.e. 0.57 g of ammonium metavanadate (V)) and 0.25 g of Cu (i.e. 0.91 g of cupric (II) nitrate). The solution was then evaporated and dried for overnight. The obtained catalysts were calcined under a continuous feed of air (60 cm^3/min) in a furnace whose temperature was increased from room temperature to 773 K at a heating rate of 10 K/min and held for 5 h to remove the organic residues. After calcinations, the catalysts were stored in a dessicator.

Characterization

XRD patterns of the TiO_2 support and metal supported catalysts were obtained by using X-ray diffractrometer, D 5000 (Siemens AG) using Cu Kα radiation equipped with Ni filter with a detection range of 2θ = 20-80 and a resolution of 0.04.

BET surface area and porosity of the catalysts were measured by Micromeritics ASAP 2020.

XRF was performed to determine the bulk composition of catalysts. The analysis was performed using Siemens SRS3400. The composition of the catalyst samples was obtained as metal oxide using XRF analysis. Then it was recalculated as metal and presented in Table 2.

Ammonia-temperature programmed desorption (NH_3-TPD) was carried out in a Micromeritics 2000 TPD/TPR instrument. A catalyst sample (0.1 g) was treated at

523 K for removing water and degassing in a helium flow for 1 h and then saturated with a flow of 15% NH_3/He mixture after cooling to room temperature. After purging with helium at room temperature for 1 h to remove weakly physisorbed NH_3, the sample was heated to 1023 K at a rate of 10 K/min in a helium flow (30 cm^3/min).

FTIR spectra were recorded on a Nicolet impact 6700 instrument, in the range of 650-4000 cm^{-1} and with a spectral resolution of 4 cm^{-1}. Each sample was mixed with KBr with a sample: KBr ratio of 1:100 and then pressed into a thin wafer.

Scanning electron microscopy (SEM - JEOL JSM-5800LV), operated using the back scattering electron (BSE) mode at 20 kV and Energy dispersive X-ray spectroscopy (EDX - Link Isis Series 300 software) were used to determine the morphology and elemental distribution of the catalyst samples.

Experimental setup and product analysis

The oxidation of benzene by H_2O_2 was carried out in a 125-cm^3 round flat bottomed flask at 303 K and at a pressure of 1 atm with a high speed stirrer. The reaction system consisted of two liquid phases: an organic phase containing benzene and acetonitrile, and an aqueous phase containing acetonitrile and 30 wt% H_2O_2.

In typical experiment, 0.2 g of catalyst was added to a liquid mixture containing 40 cm^3 of acetonitrile, 30 cm^3 of H_2O_2 (0.32 mol) and 11 cm^3 of benzene (0.16 mol). Note that a preliminary study was carried out to investigate the effect of mass transfer resistance by varying the stirring speed (the results are not shown here). The conversion increased with increasing speed and, finally, leveled off at a speed of 600 rpm. Therefore, a speed of 600 rpm was used to ensure negligible mass transfer resistance in this study.

The feed and products were analyzed by a gas chromatography (GC 9A, Shimadzu Corp.) with a packed column of GP 10% SP-2100. The injection and detector temperatures were 523 K. The initial and final column temperatures were 383 K and 443 K, respectively with a temperature programmed rate of 10 K/min. The products were also analyzed by GC-MS (Agilent Technologies 6890 N Network GC system and 5973 Mass selective Detector) especially for some product species which cannot be detected by the FID detector.

The terms of reaction performance were defined as follows.

$$\text{Conversion of benzene} = \frac{\text{mole of benzene reacted}}{\text{initial mole of benzene}}$$

$$\text{Selectivity of phenol} = \frac{\text{mole of phenol produced}}{\text{mole of benzene reacted}}$$

$$\text{Yield of phenol} = \frac{\text{mole of phenol produced}}{\text{initial mole of benzene}}$$

$$\text{Turn over frequency (TOF)} = \frac{\text{mole of phenol produced}}{\text{mole of metal catalyst} \times \text{reaction time}}$$

Results and discussion

Catalysts

The formulas of catalysts with different percent metal loadings are abbreviated by using subscripts; for example, $Fe_5V_1Cu_1/TiO_2$ represents a catalyst with 5 wt% Fe and 1 wt% V and 1 wt% Cu loaded on TiO_2.

The chemical compositions of all catalysts were determined by elemental chemical analysis, by XRF and SEM-EDX as summarized in Table 2. XRF results representing the percent of metal loading in the bulk of catalyst showed that Fe was

mostly lower than 5 wt% loading. Vanadium showed higher percent metal loadings than calculations while copper showed the opposite trend likely due to the difficulty for copper to diffuse inside the support pores during the catalyst preparation. The analysis of percent loading on the surface by SEM-EDX showed that the percent loadings were close to those results from the XRF analysis. It should be noted that although the observed values of percent metal loading are different from the calculated values, they were usually increased when the catalysts were prepared with a higher percent of metal loading. Regarding the textural properties of the samples, the specific surface area of catalysts was remarkably decreased at high ratios of Cu/Fe and V/Fe loading as shown in Table 3.

The XRD patterns of the catalysts and the blank TiO_2 support were determined (not shown). However, no obvious peaks of Fe, Cu and V metals were observed when compared with the pattern of the blank TiO_2 even at a high range of metal loading. This observation was similar to the previous work [11]. FTIR spectra of the catalysts were recorded; however, no different peaks were observed (the results are not shown here). Both the acidity and the distribution of the acid strength of the catalysts were determined by the NH_3-TPD. As shown in Figure 1, only one peak ($T \approx 443$ K) was observed for Fe/TiO_2. However, when second and third metals were loaded on the catalyst, the acid properties of the catalyst were changed. A new peak at a lower temperature ($T \approx 373$ K) was observed in $FeCu/TiO_2$, FeV/TiO_2 and $FeCuV/TiO_2$ catalysts. The peak observed in the Fe/TiO_2 at $T \approx 443$ K disappeared but there are more peaks present at higher temperatures. The peaks at high temperatures may be contributed from the decomposition of the adsorbed ammonia. Regarding the percent loading of V and Cu, it is likely that the acidity of the catalyst should be higher when

the percent loading was increased as observed by the broadening of the low temperature peak.

Effect of operating parameters on the hydroxylation of benzene to phenol

Influence of reaction time

As shown in Figure 2, the yield of phenol increased with reaction time until 4 h. Then, it decreased especially in the case of high metal loading. The hydroxyl radicals are produced from the interaction of H_2O_2 with the catalyst. The reaction occurs similar to Fenton chemistry, through the participation of hydroxyl radical in the activating benzene toward the formation of phenol. Increasing the reaction time increased the concentration of phenol in the system; and then, phenol could be further oxidized to other byproducts (benzoquinone, hydroquinone and catechol) at higher reaction time, resulting in the decrease of the phenol concentration [11]. According to the above results, the reaction time of 4 h will be used in the subsequent studies. It should be noted that acetonitrile, which was employed as a solvent in this study, is not an inert solvent as reported by the study of Stockmann et al. [21]. Our preliminary blank test without benzene indicated that there were many products detected. However, fortunately, the phenol product was not obtained in the blank test without benzene as a reactant. Due to the great variety of byproducts from the reaction system, the quantitative analysis of the byproducts was not determined in this study.

Effect of percent loading of the second metal and the third metal

The mixed metal oxides with different ratios of metal supported on TiO_2 were tested in this work. The results summarized in Table 3 revealed that within the studied

ranges of percent loading of V and Cu, the multi metal oxide catalysts were more active for the hydroxylation of benzene to phenol than the Fe/TiO_2 although the increase of the percent loading of second metal and third metal decreased the BET surface area and pore volume particularly at high values of metal loading.

When Cu or V was loaded on the catalysts as in the cases of binary metal oxide catalysts ($Fe_5Cu_{2.5}/TiO_2$ and $Fe_5V_{2.5}/TiO_2$), the presence of the second metal significantly improved the conversion and TOF as reported in the previous work [11]. However, lower selectivity was observed for the case with Cu addition. The use of the second metal significantly improved the yield of phenol from 1.2% (Fe_5/TiO_2) to 5.96% ($Fe_5Cu_{2.5}/TiO_2$) and 6.31% ($Fe_5V_{2.5}/TiO_2$). When the third metal was loaded in the catalyst ($Fe_5V_{2.5}Cu_{2.5}/TiO_2$), the yield of phenol could be improved to 7.15% but the TOF was slightly lowered.

The effect of percent loading of second and third metal oxides was investigated. Both the percent metal loadings of V and Cu in the catalyst were at the same value for all catalysts. The percent loading of metal oxides obviously influenced the yield of phenol and TOF. The increase of the V and Cu loadings improved the benzene conversion; however, the phenol selectivity and TOF significantly reduced. The decrease of TOF at high metal loading could be due to the reduction of dispersion of the catalyst metal. The optimum percent loading of V and Cu which offered the highest phenol yield was 2.5 wt% ($Fe_5V_{2.5}Cu_{2.5}/TiO_2$) giving a phenol selectivity of more than 70%. The improved yield of phenol by the increase of metal loading was mainly contributed by the increase in the conversion. It is noted that the amounts of metal oxides in the catalysts have the effect on decomposition of H_2O_2 to hydroxyl radical and consequently the reactions taking place in the system.

Effect of the amount of catalyst

The effect of the amount of the catalyst was shown in Figure 3. It was found that increasing the amount of catalyst improved the conversion and phenol yield up to 0.5 g. However, further increasing of the amount of catalyst to 1 g decreased the yield of phenol for high V-Cu content, because increasing the amount of catalyst also increased the side reaction of phenol to other products.

The amount of catalyst had the effect on decomposition of H_2O_2 by Fenton reaction [11-12].

$$Fe(II) + H_2O_2 \longrightarrow Fe(III) + OH^{o} + OH^{-} \qquad (1)$$

The increased amounts of catalyst increased the amount of hydroxyl radical in the reaction which is necessary for the oxidation reaction of benzene to produce cyclohexadienyl (CHD) radical as follows.

$$OH^{o} + \text{benzene} \longrightarrow CHD \qquad (2)$$

$$CHD + Fe(III) \longrightarrow \text{phenol} + Fe(II) + H^{+} \qquad (3)$$

Although, the hydroxyl radical was very important for production of phenol, excessive hydroxyl radical can react with phenol to byproducts. In the selective oxidation of benzene to phenol, it is therefore essential to control the amount of hydroxyl radical per reactant.

Effect of the ratio of H_2O_2/benzene

As shown in Figure 4, it was found that the yield of phenol initially increased, leveled off and then decreased with the increase in the oxidant/benzene mole ratio. In the study, the volume of benzene remained constant while that of H_2O_2 changed. The conversion of benzene increased with the increased ratio of H_2O_2/benzene but the selectivity of phenol decreased because the amount of H_2O_2 influenced the amount of hydroxyl radical to react with benzene to hydroquinone, cresol and benzoquinone (not shown). The best value was observed at the ratio of H_2O_2/benzene of about 2 for all catalysts.

The use of high amount of H_2O_2 resulted in high amount of hydroxyl radical in the reaction. It increased the conversion and yield of phenol but excessive H_2O_2 caused a problem on further oxidation of phenol to byproducts.

Effect of the amount of ascorbic acid

Figure 5 shows the influence of the amount of ascorbic acid on the catalytic performance during the hydroxylation of benzene. The ascorbic acid is well known as a good reducing agent. It changes the state of metal catalyst from Fe(III) to Fe(II) or V(V) to V(IV) and Cu(II) to Cu(I) [8, 10-12]. The yield of phenol increased with the increase in the amount of ascorbic acid, but the use of large amount of ascorbic acid tended to inversely decrease the yield of phenol for all catalysts. The excessive amount of ascorbic acid promoted the decomposition of H_2O_2, resulting in higher amount of hydroxyl radical and consequently higher possibility for further oxidation of phenol to other byproducts.

In the cases of Cu and V, the formation of phenol proceeded through the similar mechanism as that of Fenton chemistry by replacing the redox of Fe(III)/Fe(II) to that of Cu(II)/Cu(I) as well as V(V)/V(IV). In the three phase reaction system, the reaction occurs in the aqueous polar phase. The catalyst-reducing agent is actually dissolved only in the water rich phase.

$$2\ Fe(III) + \text{ascorbic acid} + 0.5\ O_2 \longrightarrow 2\ Fe(II) + \text{Dehydroascorbic acid} + H_2O \quad (4)$$

$$2\ Fe(II) + O_2 + 2H^+ \longrightarrow 2Fe(III) + H_2O_2 \quad (5)$$

$$Fe(III) + H_2O_2 + H^+ \longrightarrow Fe(II) + OH^{o} + H_2O \quad (6)$$

Conclusion

The phenol synthesis from benzene and H_2O_2 catalyzed by FeVCu/TiO_2 with different values of metal loading was investigated. $Fe_5V_{2.5}Cu_{2.5}$ catalyst was found to offer the highest yield. The increase of the percent loading of the second metal and third metal improved the yield of phenol; however, the TOF decreased probably due to the lowering of dispersion of the catalyst samples at high values of metal loading. It was observed that the quantity of second and third metals also influenced the acid properties of the catalyst. The optimum condition for the system is: a reaction time of 4 h, catalyst weight of 0.2 g, the H_2O_2: benzene molar ratio of 2 and 6.25 g of ascorbic acid per mole of benzene.

Acknowledgements

Financial supports from the Thailand Research Fund and Commission on Higher Education are gratefully acknowledged.

References

[1] J. S. Choi, T. H. Kim, M. B. Saidutta, J. S. Sung, K. I. Kim, R. V. Jasra, S. D. Song, Y. W. Rhee, *J. Ind. Eng. Chem.*, **10**, 445 (2004).

[2] L. V. Pirutko, A. K. Uriarte, V. S. Chernyavsky, A. S. Kharitonov, G. I. Panov, *Micropo& Mesopo Mater.*, **48,** 345 (2001).

[3] T. Mizuno, H. Yamada, T. Tagawa, S. Goto, *J. Chem. Eng. Japan*, **38,** 849 (2005).

[4] D. Bianchi, M. Bertoli, R. Tassinari, M. Ricci, R. Vignola, *J. Mol. Catal. A.*, **200**, 111 (2003).

[5] A. Germain, M. Allian, F. Figueras, *Catal. Today*, **32**, 145 (1996).

[6] B. Chou, J. L. Tsai, S. Cheng**,** *Micropo& Mesopo Mater.***, 48,** 309 (2001).

[7] Y. K. Masumoto, R. Hamada, K. Yokota, S. Nishiyama, S. Tsuruya, *J. Mol. Catal. A.*, **184**, 215 (2002).

[8] T. Miyahara, H. Kanzaki, R. Hamada, S. Kuroiwa, S. Nishiyama, S. Tsuruya, *J. Mol. Catal. A.*, **176**, 141 (2001).

[9] H. Kanzaki, T. Kitamura, R. Hamada, S. Nishiyama, S. Tsuruya, *J. Mol. Catal. A.*, **208,** 203 (2004).

[10] X. Gao, J. Xu, *Appl. Clay Sci.*, **33**, 1 (2006).

[11] G. Tanarungsun, W. Kiatkittipon, S. Assabumrungrat, H. Yamada, T. Tagawa, P. Prasertdam, *J. Chem. Eng. Japan*, **40,** 415 (2007).

[12] G. Tanarungsun, W. Kiatkittipon, S. Assabumrungrat, H. Yamada, T. Tagawa, P. Prasertdam, *J. Ind. Eng. Chem.*, **13**, 444 (2007).

[13] G. Tanarungsun, W. Kiatkittipon, S. Assabumrungrat, H. Yamada, T. Tagawa, P. Prasertdam, *J. Ind. Eng. Chem.*, **13**, 870 (2007).

[14] K. Teramura, T. Tanaka, T. Hosokawa, T. Ohuchi, M. Kani, T. Funabiki, *Catal. Today.*, **96**, 205 (2004).

[15] V. Parvulescu, B.L. Su, *Catal. Today.*, **69**, 315 (2001).

[16] J. Okamura, S. Nishiyama, S. Tsuruya, M. Masai, *J. Mol. Catal. A*, **135**, 133 (1998).

[17] Y. Y. Gu, X. H. Zhao, G. R. Zhang, H. M. Ding and Y. K. Shan, *Appl. Catal A.*, **328**, 10, 150 (2007)

[18] J. S. Choi, T. H. Kim, K. Y. Choo, J. S. Sung, M.B. Saidutta, S. O. Ryu, S. D. Song, B. Ramachandra and Y. W. Rhee*, Appl. Catal A.*, **290**, 1 (2005)

[19] Y.J. Seo, Y. Mukai, T. Tagawa, S. Goto, *J. Mol. Catal. A*, **120**, 149 (1997).

[20] J.Zhang, Y. Tang, G. Li, C. Hu, *Appl. Catal. A*., **278**, 251 (2005).

[21] M. Stockmann, F. Konietzni, J.U. Notheis, *Appl. Catal. A.*, **208**, 343 (2001).

Table 1 Materials and chemicals.

Metal source	Iron (III) acetylacetonate 97% (Aldrich)
	Cupric (II) nitrate 99% (SIGMA)
	Ammonium metavanadate (V) 99.5% (Carlo Erba reagenti)
Support	TiO_2 (JRC-TIO1) (Catalysis Society of Japan)
Solvent	Acetonitrile 99.8% (MERCK)
Reducing agent	Ascorbic acid 99.7% (Polskic Odczynniki Chemiczne S.A.)
Substrate	Benzene 99.7% (MERCK)
Oxidant	Hydrogen peroxide 30% wt. (MERCK)
Byproduct reference	Biphenyl 99.9% (Fluka)
	Catechol 98% (Fluka)
	Phenol 99% (Panreac Sintesis)
	Quinol 99.8% (APS)
	1,4 Benzoquinone 98% (ACROS)

Table 2 Summary of metal loading determined by SEM-EDX and XRF.

	Metal loading by SEM-EDX (wt%)			**Metal loading by XRF (wt%)**		
Catalyst	**Fe**	**V**	**Cu**	**Fe**	**V**	**Cu**
1. Fe_5/TiO_2	4.36	-	-	4.59	-	-
2. $Fe_5V_1Cu_1/TiO_2$	5.87	1.84	2.51	4.31	1.43	0.65
3. $Fe_5V_{2.5}Cu_{2.5}/TiO_2$	4.31	2.39	2.11	4.2	2.65	1.95
4. $Fe_5V_5Cu_5/TiO_2$	3.66	6.83	3.17	4.29	8.55	3.01
5. $Fe_5V_{10}Cu_{10}/TiO_2$	3.68	8.73	3.47	3.97	13.44	6.49

Table 3 Experimental results of hydroxylation of benzene to phenol using different catalysts.

Catalyst	Conversion (%)	Selectivity (%)	Yield (%)	TOF (h^{-1})	BET (m^2/g)	Pore volume (cm^3/g)
1. Fe_5/TiO_2	1.5	80	1.20	2.68	69.3	0.26
2. $Fe_5Cu_{2.5}/TiO_2$	8.4	71	5.964	9.25	62.8	0.24
3. $Fe_5V_{2.5}/TiO_2$	7.6	83	6.308	9.11	55.3	0.21
4. $Fe_5V_1Cu_1/TiO_2$	6.6	85	5.61	8.98	66.2	0.23
5. $Fe_5V_{2.5}Cu_{2.5}/TiO_2$	9.8	73	7.154	8.04	65.9	0.22
6. $Fe_5V_5Cu_5/TiO_2$	11.7	61	7.137	5.36	42.1	0.17
7. $Fe_5V_{10}Cu_{10}/TiO_2$	14.8	49	7.252	3.27	39.6	0.16

(Benzene = 11 cm^3; catalyst weight = 0.2 g; benzene/H_2O_2 mole ratio = 0.5; acetonitrile solvent 40 cm^3; temperature = 303 K; pressure = 1 atm; reaction time = 4 h)

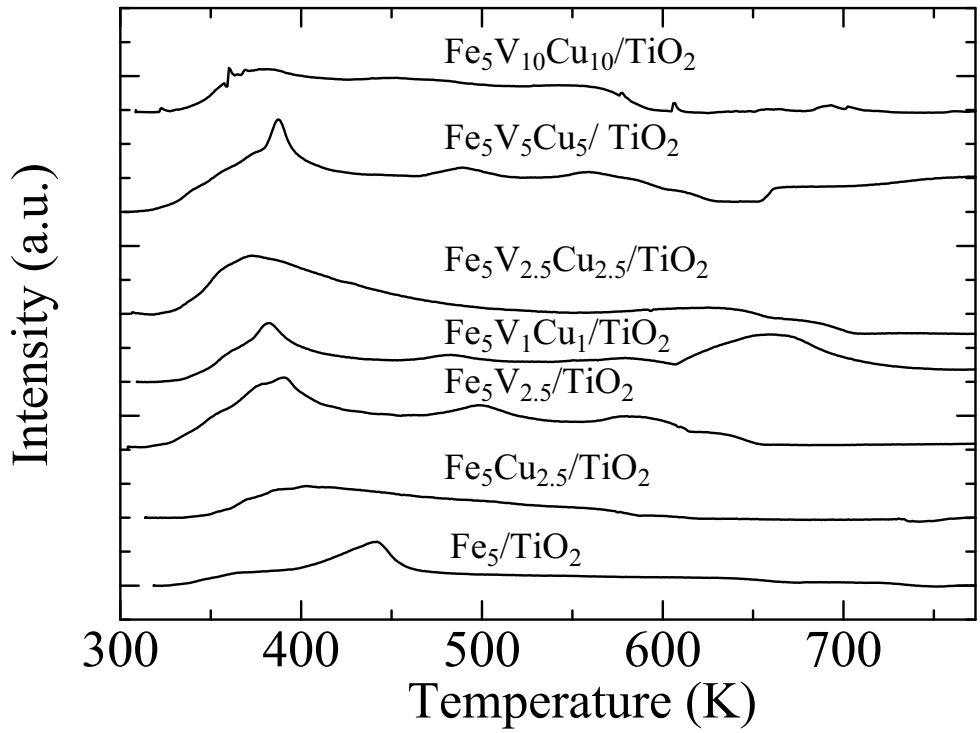

Figure 1 NH_3-TPD of different ternary metal oxide catalysts.

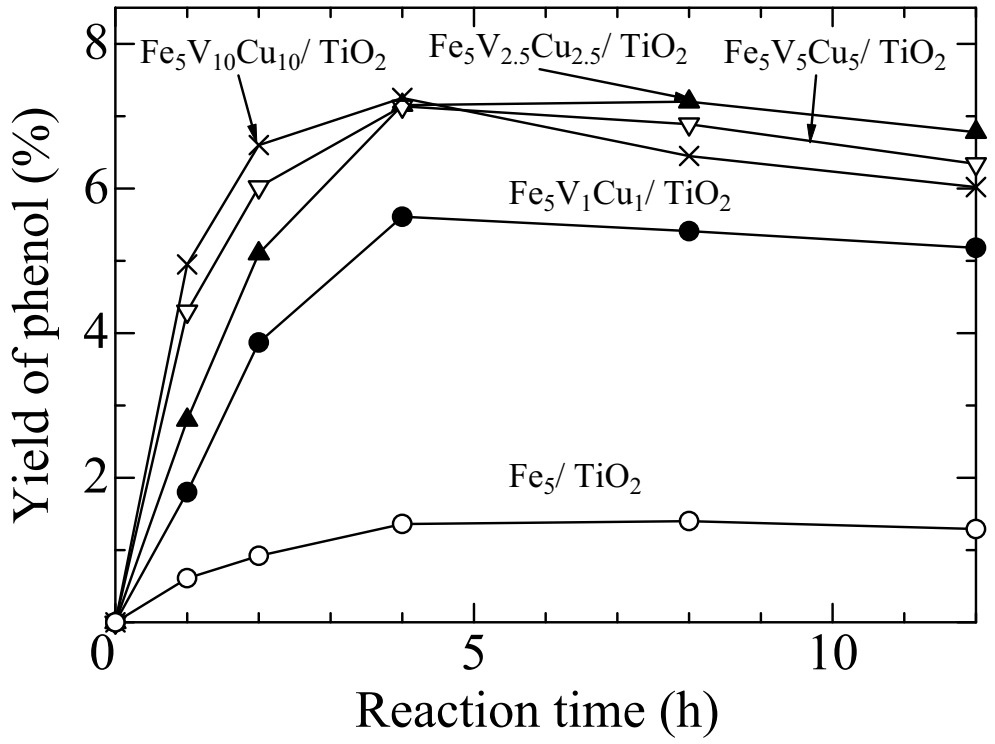

Figure 2 Influence of reaction time on yield of phenol.

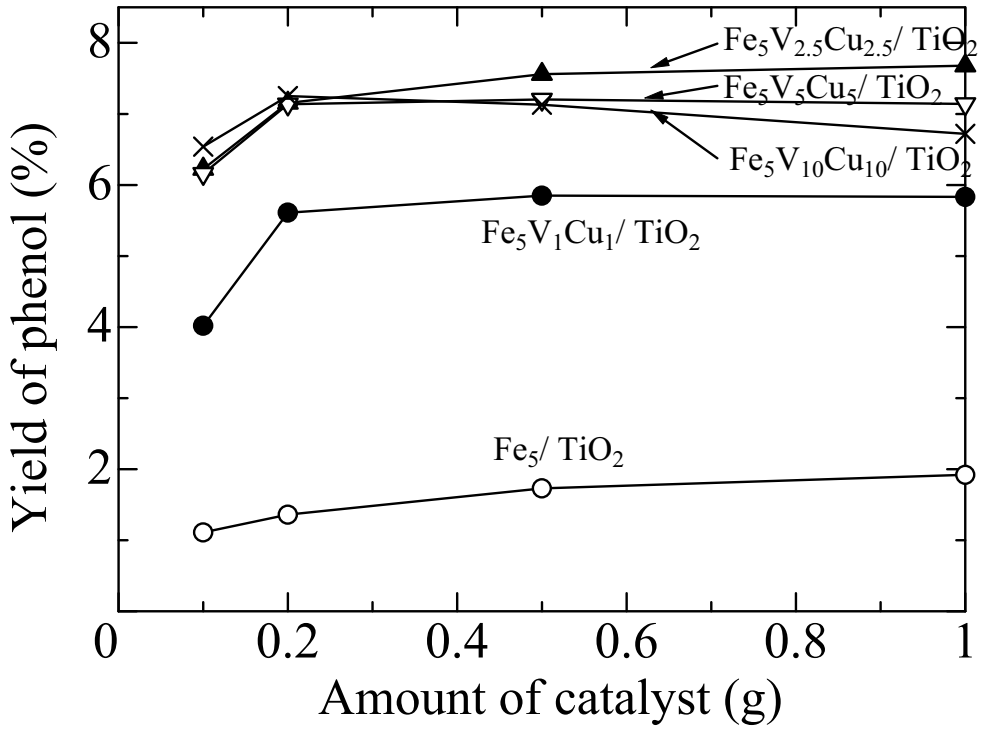

Figure 3 Influence of the amount of catalyst on yield of phenol.

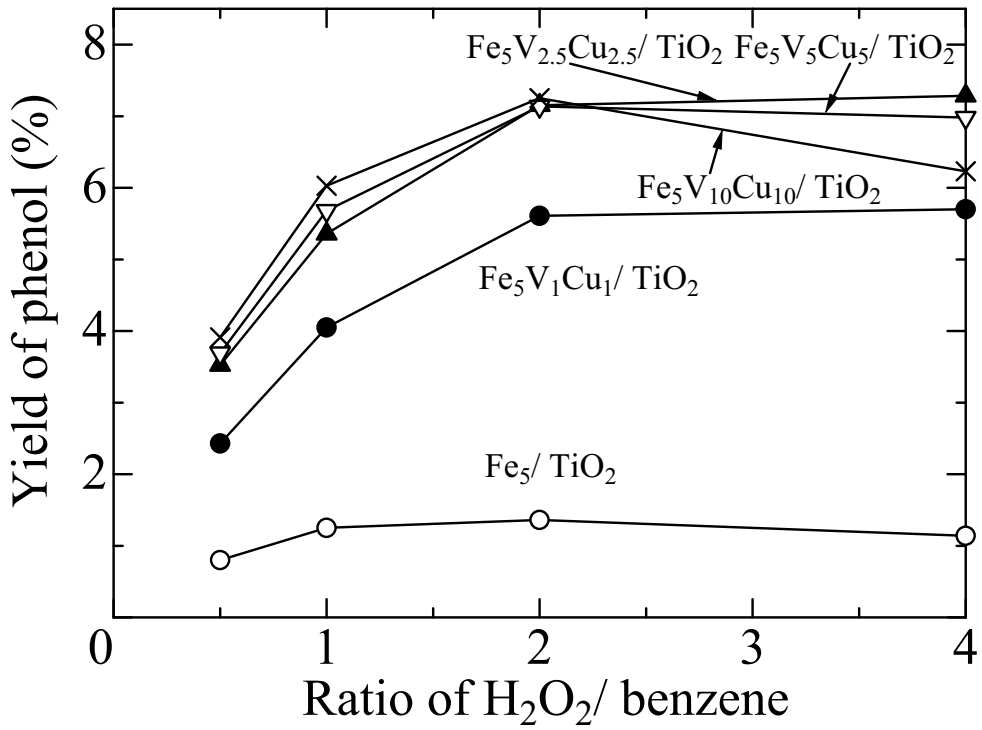

Figure 4 Influence of ratio of H_2O_2/benzene on yield of phenol.

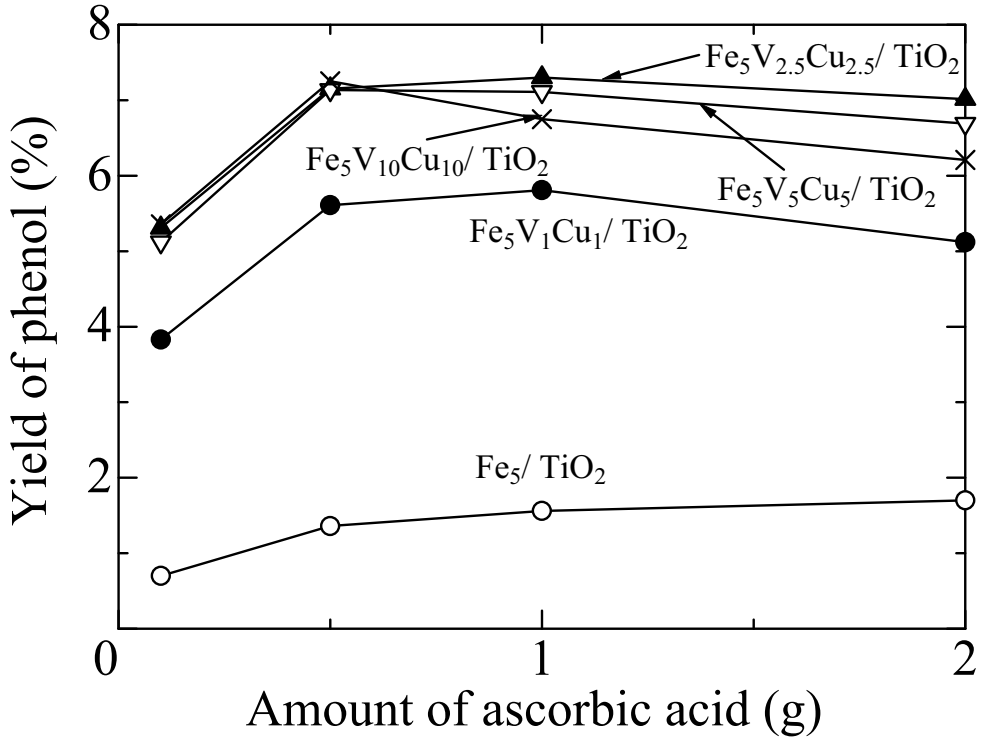

Figure 5 Influence of the amount of ascorbic acid on yield of phenol.

Appendix 17

Korean J. Chem. Eng., **24**(1), - (2007)

Carbon dioxide reforming of methane under periodic operation

Eakkapon Promaros, Suttichai Assabumrungrat†, Navadol Laosiripojana*, Piyasan Praserthdam, Tomohiko Tagawa and Shigeo Goto****

Center of Excellence in Catalysis and Catalytic Reaction Engineering, Department of Chemical Engineering, Faculty of Engineering, Chulalongkorn University, Bangkok 10330, Thailand
*The Joint Graduate School of Energy and Environment, King Mongkut's University of Technology Thonburi, Bangkok, 10140, Thailand
**Department of Chemical Engineering, Nagoya University, Chikusa, Nagoya, 464-8603, Japan
(*Received 30 May 2006 • accepted 28 August 2006*)

Abstract–The carbon dioxide reforming of methane under periodic operation over a commercial $Ni/SiO_2 \cdot MgO$ catalyst was investigated at two different temperatures, 923 and 1,023 K. According to this operation, pure methane and carbon dioxide were alternately fed to the catalyst bed where methane cracking and the reverse Boudouard reaction took place, respectively. Therefore, hydrogen and carbon monoxide products appeared separately in different product streams. The performance of this operation was compared to that of the steady state operation with simultaneous feed of both carbon dioxide and methane. At 1,023 K, the methane conversion and hydrogen yield from the periodic operation initially decreased with time on stream and eventually leveled off at values about half of those obtained in the steady state operation with co-feed of both reactants. The decreased catalytic activity was due to the accumulation of carbonaceous deposit and loss of metal active sites. However, a different trend was observed at 923 K. The methane conversion and hydrogen yield were almost constant over the time on stream, although more carbonaceous deposit was progressively accumulated on the catalyst bed during the reaction course. At this temperature, the periodic operation offered the equivalent hydrogen yield to the steady state operation. The observed behavior could be due to the different mechanisms of carbon formation over the catalyst. Finally, it was found that cycle period and cycle split did not influence the reaction performance within the ranges of this study.

Key words: Periodic Operation, Dry Reforming, Methane, Nickel Catalyst, Hydrogen

INTRODUCTION

Carbon dioxide reforming of methane is an effective way to produce synthesis gas and to utilize green house gases simultaneously. The reaction produces synthesis gas with low H_2/CO ratio, which is suitable for producing valuable chemicals such as alcohol, aldehyde and isobutene. Several supported transition metal catalysts (Ni, Ru, Rh, Pd, etc.) have been used for the carbon dioxide reforming of methane [Gadalla et al., 1988; Rostrup-Nielsen et al., 1993; Inui et al., 1997]. Nickel is well-known as an active catalyst for this highly endothermic reaction and mainly used in industry due to its low cost. A typical problem found for this reaction is catalyst deactivation due to the carbonaceous deposition, which is mainly generated from the following catalytic cracking of methane [Kim et al., 2003].

$$CH_4 \rightarrow C + 2\,H_2 \quad (1)$$

However, the presence of carbon dioxide theoretically helps the removal of deposited carbon according to the following reverse Boudouard reaction [Takano et al., 1996].

$$C + CO_2 \rightarrow 2CO \quad (2)$$

According to the above reactions, the carbon dioxide reforming of methane [Eq. (3)] can be operated periodically by feeding methane and carbon dioxide alternately.

$$CH_4 + CO_2 \rightarrow 2CO + 2\,H_2 \quad (3)$$

Under periodic operation, hydrogen and carbon monoxide are generated at different time, and therefore, these products can be directly separated without additional significant effort. This operation is attractive particularly in the case when carbon monoxide-free hydrogen is required for some applications as in a proton-exchange membrane (PEM) fuel cell. The periodic operation for this reaction is conceptually attractive; however, there is still no effort to demonstrate experimentally the benefit of the operation.

Although researches focusing on the use of carbon dioxide for removing deposited coke on catalysts are not widely performed, the uses of oxygen and/or steam are more common. It was reported that both oxidation with oxygen, and steam gasification could restore the catalytic activity of Ni-based catalyst after deactivation due to carbon formation [Zhang, and Amiridis, 1998]. In previous studies, Ni/SiO_2 catalyst could be fully regenerated at 923 K with steam for up to 10 successive cracking/regeneration cycles without any significant loss of catalytic activity [Aiello et al., 2000]. While the hydrogen production from cracking of methane over Ni guaze catalyst [Monnerat et al., 2001] could be optimized by operating reaction periodically with the catalyst regeneration in oxygen atmosphere under suitable period and cycle split. Moreover, the Ni/Al_2O_3 showed more activity with low carbonaceous deposition, by repeating many cracking/regeneration cycle (D-R treatment) [Ito et al., 1999] with carbon dioxide before using in reforming reaction.

†To whom correspondence should be addressed.
E-mail: suttichai.a@chula.ac.th

In this work, the periodic operation for the carbon dioxide reforming of methane was investigated. The operation involved two steps of 1) methane decomposition reaction and 2) catalyst regeneration via oxidation in carbon dioxide mixture of the deposited coke. The effects of operating variables of periodic operation such as operating temperature, cycle period (τ) and cycle split (s) on conversions of methane and carbon dioxide, and yield of hydrogen are investigated and compared to the results from steady state operation with simultaneous feed of both carbon dioxide and methane.

EXPERIMENTAL

1. Reaction Procedure

An industrial steam reforming catalyst, $Ni/SiO_2 \cdot MgO$, containing 55 wt% of nickel with surface area of 1.23×10^5 m^2/kg and nickel diameter of 44 nm was employed for the carbon dioxide reforming of methane in this research. A schematic diagram of the experimental setup, as shown in Fig. 1, consists of a gas feeding section, a fixed-bed reactor and an analytical section. High purity methane (99.999%) and carbon dioxide (99.999%) were used as the reactant gases. The feed was switched periodically between opening and closing by Solenoid valve (Flon industry, Japan), which was controlled by an on-off timer (Sibata BT-3). Argon was used for purging the system, and hydrogen was used for reducing catalyst before the experiment.

The reaction was carried out in a quartz tube fixed-bed reactor (internal diameter=0.011 m, length=0.5 m) heated by a temperature controlled electric oven. A thermocouple was placed in the furnace, at the level of the catalyst bed, to monitor temperature. A U-tube manometer, which was filled with silicone oil was positioned at the entrance of the reactor for indication of the pressure drop in the reactor, could be used as an emergency pressure relief valve. Experiments were performed using 0.3 g of $Ni/SiO_2 \cdot MgO$ catalyst, diluted with silicon carbide (1.0 g). The catalyst was reduced in a hydrogen flow (5×10^{-7} m^3/s) at 923 K for 1 h before use. The reaction was conducted at atmospheric pressure. The reactor effluent from periodic operation experiments was collected by a sample bag at the exit of the reactor. The sample product gas was analyzed with a TCD gas chromatograph (Schimadzu GC-8A, Japan) equipped with a Porapak-Q and Molecular Sieve 5A column. Argon was used as the carrier gas in the gas chromatograph with the flow rate of 0.5×10^{-6} m^3/s.

2. Catalyst Characterization

Spent catalyst from the deactivation and regeneration experiments was studied with a JEOL JSM-35CF scanning electron microscopy (SEM) that was operated by using the back scattering electron (BSE) mode at 15 kV. The XRD spectra of fresh and spent catalysts were measured by a SIEMENS D5000 X-ray diffractometer using Cu Kα radiation with an Ni filter in the 10-80° 2-θ angular region.

RESULTS AND DISCUSSION

1. Characteristics of Carbon Dioxide Reforming of Methane Under Periodic Operation

The behavior of the carbon dioxide reforming of methane under periodic operation was first investigated. In the first step, the catalytic cracking of methane [Eq. (1)] was carried out by feeding pure methane (4.167×10^{-7} m^3/s) to the catalyst bed operated at 1,023 K to determine the catalyst activity along time on stream of methane for 225 min. The methane conversion of $Ni/SiO_2 \cdot MgO$ was approximately 73% at the beginning and declined rapidly to about 50% within 25 min, Fig. 2. Then the conversion decreased to 15% after 50 min of reaction and fell slightly until the end of reaction. The U-tube pressure manometer indicated stable pressure drop in the first period of reaction. However, after 20 min, the pressure drop increased gradually until reaching a plateau in about 50 min of time on stream. It was revealed from the results that catalyst loses its activity due to carbonaceous deposition on the catalyst according to the methane cracking reaction, resulting in lowering conversion and increasing pressure drop within about 20 min.

After testing the catalytic activity of the methane cracking, we performed catalyst regeneration with carbon dioxide at the same operating temperature to investigate the time to restore spent catalyst. In this experiment, a spent catalyst after exposure in methane cracking for 25 min was used to prevent complete deactivation with coke formation. Significant amount of coke was accumulated in the catalyst bed after the methane cracking (not shown). The catalyst regeneration was performed by feeding pure carbon dioxide

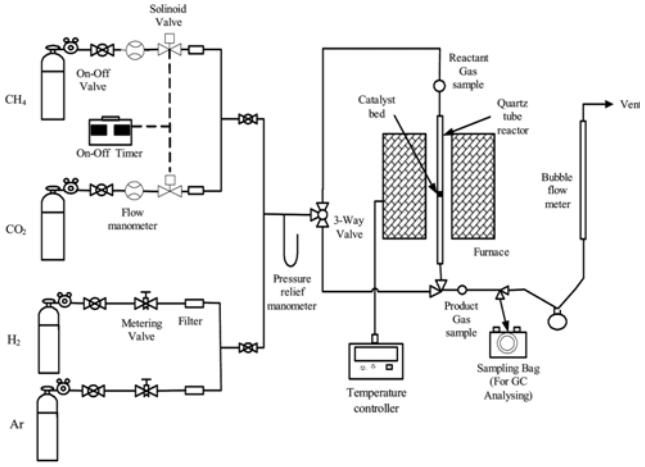

Fig. 1. Schematic diagram of the experimental setup for carbon dioxide reforming of methane under periodic operation.

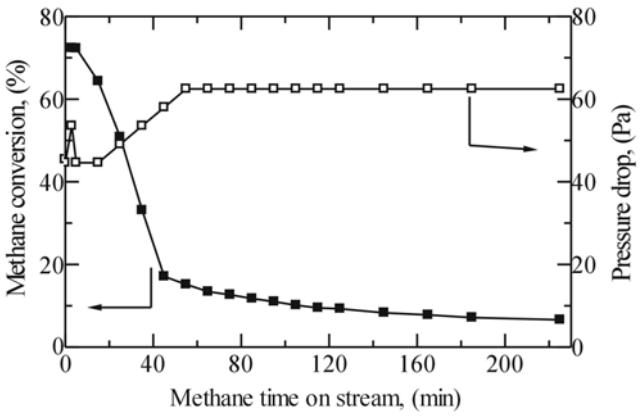

Fig. 2. Changes in catalytic activity and pressure drop of the catalytic cracking of methane over $Ni/SiO_2 \cdot MgO$ (T=1,023 K and methane flow rate=4.167×10^{-7} m^3/s).

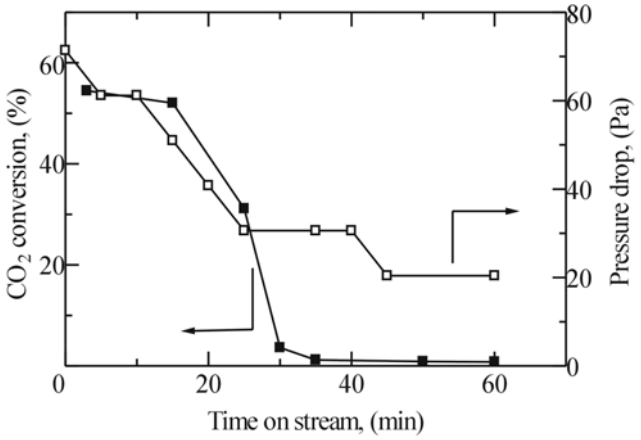

Fig. 3. Changes in CO_2 conversion and pressure drop over spent Ni/SiO_2·MgO catalyst after 25 min of methane cracking (T= 1,023 K and CO_2 flow rate=4.167×10^{-7} m^3/s).

(4.167×10^{-7} m^3/s) to the catalyst bed. Only carbon monoxide was detected as a main product according to the reverse Boudouard reaction [Eq. (2)].

Fig. 3 shows that the conversion of carbon dioxide was stable at about 54% for 20 min and then decreased steeply to about 3% after 30 min of time on stream of CO_2. Pressure drop decreased gradually from 60 Pa to 30 Pa in about 25 min, and declined slightly until the feed was stopped. It is expected that most of deposited coke could be removed from the spent catalyst within about 20 min of the regeneration step by reacting with carbon dioxide. From the above results, further studies were performed using a cracking period not to exceed 20 min for preventing complete deactivation of catalyst. Moreover, the regeneration period with carbon dioxide was not kept longer than 20 min to allow efficient utilization of carbon dioxide.

2. Performance Comparison of Carbon Dioxide Reforming of Methane Under Periodic and Steady State Operations

Performance comparison was considered for two cases of interest: steady state operation and periodic operation. All experiments were conducted at 1,023 K, atmospheric pressure and total reaction time of 200 min. For the steady state operation, a mixture of methane (2.083×10^{-7} m^3/s) and carbon dioxide (2.083×10^{-7} m^3/s) was allowed to flow through the catalyst bed in the reactor, whereas the periodic operation experiments were performed using a constant cycle split (s) of 0.5 and the flow rate of each reactant was kept at (4.167×10^{-7} m^3/s). The cycle split is defined as the duration of the cracking period divided by the duration of the cycle period (τ). In this study the cycle period (τ) was varied from 40 min (5 cycles) to 20 min (10 cycles), and 10 min (20 cycles). It should be noted that the time-average feed flow rates were equivalent in all experiments; therefore, the performance comparison was based on the same average feed rate or time on stream. Fig. 4 shows the profiles of methane conversion with time on stream for both steady state and periodic operations. It should be noted that the methane conversion of the periodic operation was time-average conversion calculated from average composition of gas product collected after the end of each cracking/regeneration cycle. It was found that the steady state operation offered a stable methane conversion at 90%, indicating no significant deactivation at least within 200 min of time on stream. In contrast, the periodic operation showed an initial conversion of about 80% which was around 10% lower than that of the steady state operation. The conversion further decreased and became stable after approximately 160 min of time on stream. It is obvious that the methane conversion from the periodic operation was inferior to that of the steady state operation over all ranges of reaction time.

The profiles of carbon dioxide conversion with time on stream are shown in Fig. 5. Similar to the previous results, the carbon dioxide conversion from the steady state operation (85%) did not change with time on stream, whereas the carbon dioxide conversion from the periodic operation decreased with increasing repeating cracking/regeneration cycles and then leveled off at high reaction cycles. However, after 160 min of time on stream the rates of coke formation and the coke removal seemed to be equivalent as the conversions of methane and carbon dioxide became nearly the same at around 40%; consequently, the conversions for both reactants no longer changed with reaction time. The profiles of hydrogen yield are shown in Fig. 6.

Clearly, periodic operation offered much lower hydrogen yield

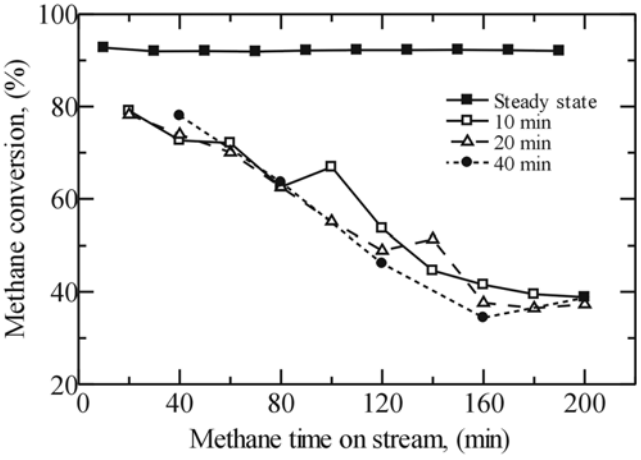

Fig. 4. Comparison of methane conversion between steady state operation and periodic operation at different cycle periods over Ni/SiO_2·MgO catalyst (T=1,023 K).

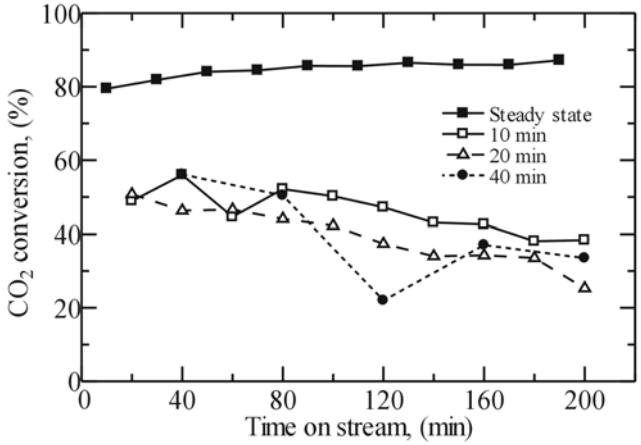

Fig. 5. Comparison of CO_2 conversion between steady state operation and periodic operation at different cycle periods over Ni/SiO_2·MgO catalyst (T=1,023 K).

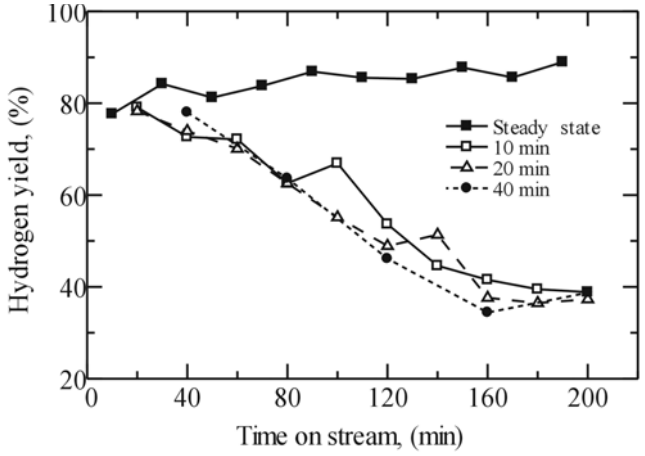

Fig. 6. Comparison of hydrogen yield between steady state operation and periodic operation at different cycle periods over Ni/SiO_2·MgO catalyst (T=1,023 K).

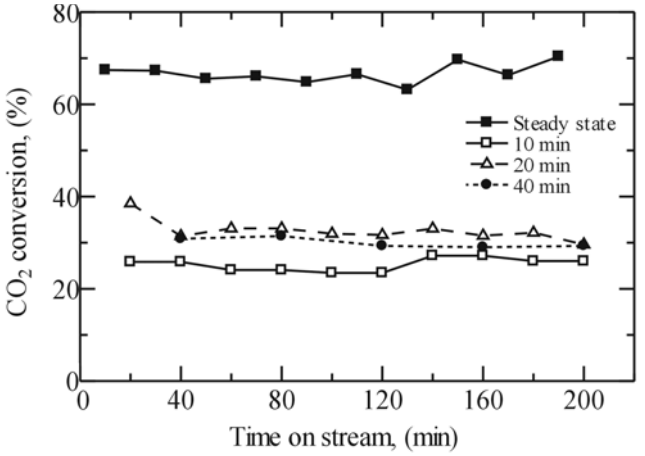

Fig. 8. Comparison of CO_2 conversion between steady state operation and periodic operation at different cycle periods over Ni/SiO_2·MgO catalyst (T=923 K).

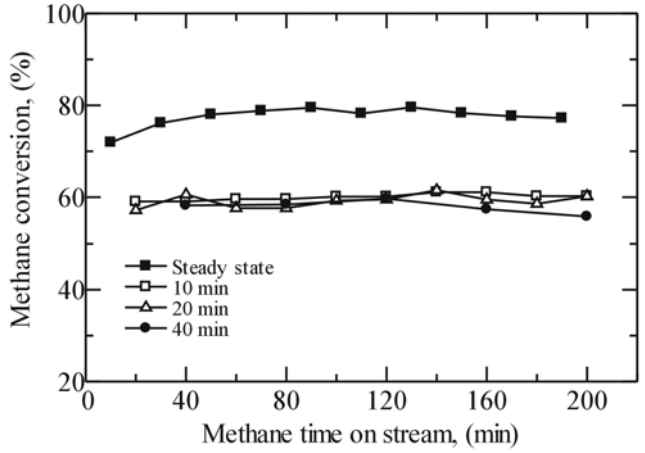

Fig. 7. Comparison of methane conversion between steady state operation and periodic operation at different cycle periods over Ni/SiO_2·MgO catalyst (T=923 K).

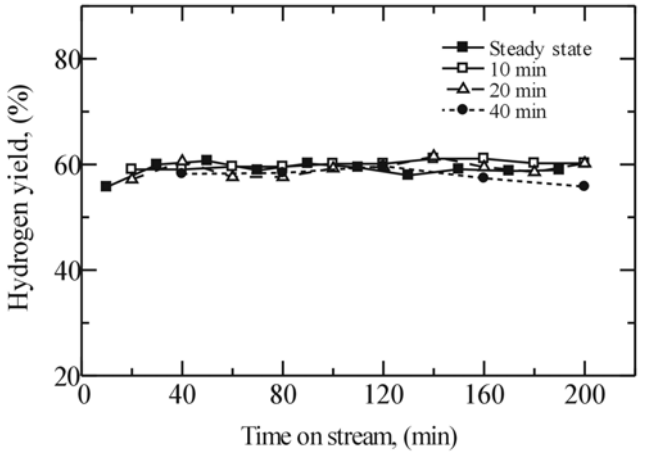

Fig. 9. Comparison of hydrogen yield between steady state operation and periodic operation at different periods over Ni/SiO_2·MgO catalyst (T=923 K).

than steady state operation. The experimental results at different cycle periods (τ=40, 20 and 10 min) indicate that the cycle period does not pronouncedly affect the reaction performance, Figs. 4-6. At higher cycle period, although the catalyst highly deactivated due to the formation of coke during the methane cracking step, more coke can be removed during the regeneration step. Therefore, the average reaction performance does not change significantly.

Another set of experiments was performed using operating conditions similar to the previous study, except that the temperature was changed from 1,023 K to 923 K. Figs. 7, 8 and 9 show the profiles of methane conversion, carbon dioxide conversion and hydrogen yield with time on stream at 923 K, respectively. The result indicates that for the steady state operation, the methane conversion at 923 K was also stable but the activity is about 10% lower than that at 1,023 K. This should be due to the lower reaction rate and less thermodynamic feasibility at lower temperature. For the periodic operation it was found that the methane conversion at 923 K was also stable at approximately 60% and independent of the cycle period. However, unlike the operation at 1,023 K, no indication of activity loss was detected at this operating temperature.

The profiles of carbon dioxide conversion with time on stream for both steady state and periodic operation at 923 K (Fig. 8) also show stable conversions at approximately 70% and 25-30%, respectively. Considering the obtained hydrogen yield (Fig. 9), it was found that the periodic operation provided hydrogen yield as high as that of the steady state operation, indicating equivalent performance of periodic operation at 923 K. Based on these results, the periodic operation seemed to become an attractive operation mode at 923 K regarding the equivalent hydrogen yield and stable performance as well as the capability to separate product streams of hydrogen and carbon monoxide.

According to the measurement of carbon deposition on the catalyst surface after exposure in the periodic operation at 923 K by comparing the conversions of methane and carbon dioxide, the results surprisingly indicate that more coke was further accumulated in the catalyst bed after each cracking/regeneration cycle. The unusual stable reaction activity throughout the reaction course at 923 K, which was in contrast to the behavior at 1,023 K reported earlier, was then

further investigated. Scanning electron microscopy (SEM) technique was used to observe the differences between catalyst samples that were subjected to 10 cracking/regeneration cycles (τ=20 min) with reaction temperature 923 K and 1,023 K, as well as a fresh catalyst sample. Both micrographs of the spent catalysts at 923 K (Fig. 10d) and 1,023 K (Fig. 10c) show the surface to be covered with filamentous carbon, in contrast to the clean surfaces of fresh catalyst (Figs. 10a and 10b).

In order to understand this dissimilar behavior, an X-ray diffraction technique was chosen to identify the crystal structure of Ni metallic and other metal forms on the catalysts. The characterizations were performed for the spent catalysts obtained after the periodic operation experiments at 923 K (τ=10 and 20 min) and 1,023 K (τ=10 min) with the cycle split (s) of 0.5. Measurements of the fresh catalyst and the spent catalyst after the steady-state operation at 923 and 1,023 K were also carried out for comparison. The XRD patterns, shown in Fig. 11, indicate that nickel contained in the fresh catalyst has crystal structure of NiO (peaks at 2θ=37.1, 43.1 and 62.7), which would be reduced with hydrogen to convert nickel oxide into the metallic nickel before the reaction is started. It also shows that the presence of carbon of graphitic nature, evident from the strong peak at 2θ=26, was accumulated in the fresh catalyst sample as well as carbon accumulated in the spent catalysts. Considering the spent catalyst from the periodic experiment with a cycle period (τ) of 20 min at 1,023 K, the strong peaks of Ni metallic crystallites at 2θ=44.5, 51.8, and 76.4 were observed with only small intensity of NiO peaks. It was presumed that NiO in the fresh catalyst could be completely reduced to metallic form after pre-reduction step. For the spent catalysts at lower temperature (923 K), the XRD patterns of the spent catalysts with τ=10 and 20 min indicated the existence of NiO peaks with lower Ni metallic intensity. It was suggested that NiO could be formed during the cracking/regeneration period and considered to be the active components for cracking period at 923 K. The XRD patterns of the spent catalysts from the steady-state operation for both temperature levels also indicate results similar to those of the periodic operation. Therefore, it is evident that the metal active sites involved in the reaction are in different form depending on the operating temperature.

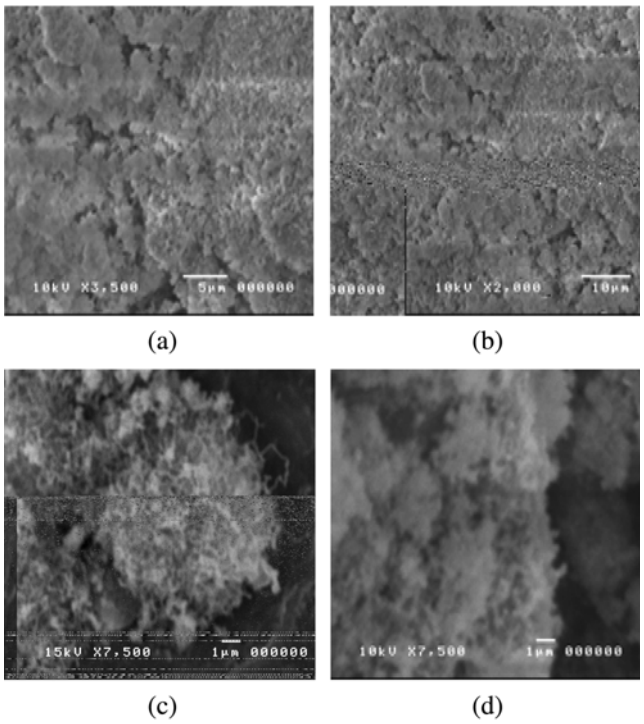

Fig. 10. SEM Micrograph of (a) and (b) fresh catalyst, (c) spent catalyst at 1,023 K, and (d) spent catalyst at 923 K after 10 successive cracking/regeneration cycles.

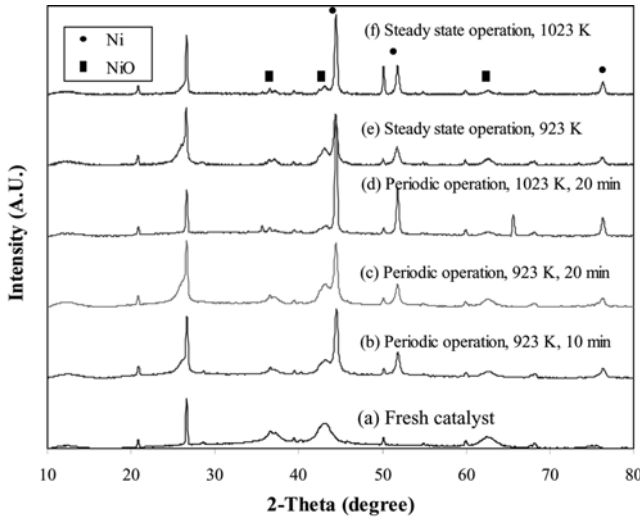

Fig. 11. XRD spectra of fresh catalyst and spent catalysts.

It can be concluded that, according to the different operating temperature and form of metal active site, the mechanisms of coke formation are different. Many researchers have suggested that the main type of carbon species which would be formed during the cracking period at high temperature was carbon whisker [Kuijpers et al., 1981; Poirier et al., 1997]. In the early stages of the deposition step, deposited carbon filaments could detach small nickel cores from bulk nickel on support. Then, the detached nickel cores which act as a growing core of whisker carbon could still accelerate the rate of carbonaceous deposition and increase their length with time on stream. After switching to the regeneration step, the carbon filaments are burned out with carbon dioxide and the nickel particles fall on the surface. The small nickel particles removed by regeneration may become inactive after the next cracking steps. Based on this suggestion, at a reaction temperature of 1,023 K, it may be stated that the growth of new carbon filaments could be terminated as a result of losing nickel active sites and no accumulation of carbon whisker on catalyst surface would occur during repeating cracking/regeneration. Consequently, the methane conversion decreased with time on stream as clearly shown in Fig. 4.

Considering the experimental results at 923 K, the formation of carbon filament was expected to be hindered by the low solubility of carbon in metal particle at low temperature. Moreover, the strong interaction between surface oxygen and metallic Ni, which results in formation of NiO in periodic operation at 923 K, was suggested to terminate the diffusivity of carbon into the nickel. These should be the cause of the different type of carbon formation at 923 K. In addition, the coke formed on the metal active sites may further move to the catalyst support, according to the drain-off phenomena that

has been reported in some reaction systems. Therefore, the accumulation of coke on the catalyst could not hinder the catalyst activity, at least within a reaction time of 200 min in this study. It should be noted that more detailed study on the Ni forms and coke formed is required to understand the behavior of the reaction system under periodic operation. It is suggested that the characterizations should be carried out separately at each reaction step of periodic operation and that operation with inert purge gas fed between each reaction step would provide additional useful data for understanding the behaviour of periodic operation.

In practical operation, it is desired, for periodic operation, that coke formation be kept as low as possible to avoid catalyst deactivation. Therefore, another set of experiments was carried out at 923 K with various values of cycle split (s). The cycle period was fixed at 20 min and the time-average flow rates of the reactant gases were kept at the same values as described earlier. It is expected that due to the slow rate of catalyst regeneration by carbon dioxide, the increase of regeneration period by lowering the feed flow rate of carbon dioxide (in order to keep the same average carbon dioxide flow rate) should help to increase the removal of coke arising from the methane cracking step and the corresponding reaction performance may be improved. The results for the cycle split (s) of 0.25, 0.4 and 0.5 are shown in Figs. 12 and 13. It was found that the decrease of the cycle split did not improve the reaction performance as expected. On the other hand, it slightly lowered both the methane and carbon dioxide conversions. This might be due to the shorter residence time during the methane cracking which caused the lower methane conversion. The decrease of carbon dioxide conversion should be due to the higher effect of mass transfer resistance at low reactant flow rate.

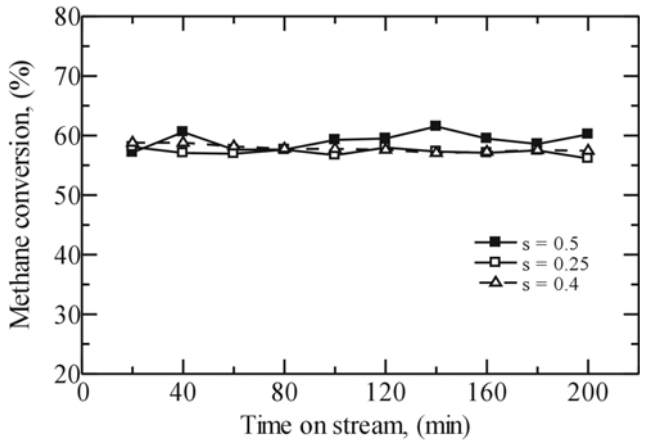

Fig. 12. Comparison of methane conversion between periodic operation at different cycle splits over Ni/SiO_2·MgO catalyst (T=923 K).

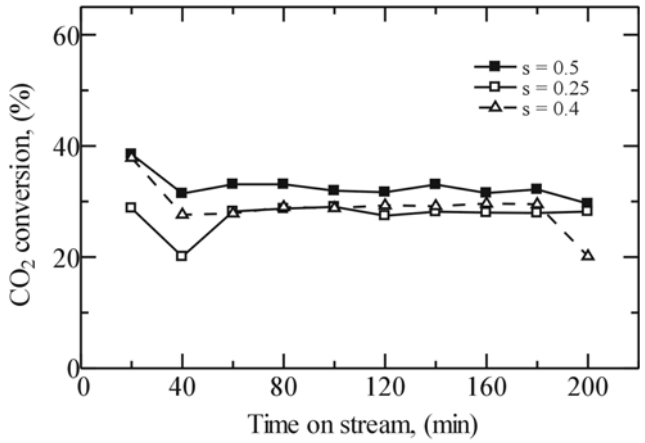

Fig. 13. Comparison of CO_2 conversion between periodic operation at different cycle split over Ni/SiO_2·MgO catalyst (T= 923 K).

CONCLUSIONS

Periodic operation was applied for the carbon dioxide reforming of methane. The effects of key parameters such as reaction temperature, cycle period and cycle split on the methane and carbon dioxide conversions and the hydrogen yield were investigated. By operating at the same time-average flow rates of the reactants, the results of the periodic operation were compared among different operating conditions and those of steady state operation. It was found that periodic operation was inferior to steady state operation at 1,023 K. However, at 923 K, the periodic operation offered the equivalent hydrogen yield of the steady state operation with an additional benefit on the separated hydrogen and carbon monoxide products in the different product streams. It was observed that the carbonaceous deposit was progressively accumulated in the catalyst bed during the course of reaction. Further studies are required to investigate the observed results in more detail.

ACKNOWLEDGMENTS

The support from The Thailand Research Fund, Commission on Higher Education, TJTTP-JBIC and the Graduate School of Chulalongkorn University is gratefully acknowledged. The authors also would like to thank Mr. Boonrat Pholjaroen for his technical assistance.

REFERENCES

Aiello, R., Fiscus, J. E., Loye, H.-C. and Amiridis, M. D., "Hydrogen production via the direct cracking of methane over Ni/SiO_2: Catalyst deactivation and regeneration," *App. Cat. A. Gen.*, **192**, 227 (2000).

Gadalla, A. M. and Bower, B., "The role of catalyst support on the activity of nickel for reforming methane with CO_2," *Chem. Eng. Sci.*, **11**, 3049 (1988).

Inui, T., Ichino, K., Matsuoka, I., Takeguchi, T., Iwamoto, S., Pu, S. B. and Nishimoto, S., "Ultra-rapid synthesis of syngas by the catalytic reforming of methane enhanced by *in-situ* heat supply through combustion," *Korean J. Chem. Eng.*, **14**, 441 (1997).

Ito, M., Tagawa, T. and Goto, S., "Suppression of carbonaceous depositions on nickel catalyst for the carbon dioxide reforming of methane," *App. Cat. A. Gen.*, **177**, 15 (1999).

Kim, M. H., Lee, E. K., Jun, J. H., Han, G. Y., Kong, S. J., Lee, B. K., Lee, T. J. and Yoon, K. J., "Hydrogen production by catalytic decomposition of methane over activated carbons: Deactivation study," *Korean J. Chem. Eng.*, **20**, 835 (2003).

Kuijpers, E. G. M., Jansen, J. W., Dillen, V. and Geus, J. W., "The revers-

ible decomposition of methane on a Ni/SiO_2 catalyst," *J. Catal.*, **1**, 75 (1981).

Monnerat, B., Kiwi-Minsker, L. and Renken, A., "Hydrogen production by catalytic cracking of methane over nickel gauze under periodic reactor operation," *Chem. Eng. Sci.*, **56**, 633 (2001).

Poirier, M. G. and Sapundzhiev, C., "Catalytic decomposition of natural gas to hydrogen for fuel cell applications," *Int. J. of Hydrogen. Energy*, **4**, 429 (1997).

Rostrup-Nielsen, J. R., "Production of synthesis gas," *Cat. Today*, **4**, 305 (1993).

Takano, A., Tagawa, T. and Goto, S., "Carbon deposition on supported nickel catalysts for carbon dioxide reforming of methane," *J. Japan Prtro. Inst.*, **39**, 144 (1996).

Zhang, T. and Amiridis, M. D., "Hydrogen production via the direct cracking of methane over silica-supported nickel catalysts," *App. Cat. A. Gen.*, **167**, 161 (1998).

Appendix 18

Elsevier Editorial System(tm) for Fuel Processing Technology
Manuscript Draft

Manuscript Number: FUPROC-D-08-00116

Title: Reactivity of Ni/SiO2.MgO toward carbon dioxide reforming of methane under steady state and periodic operations

Article Type: Research Paper

Section/Category:

Keywords: Coke; dry reforming; hydrogen; periodic operation

Corresponding Author: Professor Suttichai Assabumrungrat, Ph.D.

Corresponding Author's Institution: Chulalongkorn University

First Author: Boonrat Pholjaroen , MEng

Order of Authors: Boonrat Pholjaroen , MEng; Navadol Laosiripojana , PhD; Piyasan Praserthdam , PhD; Suttichai Assabumrungrat, Ph.D.

Manuscript Region of Origin:

Abstract:

Suggested Reviewers: Tomohiko Tagawa
Professor
tagawa@nuce.nagoya-u.ac.jp

Eric Croiset
Professor, University of Waterloo
ecroiset@cape.uwaterloo.ca

Opposed Reviewers:

Department of Chemical Engineering

Faculty of Engineering

Chulalongkorn University

April 13, 2008

Dear Professor Liu (the editor of Fuel Processing Technology),

I would like to submit a research article entitled "Reactivity of $Ni/SiO_2.MgO$ toward carbon dioxide reforming of methane under steady state and periodic operations" for your consideration for inclusion in Fuel Processing Technology. The article is original and unpublished and is not being considered for publication elsewhere.

If you have any query, please do not hesitate to contact me. I am looking forward to hearing from you.

Sincerely yours,

(Professor Suttichai Assabumrungrat)
Department of Chemical Engineering, Faculty of Engineering,
Chulalongkorn University, Bangkok 10330, Thailand
Tel: 662-2186878-82; fax:662-2186877
E-mail: Suttichai.A@chula.ac.th

Submitted to: Fuel Processing Technology

Type of contribution: Research Article

Reactivity of $Ni/SiO_2.MgO$ toward carbon dioxide reforming of methane under steady state and periodic operations

B. Pholjaroen [a], N. Laosiripojana [b], P. Praserthdam [a] and S. Assabumrungrat [a,]*

[a] *Center of Excellence in Catalysis and Catalytic Reaction Engineering,*
Department of Chemical Engineering, Faculty of Engineering,
Chulalongkorn University, Bangkok, 10330, Thailand

[b] *The Joint Graduate School of Energy and Environment,*
King Mongkut's University of Technology Thonburi, Bangkok, 10140, Thailand

[*] Corresponding authors (Email: Suttichai.A@chula.ac.th)

Abstract

The carbon dioxide reforming of methane over commercial $Ni/SiO_2.MgO$ catalyst under periodic and steady state operations were investigated at a temperature range of 650-750ºC. Under steady state operation, methane conversions tended to be constant with reaction time and increased with increasing reaction temperature. It was then observed that, at low temperature (650ºC) under the periodic operation, methane conversion was also constant at approximately 48% throughout reaction time, but for the operation at a higher temperature i.e. 750ºC, higher methane conversion (about 67%) was initially achieved but decreased dramatically with reaction time (to 27% in 240 min). The reason for the catalyst deactivation particularly under the periodic operation was further investigated. It was suggested that, at different operating temperatures, various types of coke occurred on the surface of catalyst and affected the catalytic activity. It was also found that, at low temperature under periodic operation, greater amount of coke was formed as filamentous carbon during the methane cracking period and was incompletely removed during the regeneration period. However, the deposition of this type of coke did not significantly affect the activity of catalyst. In contrast, at high temperature, lesser amount of coke was obtained but in the form of encapsulating carbon which strongly affected the activity of catalyst and resulted in the rapid catalyst deactivation.

Keywords: Coke; dry reforming; hydrogen; periodic operation

1. Introduction

Synthesis gas can be produced from several sources of hydrocarbons via different reforming reactions, which permit variations in a H_2:CO ratio. Carbon dioxide reforming of methane is attractive from an environmental view point because this reaction reduces greenhouse gases i.e. methane and carbon dioxide, which are among the main cause of the global warming problem. In certain applications such as proton-exchange membrane (PEM) fuel cell, CO-free hydrogen is required as the feed. Although carbon dioxide reforming of methane in steady-state operation can produce hydrogen, the existence of carbon monoxide and carbon dioxide in product stream is the major drawback as it is difficult and requires a costly process to separate hydrogen from these gases. A way to solve this problem is the carbon dioxide reforming of methane operated periodically by feeding methane and carbon dioxide alternately. According to this process, the first step is the catalytic thermal cracking of methane, in which methane is converted to hydrogen and coke (Eq. 1). Carbonaceous deposition typically causes plugging and catalytic deactivation problems, and thus, the second step is then applied by feeding carbon dioxide in order to regenerate the catalyst via the reverse carbon monoxide disproportionation (Eq. 2).

$$CH_4 \rightarrow C + 2H_2 \quad (1)$$

$$C + CO_2 \rightarrow 2CO \quad (2)$$

From the periodic operation, pure hydrogen can be produced separately from further gaseous product e.g. carbon monoxide. In addition, this operation also offers

another potential benefit on the heat integration within the reactor; as the exothermic heat from the catalyst regeneration can supply for the endothermic methane cracking to generate hydrogen [1].

Numerous supported transition metal catalysts (Ni, Ru, Rh, Pd, etc.) have widely been applied for the dry reforming of methane [2-5]. Rostrup-Nielsen and Bak Hansen [6] investigated the activity toward this reaction. The order of reactivity for this reaction was Ru > Rh > Ni ~ Ir > Pt > Pd, similar to their proposed order for steam reforming. They also observed that the replacing of steam with carbon dioxide gave similar activation energies, which indicated a similar rate-determining step in these two reactions. Erdohelyi et al. [7, 8] studied the influence of the catalyst support on the carbon dioxide reforming of methane over rhodium-based catalyst, and reported that the support had no effect on the activity of Rh. In contrast, Nakamura et al. [9] and Zhang et al. [10] observed that the initial turnover frequency (specific activity) of Rh crystallities was significantly affected by their supports. Zhang et al. [10] also reported that the deactivation of Rh crystallities was strongly dependent on their supports. Based on several studies, noble metal based catalysts seem to be less sensitive to coking compared to nickel based catalysts; however, noble metals are expensive and of limited availability. Nickel catalyst which has lower cost is therefore attractive for the carbon dioxide reforming of methane under periodic operation.

In the present work, the performance of carbon dioxide reforming of methane under periodic operation over an industrial steam reforming $Ni/SiO_2.MgO$ catalyst was investigated and compared to that under steady state operation at reaction temperatures between 650-750°C. Details of the carbon formation taking place during this reaction

under periodic operation were investigated by various characterization methods i.e. TPO, XRD, and BET in order to understand the behavior of catalyst toward this operation at several reaction temperatures and times. Furthermore, several pre-characterizations i.e. TPR, CH_4-TPD, and CO_2-TPD were also performed to find the suitable operation and pretreatment conditions.

2. Experimental

2.1. Catalyst

A commercial-grade reforming catalyst of 55 wt%Ni/SiO_2.MgO supplied from Japan was used in the present work. The shape of catalyst was solid cylindrical extrudate with a diameter of 3 mm and also 3 mm in length. Silicon dioxide (SiO_2) supplied by Fluka was chosen as a dilution material in this research. The average size of SiO_2 was 40-100 mesh. The ratio of Ni/SiO_2.MgO catalyst to silicon dioxide was 0.3:1 in the whole experiment.

2.2. Apparatus and procedures for catalytic reforming testing

The reaction was performed in a quartz tube (inter diameter = 11 mm) at atmospheric pressure. The quartz tube reactor was placed in the vertical direction with downward gas flow. Catalyst was placed over quartz wool which was packed for supporting the catalyst bed. The tube furnace was connected with the automatic temperature controller to supply heat to the reactor. Reactor temperature was measured by a type-K thermocouple which was placed in the furnace at the close position to the

catalyst bed. The flow rate of each reactant gas was controlled by mass flow controller (GFC17S) operated under a flow range between 0-50 mL/min. For periodic operation, each reactant feed was switched between opening and closing alternately by using a solenoid valve (Flon industry, Japan) controlled by a multi-timer (Sibata BT-3). Fig. 1 shows the schematic diagram of this lab-scale testing system.

For the catalyst testing, the mixture of catalyst with SiO_2 (0.1314 g of Ni/SiO_2.MgO with 0.438 g of SiO_2) was packed in the middle section of the reactor and then placed in the furnace. The reactor was heated up to 650°C under 30 mL/min of argon flow. When the temperature reached 650°C, the argon gas was switched off. The catalyst was reduced under 30 mL/min of hydrogen flow for 1 h. After that, the system was purged with argon again for 10 min to remove all hydrogen gas from the system and the reactor temperature was changed to a desired value (550, 650, 670, 690, 710, 730 or 750°C). For steady state operation experiment, the reaction was started by introducing 12.5 mL/min CH_4 together with 12.5 mL/min CO_2 simultaneously. For periodic operation, the multi-timer was set to control the solenoid valves to allow 25 mL/min of CH_4 to pass through the reactor for 10 min and switch to 25 mL/min of CO_2 for 10 min. The operation occurred repeatedly until the end of experimental study.

The product composition was determined by gas chromatography (Shimadzu modal 8A (GC-8A) equipped with a thermal conductivity detector (TCD)). In case of steady state operation, product gas for each reaction time was sampled from the sampling point by a syringe, whereas the product gas from periodic operation testing was collected every 10 min by using a sampling bag. Gas sample from the sampling bag was then analyzed to determine the time-average composition of the product gas.

2.3. Characterization

In order to study the physical properties, both fresh and spent catalysts were characterized by several methods as described below:

2.3.1. Temperature-programmed reduction (TPR)

The reduction temperature of fresh catalyst was measured by TPR technique using Micromeritrics Chemisorb 2750 in order to determine the amount of hydrogen consumption in reducing catalyst. A sample of 0.2 g was pre-treated in He (30 mL/min) at 250ºC for 1 h and then cooled down to room temperature. H_2 (20 mL/min) was switched into the sample while the system was heated at a ramping rate of 10ºC/min to 1000ºC. The exit gas was detected by TCD and the amount of H_2 consumed for reducing the catalyst was calculated and reported by Chemisorp TPx software.

2.3.2. Temperature-programmed desorption with CH_4 and CO_2 (CH_4-TPD and CO_2-TPD)

Adsorption ability of methane on the surface of fresh catalyst was measured by CH_4-TPD technique to determine the amount of adsorbed methane on the surface, while the basic property and carbon dioxide adsorption ability were measured by CO_2-TPD technique using Micromeritrics Chemisorb 2750 to measure the amount of adsorbed carbon dioxide on the surface.

For the CH_4-TPD, a sample of 0.3 g was pre-treated in He (30 mL/min) at 250ºC for 1 h and then reduced in H_2 (30 mL/min) at 650ºC for 1 h for the purpose of adjusting

the same condition to the catalyst before reaction. CH_4 (30 mL/min) was switched into the sample at room temperature for 1 h and then He (30 mL/min) was fed to remove adsorbed CH_4 from the surface of catalyst while the system was heated at a ramping rate of 10ºC/min to 1000ºC. The exit gas was detected by TCD. The calculation of amount of CH_4 was done and reported by Chemisorp TPx software. Regarding CO_2-TPD, the same procedure as CH_4-TPD was applied; only CO_2 was used instead of CH_4.

2.3.3. Temperature-programmed oxidation (TPO)

Temperature-programmed oxidation was used to characterize coke deposited on the spent catalysts. The operation was performed by using Micromeritrics Chemisorb 2750. The spent catalyst from the reaction was firstly pre-treated in He (25 mL/min) at 250ºC for 1 h to eliminate moisture from the catalyst and cooled down to room temperature. Then 1 vol% oxygen in helium (15 mL/min) was switched into the sample while the system was heated at a ramping rate of 10ºC/min to 1000ºC and the exit gas was detected by a TCD detector. The calculation of amount of CO_2 in the effluent gas was analyzed and reported by Chemisorp TPx software.

3. Results and discussion

3.1. Characterization of fresh Ni/SiO_2.MgO Catalyst

TPR profile of the fresh catalyst is shown in Fig. 2. Three reduction peaks were observed at 190, 616, and 813ºC. The strong peak observed at 616ºC can be assigned to the reduction of Ni species with strong interaction with silicon dioxide support. The peak

at 813ºC is assigned to the reduction of Ni species with strong interaction with magnesium oxide. According to all experiments in the present work, the reduction temperature was 650ºC and, therefore, the metallic phase should be converted from nickel oxide to metallic nickel which is more active before the reaction test.

CH_4 temperature-programmed desorption (CH_4-TPD) of fresh catalysts was carried out in order to study the methane adsorption behavior on this type of catalyst. The samples were reduced in H_2 at 650ºC for 1 h prior to adsorption of CH_4 and then the adsorbed catalysts were purged with He at the same adsorption temperature to remove physisorption. The results shown in Fig. 3 indicate that methane adsorbs on the surface of $Ni/SiO_2.MgO$ at the temperature range of 600-1000ºC and the methane adsorption at reaction temperature of 750ºC is significantly higher than that at 650ºC. Thus, the methane conversion at 750ºC should be higher than that at 650ºC.

It was proposed that basic property of catalyst improves activity of CO_2 reforming reaction. The effect of the surface basicity of the catalysts was studied by CO_2-TPD. The CO_2-TPD profile of $Ni/SiO_2.MgO$ is presented in Fig. 4. Two peaks were presented at 150 and 815ºC. The first peak at low temperature may be attributed to the desorption of adsorbed CO_2 on weak basic site, while the second peak may be related to strong basic site of the catalyst. Similar to CH_4 adsorption, it was found that CO_2 adsorption at 750ºC was higher than that at 650ºC. Thus, the activity of this catalyst in carbon dioxide reforming of methane would be better at higher temperatures.

Lastly, N_2 physisorption was also carried out by Micromeritrics model ASAP 2020. The values of BET surface area, pore volume, and pore size of fresh $Ni/SiO_2.MgO$

are 121.43 m^2/g, 0.18 cm^3/g, and 59.52 Å, respectively. The catalyst has pore diameter distribution in mesopore range with the range of 20-100 Å (not shown).

3.2. Catalytic activity in carbon dioxide reforming of methane

The behavior of the carbon dioxide reforming of methane over $Ni/SiO_2.MgO$ catalyst under periodic and steady state operations was investigated at the reaction temperature range of 650-750ºC. For periodic operation, the testing consists of two main steps: (i) methane cracking by feeding methane solely and (ii) regeneration of catalyst via reverse Boudouard reaction by feeding carbon dioxide. In contrast, for steady state operation, the operation was carried out by feeding methane and carbon dioxide simultaneously. It should be noted that the average flow rates of the reactant feeds for both operations were identical. The variations of catalytic reactivities (in terms of methane and carbon dioxide conversions and hydrogen yield) with time at different temperatures under periodic and steady state operations were shown in Figs. 5-6 and Figs. 7-9, respectively.

As shown in Fig. 5 for the periodic operation, at higher temperatures, high methane conversion was achieved at the beginning of reaction but decreased dramatically with reaction time. In contrast, for the periodic testing at lower temperature, methane conversion was almost constant throughout the reaction time. At 750ºC, $Ni/SiO_2.MgO$ catalyst showed high conversion of methane (approximately 67%) at the beginning but declined rapidly to 27% after operating for 240 min, whereas the conversion of methane at reaction temperature 650ºC started at about 48% and remained constant along the reaction time. For the testing at temperatures between 670-730ºC, methane conversions

showed the same trend. The reduction of methane conversion became more pronounced at higher temperatures. Similar trend was observed for carbon dioxide conversion under periodic operation as shown in Fig. 6. It was found that the carbon dioxide conversion at reaction temperature of 750ºC decreased from 55% at the beginning to 24% after 240 min, whereas at reaction temperature of 650ºC, carbon dioxide conversion was nearly constant at 35%. Under the periodic operation, because only the methane cracking takes place during the methane feeding, the hydrogen yield is theoretically equal to the methane conversion. It should be noted that the difference between the methane conversion and carbon dioxide conversion which is particularly large at lower temperature operation indicates that the coke generated during the methane cracking cannot be totally removed and thus accumulated on the catalyst.

Under steady state operation, as shown in Fig. 7, methane conversion did not decrease with increasing reaction time in this range of temperature studied. After exposure for 240 min, the methane conversions at 650, 670, 690, 710, 730, and 750ºC were 63, 73, 83, 81, 84, and 90% respectively. Methane conversions for steady state operation tended to be constant with reaction time and increase with increasing reaction temperature. As shown in Figs. 8-9, carbon dioxide conversions and hydrogen yield tended to be constant with reaction time but did not show clear tendency with reaction temperature. It offered the highest and lowest conversions at reaction temperatures 690 and 710ºC respectively. This is probably affected by the occurrence of the reverse water-gas shift reaction.

Comparison of the catalyst activity under the periodic operation with the steady state operation in this range of reaction temperature revealed that Ni/SiO_2.MgO showed

stability under the steady state operation. In contrast, under the periodic operation, the catalyst showed stability at low temperature but showed a rapid decline of activity over reaction time at high temperature. The reason for catalyst deactivation was then further investigated. Theoretically, the deactivation should be mainly due to the formation of carbon species on the surface of catalyst. It was suggested that, at different operating temperatures, various types of coke formation could occur on the surface of catalyst and affect the catalytic activity under periodic operation. Thus, characterization of spent catalyst was carried out to clarify the catalyst testing results, as presented in the next section.

3.3. Characterization of spent catalysts

Firstly, the changes in weight of catalyst were considered to be related to the degree of coke formation on the surface of spent catalysts. Fig. 10 shows the weights of catalyst at various reaction times and temperatures. It is clear that both reaction temperature and reaction time influence the change in catalyst weight. According to this figure, at the beginning, the catalyst was reduced with hydrogen to form metallic phase of nickel species, the weight of reduced catalyst decreased about 5.5%. Then the reforming reaction under periodic operation started and the weights of used catalysts were measured at reaction time of 90 min which was ending time of a methane cracking period. It was found that lower coke formation was observed in the system at higher reaction temperature. At the reaction time of 100 min which was ending time of a regeneration period, it was found that significant amount of coke could not be removed and remained present in the system at lower reaction temperature. Similar trends were observed at

reaction times of 190 and 200 min. It is interesting that the methane conversion still remained high for low temperature operation although the significant increase of coke accumulation was observed. This phenomenon was possibly affected by the forming of various types of coke at different reaction temperatures.

Table 1 presents the BET studies over catalyst at different conditions. It was found that reaction temperature and reaction time also affected the surface area of catalyst. The BET surface area of fresh catalyst is 104.62 m^2/g. Reducing the catalyst at 650°C with hydrogen decreased the BET surface area to 46.96 m^2/g due to the surface sintering and the change of NiO to metallic nickel. In order to investigate the effect of sintering on BET surface area, the fresh catalyst was also calcined in air at 750ºC for 3 h. It was found that high temperature dramatically affected on BET surface area of the catalyst. It should be noted that the amount of coke formed also affects the specific surface area of catalyst; at low temperature under periodic operation, BET surface areas increased after methane cracking period and decreased after regeneration with carbon dioxide.

TPO testing of used catalysts at different reaction times and reaction temperatures were carried out (Figs. 11(a)-(f)). The principle of TPO is to evaluate the amount of coke removed from the used catalyst by burning with oxygen. According to the results, the profile revealed two peaks of coke at oxidizing temperatures ca. 530 and 880ºC. The first peak was narrow and high whereas the second peak was board and low. This strongly indicates that at least 2 different types cokes were formed on the surface of catalyst. It should also be noted that after the regeneration by carbon dioxide the first peak at low

temperature shifted to a higher temperature, indicating that some easily combusted coke was removed from the catalyst surface.

The SEM micrographs of used catalysts from periodic operation in the range of reaction temperature between 650-750ºC are shown in Figs. 12(a)-11(f). The SEM experiments were carried out using JEOL JSM-35F scanning electron microscope operated under the back scattering electron (BSE) mode at 20 kV. All samples were tested after exposure in the reaction for 190 min, which was the ending time of methane cracking period. It can be seen that carbon formation in carbon dioxide reforming of methane presented the structure of filamentous carbon on the surface of catalyst over this range of temperature. From the literature, it was found that the formation of this type of carbon induced a serious pressure drop in the reactor [11]. Other type of carbon which was expected to form over this range of temperature is the encapsulated carbon. It was believed that the encapsulated carbon strongly affects the stability of catalyst by blocking the active site of metallic catalyst, nevertheless, it is difficult to prove the formation of encapsulated carbon by SEM micrograph. From SEM results, filamentous carbon was obviously found on the surface of catalyst for all reaction temperatures. It was also observed that when the high temperature was employed, the larger particle size of filamentous coke was observed.

The crystallinity and structure of catalysts were analyzed by XRD analysis. The XRD analysis was performed by a SIEMENS D5000 X-ray diffractometer connected with a personal computer with Diffract AT version 3.3. The measurement was carried out by using CuK_{α} radiation with Ni filter. The step-scan covered the angular range 10-80° (2θ) in steps of 2θ = 0.04°. The XRD patterns of used catalysts at reaction temperature

range of 650-750ºC are shown in Figs. 13(a)-(f). These patterns presented evidently the strong peaks at 2θ = 26.6 and 44.5º and several low intensity peaks at certain degrees for all samples. The peak at 2θ = 26.6º was attributed to be the coke deposited on the surface of the catalyst. The presence of main structure of metallic Ni showed peaks at 2θ = 44.5, 51.8, and 76.4º. The crystal structure of NiO was also observed for low intensity peaks at 2θ = 37.1, 43.1 and 62.7º. For tendency, higher and sharper intensity peaks of coke and Ni were found when reaction temperature was higher. This XRD results indicated that there were the differences of catalyst particle sizes at various reaction temperatures. The d-spacing of nickel and coke were then calculated by Scherrer equation as shown in Table 2. The d-spacing of nickel was obtained from peak at 44.5º whereas that of coke was obtained from peak at 26.6º. It was found that when the higher temperature was used, the higher d-spacing for both nickel and coke were obtained; this is mainly due to the effect of catalyst sintering. This result was corresponding to the result of BET surface area as high value of d-spacing induced size of particle to be larger and lessened BET surface area. It should also be noted that the d-spacing increased after regeneration with carbon dioxide and decreased after methane cracking in the next cycle. High values of d-spacing for both nickel and coke caused the blockage of active site of catalyst. Thus, it was probable to bring to the loss of stability of catalyst.

From the above results it is likely that the at low temperature under periodic operation, greater amount of coke was formed as filamentous carbon during the methane cracking period and was incompletely removed during the regeneration period. However, the deposition of this type of coke did not significantly affect the activity of catalyst. In contrast, at high temperature, lesser amount of coke was obtained but in the form of

encapsulating carbon which strongly affected the activity of catalyst and resulted in the rapid catalyst deactivation.

4. Conclusion

The carbon dioxide reforming of methane under the periodic and steady state operations in a range of reaction temperature between 650-750^{o}C was compared. It was found that Ni/SiO_2.MgO catalyst showed good stability under steady state operation for all operating temperatures, but showed stability only at low temperature for the periodic operation. According to the spent catalyst characterizations, carbon formation from carbon dioxide reforming of methane under periodic operation at the reaction temperature range 650-750^{o}C presented at least two different types of coke taking place on the surface of catalyst. At low temperature, great amount of coke was formed during the methane cracking period and was incompletely removed during the regeneration period. At this temperature, coke was mostly formed in the structure of filamentous carbon. In contrast, at high temperature, a lesser amount of coke was obtained but it was formed in encapsulating form which strongly affected the activity of catalyst and resulted in the rapid catalyst deactivation.

Acknowledgement

The research was financially supported by the Thailand Research Fund, Commission on Higher Education and the Graduate School of Chulalongkorn University. The authors also would like to thank Professor Goto and Professor Tagawa for providing the catalyst.

References

[1] B. Monnerat, L. Kiwi-Minsker, and A. Renken, Chem. Eng. Sci., 56, (2001), 633.

[2] T. Sodesawa, A. Dobashi and F. Nozaki, React. Kinet. Catal. Lett., 12, (1979), 107.

[3] L. Topor, L. Bejan, E. Ivana, N. Georgescu, Revue Chim. Bucharest, 30, (1979), 539.

[4] T.A. Chubb, Sol. Energy, 24, (1980), 341.

[5] T.A. Chubb, J.H. McCrary, G.E. McCrary, J.J. Nemecek and D.E. Simmons, Proc. Meet. Am. Sect. Int. Sol. Eng. Soc., 4, (1981), 166.

[6] J.R. Rostrup-Nielsen and J.H. Bak Hansen, J. Catalysis, 144, (1993), 38.

[7] A. Erdöhelyi, J. Cserényi and F. Solymosi., J. Catal., 141, (1993), 287.

[8] A. Erdöhelyi, J. Cserényi, E. Rapp and F. Solymosi., Appl. Catal. A: Gen., 108, (1994), 205.

[9] J. Nakamura, K. Aikawa, K. Sato and T. Uchijima., Catal. Lett., 25, (1994), 265.

[10] Z.L. Zhang, V.A. Tsipouriari, A.M. Efstathiou and X.E. Verykios., J. Catal., 158, (1996), 51.

[11] Takano, A., Tagawa, T., and Goto, S. Journal of Chemical Engineering of Japan, 27, (1994), 727.

Figure

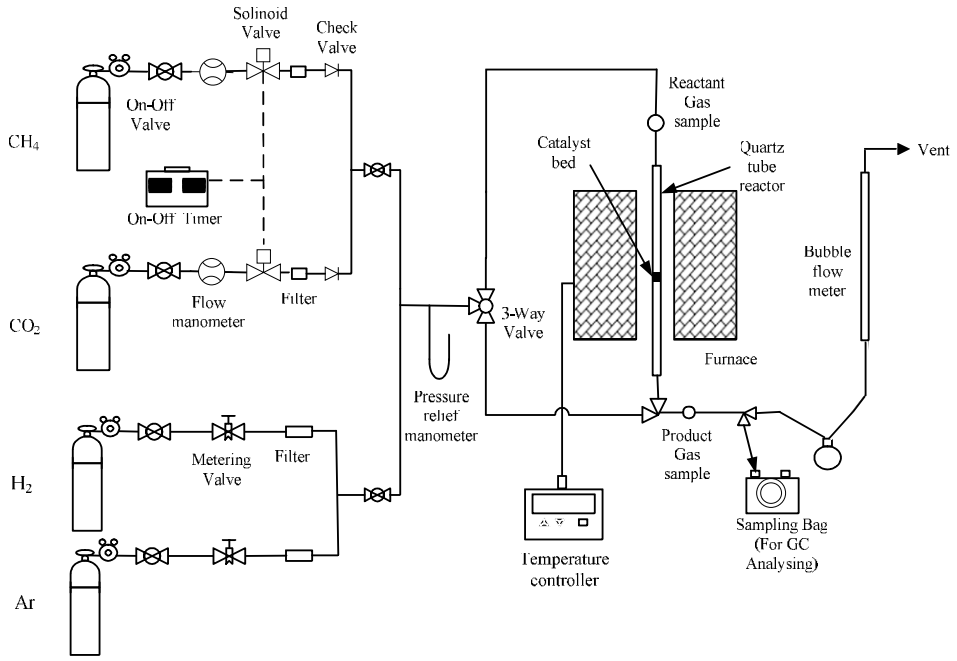

Fig.1 - Schematic diagram of the experimental setup.

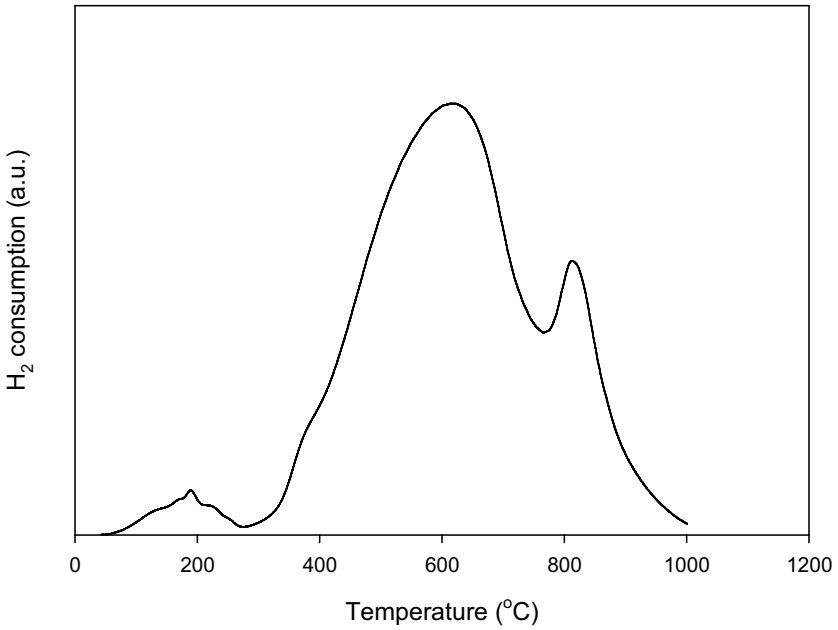

Fig. 2 - Temperature-programmed reduction profile of fresh catalyst.

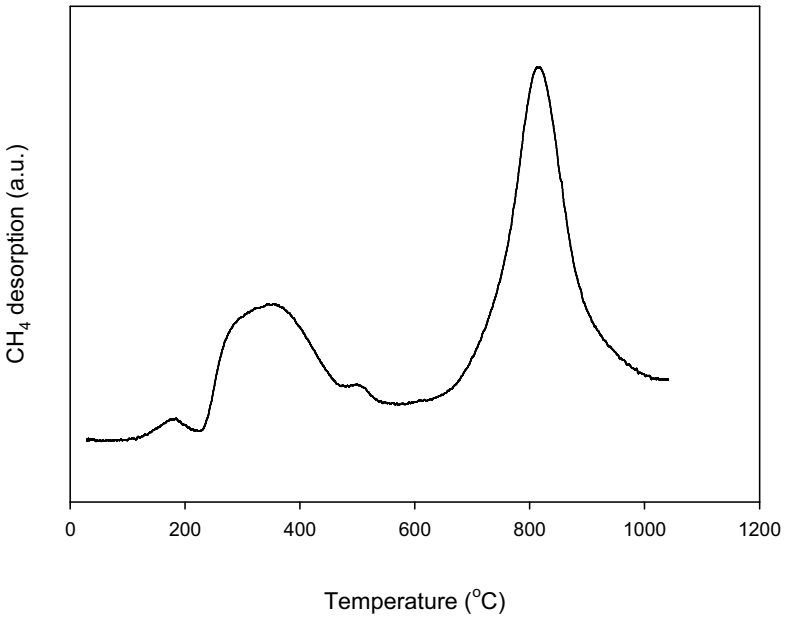

Fig. 3 - CH_4 temperature-programmed desorption profile of fresh catalyst.

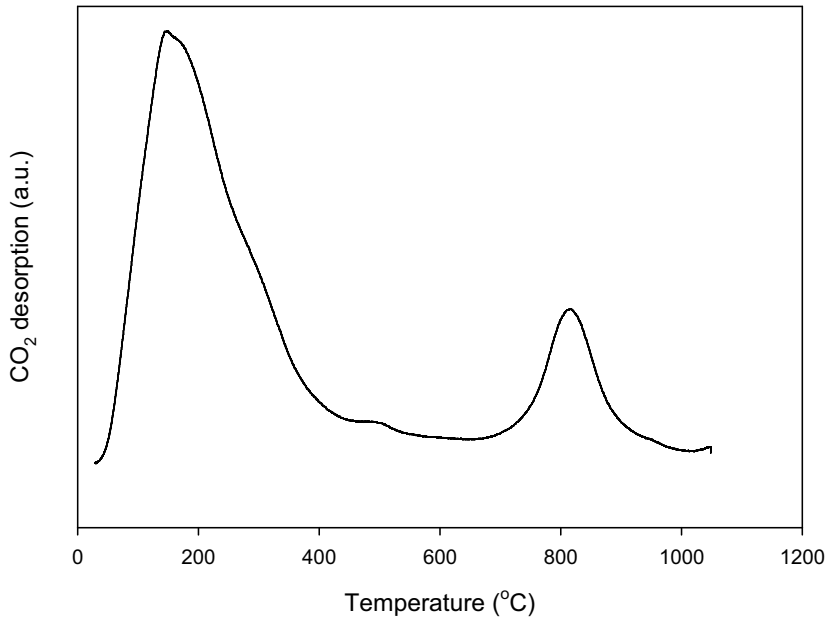

Fig. 4 - CO_2 temperature-programmed desorption profile of fresh catalyst.

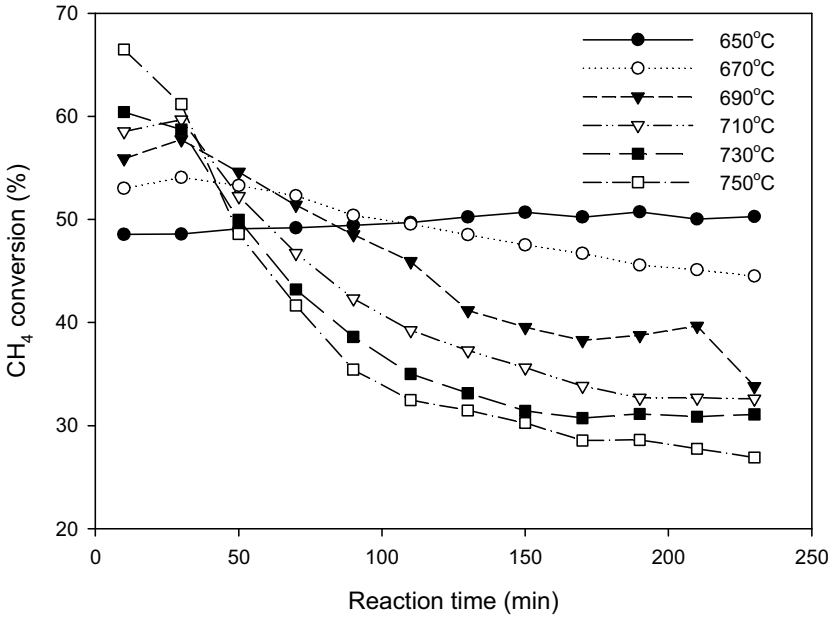

Fig. 5 - Methane conversion in carbon dioxide reforming of methane reaction under periodic operation at different reaction temperatures.

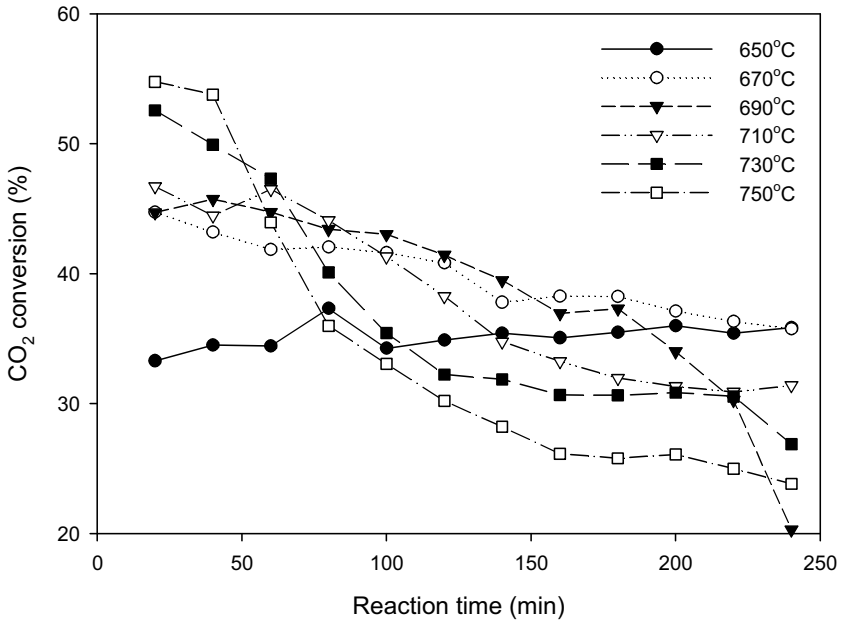

Fig. 6 - Carbon dioxide conversion in carbon dioxide reforming of methane reaction under periodic operation at different reaction temperatures.

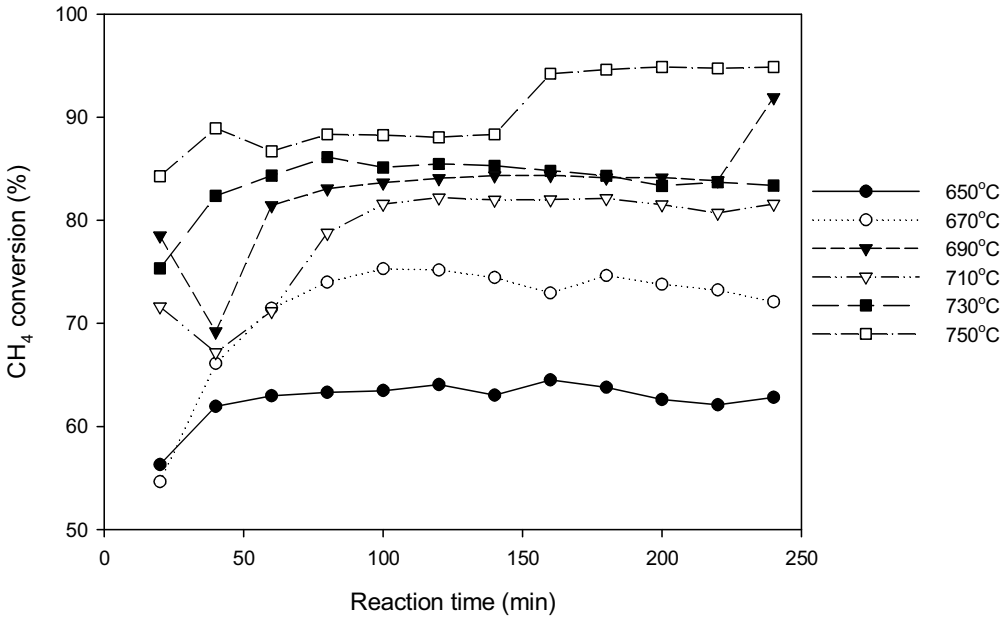

Fig. 7 - Methane conversion in carbon dioxide reforming of methane reaction under steady state operation at different reaction temperatures.

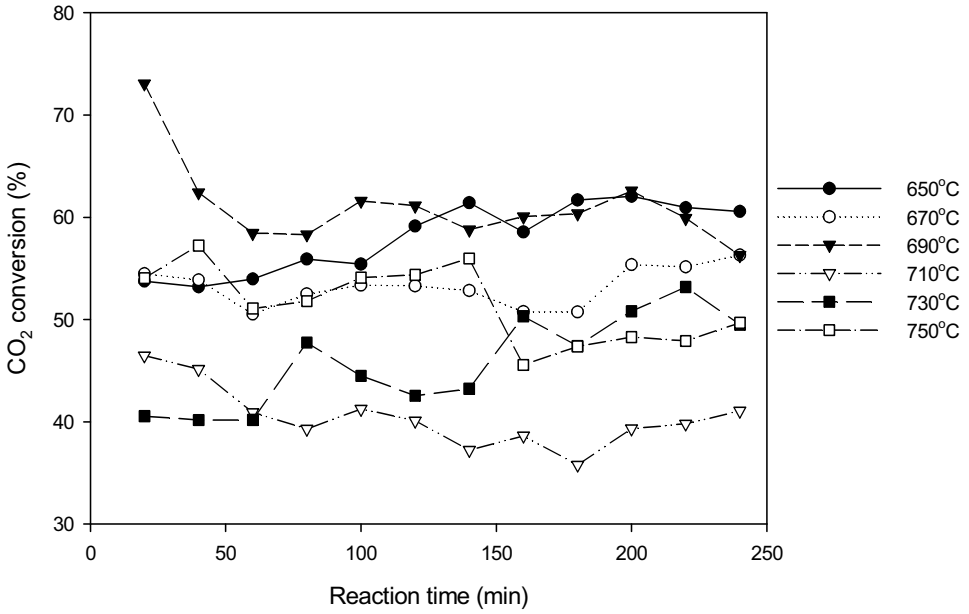

Fig. 8 - Carbon dioxide conversion in carbon dioxide reforming of methane reaction under steady state operation at different reaction temperatures.

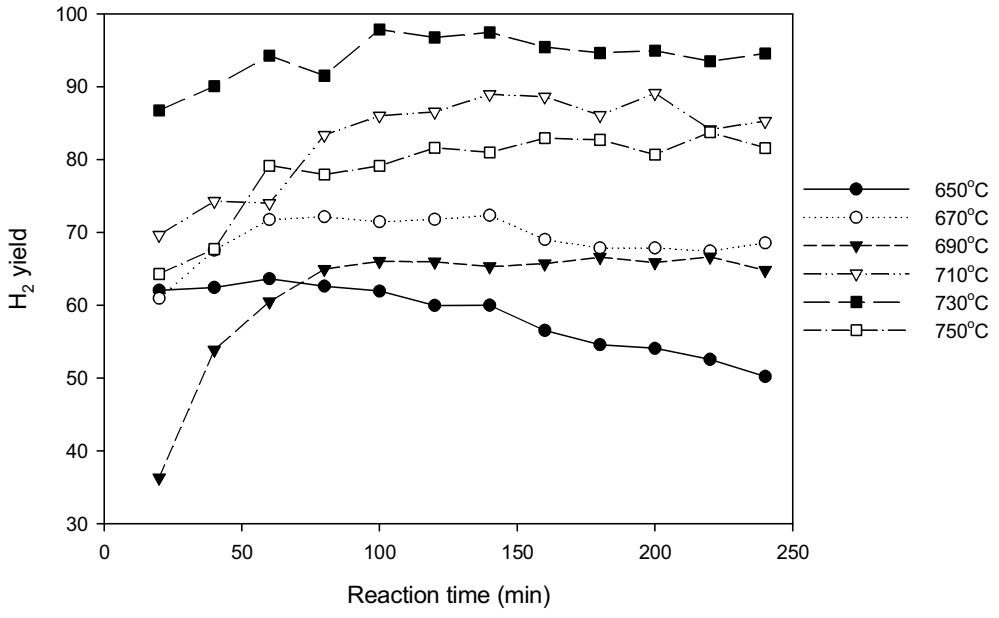

Fig. 9 - Hydrogen yield in carbon dioxide reforming of methane reaction under steady state operation at different reaction temperatures.

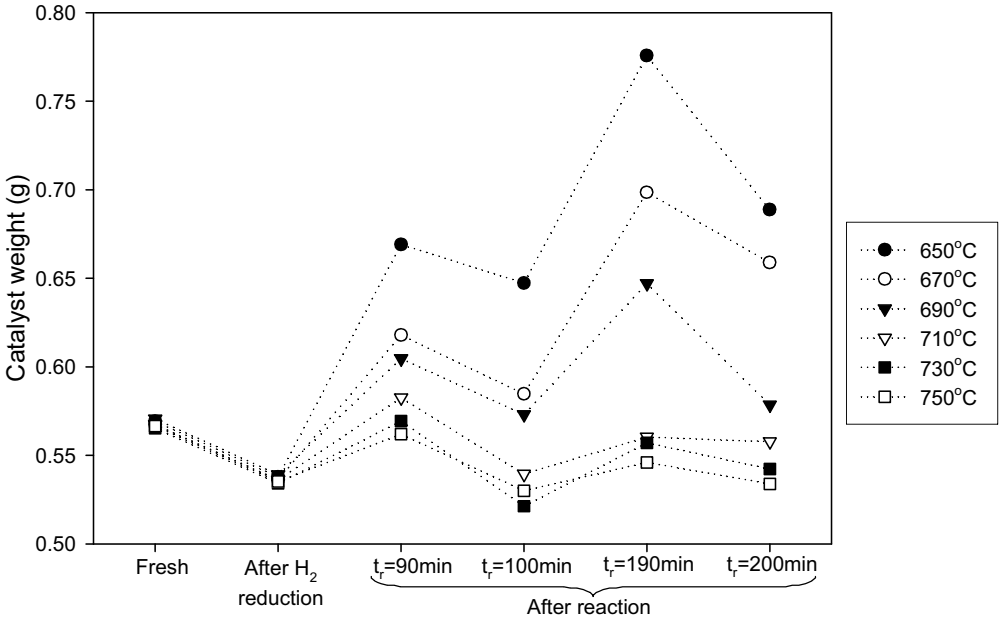

Fig. 10 - Catalyst weights before and after reaction.

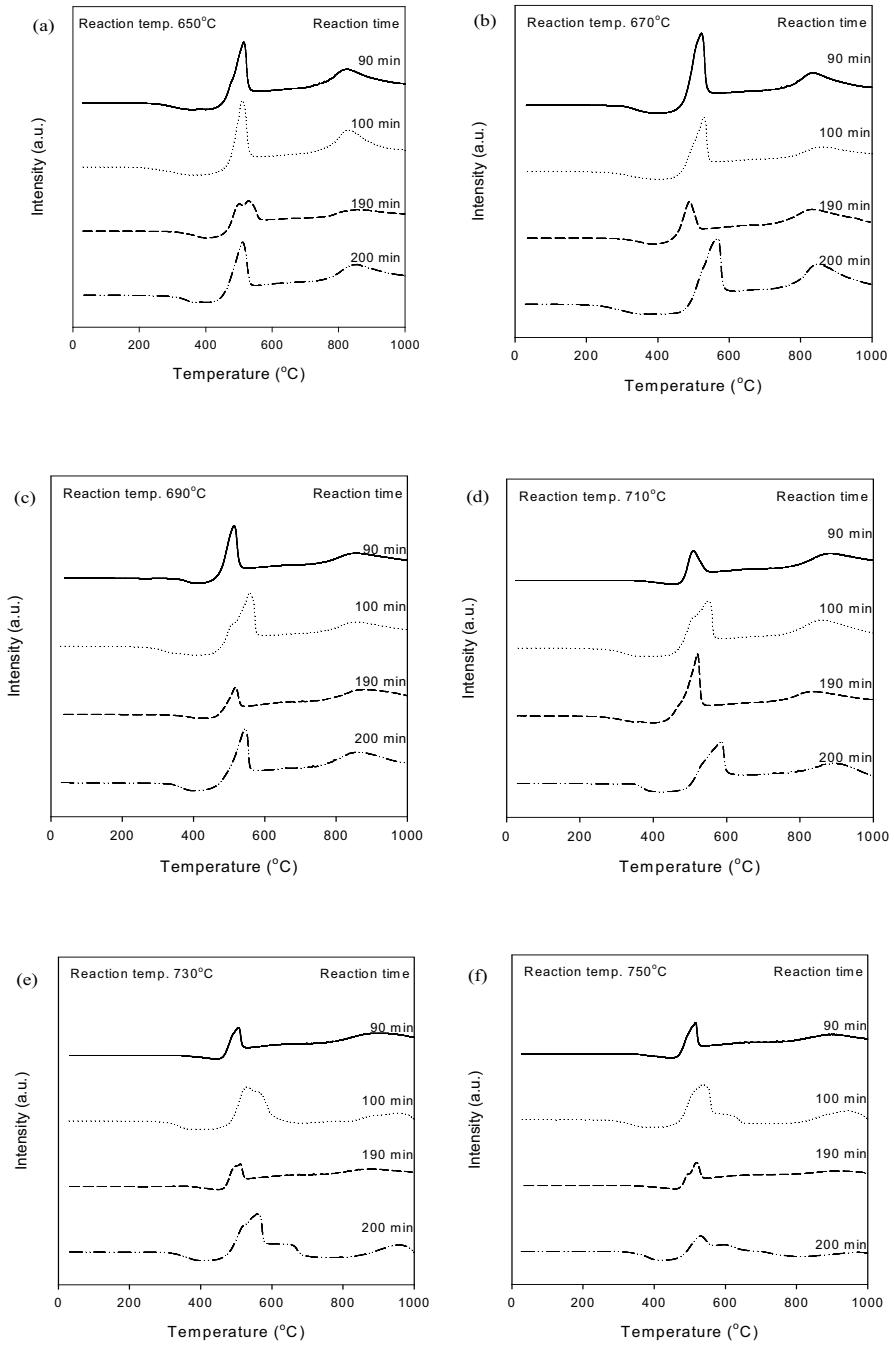

Fig. 11 - TPO profiles of used catalysts at different reaction times and reaction temperatures (a) at 650ºC (b) at 670ºC (c) at 690ºC (d) at 710ºC (e) at 730ºC and (f) at 750ºC.

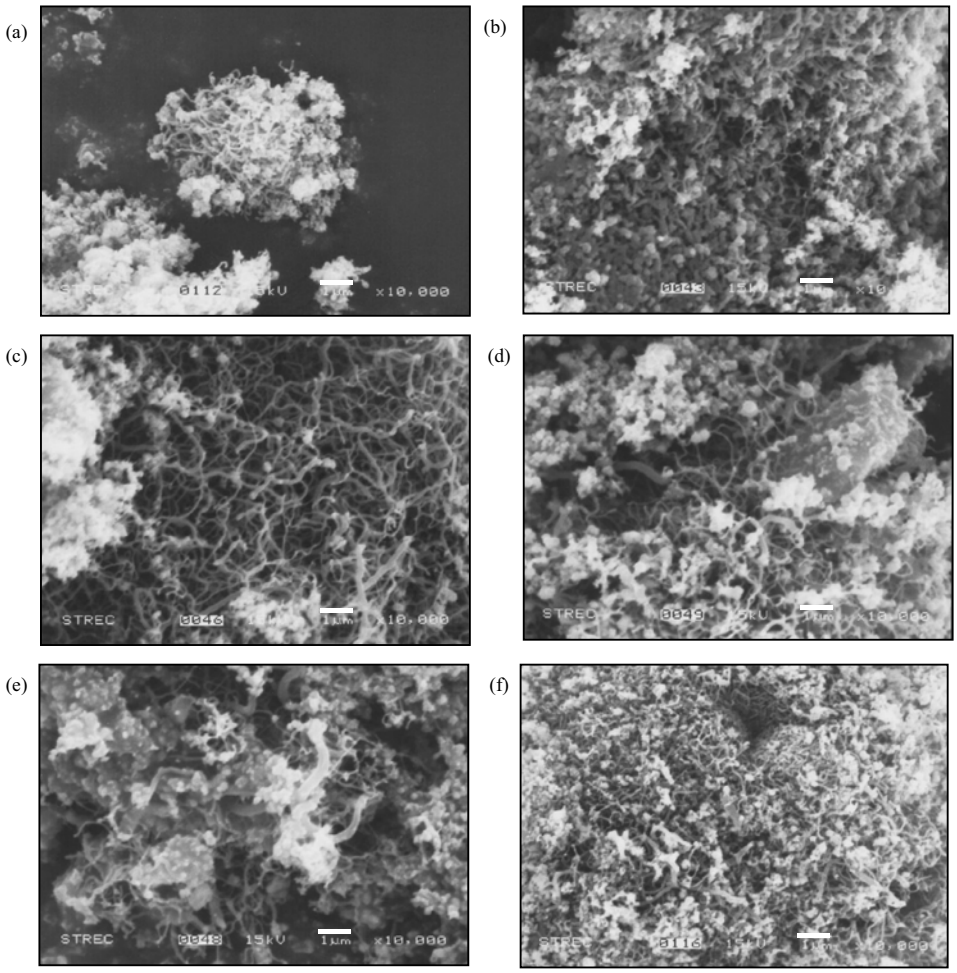

Fig. 12 - SEM micrographs of used catalysts at reaction time = 190 minutes and different reaction temperatures: (a) at 650ºC (b) at 670ºC (c) at 690ºC (d) at 710ºC (e) at 730ºC and (f) at 750ºC.

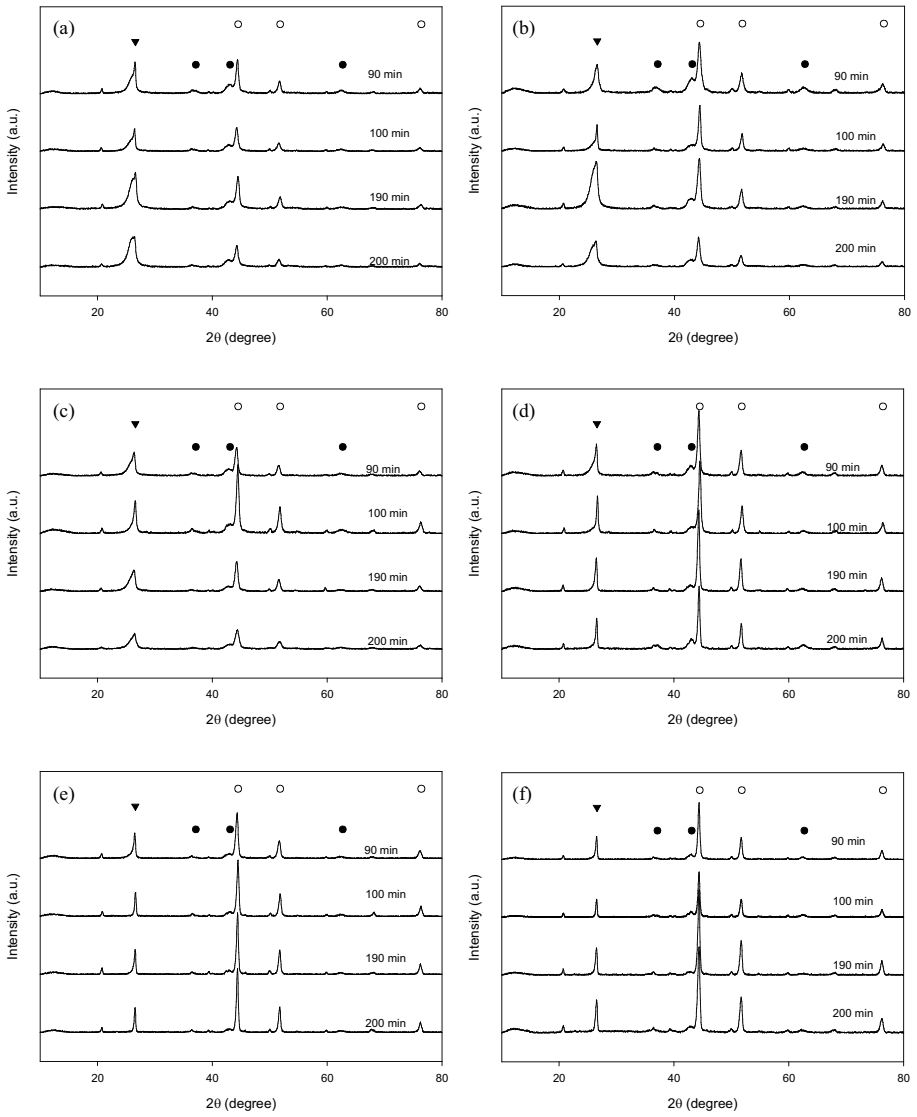

Fig. 13 - XRD patterns of used catalysts at different reaction times and reaction temperatures (a) at 650ºC (b) at 670ºC (c) at 690ºC (d) at 710ºC (e) at 730ºC and (f) at 750ºC ▾ Coke ◦ Ni • NiO.

Table 1 - BET surface areas of catalysts at different conditions.

Catalysts	Surface area (m^2/g)			
Fresh	104.62			
After reduction with hydrogen at 650ºC	46.96			
After calcination in air at 750ºC 3 h	45.43			
After reaction at	reaction time			
reaction temperature	90 min	100 min	190 min	200 min
650ºC	56.24	60.51	76.56	64.99
670ºC	33.94	50.11	78.24	51.69
690ºC	47.77	33.56	65.52	59.07
710ºC	47.89	35.95	32.30	18.55
730ºC	31.24	20.97	17.94	14.54
750ºC	20.74	19.36	20.42	14.06

Table 2 - The d-spacing of nickel and coke deposited on catalysts at different conditions.

Catalysts	d-spacing of nickel (nm)				d-spacing of coke (nm)			
Fresh	4.83				-			
After reaction at	reaction time							
Reaction temperature	90 min	100 min	190 min	200 min	90 min	100 min	190 min	200 min
650ºC	18.23	14.96	14.90	13.86	9.82	10.09	6.50	5.73
670ºC	12.97	22.72	14.54	15.45	10.39	29.26	6.34	5.95
690ºC	15.60	19.32	15.04	11.16	8.38	17.66	7.03	7.62
710ºC	20.80	22.69	25.96	27.61	16.44	33.40	24.52	31.04
730ºC	19.53	26.23	29.25	30.69	23.88	37.79	30.03	39.48
750ºC	26.88	28.25	27.92	20.90	35.75	39.34	27.36	26.10